



IntechOpen

Earthquake Ground Motion

Edited by Walter Salazar



Earthquake Ground Motion

Edited by Walter Salazar

Published in London, United Kingdom

Earthquake Ground Motion
<http://dx.doi.org/10.5772/intechopen.110918>
Edited by Walter Salazar

Contributors

Shutian Ma, Parisa Asgharzadeh, Dariush Motazedian, Laura Peruzza, Eliana Esposito, Felix Enrique Rodríguez García, Giuseppe Giunta, Giuseppe Pucciarelli, Albert Kafui Klu, Edmund Nana Asare, Jamel Seidu, Nicholas Opoku, Vincenzo Fioravante, Daniela Giretti, Haeam Kim, Prem Nath Maskey, Valeria Yanina Scapini Sánchez, Cinthya Leonor Vergara Silva, Ali Akbar Firoozi, Ali Asghar Firoozi, Yanjun Chen, Lanxin Zhu, Fangshuo Shi, Yan He, Zhengbin Li

© The Editor(s) and the Author(s) 2024

The rights of the editor(s) and the author(s) have been asserted in accordance with the Copyright, Designs and Patents Act 1988. All rights to the book as a whole are reserved by INTECHOPEN LIMITED. The book as a whole (compilation) cannot be reproduced, distributed or used for commercial or non-commercial purposes without INTECHOPEN LIMITED's written permission. Enquiries concerning the use of the book should be directed to INTECHOPEN LIMITED rights and permissions department (permissions@intechopen.com).

Violations are liable to prosecution under the governing Copyright Law.



Individual chapters of this publication are distributed under the terms of the Creative Commons Attribution 3.0 Unported License which permits commercial use, distribution and reproduction of the individual chapters, provided the original author(s) and source publication are appropriately acknowledged. If so indicated, certain images may not be included under the Creative Commons license. In such cases users will need to obtain permission from the license holder to reproduce the material. More details and guidelines concerning content reuse and adaptation can be found at <http://www.intechopen.com/copyright-policy.html>.

Notice

Statements and opinions expressed in the chapters are those of the individual contributors and not necessarily those of the editors or publisher. No responsibility is accepted for the accuracy of information contained in the published chapters. The publisher assumes no responsibility for any damage or injury to persons or property arising out of the use of any materials, instructions, methods or ideas contained in the book.

First published in London, United Kingdom, 2024 by IntechOpen
IntechOpen is the global imprint of INTECHOPEN LIMITED, registered in England and Wales, registration number: 11086078, 5 Princes Gate Court, London, SW7 2QJ, United Kingdom

British Library Cataloguing-in-Publication Data
A catalogue record for this book is available from the British Library

Additional hard and PDF copies can be obtained from orders@intechopen.com

Earthquake Ground Motion
Edited by Walter Salazar
p. cm.
Print ISBN 978-0-85466-221-0
Online ISBN 978-0-85466-220-3
eBook (PDF) ISBN 978-0-85466-222-7

We are IntechOpen, the world's leading publisher of Open Access books Built by scientists, for scientists

6,900+

Open access books available

184,000+

International authors and editors

200M+

Downloads

156

Countries delivered to

Our authors are among the
Top 1%

most cited scientists

12.2%

Contributors from top 500 universities



WEB OF SCIENCE™

Selection of our books indexed in the Book Citation Index
in Web of Science™ Core Collection (BKCI)

Interested in publishing with us?
Contact book.department@intechopen.com

Numbers displayed above are based on latest data collected.
For more information visit www.intechopen.com



Meet the editor



Dr. Walter Salazar is a structural, civil engineer who obtained a Ph.D. in Engineering Seismology from the Interdisciplinary Graduate School of Science and Engineering, Tokyo Institute of Technology, Japan, in 2004. Dr. Salazar has actively researched seismic hazards and site effects, producing several peer-reviewed maps for El Salvador, Jamaica, and the Eastern Caribbean. He has published about sixty articles in international scientific journals, books, and conferences. In 2011, Dr. Salazar received a Distinguished Salvadoran National Award and, in 2023, a National Award for Scientific Research from the National Council of Science and Technology of El Salvador. He is a Professor of Civil Structural Engineering at the Catholic University of El Salvador.

Contents

Preface	XI
Section 1	
Seismicity	1
Chapter 1	3
The Source Rupture Models and Seismogenic Structures of the Iran 2017 M_W 7.3 Earthquake <i>by Shutian Ma, Parisa Asgharzadeh and Dariush Motazedian</i>	
Chapter 2	25
A Tool for Archiving and Updating Knowledge about Past Earthquakes in Central America <i>by Laura Peruzza, Eliana Esposito, Felix Enrique Rodríguez García and Giuseppe Giunta</i>	
Chapter 3	47
The Role of Earthquake Catalogue in Seismic Tomography <i>by Giuseppe Pucciarelli</i>	
Chapter 4	61
Looming Earthquake Threat in Ghana <i>by Albert Kafui Klu, Edmund Nana Asare, Jamel Seidu and Nicholas Opoku</i>	
Section 2	
Site Effects	77
Chapter 5	79
Physical Modeling of Liquefaction in Various Granular Materials <i>by Vincenzo Fioravante and Daniela Giretti</i>	
Chapter 6	109
Comparison of Site Response Analysis (SRA) According to Ground Modelling and Structure Consideration <i>by Haeam Kim</i>	

Chapter 7	129
Generation of Site-Dependent Earthquake Ground Motion Parameters <i>by Prem Nath Maskey</i>	
Section 3	
Infrastructure	143
Chapter 8	145
Disasters and Housing Infrastructure: Evidence from the 2010 Chilean Earthquake <i>by Valeria Yanina Scapini Sánchez and Cinthya Leonor Vergara Silva</i>	
Section 4	
Tsunamis	165
Chapter 9	167
Non-seismic and Complex Source Tsunami: Unseen Hazard <i>by Ali Akbar Firoozi and Ali Asghar Firoozi</i>	
Section 5	
Instrumentation	205
Chapter 10	207
Perspective Chapter: Application of Gyroscopes in Geophysics <i>by Yanjun Chen, Lanxin Zhu, Fangshuo Shi, Yan He and Zhengbin Li</i>	

Preface

Earthquakes continue to be some of the natural phenomena that intrigue us. Civil engineers are usually attracted to structural earthquake analysis and design conforming to their consultancies and thus companies and researchers have advanced laboratory tests and software tools in the last decades. However, the quantification of earthquake ground motion is still in its infancy. This book, *Earthquake Ground Motion*, merges several fields of knowledge to improve the curricula for geoscientists and engineers. I believe that future education must be focused on connecting structural and seismology fields.

Earthquake Ground Motion is a result of the tireless efforts of twenty-three researchers from nine countries. It is organized into five sections and ten chapters.

Section 1, “Seismicity”, includes Chapters 1–4. In Chapter 1, Shutian Ma et al. present the rupture models and seismogenic structures of the Iran 2017 M_W 7.3 earthquake. The chapter is written didactically, including new findings, as the high-velocity zones are over a low-velocity zone and the final validation for a shallow dipping fault rather than a steep one. In Chapter 2, Laura Peruzza et al. propose a tool for archiving macroseismic information about historical and instrumental earthquakes in three countries in Central America (Guatemala, El Salvador, and Nicaragua) based on the results of the RIESCA project. This chapter constitutes the first and primary source of information for researchers in the region. In Chapter 3, Giuseppe Pucciarelli presents the fundamentals of seismic tomography based on theoretical and practical examples. In Chapter 4, Albert Kafui Klu et al. describe the basic features of seismicity through tectonics and an earthquake catalog in Ghana. The chapter also includes a multichannel analysis of surface waves (MASW) to characterize the soils in the country.

Section 2, “Site Effects”, includes Chapters 5–7. Chapter 5 by Vincenzo Fioravante and Daniela Giretti presents the physical modeling of liquefaction in granular materials as a recompilation of past researchers focused on Italy’s earthquake cases. They offer results of tests at different scales, from cyclic triaxial tests to small-scale models in a centrifuge. They provide behavioral tools for predicting the liquefaction phenomenon and show the efficacy of vertical and horizontal drains as a liquefaction mitigation technique. Chapter 6 by Haeam Kim presents the site response in 2D and 3D, including topographic features and the effect of the soil structure interaction on the analysis based on a time history analysis. Chapter 7 by Prem Nath Maskey describes a probabilistic seismic hazard assessment considering the effects of surface geology on seismic motion in the Kathmandu Valley.

Section 3, “Infrastructure”, includes Chapter 8, in which Valeria Scapini and Cinthya Vergara study the impact of the 2010 Chilean earthquake considering the damage to homes, the cost of reconstruction, and how households finance reconstruction using a nonlinear probabilistic and a squares regression model.

Section 4, “Tsunamis”, includes Chapter 9, in which Ali Akbar Firoozi and Ali Asghar Firoozi describes the genesis of earthquake tsunamis and non-seismic tsunamis. The chapter explores the influences of bathymetry and tectonic structures, particularly in the context of non-seismic tsunami generation.

Section 5, “Instrumentation”, includes the final chapter. In Chapter 10, Yanjun Chen, et al. review the use of gyroscopes in rotational seismology, including the observation and analysis of natural earthquakes, highspeed-railway seismology, and subsurface structure imaging.

Walter Salazar, Ph.D.

Professor,

Faculty of Engineering and Architecture,
Catholic University of El Salvador UNICAES,
Santa Ana, El Salvador

Section 1

Seismicity

The Source Rupture Models and Seismogenic Structures of the Iran 2017 M_W 7.3 Earthquake

Shutian Ma, Parisa Asgharzadeh and Dariush Motazedian

Abstract

The 12 November 2017 M_W 7.3 Iran earthquake was further studied. By analyzing Rayleigh-wave dispersion data, crustal models in the surrounding of the epicenter were obtained. It was found that there are high-velocity layers over a low-velocity zone. Using the obtained crustal models and a grid search procedure, the initial rupture depth of about 16.4 km and the rupture propagation velocity of about 1.62 km/s were retrieved. The source rupture models were established using the obtained rupture initial depth and the rupture velocity. The key features are as follows: The earthquake occurred on a shallow dip-angle fault, with ruptures spanning high-velocity layers in a depth range of approximately 7–25 km. A noteworthy observation from comparing crustal and rupture models is the existence of a low-velocity zone (layers) beneath the major rupture region (below about 25 km). It was realized that the seismogenic structure of this earthquake showed that high-velocity layers lay a low-velocity zone in the Zagros mountain seismic belt.

Keywords: 2017 M_W 7.3 Iran earthquake, source rupture model, seismogenic structure, Zagros mountain seismic belt, grid search method

1. Introduction

On 12 November 2017, a significant earthquake with a moment magnitude (M_W) of 7.3 struck the Iran-Iraq border region (**Figure 1**), causing widespread devastation and loss. The seismic impact was felt as far away as the United Arab Emirates. Tragically, the earthquake resulted in the loss of over 600 lives and injured more than 7000 individuals. Moreover, approximately 70,000 people were rendered homeless, with around 12,000 homes destroyed and an additional 15,000 homes damaged.

The epicenter of this M_W 7.3 earthquake was located in the northwest part of the Zagros mountain range. The Zagros Mountains span southwestern Iran, extending in a northwest-southeast direction from the border areas of eastern Turkey and northern Iraq to the Strait of Hormuz. These mountains were formed through the ongoing collision between the Arabian plate and Central Iran, which began in the Miocene period [1].

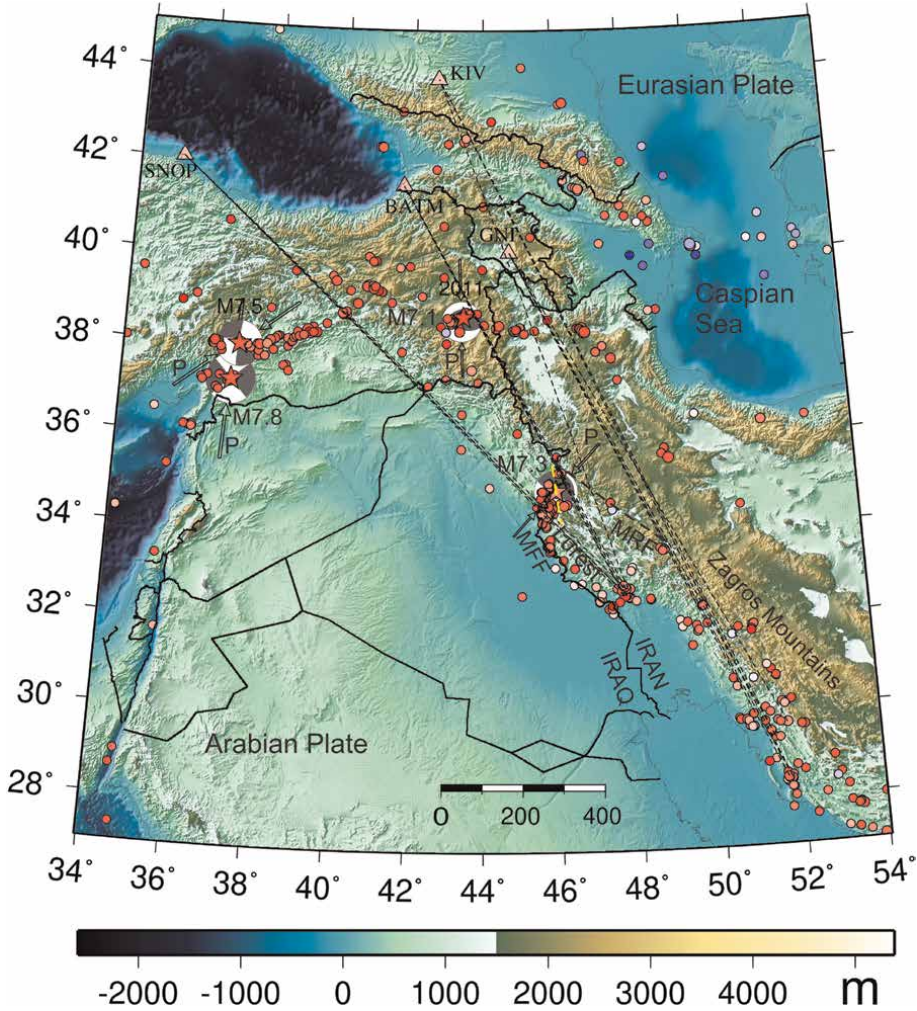


Figure 1.

Background map depicting various elements related to the 2017 M_W 7.3 earthquake study. The beach balls show the projections of the focal mechanisms for four large earthquakes: The 10 October 2011 Turkey M_W 7.1; the 12 November 2017 Iran M_W 7.3; the 6 February 2023 Turkey M_W 7.8; and the 6 February 2023 Turkey M_W 7.5 earthquakes (the used data were retrieved from <http://ds.iris.edu>). The arrows with letter P indicate the direction of compressive force. The yellow dashed line running through the beach ball indicated with M7.3 illustrates the strike of the shallow-dipping nodal plane. The solid circles show the epicenters of earthquakes with magnitude ≥ 5 , occurred between the 1 January 2000 and the 12 July 2023 (retrieved from <http://ds.iris.edu>). The long dashed lines show the 15 Rayleigh wave paths, used to obtain the crustal models in this article. The four triangles connected with the paths are the stations used to measure Rayleigh-wave dispersion data. The epicentral trend near and on the M7.3 beach ball shows the distribution of aftershocks that occurred within 1 month following the mainshock. The trend closely aligns with the strike direction. The 2017 M_W 7.3 earthquake occurred in the northwest of the Zagros mountain range [2]. This figure was created using the generic mapping tools [3].

This M_W 7.3 earthquake is one of the most significant instrumentally recorded earthquakes in the Zagros region, generating substantial interest among researchers. For instance, Barnhart et al. [4] employed interferometric synthetic aperture radar (InSAR) to analyze co- and post-seismic surface displacements, employing a fault inversion approach to determine permissible geometries, locations, and slips. Their findings indicated that the earthquake ruptured the shallow-dipping (14° – 19°) Mountain Front Fault (MFF) within the Arabian crystalline basement at depths of

approximately 12–22 km. Other researchers have also utilized InSAR techniques to study this M_W 7.3 earthquake (e.g., [2]).

The United States Geological Survey (USGS) has provided preliminary finite fault results for this earthquake. More than 10 papers have been published on or related to this earthquake (e.g., [2, 5–8]).

However, given the varied strengths and weaknesses of existing findings, we were motivated to employ a waveform inversion method to retrieve more plausible source rupture models and surface wave dispersion data to retrieve crustal models in the epicentral region. Given the tectonic activity in the region, it is crucial to study this earthquake and the crustal structures in the epicentral region to enhance tectonic research and improve seismic hazard assessment.

In this article, we present the following: (1) introductions to the crustal modeling method, source rupture inversion method, and the grid search method; (2) the average crustal model obtained through the analysis of Rayleigh wave dispersion data in the epicentral region; (3) the initial rupture depths and rupture propagation velocities derived using a grid search procedure; (4) the source rupture models obtained by using shallow-dipping nodal planes and the identification of the active fault associated with the earthquake; and (5) the exploration of the seismogenic structure, which potentially reveals high-velocity crustal layers over a low-velocity zone in the Zagros mountain seismic zone.

2. Method introduction

In this article, three methods were used: crustal model retrieval using Rayleigh-wave dispersion data, source rupture model inversions, and a grid search procedure.

2.1 Crustal velocity modeling method

The crustal velocity model utilized in this study was obtained using a Rayleigh wave dispersion method. The method consists of two steps: (1) measuring the Rayleigh-wave group velocities and (2) modeling Rayleigh-wave dispersion data to extract S-wave velocities.

2.1.1 Measurement of Rayleigh-wave group velocities

Seismograms often exhibit prominent surface wave trains. These surface waves have different frequency components, and waves with different frequencies travel at different speeds, a phenomenon known as dispersion. As these surface waves propagate through the Earth, their amplitudes decay exponentially with depth. As a result, seismograms recorded at surface stations contain valuable information about the Earth's structure. Rayleigh waves are generated by P and S waves, thus, S-wave velocity structures can be retrieved by analyzing Rayleigh-wave dispersion.

We measured the group velocities for the selected records using the multiple filter technique (MFT) developed by Dziewonski et al. [9]. A computer program developed by Herrmann and Ammon [10], was employed to implement the MFT method. In this technique, the group time for a specific frequency ω_n was determined as the time when the envelope of the filtered seismic record, as defined by Eq. (1), reaches its maximum. This time, regarded as the center of the Gaussian filter, is used to calculate the group velocity by dividing the epicentral distance by the group time.

$$h_n(\omega_n, t, r) = \int_{-\infty}^{\infty} |F(\omega)| e^{-\alpha \left(\frac{\omega - \omega_n}{\omega_n}\right)^2} \cos[k(\omega)r - \omega t] d\omega \quad (1)$$

where $F(\omega)$ is the Fourier transform of the analyzed record, $e^{-\alpha \left(\frac{\omega - \omega_n}{\omega_n}\right)^2}$ is a Gaussian window function, $k(\omega)$ is the wave number, and r is the epicentral distance.

The envelope of the filtering Rayleigh wave record can be computed using the formula proposed by B  th [11]:

$$g_n(t) = \sqrt{h_n^2(\omega_n, t) + \bar{h}_n^2(\omega_n, t)} \quad (2)$$

where $\bar{h}(\omega_n, t)$ is the Hilbert transform of $h_n(\omega_n, t)$ [9]. Herrmann and Ammon [10] introduced the formulas they used in their programs' manual.

2.1.2 Modeling Rayleigh wave dispersion data for S-wave velocities

After obtaining Rayleigh-wave dispersion data at a particular seismic station, we can utilize these data to model the S-wave velocities along the path traversed by the Rayleigh waves.

The initial step involves establishing an initial crustal model and then the model is revised by comparing the observed dispersion with the predicted dispersion generated using the crustal model. The inversion is in fact to identify a revised model that best fits the observed data.

In our inversion process, we assumed that $\delta U(\omega_k)$ was the group velocity difference between the observed and synthetic waveforms at frequency ω_k , the crustal model had N horizontal layers on the top of a half-space, and the S-wave velocity is β_n in the n th layer (n is the index for the layer). The difference at frequency ω_k ($k = 1, \dots, M$) could then be approximated using the following formula:

$$\delta U(\omega_k) = \frac{\partial U(\omega_k)}{\partial \beta_1} \delta \beta_1 + \frac{\partial U(\omega_k)}{\partial \beta_2} \delta \beta_2 + \dots + \frac{\partial U(\omega_k)}{\partial \beta_N} \delta \beta_N \quad (3)$$

The partial derivatives $\frac{\partial U(\omega_k)}{\partial \beta_n}$ ($n = 1, 2, \dots, N$) were calculated using the formula proposed by Rodi et al. [12]:

$$\frac{\partial U(\omega_k)}{\partial \beta_n} = \frac{U(\omega_k)}{C(\omega_k)} \left(2 - \frac{U(\omega_k)}{C(\omega_k)} \right) \frac{\partial C(\omega_k)}{\partial \beta_n} + \omega_k \frac{U^2(\omega_k)}{C^2(\omega_k)} \frac{\partial}{\partial \omega} \left(\frac{\partial C(\omega)}{\partial \beta_n} \right) \quad (4)$$

where $C(\omega_k)$ is the phase velocity. $C(\omega_k)$, $U(\omega_k)$, and $\frac{\partial C(\omega_k)}{\partial \beta_n}$ were obtained using standard Thomson-Haskell matrix calculations, and $\frac{\partial}{\partial \omega} \left(\frac{\partial C(\omega)}{\partial \beta_n} \right)$ were obtained by numerically differentiating $\frac{\partial C(\omega_k)}{\partial \beta_n}$ (Rodi et al., [12]).

If we let $\mathbf{m} = (\delta \beta_1, \delta \beta_2, \dots, \delta \beta_N)$, $\mathbf{d} = (\delta U(\omega_1), \delta U(\omega_2), \dots, \delta U(\omega_M))$, and $G_{k,n} = \frac{\partial U(\omega_k)}{\partial \beta_n}$ ($k = 1, 2, \dots, M; n = 1, 2, \dots, N$), we obtained a linear equation:

$$\mathbf{D} = \mathbf{Gm} \quad (5)$$

After solving this equation, we obtained a set of corrections to the S-wave velocities in the N layers ($\delta\beta_1, \delta\beta_2, \dots, \delta\beta_N$). We could form a new model by assigning the S-wave velocity in the n th layer, $\beta_{n_new} = \beta_n + \delta\beta_n$. The above steps were repeated if this new model could not generate a satisfied synthetic dispersion curve. The methods to solve Eq. (5) were extensively studied and used (e.g., [13–15]). We use the sur96 program in the package [10] to obtain our solutions.

As for the theoretical background and the technique of Rayleigh wave dispersion inversion, except for the above introduction, the pioneering work by Haskell [16], Dorman [17], and Dorman and Ewing [18] provide valuable references.

2.2 The source rupture modeling method

The procedure used to establish an earthquake rupture model is described below. One of the two nodal planes is used as the earthquake rupture plane, and a Cartesian coordinate system is set up on this plane. Usually, the x-axis is along the strike direction, and the y-axis is along the dipping direction. The selected rupture plane is divided into many small rectangles where the length of each small rectangle along the x-axis is dx and along the y-axis is dy . Each small rectangle is called a sub-fault and is treated as a point source. At a specific station, a synthetic seismogram is the summation of the synthetic seismograms generated by all rectangle sources. The source time function of all the sub-faults is usually depicted as overlapped triangles. The layout of the source rupture model can be found in Hartzell and Heaton [19]. A unit constant rupture slip vector for each sub-fault can be divided into two orthogonal vector components (one aligned along the strike and the other aligned along the dip direction). At a specific station, each component can be used to calculate a synthetic seismogram called Green's function. Any slip vector on the sub-fault can be obtained by multiplying the two constant vector components with appropriate coefficients. An inversion aims to obtain the coefficients of all the sub-faults from the observed seismograms to establish the rupture model for the earthquake.

Once a nodal plane is selected as the rupture plane, it is divided into $M \times N$ sub-faults. The slip function (source time function) of each sub-fault is depicted by overlapped L triangles with a rise time τ , which is half the length of the bottom side of the triangle. The initial constant unit slip direction (slip0) of each sub-fault is obtained through the moment tensor solution. The initial slip is separated into two components in the directions of (slip0 + 45°) and (slip0 – 45°). This breakdown is convenient for Green's function calculations.

Assuming that on a sub-fault mn ($m = 1, \dots, M; n = 1, \dots, N$) at the k^{th} component direction ($k = 1, 2$), the slip corresponding to the l^{th} triangle is X_{mnlk} , and the vertical components of the Green's functions generated at Station j are g_{mnkj} , and then the vertical component synthetic seismogram W_j at the station generated by all sub-faults at the time point t_i can be expressed as follows:

$$W_j(t_i) = \sum_{mnlk} X_{mnlk} g_{mnkj}(t_i - (l-1)\tau - T_{mn} - dl_{mn}) \quad (6)$$

where T_{mn} is the rupture start time at the mn^{th} sub-fault, and dl_{mn} is a time delay generated by the different travel path lengths between the P waves generated at the mn^{th} sub-fault and the rupture start sub-fault m_0n_0 (hypocenter). The set of X_{mnlk} that can generate a W_j , which is most similar to the observed seismogram at Station j , is the best fitting rupture model for the earthquake.

The Eq. (6) was solved using the nonnegative least squares (NNLS) method [20]. To ensure stability in the slip solution, a smoothness constraint was imposed on the spatial distribution of the total slips using a Laplacian differential operator [21]). To calculate the time delay dl_{mn} in Eq. (6), a rupture velocity is required. Additionally, to compute Green's functions, a reasonable initial focal depth and a crustal model are necessary.

2.3 Grid search method

A Grid Search is an optimization algorithm commonly used in various research fields. It is beneficial for selecting the best parameter values to optimize a model or solve a problem. The Grid Search helps identify the optimal parameter values that yield the best results by systematically evaluating the model's performance across all possible parameter combinations.

Grid searches are particularly effective when the parameter space is not too large or when the relationship between the parameters and the model's performance is poorly understood. However, they can be computationally expensive when dealing with many parameters or when the parameter space is extensive.

Let a model parameter vector $\mathbf{V} = (\nu_1, \nu_2, \dots, \nu_m)$, and an objective function $f = f(\mathbf{V})$. A simple way to set up a grid search consists in defining a vector of lower bounds $\mathbf{a} = (a_1, a_2, \dots, a_m)$ and a vector of upper bounds $\mathbf{b} = (b_1, b_2, \dots, b_m)$ for the vector \mathbf{V} . The grid search involves taking n equally spaced points for each component. All the objective function values at each grid point are calculated and compared. Pick up the vector that corresponds to the minimum (or maximum, depending on how to define the objective function) of the objective function as the solution.

The problem with this method is that the number of evaluations increases exponentially as n and m increase. Because we cannot reduce m , decreasing n is the only possible way of assuring that the evaluation process stops in a reasonable time, but this decreases the validity of the solution. For specific situations, some vector components may need dense spacing, some not; as such, the spacing number n may differ for different vector components. In our case, $\mathbf{V} = (\nu_1, \nu_2)$; ν_1 is the source rupture initial depth, whereas ν_2 is the rupture travel velocity.

3. Data for the source rupture inversions and the Rayleigh-wave dispersion inversion

The data used for the source rupture inversions are P-wave segments in the teleseismic waveform vertical records. These records contain valuable information about the earthquake source. The waveform records were downloaded from the Incorporated Research Institutions for Seismology (IRIS) database. Specifically, records within an epicentral distance of 30°–90° surrounding the epicenter were selected for analysis. Only the high-quality P-wave segments were considered in the analysis to ensure high signal-to-noise ratios. The selected records underwent an instrument response correction to account for the recording instrument's characteristics. Additionally, a band-pass filter with frequencies ranging from 0.01 to 0.1 Hz (equivalent to periods of 10–100 s) was applied to the records. The resulting dataset used for the source rupture inversion comprised 52 records.

The digital waveform records generated by moderate earthquakes around the M_w 7.3 main shock, registered at regional seismic stations, were first retrieved from IRIS. Then, the instrument responses were removed, and they converted the velocity

records into displacement records using the SAC2000 software [22]. After conducting spectral analysis on the waveform records, it was found that the strong amplitudes were within periods of approximately 2–40 s. Therefore, a band-pass filter (1–50 s) was applied to the records. Once the displacement records were obtained, those that clearly displayed Rayleigh waves within the period range of interest were selected for the dispersion data measurements.

4. Crustal velocity models in the M_W 7.3 epicentral region

The P-wave segments generated by a crustal earthquake, recorded at a teleseismic station, contain the direct P wave radiated from the earthquake source, the reflected wave pP, and the S-wave converted P wave sP. To generate Green's functions at teleseismic stations, an earth model is required. In our study, we formed an earth model by replacing the crustal part in the preliminary reference Earth model (PREM; [23]) with the crustal model obtained from Rayleigh-wave dispersion data.

At some stations, the Rayleigh waves generated by moderate earthquakes were strong enough to measure surface wave dispersion data. We retrieved waveform records from IRIS and selected 15 clean Rayleigh wave vertical records. **Figure 1** shows the 15 Rayleigh wave travel paths, connecting the four stations and the nine epicenters of the selected moderate earthquakes. These travel paths pass through the epicenter region of the M_W 7.3 earthquake.

Once a group dispersion curve of a waveform record was measured at a given station, it is used to determine an average 1-D S-wave velocity model along the source station path. The P-wave velocity and density are obtained by converting the S-wave velocity model using a Poisson ratio ($V_p/V_s = 1.732$) and the Nafe-Drake relation [24].

Fifteen crustal velocity models were retrieved around the epicenter of the M_W 7.3 mainshock, and an averaged crustal model was obtained. The average model was simplified from 20 layers to 7 to expedite the calculation time for Green's function.

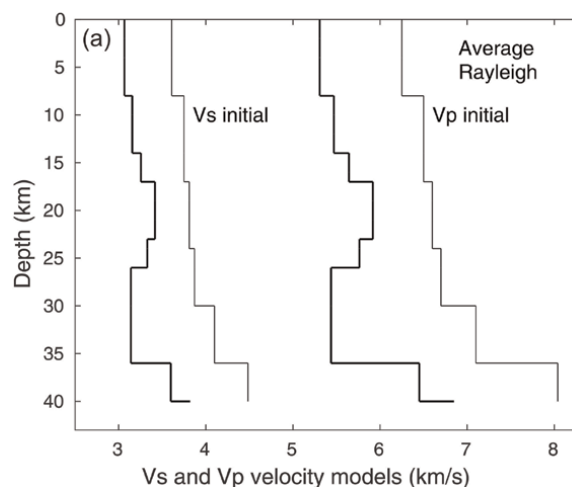


Figure 2.
 This figure displays the average crustal velocity model obtained using Rayleigh-wave dispersion data from 15 Rayleigh wave travel paths. The two thick lines represent the final average crustal velocity model. The two thin lines represent the initial model. The Rayleigh wave travel paths used for the dispersion data are those shown in **Figure 1**.

ΔH	V_p	V_s	density
8.0	5.3075	3.0656	2.5615
6.0	5.4695	3.1557	2.5941
3.0	5.6423	3.2551	2.6290
6.0	5.9186	3.4167	2.6861
3.0	5.7640	3.3283	2.6526
10.	5.4377	3.1405	2.5877
4.0	6.4516	3.5985	2.8356
0.0	6.8496	3.8205	2.9480

Table 1.
The simplified average crustal model.

Figure 2 depicts the simplified crustal model. The model parameters are listed in **Table 1**. This model was utilized for the calculation of Green's functions. For more details on the utilization of Rayleigh-wave dispersion data for retrieving crustal models, refer to the following studies: Dziewonski et al. [9], Herrmann and Ammon [10], and Motazedian and Ma [25]).

In the table, column ΔH represents the layer thickness (km), V_p represents the P-wave velocity (km/s), V_s represents the S-wave velocity (km/s), and density (g/cm^3). They are listed from top to bottom in **Figure 2**.

5. Source rupture models

In this section, we introduce the source rupture models obtained.

5.1 Selection of the rupture plane from the two nodal planes

Selecting a rupture plane from the two nodal planes is necessary when establishing a source rupture model. Typically, the distribution of aftershocks can be used to determine the rupture plane. In **Figure 1**, the smaller solid circles within and nearby the beach ball indicated by M7.3 represent the distribution of moderate aftershocks that occurred within 1 month after the main shock. The distribution trend aligns closely to the strike direction (351°) of nodal Plane 1 (the shallow-dipping plane). Thus, nodal Plane 1 was selected as the rupture plane.

5.2 The determination of the initial rupture depth and the rupture velocity

An initial rupture depth and a rupture propagation velocity are required to conduct the source rupture process inversion. A grid search scheme was employed to obtain reasonable values for these parameters. The depth range from 14.0 km to 21.0 km with an increment of 0.5 km was set, whereas the range for rupture velocity was from 1.40 km/s to 1.80 km/s with an increment of 0.05 km/s. At each grid point, the source rupture inversion was performed using the inversion code developed by Kikuchi and Kanamori, provided by Lingling Ye (personal communication). To speed up the calculations of the Green's functions, we made some revisions to the code. The average variance from all the utilized records in each grid point (each inversion) was recorded.

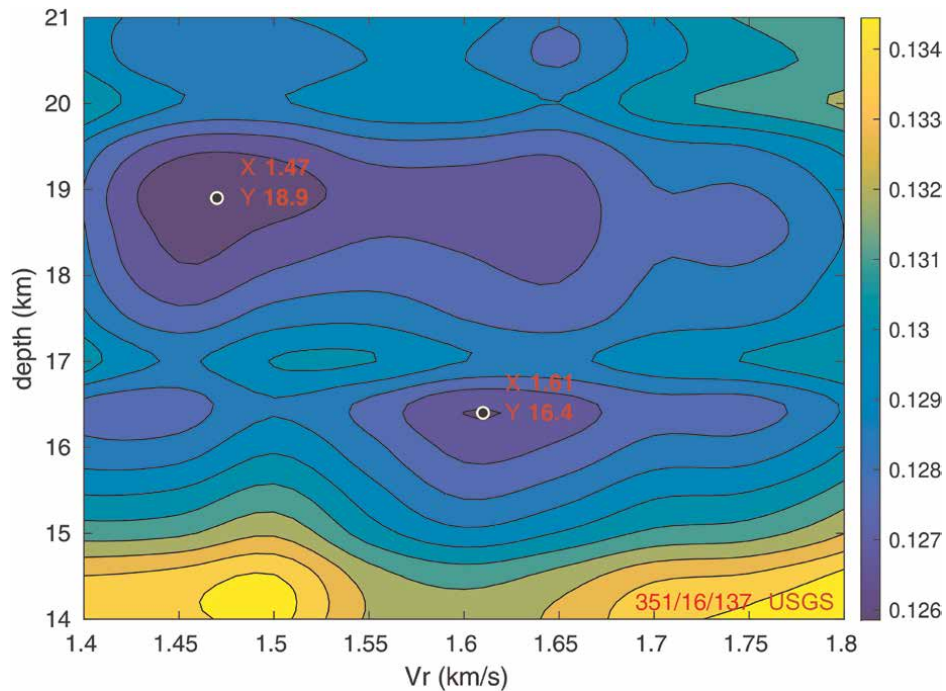


Figure 3.

The contour map of variance values. At a specific point on the map, the color of a pixel shows the variance value at that point. A deeper color shows smaller variance value. The color bar at the right side shows the variance values represented by colors. A variance value shows the fit between the observed and the synthetic seismograms. The smaller the value, the better the fit. This map depicted the changes in variance values with the rupture's initial depth and rupture propagation velocity. When the shallow nodal plane provided by the United States geological survey (USGS) was used as the rupture plane (strike/351°, dip/16°, rake/137°) to perform the grid search procedure, two minima were found (two small circles). One is at the rupture velocity of 1.47 km/s and the initial depth of 18.9 km (1.47, 18.9); its variance value is 0.1264. The second minimum is at (1.61, 16.4); its value is 0.1269. The second minimum is our preferred solution.

This variance represents the fit between the synthetic seismograms generated by the retrieved rupture model and the observed seismograms. A smaller variance value indicates a better fit. A total of 135 variance values were obtained from 135 grid points.

The contour map (**Figure 3**) illustrates the variance value changes with respect to the initial rupture depth and the rupture velocity. In the search procedure, the shallow-dipping nodal plane obtained by USGS (strike/351°, dip/16°, and rake/137°) was used. Two minima were found. One is at the rupture velocity of 1.47 km/s and an initial depth of 18.9 km (1.47, 18.9); its variance value is 0.1264. The second minimum is at (1.61, 16.4); its value is 0.1269.

5.3 Retrieving rupture models using the obtained minima

With the initial rupture depths and rupture velocities at the two minima, we retrieved two rupture models for the M_W 7.3 earthquake. **Figure 4** displays the comparison between the rupture distributions obtained using the two minima. The upper panel shows that there are four rupture patches. The phenomenon that one earthquake has four separated patches may not easily occur naturally. The bottom

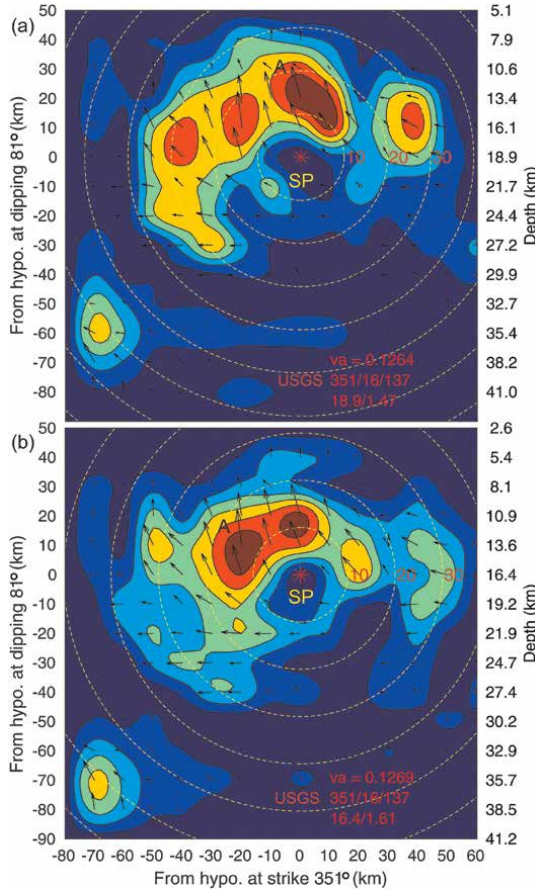


Figure 4. The comparison between the rupture distributions obtained using different minima. (a) the rupture distribution obtained using the USGS shallow-dipping nodal plane (strike/351°, dip/16°, rake/137°) at the minima (rupture velocity of 1.47 km/s, initial depth of 18.9 km). The star (*) marked with SP denotes the rupture start point. Four red areas show four rupture patches. The dashed circles represent the rupture fronts at specific time intervals, indicated as 10 (s), 20 (s), and so on. (b) the rupture distribution using the same nodal plane at the minima (rupture velocity of 1.61 km/s, initial depth of 16.4 km). One larger rupture area, indicated by letter A, was obtained.

panel shows that two patches combined to form a larger prolate patch, indicated by letter A. This shape is similar to the shapes obtained by Nissen et al. ([2]; their Figure 5). For the same earthquake, the rupture models obtained using different methods should be similar. From this common sense, we prefer to take the bottom panel of **Figure 4** as our solution.

Figure 5 compares seismograms at 24 stations, generated using the rupture model in **Figure 4(b)**. The fit between the observed (upper) and synthetic (bottom) traces is generally good. For brevity, the comparison for the remaining 28 stations is not provided; the waveform fit at those stations is similar to those shown in **Figure 5**. This figure allows for a visual comparison between the observed and synthetic waveforms, highlighting the agreement or discrepancies between the recorded and the simulated waveforms based on the obtained slip distribution. It provides, to some extent, insights into the modeling approach's accuracy and the simulated waveforms' fidelity in capturing the actual earthquake's characteristics.

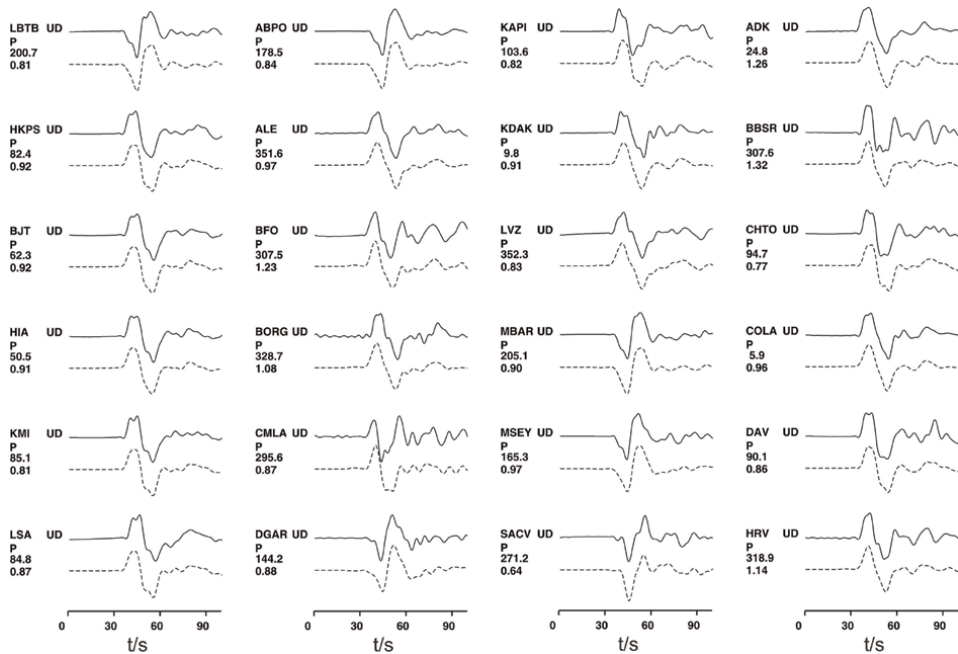


Figure 5.

The comparison between the first 24 observed and synthetic seismograms. For each pair the upper trace (solid line) represents the recorded waveform, whereas the lower trace (dashed line) represents the synthetic waveform generated using the slip distribution depicted in **Figure 4(b)**. Both the observed and synthetic waveforms were filtered with a band-pass filter, ranging from 0.01 to 0.1 Hz. The symbols and numbers on the left side of each pair indicate the station name, the P-wave vertical component, the station azimuth in degrees, and the ratio between the observed and synthetic maximum amplitudes. Among all the 52 waveform records used in the inversion, the poorest ratios were observed at stations SACV (0.64) and BBSR (1.32). They show the most discrepancies between the observed and synthetic waveforms. To save page space, the remaining 28 records were not shown up. The fit quality is similar to those displayed.

5.4 Rupture models retrieved using nodal planes obtained by other authors

We also utilized shallow-dipping nodal planes obtained by other authors. First, we show the results in detail using the nodal plane provided by Nissen et al. [2] as the rupture plane; then, list the key results using the nodal planes provided by other authors. The contour map in **Figure 6** shows variance value changes obtained using the nodal plane (strike/353.7°, dip/14.3°, rake/136.8°) provided by Nissen et al. [2]. Three minima were found. In the deeper colored region, the rupture velocity range is about 1.45–1.75; the initial depth range is about 15–19 km.

Three rupture models were generated using the above three minima (**Figure 7**). The upper panel shows the rupture distribution obtained using the nodal plane (strike/353.7°, dip/14.3°, rake/136.8°; Nissen et al. [2]) at the minimum (rupture velocity 1.62 km/s, initial depth 18.2 km). Several rupture patches were obtained. The middle panel shows the rupture distribution using the same nodal plane at the minimum (1.61 km/s, 16.1 km). One larger prolate rupture area, indicated by letter A, was obtained. The bottom panel shows the rupture distribution using the same nodal plane at the minimum (1.60 km/s, 17.2 km). One larger, oval rupture area, indicated by letter A, was obtained. The rupture distributions retrieved using different methods for the same earthquake should be similar. Because the rupture distribution in Panel (b) was similar to those obtained by Nissen et al. [2], so, we preferred to select **Figure 7(b)**.

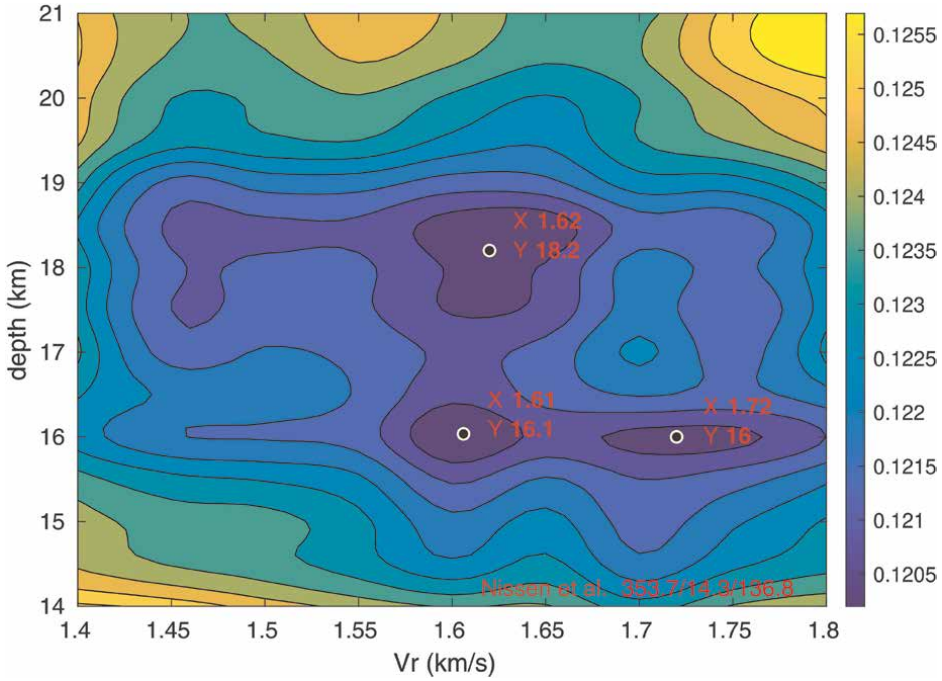


Figure 6.

The contour map of variance values. When the nodal plane (strike/353.7°, dip/14.3°, rake/136.8°) provided by Nissen et al. [2] was used as the rupture plane, three minima were found (the small circles). One minimum is at the rupture velocity 1.62 km/s and the initial depth 18.2 km (1.62, 18.2); its variance value is 0.1199. The second is at (1.61, 16.1); its value is 0.1194. And the third is at (1.72, 16.0); its value is 0.1211. The second minimum is our preferred solution.

Other authors have also retrieved rupture planes for the 2017 M_W 7.3 Iran earthquake. The key results obtained using their nodal planes for preferred minima are listed in **Table 2**.

In the table, the initial rupture depths (km, i.d.) and the rupture velocities V_r (km/s) were measured on a computer screen. The major slip (m. s.) depth (km) means the centre depth of the major rupture patch, visually estimated. L.P. means long period; B. W. means body waves; St. NP means Steep nodal plane. The other parameters are understandable.

6. A rupture model retrieved using a steep nodal plane as the rupture plane

All the previous models were obtained using shallow-dipping nodal planes as the rupture plane. This section presents the modeling results obtained using the same procedure but with a steep-dipping nodal plane.

Figure 8 displays the contour map depicting the variance values. In the search procedure, the steep-dipping nodal plane by The Global Centroid Moment Tensor (GCMT) (strike/121°, dip/83°, and rake/82°) was used. The small circle represents the obtained minimum variance value (0.1535), occurred at a depth of approximately 15.4 km and a rupture velocity of about 1.62 km/s. **Figure 9** illustrates the slip distribution on the steep-dipping nodal plane. Several rupture patches were scattered

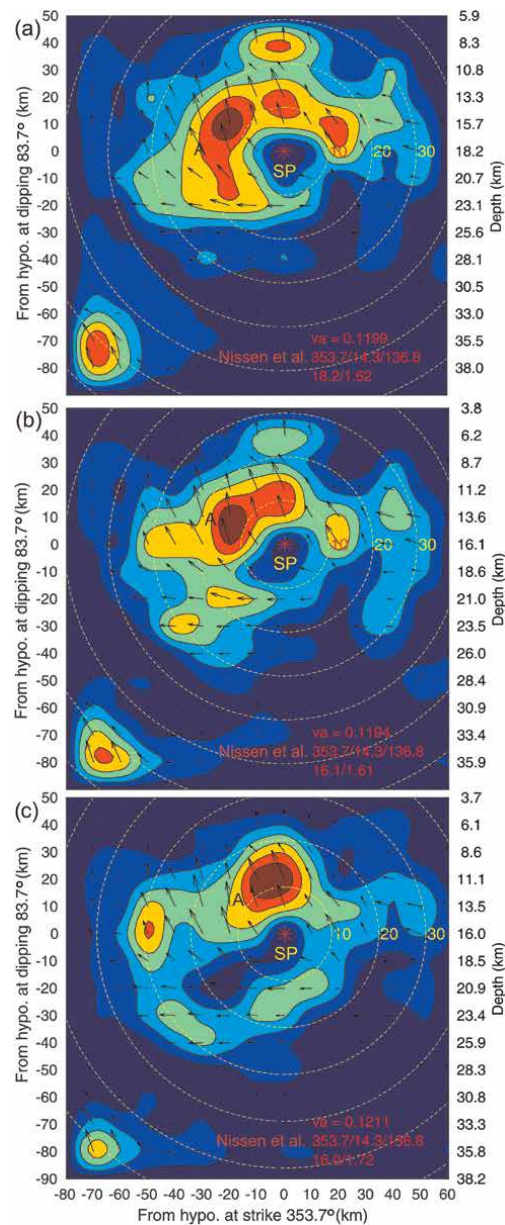


Figure 7.
 The comparison between the rupture distributions obtained using different minima. (a) the rupture distribution obtained using the nodal plane (strike/353.7°, dip/14.3°, rake/136.8°) provided by Nissen et al. [2] at the minimum (rupture velocity of 1.62 km/s, initial depth of 18.2 km). The star (*) marked with SP denotes the rupture start point. Several rupture patches were obtained. (b) the rupture distribution using the same nodal plane at the minimum (1.61 km/s, 16.1 km). One larger prolate rupture area, indicated by letter A, was obtained. (c) the rupture distribution using the same nodal plane at the minimum (1.60 km/s, 17.2 km). One larger, oval rupture area, indicated by letter A, was obtained. The rupture distribution (b) was our preferred solution.

within a 5–70 km depth range. **Figure 10** compares the first 20 observed and synthetic seismograms generated using the rupture model shown in **Figure 9**. The poorest ratio occurred at station CMLA, with a ratio of 0.52.

Authors	data	Strike (°)	Dip (°)	Rake (°)	i.d.	Vr	va	m. s. depth
USGS	L. P.	351.0	16.0	137.0	16.4	1.61	0.1269	14
GCMT	L. P.	351.0	11.0	140.0	16.4	1.59	0.1153	16
Nissen et al. [2]	B. W.	354.0	17.0	142.0	16.3	1.65	0.1268	13
Nissen et al. [2]	InSAR	353.7	14.3	136.8	16.1	1.61	0.1194	14
Barhart et al. [4]	InSAR	351.0	15.0	128.0	16.6	1.65	0.1258	14
Vajedian et al. [5]	InSAR	354.4	17.5	141.5	16.5	1.65	0.1278	14
Feng et al. [6]	InSAR	353.5	14.5	135.6	16.4	1.60	0.1210	14
Ding et al. [7]	InSAR	354.7	16.3	137.3	16.1	1.63	0.1249	14
Chen et al. [8]	InSAR	351.0	15.0	135.0	16.5	1.62	0.1235	14
Average		352.7	15.2	137.0	16.4	1.62	0.1235	14
GCMT	St. NP	121.	83.	82.	15.4	1.62	0.1535	18

Table 2.
The rupture plane parameters by different authors and the key rupture parameters.

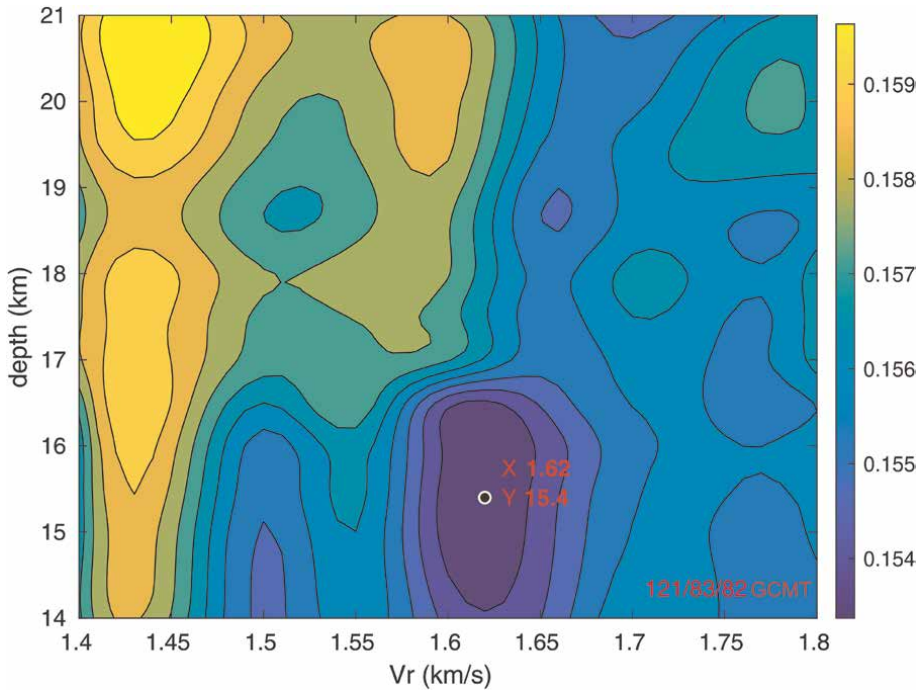


Figure 8.
The contour map of variance values. When the steep-dipping nodal plane (strike/121°, dip/83°, rake/82°) provided by GCMT was used as the rupture plane, one minimum variance at the rupture velocity was 1.62 km/s and the initial depth of 15.4 km was found; its variance value is 0.1535.

This test demonstrates that the minimum variance value (0.1535) obtained using a steep-dipping nodal plane was notably larger than those obtained using shallow-dipping planes (Table 2). One major rupture patch was as deep as more than 60 km

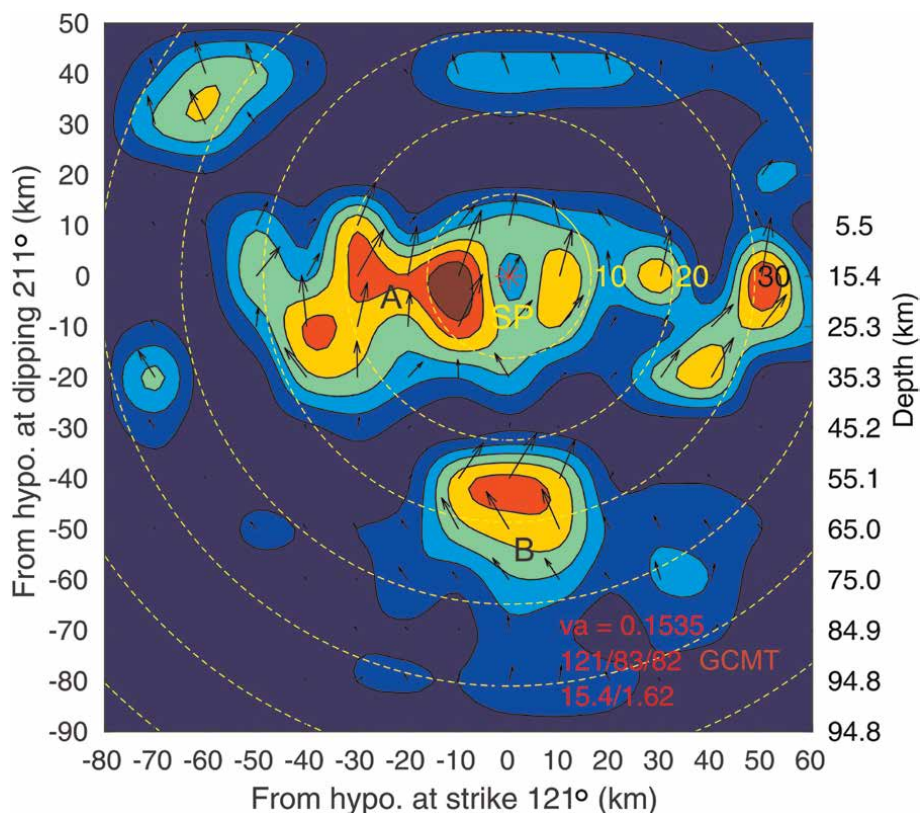


Figure 9.
 The distribution of the slip on the GCMT steep dip nodal plane (strike/121°, dip/83°, rake/82°). The star (*) marked with SP indicates the rupture start point at depth of 15.4 km. Multiple patches along the rupture plane were scattered at depths ranging from approximately 5–70 km. The rupture velocity of 1.62 km/s was used in the inversion.

(Figure 9), which is beneath the crust. It is impossible for this M_W 7.3 crustal event to have a major rupture patch beneath the crust. Therefore, the steep-dipping nodal plane could be ruled out to be the rupture plane.

7. The seismogenic structure of the 2017 M_W 7.3 Iran earthquake

The 2017 M_W 7.3 Iran earthquake occurred along the boundary between the Arabian and Eurasian plates in the Zagros mountain seismic zone (e.g., Nissen et al., [2]). The compressive force in the epicentral region is oriented northeastward (Figure 1), approximately perpendicular to the trend of the Zagros Mountains. In the epicentral region, a low-velocity zone exists from a depth of about 25 km to approximately 36 km beneath a high-velocity zone (Figure 2). The materials in the low-velocity zone are considered to be ‘soft,’ whereas stress accumulates in the ‘hard’ layers (high-velocity zone) at depths of about 7–25 km. When the stress strength in the ‘hard’ layers becomes strong enough, the crust in that region undergoes breakage, resulting in the M_W 7.3 earthquake. The source rupture modeling presented in Figure 4(b) and Figure 7(b) indicates that the ruptures occurred within a depth range of about 7–25 km, consistent with the depth range of the ‘hard’ layers. This suggests that the

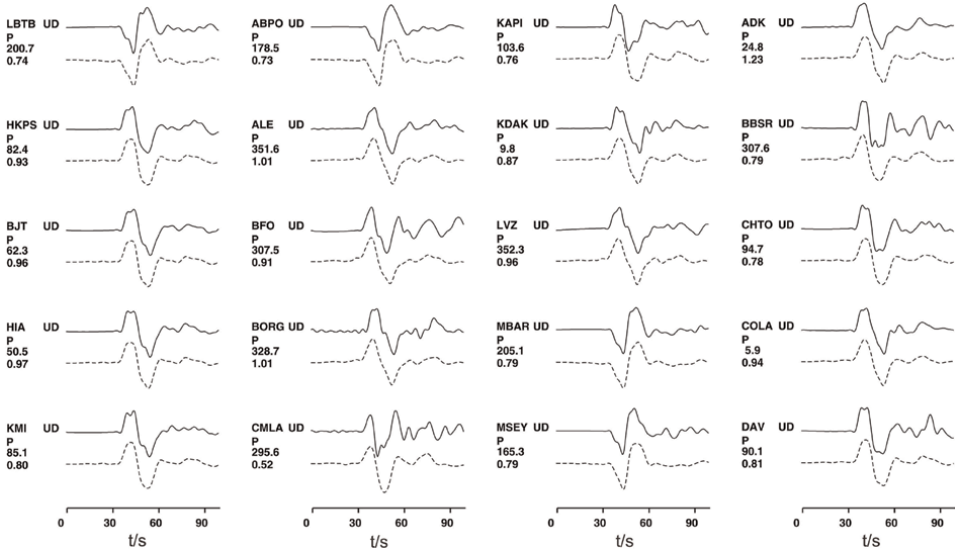


Figure 10.

The comparison between the first 20 observed and synthetic seismograms. For each pair the upper trace represents the recorded waveform, whereas the lower trace represents the synthetic waveform generated using the slip distribution depicted in Figure 9. Among all the 52 waveform records used in the inversion, the poorest ratios were observed at stations CMLA (0.52) and ADK (1.23). To save page space, the remaining 32 records were not shown up; the fit quality is similar to those displayed. The variance value is 0.1535.

seismogenic structure of the 2017 M_W 7.3 earthquake possibly involves the high-velocity layers overlying the low-velocity layers along a significant seismic activity belt.

Overall, the modeling results introduced above indicate that the seismogenic structure of the 2017 M_W 7.3 earthquake likely involves the interaction between high-velocity layers and low-velocity layers along a seismic activity belt. The rupture models obtained using different shallow-dipping nodal planes consistently showed rupture patches distributed within the depth range of the high-velocity layers, reinforcing the correlation between the seismic activity and the properties of the subsurface layers.

8. Conclusions

The source rupture models of the 2017 M_W 7.3 Iran earthquake were established, and the crustal model in the source region was constructed. The ruptures obtained using different shallow-dipping nodal planes provided by different authors showed similar trends. The optimal initial rupture depths were about 16.4 km, and the rupture velocities were around 1.62 km/s. The rupture models retrieved using those shallow-dipping nodal planes exhibited rupture patches distributed within a depth range of about 7–25 km.

Unlike the common practice that the rupture's initial depth and the rupture velocity are assumed or by trade-and-errors when the rupture modeling is performed, we used the grid search method to determine the optimal initial depth and rupture velocity. For each nodal plane used as the rupture plane, two or three minima formed by the initial depth and the rupture velocity were found. One minimum was selected

by analyzing the shapes of ruptures and comparing the solutions obtained by other authors for the same earthquake. If solutions from other authors for the same earthquake are not available at the moment, we do not have an effective way to select the best minima.

To validate the selection of the shallow-dipping nodal plane as the rupture plane, we tested a steep-dipping nodal plane as the rupture plane. The test revealed that the minimum variance (0.1535) was obviously larger than that (~ 0.1235) achieved using the shallow-dipping nodal planes. The worst maximum amplitude ratio between observed and synthetic data was 0.52 at station CMLA, a significant deviation from the ideal ratio of 1.0. In contrast, when the shallow nodal plane was employed as the rupture plane, the worst maximum amplitude ratio was 0.64. The rupture distribution associated with the steep-dipping nodal plane also exhibited a scattered pattern ranging from approximately 5–60 km in depth. As a crustal event, the ruptures less likely occurred beneath the crust. Based on the above discussion, it can be concluded that the selection of the shallow nodal plane as the rupture plane was justified. This test also indicates that modeling two nodal planes for the 2017 M_W 7.3 earthquake facilitated the identification of the most likely rupture plane. However, it is important to note that for other earthquakes, the rupture plane may not be discernible through modeling two nodal planes, as demonstrated by Motazedian and Ma [26].

Barnhart et al. [4] used InSAR observations of both the co- and post-seismic displacement to image the M_W 7.3 earthquake sequence. They implemented an iterative fault-slip inversion approach designed to elucidate the geometry and location of faults associated with this sequence. They found that InSAR observations are best described by co-seismic slip on a shallow-dipping ($15\text{--}19^\circ$) plane that dips eastward at depths of 12–22 km. The rupture plane we identified was the shallow-dipping plane. The depth range of the major rupture we obtained (**Figure 4b**) was consistent with that obtained by Barnhart et al., [4].

The compressive force in the epicentral region is in the northeast direction. The epicentral region has a low-velocity zone under a high-velocity zone. This feature was displayed by the crustal models retrieved using the Rayleigh-wave dispersion data (**Figure 2**). The stress is accumulated in the ‘hard’ layers (high-velocity layers) above the ‘soft’ zone (low-velocity layers). When the accumulated stress is strong enough in the ‘hard’ layers, the crust there had to be broken, leading to the occurrence of this M_W 7.3 earthquake. Based on results obtained using several shallow-dipping nodal planes as the rupture planes, we conclude that the 2017 M_W 7.3 Iran earthquake occurred on a shallow-dipping fault at a depth range from about 7–25 km in the high-velocity layers over a low-velocity zone; the initial rupture depth was about 16.4 km, and the rupture propagation velocities were about 1.62 km/s. The central depths of the major ruptures were about 14 km.

The features exhibited by **Figure 2** were also supported by the Love-wave dispersion inversion. The related article will be published. The factors leading to the uncertainty in the crustal model are multiple. One of them is the uncertainty in the measured dispersion data. It turned out that this uncertainty did not change the crustal features retrieved using the Rayleigh-wave dispersion data [27].

The epicenter of the 2017 M_W 7.3 earthquake is in the Lurestan arc region (e.g. Nissen et al., [2]). In the Lurestan arc region, the depth to the magnetic basement from spectral analysis of aeromagnetic data is about 16 km [28]. The initial rupture depth we retrieved is about 16.4. This may imply that the earthquake nucleated at the bottom of the basement.

Viewing this M_W 7.3 earthquake in a larger background, it can be seen that it is located in the boundary region between the Arabian Plate and the Eurasian Plate (**Figure 1**). Other large earthquakes also occurred in this corner region: 2011 M_W 7.1; 2023 M_W 7.8, and M_W 7.5 Turkey earthquakes. The time intervals between the 2011 Turkey M_W 7.1 and 2017 Iran M_W 7.3, 2017 Iran M_W 7.3 and 2023 Turkey M_W 7.8 and M_W 7.5 are about 6 years. The compressive forces were at a similar direction for the M_W 7.1 and M_W 7.8; they were at another similar direction for the M_W 7.5 and M_W 7.3. The locations, intervals, and forces of large earthquakes are another topic. Here, we only mention the above phenomena.

Nissen et al. [2] estimated that the rupture velocity of this 2017 M_W 7.3 earthquake is about 1.5–2.0 km/s, whereas the rupture velocity we obtained is about 1.62 km/s. These velocity values are at the lower end of the range of rupture velocities observed in large earthquakes globally (e.g., Chounet et al., [29]).

The grid search method was used to look for the optimal values of the rupture velocity and the rupture's initial depth. We found that for each nodal plane used as a rupture plane, two or three minima appeared. It is crucial to consider the unique characteristics of each seismic event. Further investigations into the phenomenon of multiple minima and improved methodologies for rupture plane determination will advance our understanding of earthquake source characterization and hazard assessment.

By source rupture modeling and crustal velocity modeling, the 2017 M_W 7.3 Iran earthquake occurred in the high-velocity layers over a low-velocity zone along the boundary between the Arabian plate and the Eurasian plate within the seismic zone of the Zagros. This finding highlights the significance of the seismogenic structure in earthquake occurrence and contributes to our understanding of the earthquake processes in the region, providing valuable insights for future seismic hazard assessments.

Acknowledgements

This research was made possible through the support of the Natural Sciences and Engineering Research Council of Canada under the Discovery Grant program. We would like to express our gratitude to editor Walter Salazar for the improvement of this chapter. We would also like to acknowledge the following programs and tools in our data processing and figure preparation: SAC2000, Rdseed, geotool, MATLAB, and Generic Mapping Tools (GMT). Special thanks go to Lingling Ye at the Department of Earth and Planetary Sciences, University of California, Santa Cruz, California, for providing us with a version of the source rupture modeling code. We are sincerely grateful for her assistance.

Data sources


In this study, the seismograms, GCMT, and USGS nodal plane solutions utilized were obtained from the Incorporated Research Institutions for Seismology (IRIS) database, accessed at <http://www.iris.edu> (last accessed May 29, 2023). Certain information presented in the introduction section was revised based on a web page of the U.S. Geological Survey (<https://earthquake.usgs.gov/earthquakes/eventpage/us2000bmcg#executive>; last accessed the 31 July 2018).

Author details

Shutian Ma*, Parisa Asgharzadeh and Dariush Motazedian
Department of Earth Sciences, Carleton University, Ottawa, Ontario, Canada

*Address all correspondence to: shutian33@yahoo.ca

IntechOpen

© 2023 The Author(s). Licensee IntechOpen. This chapter is distributed under the terms of the Creative Commons Attribution License (<http://creativecommons.org/licenses/by/3.0>), which permits unrestricted use, distribution, and reproduction in any medium, provided the original work is properly cited. 

References

- [1] McQuarrie N, Stock JM, Verdel C, Wernicke BP. Cenozoic evolution of Neotethys and implications for the causes of plate motions. *Geophysical Research Letters*. 2003;**30**(20). DOI: 10.1029/2003GL017992
- [2] Nissen E, Ghods A, Karasözen A, Elliott JR, Barnhart WD, Bergman EA, et al. The 12 November 2017 mw 7.3 Ezgeleh-Sarpolzahab (Iran) earthquake and active tectonics of the Lurestan arc. *Journal of Geophysical Research: Solid Earth*. 2019;**124**: 2124-2152. DOI: 10.1029/2018J B016221
- [3] Wessel P, Smith WHF. New, improved version of the generic mapping tools released, *Eos trans. AGU*. 1998;**79**(47):579
- [4] Barnhart WD, Brengman CMJ, Li S, Peterson KE. Ramp-flat basement structures of the Zagros Mountains inferred from co-seismic slip and afterslip of the 2017 M_W 7.3 Darbandikhan, Iran/Iraq earthquake. *Earth and Planetary Science Letters*. 2018;**496**:96-107
- [5] Vajedian S, Motagh M, Mousavi Z, Motaghu K, Fielding EJ, Akbari B, et al. Coseismic deformation field of the mw 7.3 12 November 2017 Sarpol-e Zahab (Iran) earthquake: A decoupling horizon in the northern Zagros Mountains inferred from InSAR observations. *Remote Sensing*. 2018;**10**(10):1589. DOI: 10.3390/rs10101589
- [6] Feng W, Samsonov S, Almeida R, Yassaghi A, Li J, Qiu Q, et al. Geodetic constraints of the 2017 Mw7.3 Sarpol Zahab, Iran earthquake, and its implications on the structure and mechanics of the northwest Zagros thrust-fold belt. *Geophysical Research Letters*. 2018;**45**:6853-6861. DOI: 10.1029/2018GL078577
- [7] Ding K, He P, Wen Y, Chen Y, Wang D, Li S, et al. The 2017 mw 7.3 Ezgeleh, Iran earthquake determined from InSAR measurements and teleseismic waveforms. *Geophysical Journal International*. 2018;**215**: 1728-1738
- [8] Chen K, Xu W, Mai PM, Gao H, Zhang L, Ding X. The 2017 mw 7.3 Sarpol Zahāb earthquake, Iran: A compact blind shallow-dipping thrust event in the mountain front fault basement. *Tectonophysics*. 2018; **747-748**:108-114
- [9] Dziewonski A, Bloch S, Landisman M. A technique for the analysis of transient seismic signals. *Bulletin of the Seismological Society of America*. 1969;**59**:427-444
- [10] Herrmann R, Ammon C. *Computer Programs in Seismology*, version 3.30,. Missouri, USA: Saint Louis University; 2002
- [11] Båth M. *Spectral Analysis in Geophysics*. Amsterdam: Elsevier; 1974. p. 563
- [12] Rodi WL, Glover P, Li TMC, Alexander SS. A fast, accurate method for computing group-velocity partial derivatives for Rayleigh and love modes. *Bulletin of the Seismological Society of America*. 1975;**65**:1105-1114
- [13] Badal J, Corchete V, Payo G, Canas JA, Pujades L, Serón FJ. Processing and inversion of long-period surface-wave data collected in the Iberian Peninsula. *Geophysical Journal International*. 1990;**1990**(100):193-202

- [14] Badal J, Corchete V, Payo G, Serón FJ, Canas JA, Pujades L. Deep structure of the Iberian Peninsula determined by Rayleigh wave velocity inversion. *Geophysical Journal International*. 1992;**108**:71-88
- [15] Kafka AL, Reiter EC. Dispersion of R_g waves in southeastern Maine: Evidence for lateral anisotropy in the shallow crust. *Bulletin of the Seismological Society of America*. 1987; **77**(3):925-941
- [16] Haskell NA. The dispersion of surface waves on multi-layered media. *Bulletin of the Seismological Society of America*. 1953;**43**:17-34
- [17] Dorman J. Period equation for waves of Rayleigh type on a layered, liquid-solid half space. *Bulletin of the Seismological Society of America*. 1962; **52**:389-397
- [18] Dorman J, Ewing M. Numerical inversion of seismic surface wave dispersion data and crust-mantle structure in the New York-Pennsylvania area. *Journal of Geophysical Research*. 1962;**16**:5227-5241
- [19] Hartzell SH, Heaton TH. Inversion of strong ground motion and teleseismic waveform data for the fault rupture history of the 1979 Imperial Valley, California, earthquake. *Bulletin of the Seismological Society of America*. 1983; **73**:1553-1585
- [20] Lawson C, Hanson R. Solving Least Squares Problems. Philadelphia, PA: Society for Industrial and Applied Mathematics; 1995
- [21] Yagi Y, Mikumo T, Pacheco J, Reyes G. Source rupture process of the Tecomán, Colima, Mexico earthquake of 22 January 2003, determined by joint inversion of teleseismic body-wave and near-source data. *Bulletin of the Seismological Society of America*. 2004; **94**(5):1795-1807. DOI: 10.1785/012003095
- [22] Goldstein P, Dodge D, Firpo M, Minner L. SAC2000: Signal processing and analysis tools for seismologists and engineers. In: Lee WHK, Kanamori H, Jennings PC, Kisslinger C, editors. *The IASPEI International Handbook of Earthquake and Engineering Seismology*. London: Academic Press; 2003. DOI: 10.1016/S0074-6142(03)80284-X
- [23] Dziewonski A, Anderson D. Preliminary reference earth model. *Physics of the Earth and Planetary Interiors*. 1981;**25**:297-356
- [24] Ludwig WJ, Nafe JE, Drake CL. Seismic refraction. In: Maxwell AE, editor. *The Sea*. Vol. 4. New York: Wiley-Interscience; 1970, 1970. pp. 53-84
- [25] Motazedian D, Ma S. Crustal shear-wave velocity models retrieved from Rayleigh-wave dispersion data in northern Canada. *Bulletin of the Seismological Society of America*. 2014; **104**(4):1976-1988. DOI: 10.1785/0120130265
- [26] Motazedian D, Ma S. Studies on the source parameters of the 23 June 2014 Rat Islands, Alaska, M_W 7.9 earthquake sequence. In: Salazar W, editor. *Recent Advances, New Perspectives and Applications*. London, UK, London, UK: IntechOpen; 2023. DOI: 10.5772/intechopen.104004
- [27] Motazedian D, Ma S, Crane S. Crustal shear-wave velocity models retrieved from *Rayleigh* wave dispersion data in north-eastern America. *Bulletin of the Seismological Society of America*. 2013;**103**(4):2266-2276. DOI: 10.1785/0120120187
- [28] Teknik V, Ghods A. Depth of magnetic basement in Iran based on

fractal spectral analysis of aeromagnetic data. *Geophysical Journal International*. 2017;**209**:1878-1891

[29] Chounet A, Vallée M, Causse M, Courboulex F. Global catalog of earthquake rupture velocities shows anticorrelation between stress drop and rupture velocity. *Tectonophysics*. 2018; **733**:148-158

A Tool for Archiving and Updating Knowledge about Past Earthquakes in Central America

*Laura Peruzza, Eliana Esposito,
Felix Enrique Rodríguez García and Giuseppe Giunta*

Abstract

In 2019, we released a prototype version of an online tool called MARCA-GEHN that combines an earthquake catalog and a macroseismic archive for a Central American (CA) sector, which was realized as part of an international project between Italy and four CA countries (Guatemala, El Salvador, Honduras, and Nicaragua). The aim was to build a transnational, common, quality-controlled archive of macroseismic observations capable of documenting and updating the parameters of the main earthquakes recorded in the international historical and instrumental catalogs. Collecting the original documents, critically revising them, and organizing them in a public, open data format is a long, potentially endless process. Thanks to past experience in Europe and the additional efforts of the local CA scientific communities, MARCA-GEHN was updated in 2023. The current database contains about 70 earthquakes with intensities observed at the sites, about 2200 intensity points related to more than 1100 locations. This archive can help improve information on past and current earthquakes, and it is a powerful tool for constraining the seismic sources, a key element of hazard and risk analyses. We briefly present the structure of the archive, the shortcuts for the queries, some results obtained so far, and potentialities for the future.

Keywords: MARCA-GEHN, macroseismic intensities, El Salvador, Guatemala, Honduras, Nicaragua, earthquake catalog, Central America

1. Introduction

Central America is one of the most prone and vulnerable areas in the world to earthquakes, which have caused casualties and high economic and social damage since ancient times. The culture of “risk” necessarily occupies an important place for Central American governments, along with the attempt to regionalize protection and mitigation, especially due to the pressure of events that are often difficult to manage due to their intensity and territorial dimensions.

Knowledge of previous earthquakes in an area is the starting point for any seismic hazard and seismic risk assessment. Both methodological approaches, estimating

seismic hazard by probabilistic methods and models or by deterministic earthquake scenarios, are mainly based on parametric earthquake catalogs; they derive from quantitative measurements of instrumental seismology and qualitative assessment of macroscopic impacts or damages caused by earthquakes, a research area of macroseismology. The short time span covered by instrumental seismic data (about a century) may not be sufficient to adequately reconstruct the seismic behavior of a country, and to fill this gap it is necessary to obtain non-instrumental information from historical sources. On the other hand, macroseismology is concerned with the parameterization of earthquakes—that is, the definition of time of occurrence, location, depth, and magnitude—through the collection and mapping of witness reports of felt earthquakes, a fundamental discipline for extending earthquake catalogs back to the time of instrumental seismology. In many countries, there is no or insufficient information from before instrumentation; in some others (e.g., Italy, Greece, Japan), the earthquake catalog useful for hazard analysis is obtained mainly from macroseismic data.

The historical seismicity of Central America is based on regional and national catalogs and on documents, reports, and monographs on individual seismic events, which often do not include estimates of epi/hypocentral parameters, intensity values, or isoseismal drawings. Since the 1960s, only a dozen scientific papers (or seismic catalogs) have been found that rely on new historical sources, some of which provide partial seismological interpretations, in terms of macroseismic analyses with the definition of focal parameters (e.g. [1–5]). In 1999, Peraldo and Montero [1] published, with great compilatory and interpretive effort, an earthquake catalog containing seismic information obtained directly from archives and/or other referenced sources, according to modern practices. They also provided new seismological interpretations as well as the definition of focal parameters of the most destructive earthquakes recorded in Central America. Regarding the parametric catalogs, the main catalog in [2] includes about 17,000 earthquakes; it merges at least 30 different earthquake catalogs that include both macroseismic and instrumental observations, without additional information on macroseismic records or historical sources.

As part of an international collaborative project, we pursued the realization of the first cross-national prototypical archive of macroseismic data points for the four participating countries in Central America. The database MARCA-GEHN (Macroseismic ARchive for Central America countries—Guatemala, El Salvador, Honduras, and Nicaragua) was realized by adopting best practices and lessons learned in Europe in the field of macroseismology, involving local scientific communities and government institutions. The prototype online platform has been publicly available on the Internet since 2019 and seeks to address the different data availability and problems encountered at the borders of neighboring countries. The database takes into account the many specificities of Central American countries exposed to a variety of seismogenic processes, at different levels of ground shaking, and the availability of non-uniform instrumental and historical seismic data. The prototypical archive of macroseismic data represents a dynamic seismic catalog since it can be continuously updated depending on the progress of historical research; it is also designed for the integration of new descriptive data that can better contribute to define the seismic scenario of individual events, such as the main social and economic elements: fatalities, injuries, elements of historical structures related to seismic impacts, temporary and permanent earthquake-related geological effects on the environment, and damage effects due to anomalous sea waves. The coexistence of different tectonic regimens (cortical, interphase, and intraplate subduction) can lead to the differentiation of earthquake impacts on the population, building stock, and natural environment, which are the subject of the documentation searched by macroseismology.

In this work, an attempt was made to verify the quality of the information on the selected seismic events in terms of their geographical location and the reliability of the bibliographic sources. Efforts were also made to verify or assign missing parameter values for each earthquake. As mentioned above, this work should be considered as a first attempt to standardize the available information and its bibliographic references for a limited number of seismic events and to organize them in a publicly available macroseismic database that can be enriched, maintained, and regularly updated through local and international efforts.

2. The online MARCA-GEHN archive

Within the RIESCA project (“Proyecto de formación aplicada a los Escenarios de Riesgo con la vigilancia y monitoreo de los fenómenos volcánicos, sísmicos e hidrogeológicos en América Central”), funded by the Italian Agency for Development Cooperation (AICS) for the period 2017–2021 and coordinated by the University of Palermo, we developed the first prototype online archive of macroseismic data points for four Central American countries.

The project was scheduled to end with the onset of the pandemic COVID-19, and the very last stages were diluted in remote work sessions. Nonetheless, the online archive (version 1.6) has been publicly available since September 2020, and a monographic, bilingual open-access issue was published in 2021 [6]. In 2022–2023, we updated some content of the archive and published it on a new domain (version 2.0, <https://marca-gehn.info>). This book chapter summarizes the main features and capabilities of the data collection. For a more detailed and complete description, readers may refer to the monograph already cited.

To archive the data, we resorted to a programming tool that easily converts tables of macroseismic intensity data into interactive maps. It is called MIDOP (Macroseismic Intensity Data Online Publisher, [7]) and is also used for other macroseismic archives worldwide.

The online database MARCA-GEHN is mainly based on:

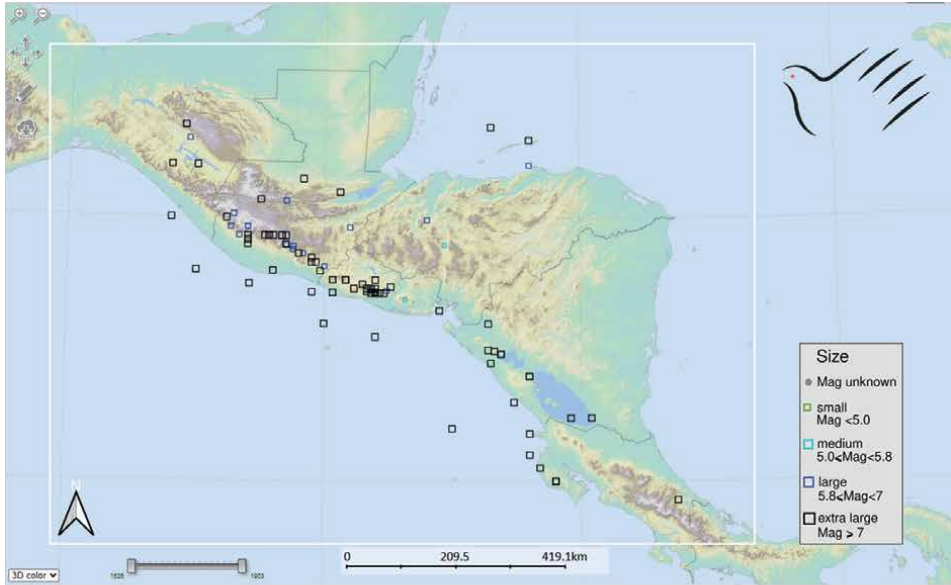
1. an earthquake catalog table: it contains the basic parametric information for selected earthquakes, given in accordance with the reference source;
2. the set of collected macroseismic data point sets (MDP set, sometimes referred to as a set of intensity points or, in the past, as a macroseismic field): an MDP set represents the “picture” in terms of impact and damage on the built and natural environment for a given earthquake listed in the catalog, given according to a categorization made by using appropriate intensity scales.

2.1 The reference parametric catalogs

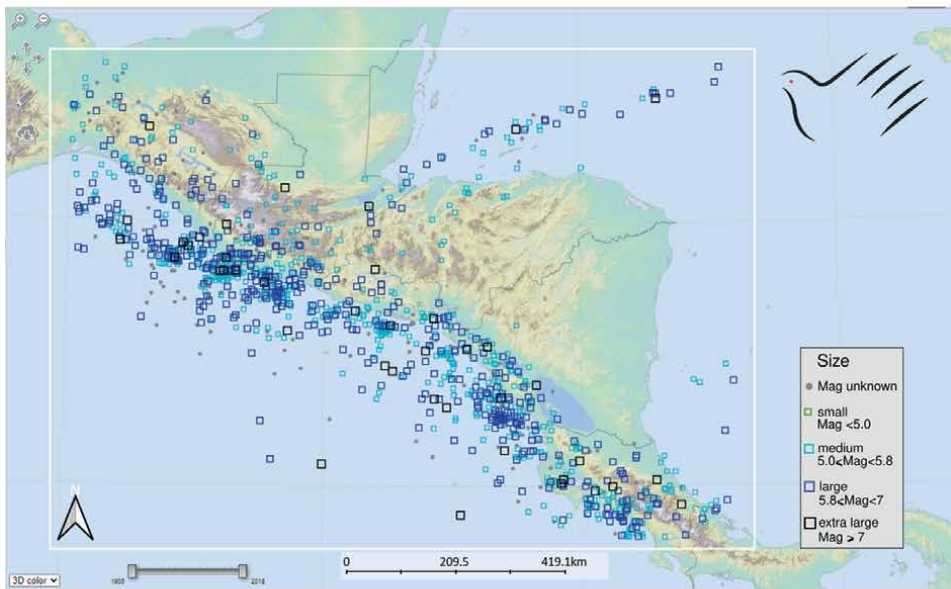
We have relied on internationally published catalogs as the primary source of parametric datasets for unique earthquake identification. This choice is motivated by traceability, consistency, and sometimes more structured access to the original data; however, regional and national earthquake catalogs also exist, and a brief inventory for Central America can be found in [6].

Most of the records related to the pre-instrumentation period, namely the 1500–1903 time window, are derived from the Global Historical Earthquake catalog

GHEC v.1 [8, 9]. They were selected if the epicentral solution adopted by the GHEC compilers is within the geographic area of interest to us (a rectangular area with coordinates [95°W, 9°N; 82°W, 18°N], white frame in **Figure 1**); some records below



(a)



(b)

Figure 1. Epicentral map representing the MARCA-GEHN reference earthquake catalog; a) historical time frame, namely from 1500 to 1903, mainly based on GHEC v.1 [8, 9]; b) events from 1904 to 2018, mainly based on the solutions proposed by the ISC-GEM Global Instrumental Earthquake catalog, v.9.1 [10]. The geographic boundaries include the four Central American countries involved in data collection in the RIESCA project, i.e., Guatemala, El Salvador, Honduras, and Nicaragua.

the magnitude threshold M7+ assumed by GHEC were taken from the catalog [1]. From 1526 to 1903, 92 events are listed in the catalog table, 1/3 of them provided by a MDP set.

For the so-called “instrumental” period, i.e., 1904 onward, the parametric reference list of earthquakes comes from the ISC international catalogs and bulletins. The ISC-GEM Global Instrumental Earthquake catalog, v.9.1 [10] and its supplement, which lists events with poorly defined parameters, have been available since June 2022 and have been adopted by Marca-GEHN v.2.0. The time window now includes 2018 with a magnitude cutoff of M5–5.5+, for continental events and about M5.5+ elsewhere. We selected events in the same geographic area as before (**Figure 1b**), resulting in 1253 records; the catalog table is thus incremented by about 260 events from the ISC catalog v.6.0 used in the previous publication MARCA-GEHN in [6], with almost all new events related to the last three years. In the instrumental part of the catalog, the percentage of events provided by an MDP set decreases to about 3%, but it increases to about 25% if we assume the same magnitude threshold used in the pre-1904 period.

The global features of seismicity in Central America shown in **Figure 1** are primarily due to the tectonic setting characterized by the convergence of the North American Plate, the Caribbean Plate, and the Cocos Plate. Their interaction creates a complex tectonic environment in which transcurrent margins, subduction zones, and volcanic arc seismicity coexist. It is worth noting that until recent decades, earthquake distribution has been severely affected by uncertainties in spatial localization and incompleteness in magnitude, due to population distribution and discontinuous and inadequate instrumental monitoring (especially in offshore areas).

Similar to previous versions, the Marca-GEHN 2.0 catalog allows searching in space (circular or polygonal areas, using the interactive pencil tool) and in time (time cursor tool), different layouts for topography, and exporting the resulting maps in Google Earth format (.kml). A promising new feature was also added in the latest release to link directly to the referenced source of the earthquake record; when an earthquake is selected from the main list (upper left panel), a link appears near the origin time in the lower left panel, leading to an external page of the parent catalog where additional information is immediately available. We intend to propose a similar reverse link in the cited international catalog in the future, directed to the event page MARCA-GEHN.

Some other minor adjustments have also been made to MIDOP, such as the display of epicenters for records without an assigned magnitude or the display of the lowest intensity levels.

2.2 The macroseismic data point (MDP) sets

Assigning intensity to an earthquake means checking the correspondence between the macroscopic effects for as many sites as possible and the description categorized (formally in degrees) by the macroseismic scale; if the formulation of the macroseismic scale does not take into account a statistical distribution of effects, it is essential to summarize the information contained in the various available sources and then compare it with the scenarios represented in the degrees of the macroseismic scale.

The available observations reflect the temporal and cultural environment of the sites studied (building types, materials, but also societal organization, and lexis used in documentary accounts). Although the macroseismic scales aim to establish objective evaluation criteria, it is often not easy to assign a precise degree of intensity.

Frequently, the macroseismic observations provide ambiguous or even contradictory information: When some indicators point to a certain degree, but others are typical of lower or higher degrees, it is a common practice to formalize this uncertainty by intensity intervals (e.g., VI-VII), a solution that is sometimes transformed into an intermediate value (6.5); this is an incorrect use that must be abandoned in order to respect the discrete and ordinal, but not numerical, definition of intensity degrees. In the last 30 years, great progress has been made in the study of historical earthquakes, especially in the search and selection of authoritative sources, in the definition of procedures that allow tracing the paths followed in the analysis, and in the method of data synthesis, which is crucial for evaluating the reliability of historical data. These results have been possible thanks to the stimulating cooperation between historians and seismologists, especially in European countries (see, for example, [11]).

In the Americas, the first written documents on earthquakes date from the XVI century, although rare pre-Hispanic sources have been discovered. Today's knowledge of the historical seismicity of Central America is based on some valuable regional and national data collections, as well as on papers, reports, and monographic volumes that also describe research results for individual seismic events. These are mostly descriptive seismological compilations that often do not include estimates of focal parameters, intensity values, or isoseismal drawings. For a more complete inventory of data collections for CA and their linkage, we refer the reader to [6]. The macroseismic scale most commonly used in Central and South America is the Modified Mercalli intensity scale (MM), which is composed of 12 increasing intensity levels with a hierarchical classification of observed effects that include human perceptibility in the lower levels, low to moderate damage to objects and buildings in the middle levels, and extensive destruction of buildings and also permanent environmental impacts in the highest levels. In our case study, but also more generally in the global application of macroseismic scales, the recovery of basic contemporary key information, e.g., on masonry typology, vulnerability, and population density at the time of the earthquake, is of great importance.

The compilation of the MDP set for a given earthquake begins with the identification of data sources and reference studies from which macroseismic intensities can be obtained and geographically referenced. In our case of the RIESCA project, since we are working remotely and irregularly, we have resorted to an online Google®TM form set up for data entry by users belonging to different institutions and located in different countries. The compiler uses an event code (EVENTID) to select the unique identifier of the earthquake to which each individual Intensity Data Point (IDP) must refer. It then establishes a unique correlation between some parameters of the earthquake (e.g., time of occurrence, location, and magnitude) and the information related to a single location for that event. In a second section of the form, the location of the individual site must be entered with administrative and geographic identifiers that can be customized according to the administrative levels of each country. The site code (SITEID), rather than the geographic coordinates, is the linking element for site searches and for creating a seismic history at the site, i.e., the temporal list of effects related to a site, described later. In a third section of the form, the site-specific macroseismic value must be entered: This is done by selecting from drop-down menus to force the compiler to uniquely identify the intensity scale used and to avoid mismatches or unconventional intensity assignments (e.g., values spanning multiple degrees, 6–8, as sometimes found in the sources). Intensity values are always given in Roman numerals, in accordance with the original definition of the macroseismic scale; other commonly used annotations (e.g., not felt -NF-, heavy damage -HD-)

are also allowed. Finally, additional information such as the type and reference of the data source, quality identifiers for both the source and the intensity assignment, the annotation, and the name of the compiler are recorded.

The Google® form was used for initial data collection after training was provided in San Salvador in November 2017. The form remains available for input of new data, and potential data providers can express interest in contributing to the next version of MARCA-GEHN, also to fill the gap in cross-border data gathering. For given collection deadlines, the final revision post-processing, conducted by a small pool of experienced staff, has made it possible to address errors such as inconsistent geographic locations, control anomalous intensity values, integrate the MDP set with additional sources not previously included, and close the data gap in neighboring countries.

An MDP set is accessible online by querying the earthquake, scrolling, and selecting the appropriate record in the catalog window (see **Figure 2**, top left panel): then a map of all georeferenced points appears in the main panel (right panel), and the list of all locations related to the earthquake is also interoperable in the bottom left panel. Here, in the header, additional information is given. They concern the main reference for the MDP set (click on the event code of the MDP set), the main parameters assigned in the original cat (Epicenter OrCat, represented in the map by a red star), the modified location or magnitude finally proposed by this work (Preferred, green open square). In the map, the intensity data points are shown scaled according to the legend: The map can be zoomed, adjusted, printed, or exported in .kml format. The IDP list can be downloaded in three different formats, and an external link to the MDP is also available. As mentioned above, a new direct link to the event page in the origin catalog has also been added.

Figure 2 shows the macroseismic data set for the 1976 Guatemala earthquake, the deadliest event documented at MARCA-GEHN with an estimated 23,000 fatalities. The MDP set was derived from the USGS Atlas Shakemap compilation, which in turn

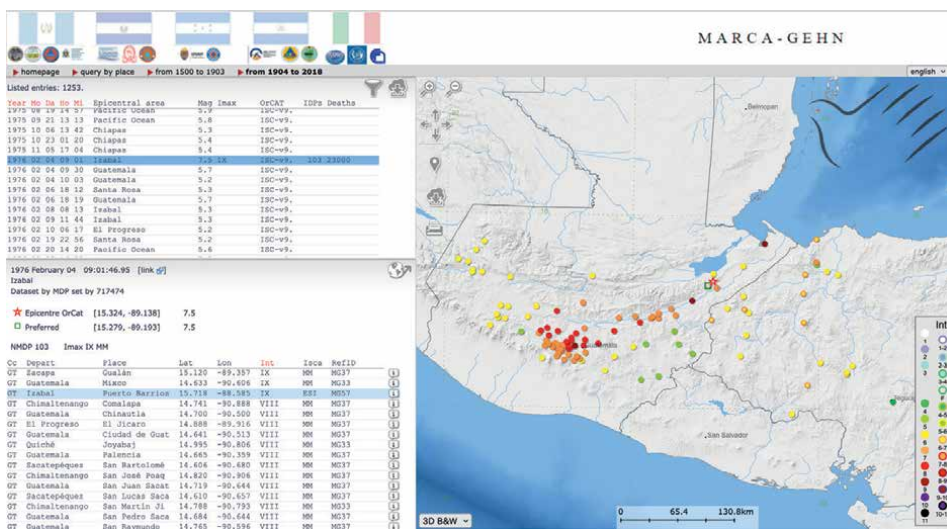


Figure 2. *Macroseismic data point set (MDP) for the Guatemala earthquake of February 4, 1976. Intensities in the Guatemala area are from the study of [12], and in Honduras, they were taken ad hoc from the press. An intensity point based on the ESI scale was also added.*

uses the contemporary technical report of [12]. Original sources from the press were used for some localities in Honduras (see Appendix 1 of [6] for the complete list of reference codes).

This earthquake represents a turning point for seismological knowledge of the area, not only because of the extensive damage surveys, the collection of macroseismic questionnaires sent to the most remote areas [12], the geological fieldwork to map surface faults, landslides, and liquefaction, but also because of the pioneering analyses of the instrumental recordings. The location of the surface ruptures and the instrumental data indicate that the February 4, 1976 earthquake was a shallow-depth tectonic earthquake triggered primarily by a slip on the Motagua fault [13, 14].

The main fault was identified in a discontinuous line about 240 km long in the Motagua Valley and west of the valley; [15] assign a sinistral strike-slip rate of 14–22 mm/year; a subparallel segment is mapped for about 110 km east of the 1976 epicenter. Some authors [16, 17] suggest a complex source with an asymmetric bilateral fault extending east and west along the Motagua fault, with the largest moment release occurring ~90 km west of the epicenter near a striking change of the surface fault. Several northward to NE trending secondary fault ruptures, called the Mixco system, were identified in the Mixco area. Among these, reactivation of a segment at least 21 km long was observed [13, 18]. The macroseismic data are crucial in this case both to identify the complexity of the earthquake ruptures and to determine possible similarities or differences in the damage patterns of previous events.

2.2.1 Georeferencing and searching the localities

As mentioned earlier, the location of the individual site must be entered with some administrative and geographic identification data. The MIDOP software can be adapted to the administrative levels of each country: The modified version we used allows five levels of identifiers (string variable) and three numerical values (for the geographic coordinates -latitude, longitude- and the site identification code -SITEID-). In Central America, we adopted the ranking of the country code (CC), geographic regions (if defined by the country), regional administrative areas (Departamentos), municipalities (Municipios), and finally the specific site (Locality) to which the intensity point refers. The geographic coordinates and a unique identification code for the locality are taken, when possible, from the general inventory of localities (Free Gazetteer data, available at <http://www.geonames.org/>). If they are not inserted correctly, this datum can be adjusted/unified in the post-processing phase. This structure is flexible and powerful and is the core of the query by places, the query of the database, which is the alternative to the query by earthquakes.

A place can be identified by a string search (drop-down menu), in the alphabetical list, or by area selection. The list of localities briefly displays the name of the site, the country code (a field that is generally omitted because macroseismic archives are usually national archives), the maximum intensity observed at that site, and the number of observations related to that location. On the specific web page for each location, all other information uploaded to the archive is then structured, and external references to the geographic database are also linked (see the example for Ahuachapán in the region of the same name with SITEID 3587426, direct link to https://marca-gehn.info/v2.0/query_place/call_place.htm?place=3587426).

Correct site identification is anything but a trivial matter. Some problems encountered in compiling MARCA-GEHN, most of which have been resolved, are:

- The identification of the inhabited/potentially affected site in relation to the barycentric coordinates of the actual administrative area. Several cases were manually relocated after being verified with Google tools;
- The location of the site at the time of the earthquake; several urban centers were relocated after disasters (Guatemala City, for example, is the best known and most traceable case);
- The identification of sub-areas within the largest metropolitan communities that deserve to be called a “locality” and for which a differential intensity assessment is useful. See, for example, the case study of the December 26, 1917 earthquake, with about 70 intensity points within Guatemala City (**Figure 3**), obtained by damage estimates based on photographs [19].
- Georeferencing of sites for the use of “unconventional” intensity scales that relate to geologic or environmental, rather than inhabited, locations, as discussed below.

2.2.2 The use of multiple intensity scales

One of the distinguishing features of MARCA-GEHN is the collection of macroseismic information that cannot be uniform because it comes from different documentary sources, and the use of multiple intensity scales to preserve the integrity of the original study or the nature of the multiple observations collected. The reason for this

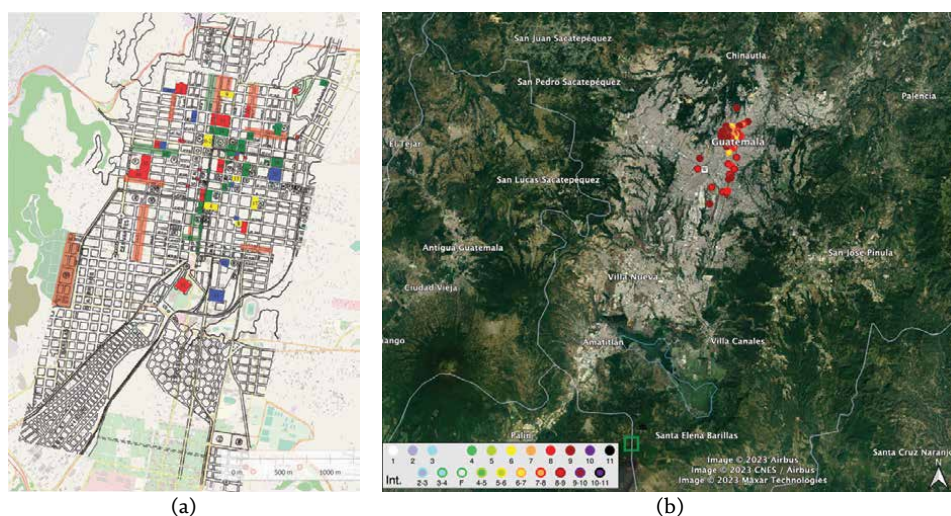


Figure 3.
 The Guatemala City for the 1917–1918 earthquakes: a) distribution of damaged buildings and b) inferred intensity points. The degree of damage is assigned to individual buildings by photo comparison [19], and the intensities are indicative of the local seismic response in urban areas, as they help identify “quadras” susceptible to amplification. More details in [6].

decision is mainly due to the time constraints of the RIESCA project that supported the realization of the archive, as it was not compatible with conducting a full revision study for each earthquake to reinterpret and homogenize the original sources. We discarded the possibility of using simplifying conversion relationships between different intensity scales, as they proved to be critical (see [20]). Finally, by archiving the standard macroseismic intensities, which are usually related to the building stock, we collected additional information on the geologic and environmental consequences of earthquakes that can now be classified by nontraditional intensity scales and that can provide additional clues for knowing the causative source of the earthquake.

Thus, we tolerate the coexistence of non-uniform but original intensity values, as this will allow more reliable harmonization of the intensity dataset and integration of different expertise in the future.

Only in a few cases did we reevaluate intensities assigned using a different scale, relying on available documentary sources, since the original values were on a 10° scale that is incompatible with the graphical representation (e.g., the 1915 September 7 earthquake [21]).

The latest MARCA-GEHN 2.0 archive uses these scales:

- the Modified Mercalli intensity scale (MM) in the 1956 formulation given by Richter in 1958 (for a review of intensity scales see [22];
- the Mercalli-Cancani-Sieberg (MCS) scale as formulated by Sieberg in 1923 [23];
- the Medvedev-Sponheur-Karnik scale (MSK, [24]);
- the DidYouFeelIt (DYFI) proxy scale [25];
- the Environmental Intensity scale (ESI) [26, 27] for geological intensities;
- the Tsunami Intensity scale (TSU) [28].

Even though all scales are in a 12° range, their values cannot be treated together, and users must be strict when merging data from different macroseismic scales.

The collection of ESI and TSU data points began coincidentally to document the effects of one of the largest magnitude earthquakes of the last century, the so-called slow-quake near the coast of Nicaragua in 1992. No relevant seismic shaking effects on buildings were reported, but enormous and diffuse tsunami effects were reported, exceeding those expected given the assumed size of the rupture. A more detailed description can be found in ([6], p. 136 ff).

During the last update, some ESI data points on Guatemala earthquakes of the XVIII and XIX centuries were added to map the geologic seismo-induced effects. They seem to be a promising tool to distinguish between surface and deep causes of past earthquakes.

3. First results

Measuring the outcome of an open-access database usually involves evaluating its impact, use, and added value for users and, more generally, for the reference community. Most of the key metrics and methods that can be used to quantify the

outcomes of an open-access database are not applicable to MARCA-GEHN because the platform has not yet been configured for such purposes, e.g., tracking user participation, downloads, and page views. Previous citations are also limited because the first version of the archive was launched during the difficult times of the COVID-19 pandemic. Last but not least, the database is explicitly described as “prototypical” and incomplete. Nevertheless, some numbers are indicative of the amount of data collected so far.

MARCA-GEHN V.2.0 contains an earthquake catalog with 1345 parametric records obtained from international public sources. Sixty-seven earthquakes were provided by MDP sets, i.e., a list of intensity data points representing quality-checked and georeferenced observations collected during our studies. The total number of IDPs is 2167; most of the observations are related to Guatemala, which also experienced the deadliest earthquake in 1976. Most IDPs are given in the Modified Mercalli intensity scale (MM), followed by DYFI proxy intensities representing recent earthquakes; other intensity scales have been used depending on data availability.

The MDP sets vary in number from datasets with only a few points (6 earthquakes with less than 4 localities) to well-documented events (14 earthquakes with more than 50 IDPs). It is worth noting that the events studied were not selected *a priori*, e.g., using rules based on date or magnitude: They were collected to meet the diverse needs and interests of participating countries and researchers from CA. The magnitudes represented in the MDP sets range from M4.3–4.5 for some earthquakes in Honduras to M8.1 (1862 El Salvador earthquake). It must be clearly stated that magnitudes are not uniform, as they are determined by a variety of methods and instruments. Some parametric records of the studied events were modified with respect to the time of origin (date, time), the name of the epicentral area, or the preferred coordinates with respect to the catalog from which they originated. In addition, 20 events were given a number of fatalities, although sometimes this information can only be indicative. Even if the percentage of earthquakes coming from macroseismic data is low, it should be taken into account that the earthquake catalog is not declustered, as can be the case in other macroseismic databases (e.g., AHEAD, [29]).

Efforts to compile MDPs at the international scale (and thus integrate information across boundaries) and collect intensity values assigned by various scale metrics (e.g., MM, MSK, DYFI, including geologic and tsunami data) are specific choices introduced in MARCA-GEHN. They may represent improvements for enhancing data collection, but may also be viewed as limitations for users who are not sufficiently aware of the different origins and purposes of the data.

We provide some additional considerations here about the potential feedback of this data collection in nearby fields, such as seismotectonics, seismic hazard assessment, and site response studies.

3.1 The identification of the causative sources of earthquakes

The damage distribution resulting from an earthquake can provide valuable information for deciphering its causative source, i.e., the fault responsible for the seismic event. The basic assumption of uniform, isotropic propagation of seismic waves, with energy decreasing from a point source, is firmly established in the seismological literature. According to this view, the extent of the damage/perception areas is in some sense indicative of the energy and depth of the source, while asymmetric patterns in the distribution of the strongest intensities can be attributed to the orientation/finiteness of the causative fault. In the real world, such simplistic

assumptions are often violated because of the characteristics of the rupture, the propagation and local amplification properties, the complexity of earthquake sequences, and last but not least, the availability of “observers.” From the pioneering representations of damage distribution based on the isoseismal drawings to more recent formalizations of epicenter, magnitude, and propagation properties through mathematical constraints on the distribution of intensity data points (e.g., [30–32]), macroseismic data remain fundamental ingredients for addressing seismic sources in the pre-instrumental era.

At MARCA-GEHN, preliminary analysis of the macroseismic data sets collected to date has in some cases allowed different interpretations of the causative source than those adopted in the original catalog, in terms of earthquake location, proposed depth, and representative magnitude. For example, these changes are proposed to date:

- For the two earthquakes of 1859 and 1862, which occurred in western El Salvador and eastern Guatemala, offshore displacement with a decrease in magnitude is proposed (see [6], from page s41). The December 20, 1862 earthquake is the strongest event reported in the historical subsection of the catalog: an origin time is added with respect to the parent catalog [8]. The changes are motivated by critical reading of several accounts of the events, analogy of tsunami effects with recent events, and some consideration of cumulative damage.
- For the 1719, 1747, 1765, and 1874 events, reinterpretations as shallower magnitude events are preferred; we favor attributing them to the cortical volcanic-tectonic regime, in some cases the changes are also supported by the mapped geologic effects.
- For some events, relocations for mislocation in the origin catalogs are given (e.g., 1733 on the border of El Salvador, Honduras, and Guatemala; 1898 in Nicaragua; 1915 in El Salvador; 1917 Guatemala City; 1931 in Nicaragua).
- Finally, for one of the deadliest events in the historical part of the catalog, the 1773 earthquake, a relocation far away from the mapped sites to the interior of Guatemala is preferred, which now follows the proposal of activation of the Polochic-Motagua fault from the literature (**Figure 4**) [1].

A note is necessary. The modifications proposed for some events are preliminary, and the alternative parameters are given as “preferred” and do not replace the original solution. An exhaustive study for an earthquake could take a long time, which was outside the time span of the RIESCA project. Also, the impact of the proposed changes on a conventional seismic hazard analysis is now likely to be very limited. However rapid access to the maps, data points, referenced sources, and direct linkage to the repositories of the origin catalog have unprecedented potential to accelerate the collaborative growth of a transdisciplinary community that refines and uses these data.

3.2 Maximum observed shaking

One of the products of a macroseismic intensity database is a map of maximum observed intensities, a very basic representation of seismic hazard. In

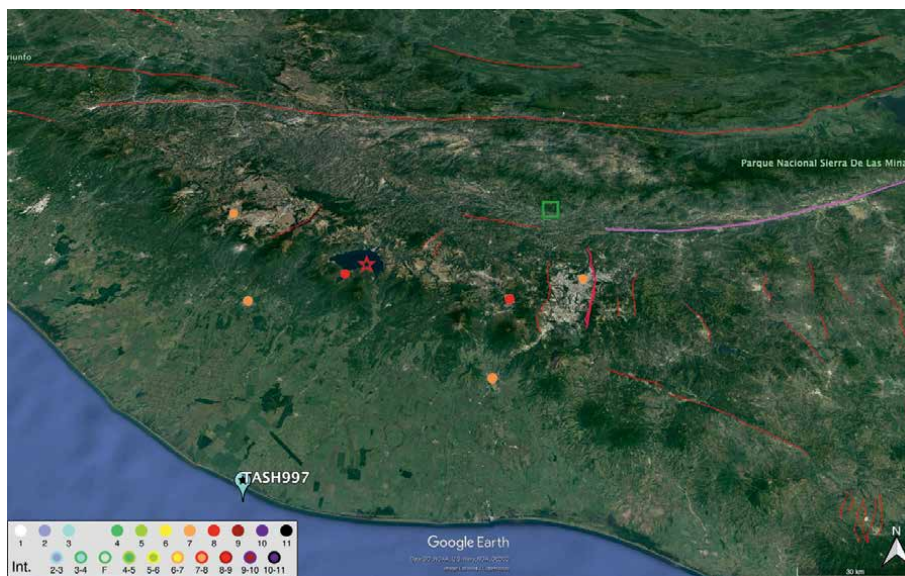


Figure 4.
 MDP set for the July 29, 1773 earthquake. The red star shows the epicenter adopted in GHEC [8] and taken from [33]; the light blue pin is the epicenter proposed by [34]; the green square is our preferred earthquake location given by [1]; the assign the event to the Polochic-Motagua fault (in purple). Redrawn from [6].

MARCA-GEHN, such a map appears on the entry page of the “Query by place” option, with the highest value at each locality represented by a color-coded dot. In **Figure 5**, the spatial distribution of the maximum intensity (I_{max}) is related to the municipalities, with their administrative areas filled in in color and, in addition, all the other sites studied are shown. Note that all MM /MSK/MCS/DYFI intensity data points are plotted together, while the geological and tsunami intensities (ESI/TSU data points) are not. This is still not a rigorous presentation, but it is an acceptable compromise to convey the effects of past earthquakes to a broad audience.

The maximum intensities follow the major fault systems and run in an almost continuous reddish band (intensities VIII and above) along the Pacific Coast volcanic belt from the Guatemalan-Mexican border to Managua in Nicaragua. A similar but less uniform stripe with intensities of VI and above follows the transform fault system from Lake Izabal in Guatemala to the Atlantic coast of Honduras.

Note the extent of the municipalities, which range from a few square kilometers in the most populated areas to huge chunks of territory in the wildest regions of Guatemala, Honduras, and Nicaragua. It should also be noted that some communities are not represented by intensity data points, even if they are located near highly damaged areas. For example, this is the case for some localities on the Pacific coast of Guatemala (SW of the capital): We suspect that this is mainly due to uneven population density and/or economic and cultural importance at the time of the major earthquakes, as reports, especially for historical earthquakes, usually refer to the main cities.

Future studies could also help inform research efforts to fill the knowledge gap on some seismic sources (e.g., the depression zone in Honduras) or in areas where there is little documentary evidence of past earthquakes (e.g., southern Nicaragua and the Pacific coastal strip of Guatemala).

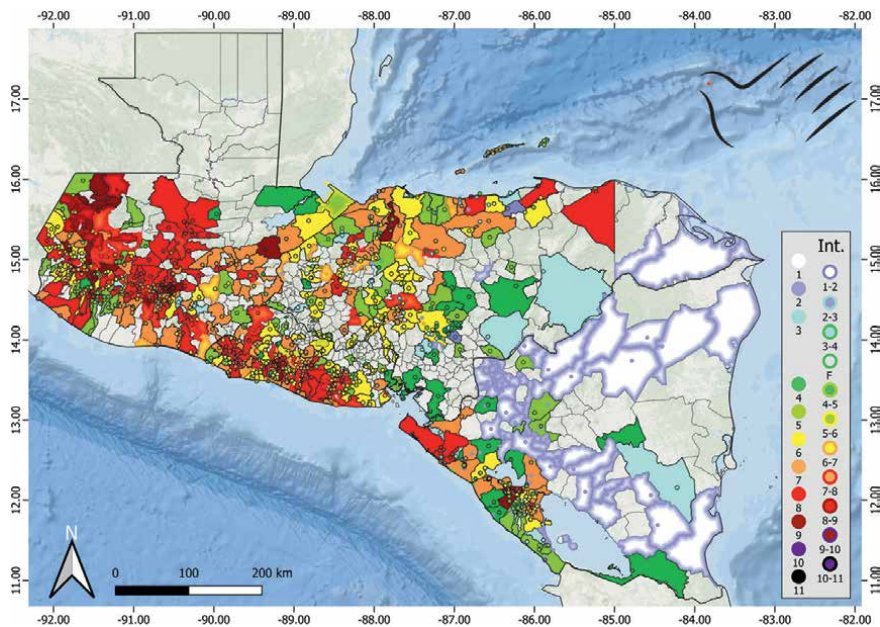


Figure 5. Maximum observed intensities as given in MARCA-GEHN (V2.0) for the four countries involved in the RIESCA project. The area of the municipality is indicated with the maximum value according to the color code of the legend on the right. In gray, the municipalities are without data.

3.3 Seismic histories at a site

Similar to the Imax map, the seismic history of a site is an interesting way to present and communicate the relevance of earthquakes to professionals and also to the general public. The collection of long and rich seismic site histories also allows alternative approaches to seismic hazard assessment that are not based on any assumptions about the seismogenic sources (e.g., the site intensity approach, [35]). The data stored to date in MARCA-GEHN are a first attempt at such data-driven studies, although they are not sufficient for reliable application to Central American sites. **Figure 6** shows the seismic histories of Guatemala City and San Salvador, two capitals of the four countries involved in the RIESCA project.

With 20 observations (**Figure 6a**), San Salvador is the most populated seismic site history in the current database (version 2.0). The collected data, which are still very incomplete, range from the beginning of the Spanish invasion (1719, San Vicente earthquake) to a moderate offshore earthquake in 2018. The highest observed intensity is attributed to the 1986 San Salvador earthquake (IX), followed by the January 2001 earthquake and the 1719 one (VIII). Note that the effects above the first damage condition (intensity \geq VI) are presented 11 times. We acknowledge that the intensities obtained by the DYFI survey should be considered with great caution since the damage conditions are sometimes supported by very few questionnaire compilations.

Guatemala is known to have had its capital moved from its original location at least three times due to earthquake damage, and the country's seismic history includes many devastating earthquakes. Currently, Guatemala City covers 228 square kilometers and is the most populous city in Central America, with about three million inhabitants. It is therefore very difficult to consider it as a single place, as the MIDOP engine

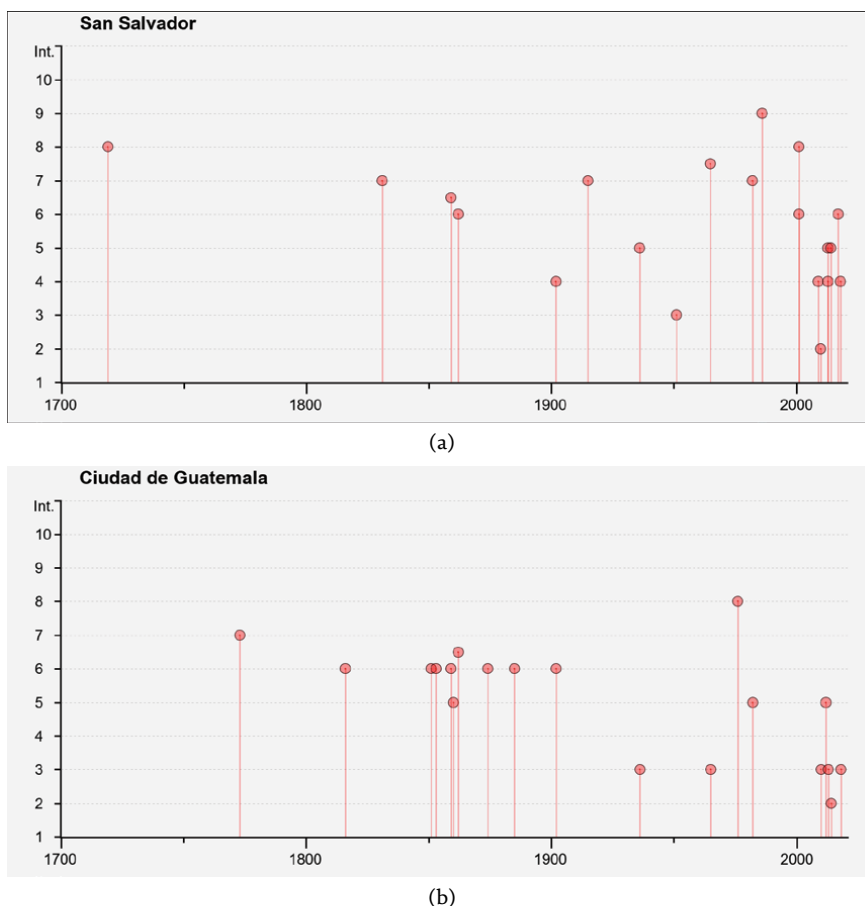


Figure 6.
 Seismic site history for: a) San Salvador (SV), available at https://marca-gehn.info/v2.0/query_place/places/./call_place.htm?place=3583361; (b) Guatemala City (GT), available at https://marca-gehn.info/v2.0/query_place/places/./call_place.htm?place=3598132.

has technically done. In this version, the seismic history of the Guatemala City site includes 19 earthquakes (**Figure 6b**), from the Santa Maria de Santiago earthquake of 1773 to the moderate offshore event in El Salvador on January 3, 2018. Note that after the 1773 earthquake, the capital city of Antigua Guatemala (https://marca-gehn.info/v2.0/query_place/places/./call_place.htm?place=3599699) was moved to its current location in 1776, which explains why there are no earthquakes before that date; also note that the 1917–1918 seismic sequence represented by the December 26, 1917, MDP record with 71 IDPs all located in the broad area of the city is not shown on the graph in **Figure 6b**. This is a typical case where assessing intensity at a more detailed scale than the administrative level of the municipality causes some problems. If we assume that the intensity of the 1917 event in Guatemala City can be estimated “globally” at VIII–IX, this results in the highest value observed so far, exceeding the value given for the devastating 1976 earthquake.

For more details, we invite readers to also surf to the list of nearest localities (within 15 km) that appears below the time graph, at the link provided in the caption of **Figure 6**.

Similar conditions with very strong lateral variability of damage due to local site responses (amplification and permanent surface deformation or liquefaction) are reported for Managua (NI) during the December 23, 1972 earthquake, where IDPs were assigned to subsectors of the city. Finally, in Tegucigalpa (HN), initial damage conditions were reached only once, in 1774, while more or less distant earthquakes are felt quite frequently (degrees III and IV): consider that most data for Honduras come from DYFI questionnaires, with all their advantages and disadvantages.

These examples underscore the need for additional basic research efforts on historical and contemporary documentary sources for all countries from CA to increase the reliability of macroseismic intensity assessments.

4. What next?

The macroseismic archive for the countries of Central America-Guatemala, El Salvador, Honduras, and Nicaragua (MARCA-GEHN) was developed in 2017–2020 under the RIESCA project funded by the Italian Agency for Development Cooperation (AICS). The database was updated in 2022–2023 based on the voluntary efforts of some authors.

Guatemala, El Salvador, Honduras, and Nicaragua are exposed to a variety of seismogenic processes, ground shaking of different relevance, and non-uniform instrumental and historical seismic data availability. In addition, local reference institutions sometimes face limited human and material resources, and in general, macroseismology research is not considered as important as instrumental seismology. The RIESCA project has attempted to adapt European best practices in macroseismology research to publish a publicly available online prototype database of macroseismic observations for some countries in CA. The working group has adopted some simplified solutions to solve the problems related to data collection, sharing and verification, and remote working, a problem exacerbated by the COVID-19 pandemics in the final phase of the project. Another special aspect is that MARCA-GEHN has tried to solve problems occurring at the borders of neighboring countries, whereas studies usually focus on the national level.

We have resorted to international earthquake catalogs (GHEC and ISC) to relate the table of IDPs to a specific parametric record. This choice is mainly motivated by the need to clearly identify the data sources (e.g., original seismic phase readings and location for instrumental earthquakes, documentary source studies for historical events); we also pursue the hope of contributing to the improvement of the next versions of these international databases or other publicly available repositories of metadata needed for other applications (e.g., seismic hazard assessment). Viewed in this light, the online database has great potential to serve a large community of researchers and stakeholders, experts, and the general public, but it needs a strategy to ensure continued maintenance and regular updates over the long term.

A major limitation of MARCA-GEHN is the incomplete inventory of primary sources; on the other hand, the most devastating earthquakes of the last two centuries have been studied in some detail. Geologic deformation in the area is often so rapid that many seismic sources have been active during this limited period, and recent earthquakes can be used to make some analogies with the oldest and less documented earthquakes. Some technical issues with the presentation of macroseismic data with different objectives (e.g., geologic or tsunami effects versus intensity data points

based on building stock effects) also need to be addressed to allow the easiest use of the database contents.

We hope that this tool will increase the interest of local institutions in using macroseismic data, as interdisciplinary studies that consider the historical, socio-economic, geological, and seismological aspects of earthquakes together are paramount to safer and better-prepared communities.

Acknowledgements

The development of the online database was supported by the RIESCA project “Escenarios de Riesgo en Centroamérica”, funded by AICS - Italian Agency for Development Cooperation and coordinated by the University of Palermo. The current version 2.0, published in 2023, is thanks to the voluntary efforts of the authors, and to the support of the OLLIN network (IGCP 669) funded by UNESCO- IUGS; the websites are maintained by UNAH and OGS. We thank all participants in the data collection listed in the first monographic description of the work (<https://bgo.ogs.it/issues/2021-vol-62-suppl-2>). The MARCA-GEHN archive uses a beta version of MIDOP provided by Mario Locati: we thank him for his repeated help and support.

Conflict of interest

The authors declare no conflict of interest.

Notes/thanks/other declarations

The archive MARCA-GEHN is available without user registration.

The first public version V.1.6 (September 2020) and the current version V.2.0 are published on the website <http://marca-gehn.info> hosted in Honduras; for security and redundancy reasons, the latest version is also accessible at <http://marca-riesca.inogs.it> managed in Italy.

Author details

Laura Peruzza^{1*}, Eliana Esposito², Felix Enrique Rodríguez García³
and Giuseppe Giunta⁴

1 National Institute of Oceanography and Applied Geophysics OGS, Trieste, Italy


2 National Institute of Oceanography and Applied Geophysics OGS, Italy

3 Earth Physics Department, Autonomous National University of Honduras UNAH,
Tegucigalpa, Honduras

4 DiSTeM, University of Palermo, Palermo, Italy

*Address all correspondence to: lperuzza@ogs.it

IntechOpen

© 2023 The Author(s). Licensee IntechOpen. This chapter is distributed under the terms of the Creative Commons Attribution License (<http://creativecommons.org/licenses/by/3.0>), which permits unrestricted use, distribution, and reproduction in any medium, provided the original work is properly cited. 

References

- [1] Peraldo G, Montero W. Sismología histórica de América Central. México: IPGH; 1999. p. 346
- [2] Rojas W, Bungum H, Lindholm C. Historical and recent earthquakes in Central America. Review in Geological America Central. 1993;**16**:5-22
- [3] Grases J. Terremotos Destructores del Caribe 1502-1990: UNESCO-RELACIS, Regional Office of Science and Technology of UNESCO for Latin America and the Caribbean. 1994. 132 p
- [4] Feldman L. Mountains of Fire, Lands That Shake: Earthquakes and Volcanic Eruptions in Central America (1505-1899). USA: Labyrinthos; 1993
- [5] Ambraseys N, Adams R. Large central American earthquakes 1898-1994. Geophysical Journal International. 1995;**127**:665-692
- [6] Peruzza L, Esposito E, Rodríguez García FE, García Castro RA, Santos P, Marroquín G, et al. MARCA-GEHN, a prototype macroseismic archive of four Central America countries. Bulletin of Geophysics and Oceanography. 2021;**62**(Suppl. 2):s1-s198
- [7] Locati M, Cassera A. MIDOP: Macroseismic Intensity data online Publisher. Rapporti Tecnici INGV. 2010;**123**:92
- [8] Albini P, Musson RMW, Gomez Capera AA, Locati M, Rovida A, Stucchi M, et al. Global Historical Earthquake Archive and Catalogue (1000-1903). Pavia, Italy: GEM Foundation; 2013. p. 202
- [9] Albini P, Musson RMW, Rovida A, Locati M, Gomez Capera AA, Viganò D. The global earthquake history. Earthquake Spectra. 2014;**30**:607-624. DOI: 10.1193/122013EQS297
- [10] International Seismological Centre (ISC). ISC-GEM Earthquake Catalogue V9.0. 2022. DOI: 10.31905/d808b825. Available from: <http://www.isc.ac.uk/iscgem/citing.php>
- [11] Albini P, Moroni A, editors. Materials of CEC Project Review of Historical Seismicity in Europe. Vol. 2. Milano: CNR; 1994. p. 254
- [12] Espinosa AF. The Guatemalan earthquake of February 4, 1976, a preliminary report. In: Geological Survey Professional Paper 1002. Washington D.C, United States: Geological Survey; 1002. 1976. p. 90. DOI: 10.3133/pp1002
- [13] Plafker G. Tectonic aspects of the Guatemala earthquake of 4 February 1976. Science. 1976;**193**:1201-1208. DOI: 10.1126/science.193.4259.1201
- [14] Bucknam RC, Plafker G, Sharp RV. Fault movement (afterslip) following the Guatemala earthquake of February 4, 1976. Geology. 1978;**6**:170-173. DOI: 10.1130/0091-7613(1978)6<170:FMAFTG>2.0.CO;2
- [15] Franco A, Lasserre C, Lyon-Caen H, Kostoglodov V, Molina E, Guzman-Speziale M, et al. Fault kinematics in northern Central America and coupling along the subduction interface of the Cocos Plate, from GPS data in Chiapas (Mexico), Guatemala and El Salvador. Geophysical Journal International. 2012;**189**:1223-1236. DOI: 10.1111/j.1365-246X.2012.05390.x
- [16] Young CJ, Lay T, Lynnes CS. Rupture of the 4 February 1976 Guatemalan

earthquake. Bulletin in Seismology Society in America. 1989;**79**:670-689. DOI: 10.1785/BSSA0790030670

[17] Yoshida S. Waveform inversion methods for the earthquake. Journal of Physics of the Earth. 1995;**43**:183-209. DOI: 10.4294/jpe1952.43.183

[18] Langer CJ, Bollinger GA. Secondary faulting near the terminus of a seismogenic strike-slip fault: Aftershocks of the 1976 Guatemala earthquake. Bulletin in Seismology Society in America. 1979;**69**(2):427-444

[19] Esposito E. Macroseismic Evaluation of the Damage Produced by the 1917-1918 Earthquakes in Guatemala City, by Photos, before and after the Seismic Sequence. Napoli, Italy: RIESCA; 2019. p. 105

[20] Musson RMW, Grünthal G, Stucchi M. The comparison of macroseismic intensity scales. Journal of Seismology. 2010;**14**:413-428. DOI: 10.1007/s10950-009-9172-0

[21] Lardé J. El terremoto del 6 de Septiembre de 1915 y los demás terremotos de El Salvador. Edición de la Revista de la Enseñanza. 1916;**1916**:76

[22] Musson RMW, Cčić I. Intensity and intensity scales. In: Bormann P, editor. New Manual of Seismological Observatory Practice (NMSOP-2). Vol. 12. Potsdam: Deutsches GeoForschungsZentrum GFZ; 2012. p. 41. DOI: 10.2312/GFZ.NMSOP-2_ch12

[23] Sieberg A, Scala MCS. Mercalli-Cancani-Sieberg. Geologie der Erdbeben, Handbuch der Geophysik. 1930;**2**:552-555

[24] Medvedev S, Sponheuer W, Karnik V. Neue seismische Skala Intensity scale of earthquakes, 7. Tagung der Europäischen Seismologischen Kommission vom

24.9. bis 30.9.1962. In: Veröff J, editor. Institut für Bodendynamik und Erdbebenforschung in Jena, 77. Berlin: Deutsche Akademie der Wissenschaften; 1964. pp. 69-76

[25] Atkinson GM, Wald J. “Did you feel it?” Intensity data: A surprisingly good measure of earthquake ground motion. Seismological Research Letters. 2007;**78**(3):362-368. DOI: 10.1785/gssrl.78.3.362

[26] Michetti AM, Esposito E, Guerrieri L, Porfido S, Serva L, Tatevossian R, et al. Environmental Seismic Intensity scale – ESI 2007 La scala di Intensità Sismica basata sugli effetti ambientali – ESI 2007. In: Memorie descrittive della carta geologica D’Italia. Rome: LXXIV, APAT; 2007. p. 74

[27] Silva PG, Michetti AM, Guerrieri L. Intensity scale ESI 2007 for assessing earthquake intensities. In: Beer K, Patelli A, editors. Encyclopedia of Earthquake Engineering. Berlin, Heidelberg: Springer; 2015. p. I20. DOI: 10.1007/978-3-642-36197-5_31-1

[28] Papadopoulos G, Imamura F. A proposal for a new tsunami intensity scale. In: International Tsunami Symposium (ITS) 2001 Proceedings, Session 5. Seattle: IUGG; 2001. pp. 569-577

[29] Locati M, Rovida A, Albini P, Stucchi M. The AHEAD portal: A gateway to European historical earthquake data. Seismological Research Letters. 2014;**85**(3):727-734. DOI: 10.1785/0220130113

[30] Peruzza L. Macroscopic intensity versus distance: Constraints to the attenuation model. In: Cakmak AS, Brebbia CA, editors. Soil Dynamics and Earthquake Engineering VII. Southampton: Comp. Mech. Publ; 1995. pp. 215-222. DOI: 10.2495/SD950251

- [31] Bakun WH, Wentworth CM. Estimating earthquake location and magnitude from seismic intensity data. *Bulletin of the Seismological Society of America*. 1997;**87**:1502-1521
- [32] Gasperini P, Vannucci G, Tripone D, Boschi E. The location and sizing of historical earthquakes using the attenuation of macroseismic Intensity with distance. *Bulletin of the Seismological Society of America*. 2010;**100**:2035-2066
- [33] White RA, Ligorria JP, Cifuentes IL. Seismic history of the middle America Subduction Zone along El Salvador, Guatemala, and Chiapas, Mexico: 1526-2000. In: *GSA Special Paper 375. El Salvador: Natural Hazards in El Salvador*; 2004. pp. 379-396. DOI: 10.1130/SPE375
- [34] Tanner J, Shepherd JB. Seismic Hazard in Latin America and the Caribbean. *IPGH*. 1997;**1**:144
- [35] Albarello D, Mucciarelli M. Seismic hazard estimates using ill-defined macroseismic data at site. *Pure and Applied Geophysics*. 2002;**159**:1289-1304. DOI: 10.1007/s00024-002-8682-2

The Role of Earthquake Catalogue in Seismic Tomography

Giuseppe Pucciarelli

Abstract

Seismic tomography is a process used to know a structure in the depth of a determined part of Earth. It consists of two parts. The first one, the so-called Forward Problem, provides a computation of theoretical traveltimes starting from an estimate of hypocentral parameters obtained by earthquakes registered by a specific network of seismic stations. The second one, the so-called Inverse Problem, aims at providing a 3-D seismic velocity model obtained minimising residuals, that is the difference between theoretical and observed traveltimes. The production of a well-distributed earthquake catalogue is really important to obtain a well-performed seismic tomography. So, it is relevant to the description of the rules to achieve an acceptable and performing earthquake catalogue for seismic tomography. Three examples are shown: local tomography, regional tomography, teleseismic tomography. In each of them, broad relevance has been given to the theoretical background and to the formation of an earthquake catalogue with just a hint (images only) to the final results.

Keywords: seismic catalogue, seismic tomography, earthquake catalogue, earthquake hazard, earthquake history

1. Introduction

Through the word tomography, a process adopted in many known sciences (for example, medicine, oceanography, etc...) has been described. A process with an only aim: studying the internal structure of a determined system by means of a series of sources that enlighten it. For example, the Computer Axial Tomography (CAT) is used in medicine and consists of X-Ray beams that barrage the body of a person to light up his (or her) internal. Seismic tomography works in the same way. This process allows us to know the principal characteristics of a structure in the depth of a determined part of Earth. Seismic tomography could be divided into three categories: seismic refraction tomography, attenuation seismic tomography and the “classic” traveltime seismic tomography. For brevity, only the last one will be described in this chapter.

1.1 Traveltime seismic tomography: a general description

A traveltime seismic tomography follows the established model of a so-called Inverse Problem [1]. That is, the following structure is implemented in this way (**Figure 1**):

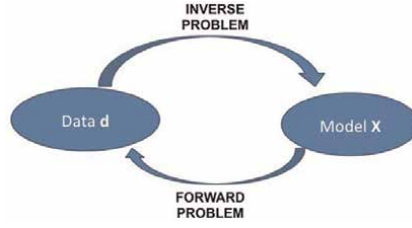


Figure 1.
Graphic description of an inverse problem.

Part 1, Forward Problem - Theoretical traveltimes starting from an estimate of hypocentral parameters are computed. This estimate is obtained by a 1-D starting velocity model.

Part 2, Inverse Problem – Estimate of the hypocentral parameters through a comparison between theoretical and observed results.

In this regard, for each datum, the estimate of residual (Eq. (1)) that is the difference between the observed travel times (labelled $Tr.time^{obs}$) and these theoretical travel times (labelled $Tr.time^{teo}$) takes considerable importance. This is because the entire process stops when the residual touches its minimum value.

$$Residuals = Tr.time^{obs} - Tr.time^{teo} \quad (1)$$

Generally, traveltime seismic tomography is a non-linear problem [2]. A generic travel time $Tr.time$ along a ray r is given by:

$$Tr.time = \int_{r(s)} s(r) ds \quad (2)$$

where s is the slowness, that is the reciprocal of velocity of seismic wave v . Using slowness instead of velocity, we could affirm that (Eq. (2)) is linear. This affirmation is wrong. In fact, rays are curves of stationary travel time and therefore depend on the slowness. So, slowness compares both in the integrand and it determines ray position $r(s)$ in (Eq. (2)). Before proceeding, we should linearize (Eq. (2)). For obtaining this result, Fermat's principle has invoked. It says that the travel along a ray does not change to first order when this ray is perturbed. This principle has been applied to the following equation:

$$|\nabla Tr.time|^2 = s^2 r \quad (3)$$

It is the *eikonal equation*, that is an equation which describes the propagation of a wavefront $Tr.time$ and its solution allows us to compute traveltimes. By means of a systematic permutation approach, eikonal equation can be linearized. For solving it, 1-D velocity model has been discretized in a sort of grid (*Jeffreys-Bullen model*, AK135, IASP91) (**Figure 2**). In this way, seismic tomography becomes a typical matrix problem solvable by means of specific numerical algorithms (MTT, difference finite eikonal equation, Fast Marching for the forward problem, least squares for the inverse problem [3]).

Performing a seismic tomography obviously has the goal of obtaining good results. A goal can be reached if all the characteristics used for realising a seismic tomography

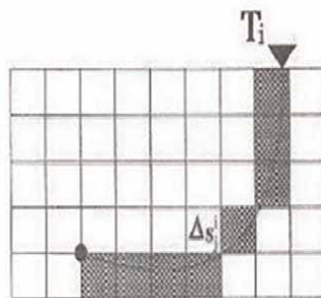


Figure 2.
 Schematic description of a grid for traveltime seismic tomography. T_i is the i -th traveltime used for the inversion, Δs_j is the grid step for T_i traveltime through j -th grid cell, “point” symbolises hypocenter, “triangle” symbolises seismic station.

are refined. For example, numerical characteristics (choice of grid limits, grid tests, etc. ...), informatics, computing characteristics (capability of computers, software elaboration, software graphic). But one characteristic is fundamental: the assembly of an opportune database of seismic events. Who performs a seismic tomography should answer to following guidelines questions: (1) How many seismic events are needed? (2) By what criteria (magnitude, type, period) seismic events are selected? (3) By what criteria (geometrical distribution, acquisition of a determined seismic event) a network of seismic stations is selected? Relevant questions that have not absolute answers but these last ones could change depending on the geophysical situation. In this proposal, three different situations are shown. That is, a local, a regional and a teleseismic traveltime tomography. Three different situations with the aim of finding a common denominator in the production of a seismic catalogue.

1.2 The example of a local seismic tomography

The first one is a local seismic tomography (that is a seismic tomography of an area almost 100x100 km) of Campania and Basilicata, two regions of South Italy that on 23th of November 1980 were shattered by a disastrous earthquake ($M_W = 6.9$, 2483 dead people and 7700 injured) [4]. In this case, the seismic catalogue consists of 665 events that are the aftershocks (**Figure 3**) acquired by the Italian seismological network and temporary seismic network in the period 1–15 December 1980 (107 stations) for a total of 18,625 P phases. Following the guidelines of questions previously mentioned, it is possible to understand that:

(1) Considering the strong magnitude of mainshock and consequently big number of aftershocks, it seems quite reasonable that two weeks of continuous acquisition are enough for having a complete database; (2) Being a local seismic tomography, it makes little sense to operate a strong selection from point of view of magnitude (except for instrumental earthquakes); (3) a strong set of local seismic station has been chosen with the support of Italian seismological network for having a better geometrical distribution (**Figure 4**).

An image of a horizontal section of local Irpinia tomography is shown (**Figure 5**).

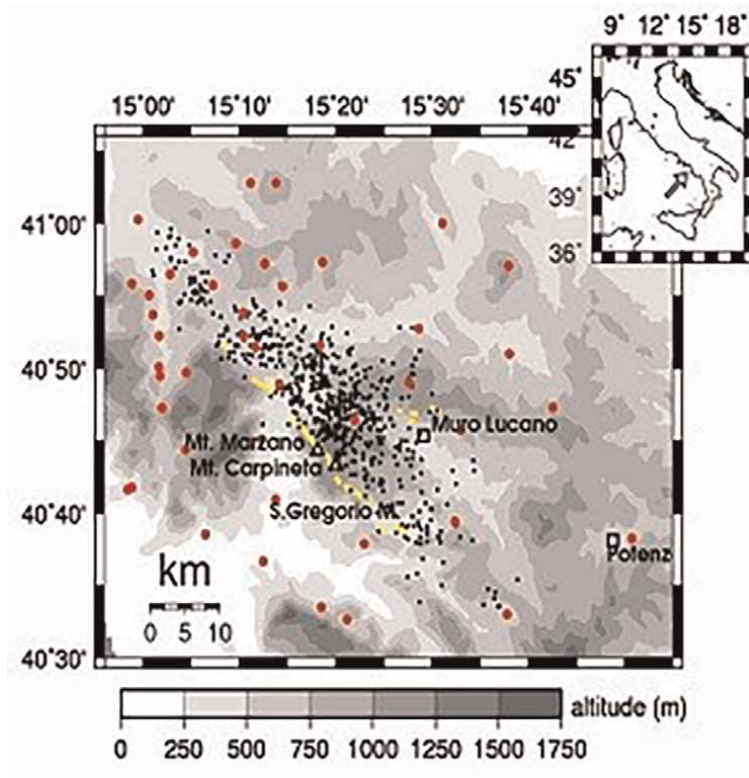


Figure 3.
Geographical distribution of aftershocks of Irpinia earthquake (23rd November 1980) used to construct earthquake catalogue for local Irpinia traveltimes seismic tomography.

1.3 The example of a regional seismic tomography

The second one is a regional seismic tomography of circum-arctic [5]. That is, a tomography with a database composed of earthquakes whose epicentral distance is included in the range [100 km; 1400 km]. In this way, whereas the epicentral distance is greater than the similar one in local earthquakes, seismic rays could “illuminate” a higher depth. For producing an optimal database, in these cases, a database of the *International Seismic Centre* (ISC) is used. It is a database consisting of 4 million seismic events, not only earthquakes but also artificial explosions and a network of even 50 million individual seismic stations.

In this regional seismic tomography of circum-arctic (**Figure 6**), P waves of local earthquakes recorded by ISC seismic stations (number not specified) at a regional distance in a period [1964–2007] are used for producing the database (**Figure 7**).

Grid for tomography is 7000 x 7000 x 50 km in depth, with a maximum depth of 640 km (that is, near at range of maximum depth at which an earthquake can occur, 660–700 km in the lower mantle). In this work, more inversions have been performed at different orientations and their average in one model has been considered. The distribution of events and the seismic station is very irregular for the simple reason that in the central part of the circum-arctic region there are not seismic stations and consequently there is very poor ray coverage. Answering the “guideline questions”, it is possible to notice:

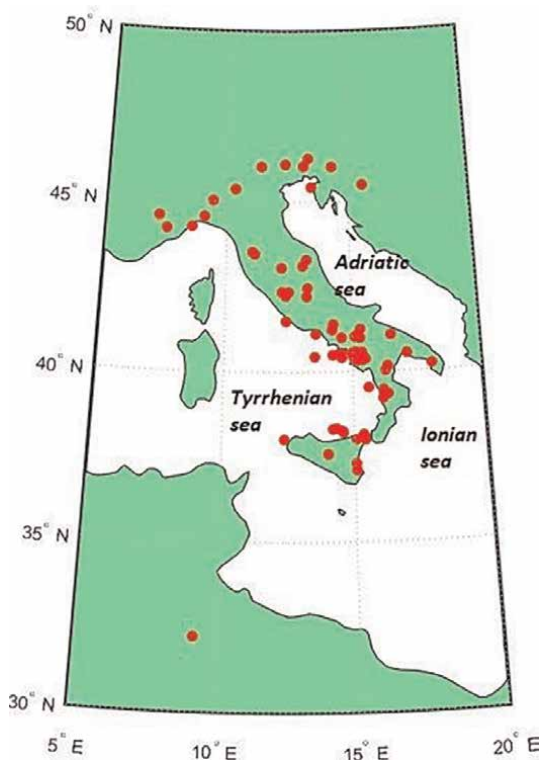


Figure 4.
 Network of seismic stations for local Irpinia traveltime seismic tomography.

(1) The huge number of seismic events and making recourse to the ISC seismic catalogue represent an obvious choice because of the goal of tomography (that is, the study of greater depths); (2) The huge number of data is strictly connected with the risk of poor quality. Indeed, a preprocessing and a selection of data by means of determined (but not specified) criteria has been performed; (3) Considering the geographical peculiarity of the zone, even in this case the choice of network stations is obliged.

Images of horizontal sections of regional Circum-Arctic tomography have been shown (**Figure 8**).

1.4 The example of a teleseismic tomography

The third and last (but not the least) case is a teleseismic tomography of *Southern Tyrrhenian* [6, 7]. Teleseisms are earthquakes whose epicentral distance (expressed in angular distance) is greater than 30° (**Figure 9**). The *Tyrrhenian Sea* is a back-arc basin (that is, it is a basin made up of oceanic crust associated with a roll-back subduction that is a result of the subducting Ionian slab since the Tortonian Age (10 Ma) [8]. At the present day, most of the oceanic lithosphere in the Tyrrhenian-Apennine system has been consumed with the exception of the 74 Calabrian arc sector where there is still subducting Ionian lithosphere, confined to the southwest by the Malta Escarpment [9].

Teleseismic tomography has been chosen because the 3D models obtained only to describe in a good way the crust and the first part of the upper mantle (maximum

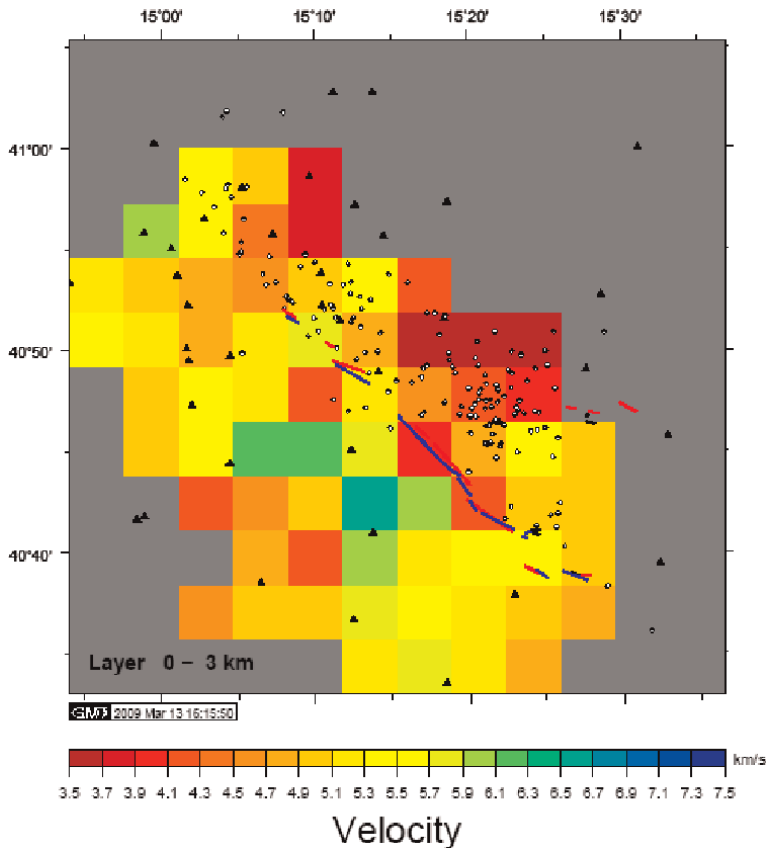


Figure 5.
Horizontal section of Irpina local tomography at 3 km depth.

reached depth of Southern Tyrrhenian local tomographies is 350 km) and in scientific literature there are few works of teleseismic tomography regarding Southern Tyrrhenian [10].

The used database consists of 2979 teleseisms recorded (**Figure 10**) by 285 Italian ISC seismic stations (**Figure 11**) from 1980 to 2012 with a total of 18,515 arrival times relating to P phases. For obtaining a better stability, a preprocessing of data has been performed by means of the following criteria:

- magnitude >6
- epicentral distance included in the range [20°; 100°]
- station residual included in the range [−2 seconds; 2 seconds]
- each teleseism must be recorded by almost 10 stations

The distribution of the seismic station is coherent with the area object of tomographic investigation because ISC Southern Italy has been chosen. Grid for tomography has been constructed following these criteria: 0–500 km in depth; 7°–20° E in

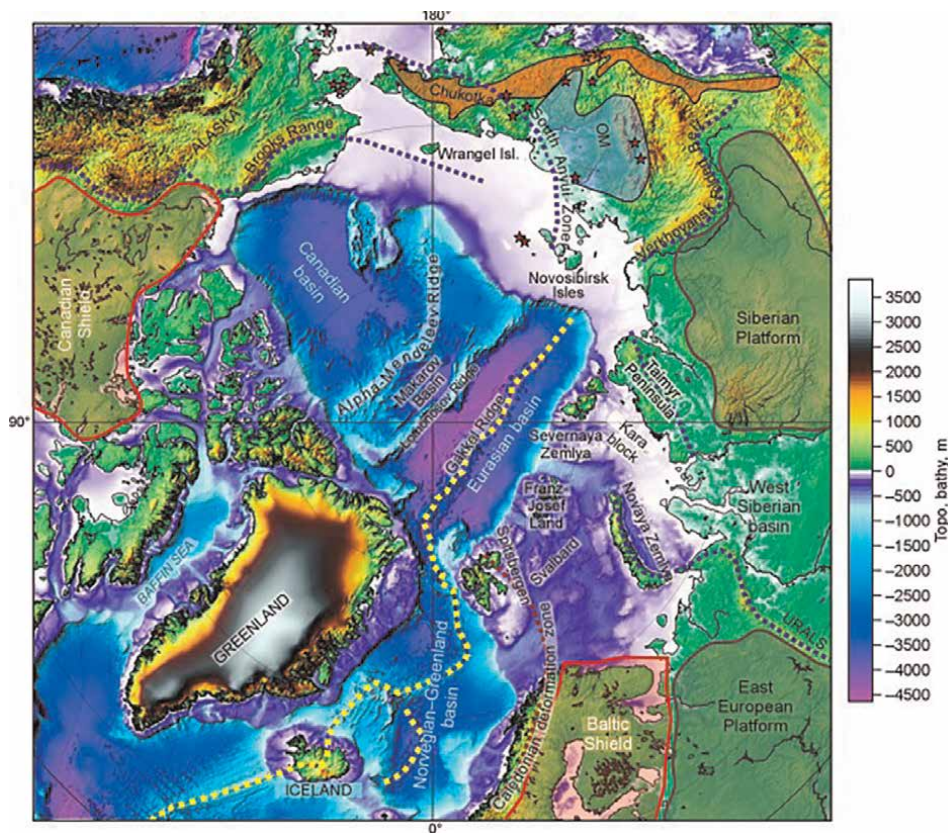


Figure 6.
Topographic/bathymetric map of Circum-arctic region.

longitude; 35°–48° N in latitude while grid spacing is 50 km in depth; 0.8 degrees in longitude, 0.4 degrees in latitude (**Figures 12 and 13**). Answering three guidelines questions: (1) Being (fortunately) teleseisms seismic events not very common, it seemed very reasonable that a very large period (32 years) was considered; (2) Chosen criteria of preprocessing data have been established to obtain data uniformity; (3) For obtaining a good ray coverage in the tomographic area, it seemed very reasonable, considering their availability, the choice of all available ISC Southern Italy seismic stations.

2. Conclusions

The topic of this chapter concerns the role of the formation of a seismic catalogue for performing a traveltime tomography. Three several typologies have been shown: a local, a regional and a teleseismic one.

For all typologies, the seismic catalogue is composed of P seismic phases. This is because of the stability of this phase and the overall presence and easiness of picking on a seismogram. The strong differences among these typologies of tomographies regard the formation of the database, above all in number and period of acquisition of

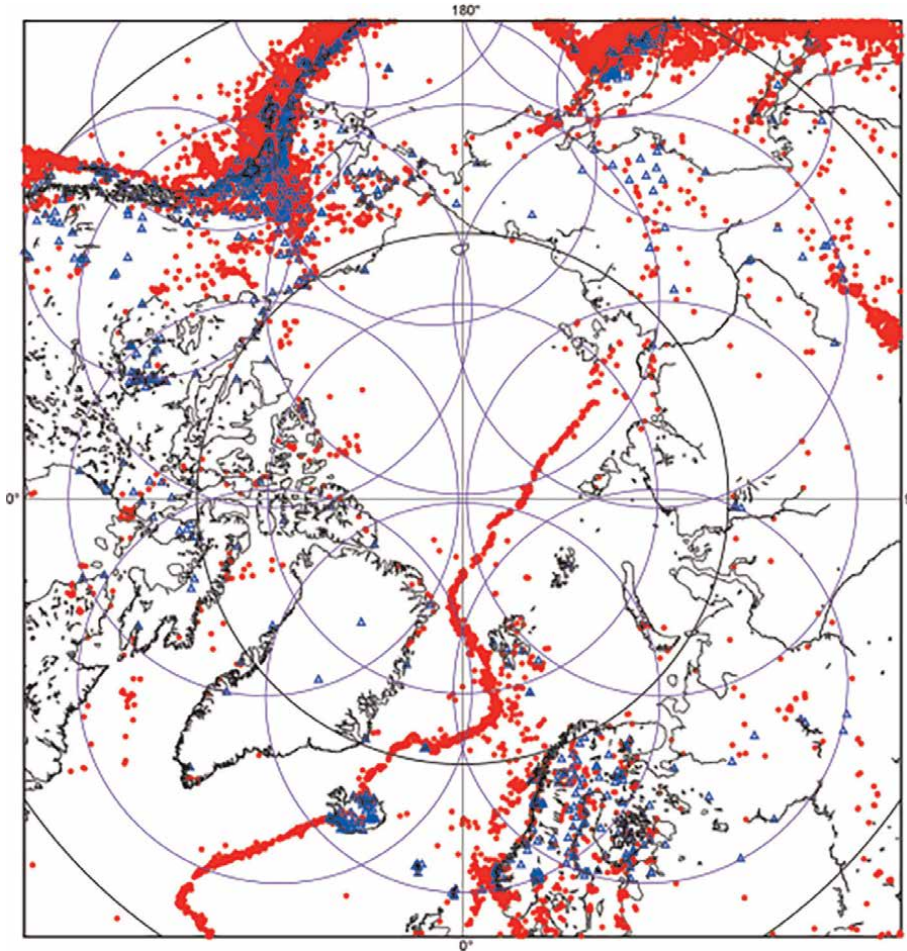


Figure 7. Distribution of seismic events and seismic stations in circumpolar region. Red dots represent ISC seismic events, blue triangles are seismic stations.

events, choice of seismic stations and their geometrical distribution in the area of investigation.

As regards local tomography – that has as its goal the “illumination” of shallow depths – it seems reasonable that the construction of a database composed of seismic events in the hundreds acquired by a network of seismic stations. The geometrical distribution of these last ones is simply the current network of seismic stations in the area of investigation. A more stable case for local tomography is (as in the case of example) when seismic events are aftershocks of a main event. This is for two reasons: 1) a practical reason because in a few days, the construction of the database has been performed; 2) a “scientific” reason because the magnitude of aftershocks is more or less similar, therefore there is a major uniformity and sturdiness of data.

As regards regional and teleseismic tomography, making recourse to the ISC catalogue is almost obliged because regional and teleseismic events could be acquired by local seismic stations but in lots of situations their archives are not rich events in enough number for performing a tomography. This choice implicates two consequences: 1) the construction of a database for a period of almost 30–40 years; 2) the

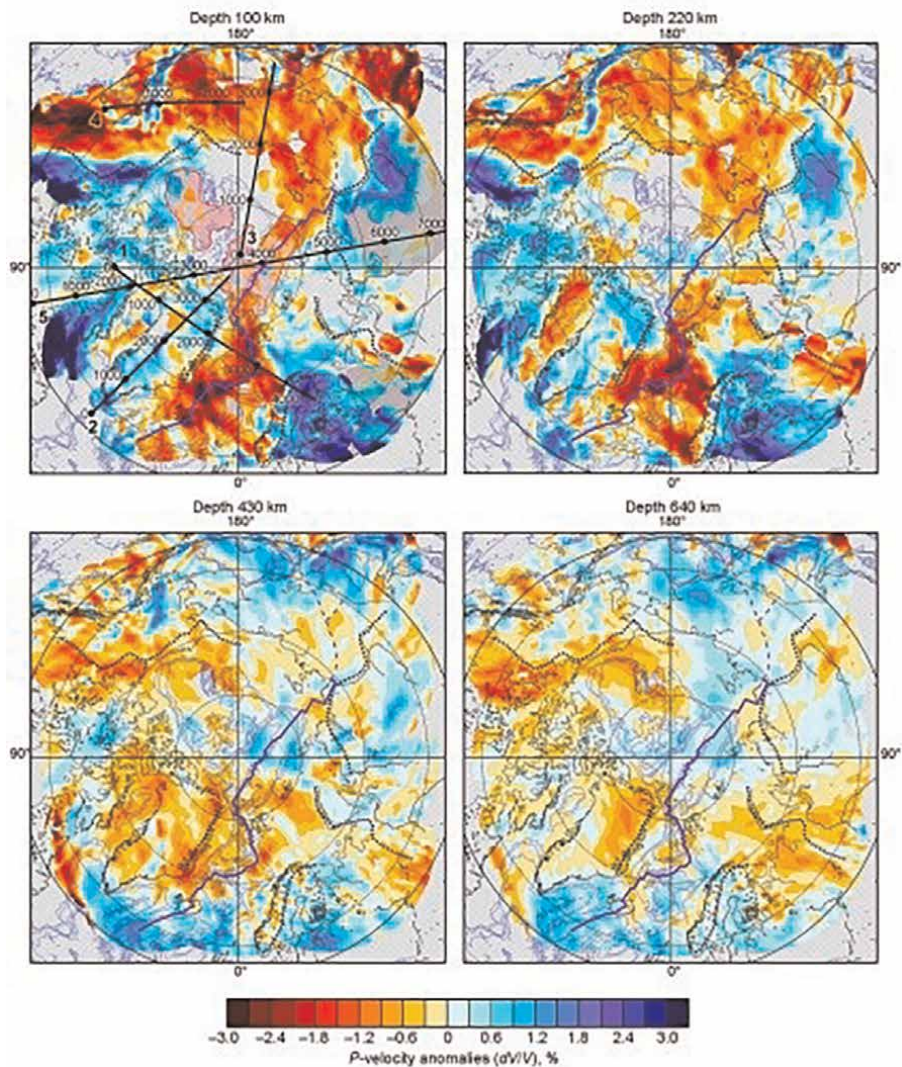


Figure 8.
Distribution of seismic events and seismic stations in Circum-arctic region. Red dots represent ISC seismic events, blue triangles are seismic stations.

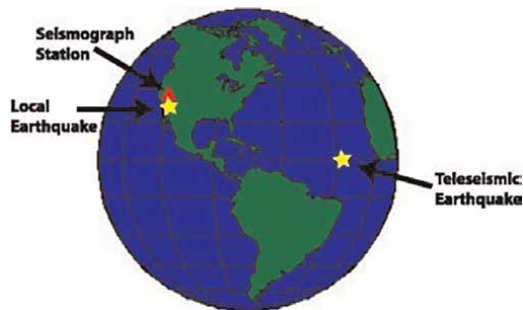


Figure 9.
Graphical representation of a comparison between local and teleseismic earthquake.

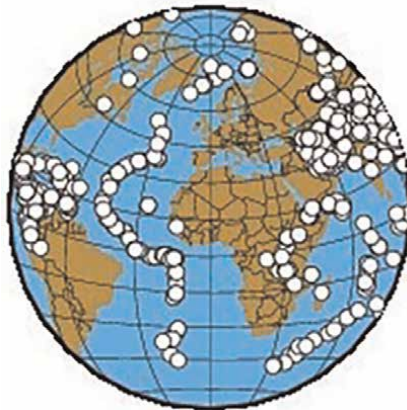


Figure 10.
Map of events (white dots) for southern Tyrrhenian teleseismic tomography.

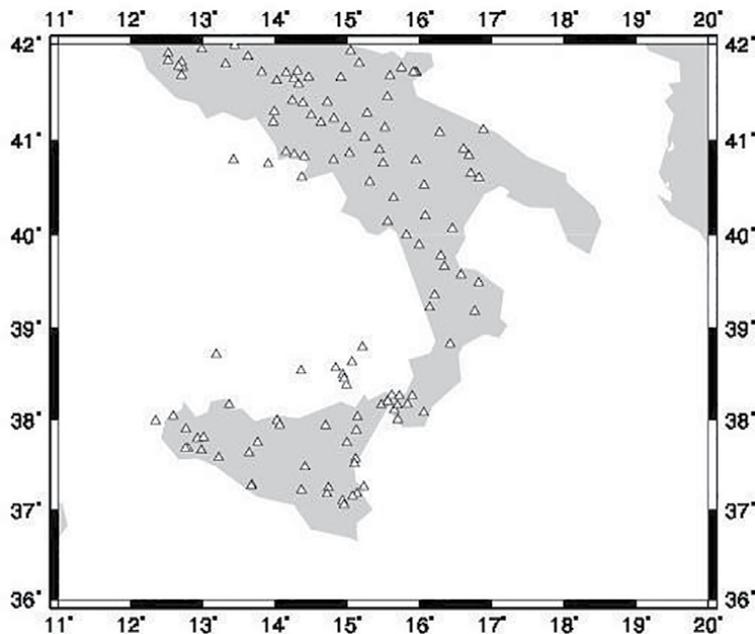


Figure 11.
Map of ISC seismic stations (white triangles) for southern Tyrrhenian teleseismic tomography.

development of “a priori” conditions to select data for performing a sort of “data preprocessing” in such a way the used data are “clean” and ready to be analysed for a tomography. In this way, the number of data is one-two order of magnitude greater than its equivalent for the local one.

Regarding the network of seismic stations, local tomography establishes the restriction to use a network of local seismic stations geometrically distributed in the area of investigation in a uniform way while the use of ISC seismic catalogue offers

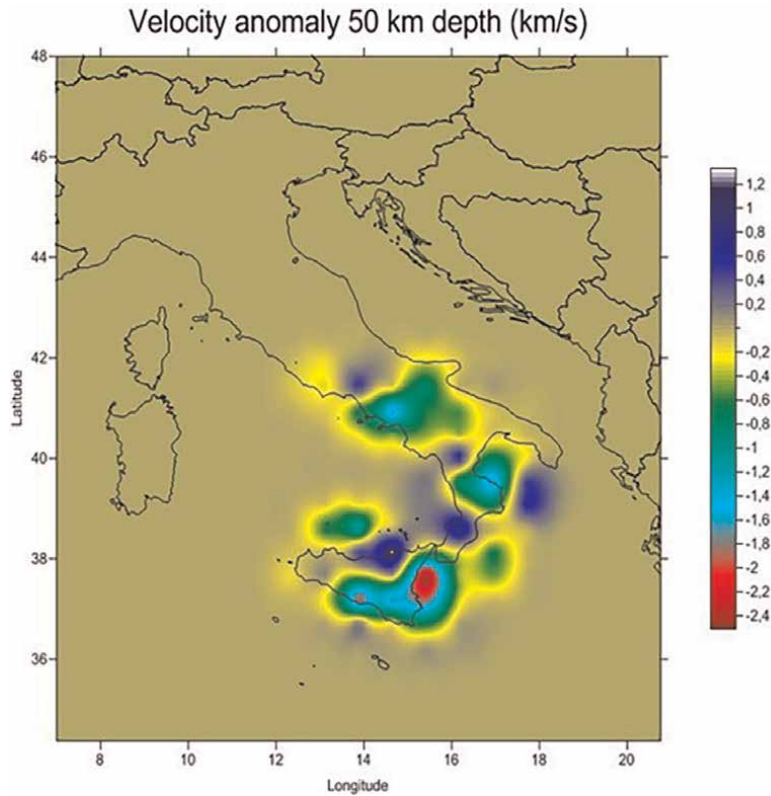


Figure 12.
Horizontal section of southern Tyrrhenian teleseismic tomography at 50 km depth.

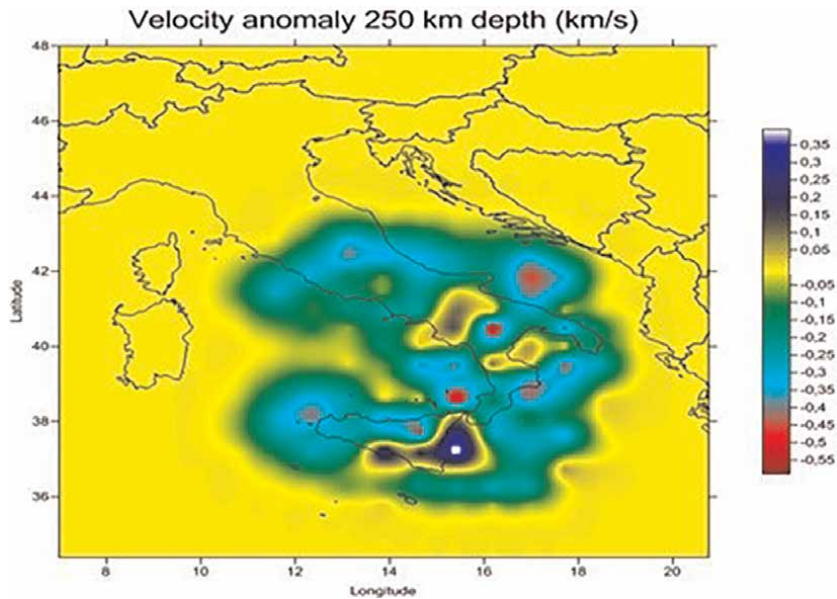


Figure 13.
Horizontal section of southern Tyrrhenian teleseismic tomography at 250 km depth.

more freedom of choice, although the use of seismic stations located in the area of investigation is more advisable.

Therefore, a construction of a correct seismic catalogue is a necessary (but not sufficient) condition to perform an optimal traveltime seismic tomography.


Author details

Giuseppe Pucciarelli

Institute “Magliano” Department of Mathematics and Physics, Larino, Italy

*Address all correspondence to: giuseppepucciarelli86@gmail.com

IntechOpen

© 2023 The Author(s). Licensee IntechOpen. This chapter is distributed under the terms of the Creative Commons Attribution License (<http://creativecommons.org/licenses/by/3.0>), which permits unrestricted use, distribution, and reproduction in any medium, provided the original work is properly cited. 

References

- [1] Tarantola A. Inverse Problem Theory: Methods for Data Fitting and Model Parameter Estimation. Amsterdam: Elsevier; 1987 ISBN: 0898715725
- [2] Nolet G. Seismic wave propagation and seismic tomography. In: Nolet G, editor. Seismic Tomography. Seismology and Exploration Geophysics. Vol. 5. Dordrecht: Springer; 1987. DOI: 10.1007/978-94-009-3899-1_1
- [3] Paige CC, Saunders MA. LSQR: An algorithm for sparse linear equations and sparse least squares. ACM Transactions on Mathematical Software. 1982;**8**(1): 43-71. DOI: 10.1145/355993.356000
- [4] Pucciarelli G. Tomographic Inversion of Data Acquired by Aftershocks in Period 1–15 December 1980 of the Campano-Lucano Earthquake, 23th Novembre 1980. University of Salerno, Dept of Physics; 2009. DOI: 10.14273/unisa-968
- [5] Yakovlev AV, Bushenkova NA, Yu KI, Dobretsov NL. Structure of the upper mantle in the Circum-arctic region from regional seismic tomography. Russian Geology and Geophysics. 2012; **53**:963-971. DOI: 10.1016/j.rgg.2012.08.001
- [6] Pucciarelli G. Seismic Tomography of Southern Tyrrhenian by Means of Teleseismic Data. University of Salerno, Dept of Physics; 2017. DOI: 10.14273/unisa-968
- [7] Pucciarelli G. Seismic tomography of southern Tyrrhenian by means of teleseismic data. In: Proceedings of GNGTS 38th National Congress. Rome: University of Salerno, Dept of Physics; 12–14 November 2019. DOI: 10.13140/RG.2.2.14144.89609
- [8] Chiarabba C, De Gori P, Speranza F. The southern Tyrrhenian subduction zone: Deep geometry, magmatism and Plio-Pleistocene evolution. Earth and Planetary Science Letters. 2008;**268**: 408-423. DOI: 10.1016/j.epsl.2008.01.036
- [9] Calò M, Dorbath C, Luzio D, Rotolo SG, D'Anna G. Seismic velocity structures of southern Italy from tomographic imaging of Ionian slab and petrological inferences. Geophysical Journal International. 2012;**191**(2): 751-764. DOI: 10.1111/j.1365-246X.2012.05647.x
- [10] Montuori C, Cimini GB, Favali P. Teleseismic tomography of the southern Tyrrhenian subduction zone: New results from seafloor and land recordings. Journal of Geophysical Research. 2007;**112**(B03311):2007. DOI: 10.1029/2005JB004114

Looming Earthquake Threat in Ghana

*Albert Kafui Klu, Edmund Nana Asare, Jamel Seidu
and Nicholas Opoku*

Abstract

The earthquake catalogue of Ghana since the first recorded earthquake and recently collected seismic data in earthquake-prone locations of the Greater Accra Region, Ghana's capital, are covered in this chapter. This study lists the locations, periods, magnitudes, and intensities of 44 earthquakes and tremors from the past 408 years using the country's seismic inventory. The HoliSurface approach was also utilised to conduct Multichannel Analysis of Surface Wave (MASW) surveys to collect seismic data from 22 sites in the southern Greater Accra Region's seismically active zones. The earthquake catalogue data and geophysical data will help determine if Ghana is facing a major earthquake. This analysis shows that consistent earth tremors over the previous few years increase the risk of a devastating earthquake. The Gutenberg-Richter relations further emphasise the probabilities of a looming earthquake threat in the Ghana. The geophysical investigations also revealed areas with relatively weak subsurface materials that might contribute to more destruction in the event of an earthquake. The fundamental periods of the sites being in resonance with the buildings is also another disaster in waiting.

Keywords: earthquake catalogue, thrust fault, shear wave velocity, shear modulus, site classification, resonance effect

1. Introduction

Despite the fact that Ghana is located far away from the active global plate boundaries, the country has suffered damaging earthquakes as far back as 1615. Over the years, it was observed that earthquakes in Ghana have been concentrated in the southern part of the country [1–3]. Knowledge of Ghana's earthquake dataset will serve as a medium for understanding the trend in the country's seismic activity and serve as reliable input data for seismic hazard assessment. There is much importance in cataloguing historical earthquake events on a national scale so as to be well-informed on the level of seismicity of the area in question [4]. Furthermore, the catalogued records could be subsequently processed, analysed and utilised for future predictions such as the return periods, magnitude and intensity of potential earthquakes, ground response analyses and tectonic investigations among others. All these pieces of information would go a long way to assist in hazard assessment activities,

disaster preparedness and control, designation of construction sites, urban planning activities and other mitigation and disaster prevention mechanisms.

The use of shear wave velocity (V_s) is commonly employed to estimate ground motion and predict the impact of earthquakes [5, 6]. Thus, conducting an on-site survey to measure V_s is considered a practice in earthquake related engineering. Shear wave velocity directly correlates with the stiffness or rigidity of materials as indicated by the elastic shear modulus (G). Therefore, V_s acting as a substitute for G is extensively utilised in the fields of construction, engineering and seismic response studies. It is crucial to conduct tests and accurately interpret the results to ensure assessment of resistance against seismic activity. One key quantitative measure used for site evaluation is V_{s30} , which represents the shear wave velocity within the 30 meters of soil or rock [7]. This measure is widely used as an indicator for assessing site response in engineering practices. As a result, it finds application in seismic construction regulations set by organisations like the European Committee for Standardisation [8] and the National Earthquake Hazards Reduction Program (NEHRP) [9]. The parameter V_{s30} is frequently incorporated into ground motion prediction equations (GMPEs) to characterise sites and facilitate micro zonation purposes [10, 11].

2. Location and geology

The geological formations in Ghana are predominantly composed of ancient rocks dating back to the Paleoproterozoic, Neoproterozoic, and potentially the early Palaeozoic eras. However, it is worth noting that in the coastal regions, the prevalence of Palaeozoic, Mesozoic, and Cenozoic rocks is more pronounced. The primary Precambrian rock formations encompass the metamorphosed and folded Dahomeyan, Birimian, Tarkwaian System, Togo Series, and the Buem Formation. The Palaeozoic geological strata encompass notable formations such as the Voltaian System and the Sekondi-Accraian Formations [12]. The continental platform of West Africa was formed through the amalgamation of the Paleoproterozoic Complex, Voltaian Basin, Akwapim-Togo Belt, and Pan-African Province during the Neoproterozoic—Cambrian Pan-African tectono-metamorphic event. The geological stability of this platform was rather consistent, with only minor sedimentary basins forming at its limits and tectonic events occurring as a result of the Atlantic Ocean's formation [12, 13].

The tectonic configuration of Southeastern Ghana and its offshore region is distinguished by the presence of three separate zones exhibiting unique tectonic components. The geological features under consideration include the Akwapim fault zone, faults located in the coastal area and near the coast shelf, with the primary characteristic being the coastal boundary fault, as well as the Romanche Fracture Zone [2, 4, 14]. The St. Paul's transform zone system, which extends from Cote D'Ivoire and turns eastward to form the Akwapim thrust fault, intersects with the splay of the Romanche transform fault, giving rise to the Coastal boundary fault. This geological configuration has implications for the seismicity of the Accra region, as the activation of the St. Paul's transform zone system can partially influence seismic activity in this area. The fault system under consideration comprises of splays originating from the Romanche fault and the eastward deviation of the St. Paul's fault system. This fault system has been associated with various seismic events of historical significance in the Accra region [14]. The zone encompasses various areas, including Weija, Gbawe, Bortianor, and Accra central, among others. The geological map of Southern Ghana (**Figure 1**) reveals the presence of the Akwapim fault zone, which extends in a

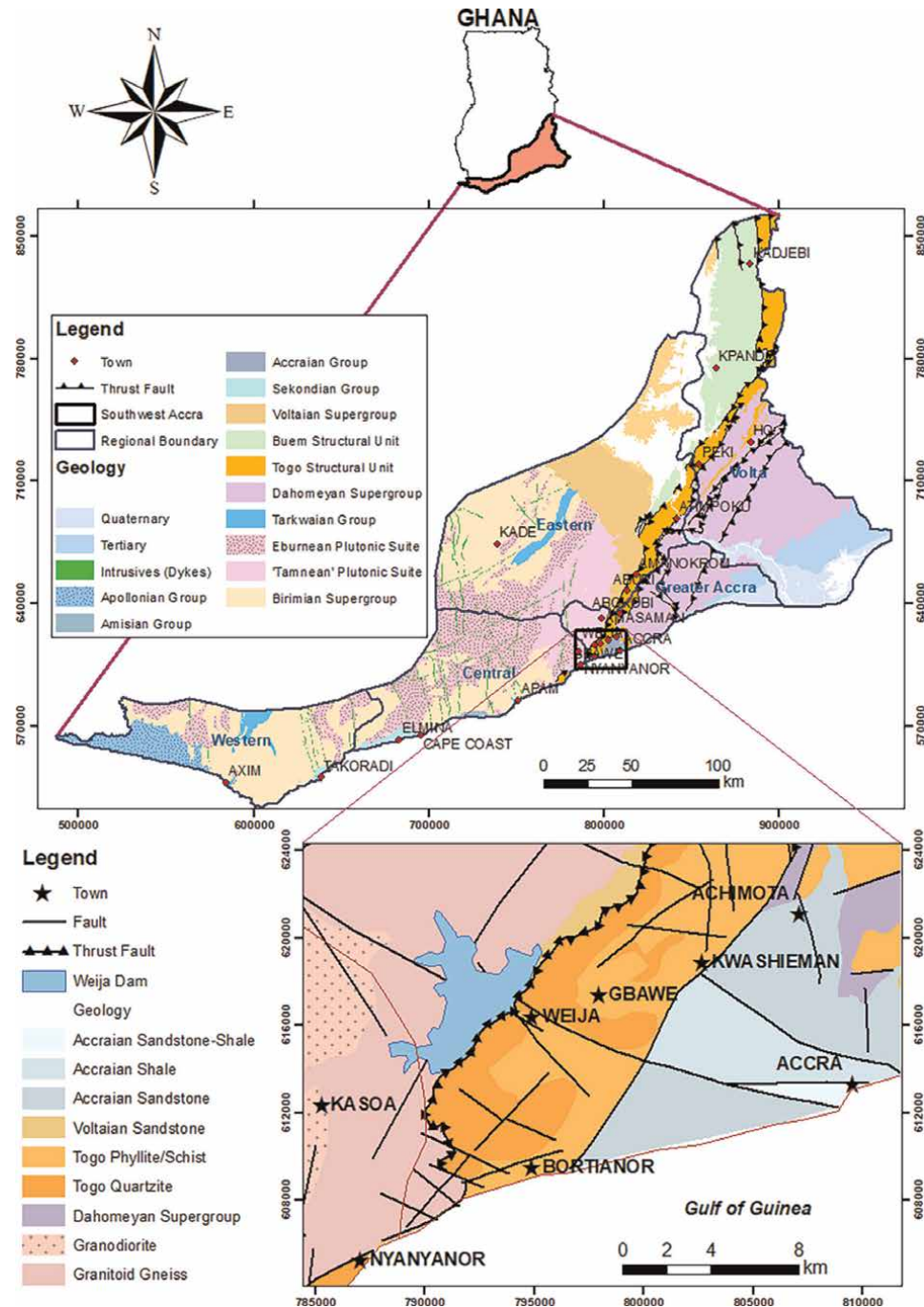


Figure 1.
Geological map of earthquake-prone zones in Ghana [15].

northeast-southwest direction. This fault zone acts as a boundary, separating the Birimian supergroup located to the west from the Pan African Mobile Belt situated to the east. The region in question is known for being the primary location of both

historical and modern seismic events within the country. This can be attributed to the inherent instability present at the contact point of the thrust fault in this area.

3. Earthquake catalogue of Ghana

The first ever documented earthquake in Ghana occurred within the Elmina township in 1615. This earthquake was estimated to have an epicentral intensity of 8. However, the first destructive earthquake in the country was recorded in December, 1636 within a town known as Axim; the quake had a surface wave magnitude of 5.7. In June 1939, the most destructive earthquake in Ghana’s history occurred in Accra. This earthquake had a magnitude of 6.3, causing 130 injuries, 17 deaths and destruction of many buildings and properties [4, 14, 16]. The 1939 earthquake was followed by a series of minor earthquakes and earth tremors.

Over the 408-year earthquake period, the Greater Accra Region recorded the highest number of earthquake events (over 27), with Accra and Weija having the highest occurrences of at least 10 each (**Figure 2**). Other areas within the region that have experienced the phenomenon are Amasaman, Kwashiman, Achimota, Kokrobite, Abokobi, Bortianor and Gbawe among other suburbs. These areas are found within the Southwestern section of the region and are noted to record earthquake/tremor events most frequently, especially from 1964 till date. The Central Region records the second-highest number of earthquakes in the country. This region is situated to the immediate west of the Greater Accra Region, hence manifesting some seismic traits of the seismically active region. Coastal towns in the region such as

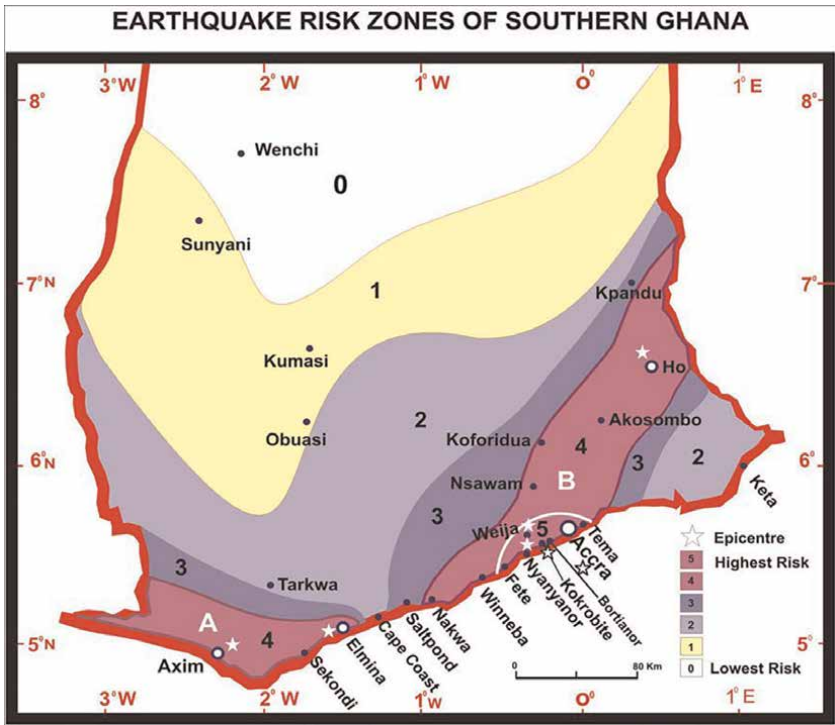


Figure 2. Seismic zonation map of Ghana showing the earthquake risk zones [14].

Elmina, Cape Coast, Apam, Gomoa Fete and Nyanyanor have all been hit by earthquakes and tremors with different magnitudes [4].

The Western Region, where the first recorded destructive earthquake occurred is one of the scarcely stricken regions along the coast. After the 1636 event in Axim, the next was recorded in 2007 in Takoradi, the regional capital. This trend might seek to portray the Western Region as one of the most seismically stable regions in the country with regards to the return period of earthquakes. It should however be noted that anytime there is an earthquake activity in the region, the magnitudes are relatively high (5.7 and 5.2). The Volta and Eastern Regions have also recorded earthquake events in the past. One of the highest earthquake magnitudes/intensities (6.5/9 I_0) in the country was recorded in Kpando in 1862. Other towns within the Volta Region that have recorded such an event are Ho, the regional capital, Kadjebi and Peki. The towns within the Eastern Region that have recorded earth tremor events are Amanokrom, Kade, Atimpoku and Aburi among others [4, 15].

Over the past 5 years (2018 to 2023), earth tremors have been occurring within the Greater Accra Region at an alarming rate with Richter magnitudes ranging from 2.6 to 4. This continuous occurrence has raised an eyebrow; giving indications of a pending potential massive earthquake event. The continuous tremors result in gradual loss of friction between the fault planes due to the wearing off of rock fragments during the movement of the blocks. As this phenomenon continues, the fault planes would no longer be able to resist the sliding of the blocks past each other when a seismic wave triggers. This phenomenon would result in a greater displacement of the blocks, producing a much more intensive seismic activity.

The earthquake catalogue presented in **Table 1** can be analysed to provide further earthquake parameters such as the probability of recurrence, annual frequency of

Year	Month	Latitude	Longitude	Magnitude (ML)	I_0	Location	Reference
1615	—	5.1	−1.3	—	8	Elmina	AMB
1636	December	5.1	−2.2	5.7	9	Axim	AMB
1836	December	5.1	−1.28	—	6.5	Cape Coast	AMB
1862	July	7.0	−0.4	6.5	9	Kpando	AMB
1870	November	5.3	−0.7	4.5	5	Apam	AMB
1872	April	5.5	−0.4	4.9	7	Accra	AMB
1889	April	5.9	−0.2	4.0	4	Amanokrom	AMB
1906	November	6.5	−0.3	5.0	7.5	Ho	ALY
1907	February	6.1	−0.9	4.1	4	Kade	AMB
1910	December	5.6	−0.2	—	5	Accra	AMB
1911	June	5.5	−0.2	—	4	Accra	AMB
1939	June	5.4	−0.25	6.3	8	Accra	ALY
1948	—	6.2	−0.4	—	4	Atimpoku	AMB
1950	October	7.5	−0.5	—	4	Kadjebi	AMB
1964	March	5.9	−0.39	4.4	6	Amasaman	AMB
1966	—	5.58	−0.35	—	4	Weija	ALY
1969	February	5.5	−0.2	4.8	5.5	Accra	ALY

Year	Month	Latitude	Longitude	Magnitude (ML)	Io	Location	Reference
1977	November	5.58	−0.38	2.3	—	Weija	GSD
1978	February	6.58	0.13	2.9	—	Peki	GSD
1978	September	5.53	−0.35	3.9	—	Weija	GSD
1979	January	5.5	−0.33	2.3	—	Kasoa	GSD
1987	November	5.58	−0.32	2.6	—	Weija	GSD
1988	March	5.6	−0.11	3.5	4	Accra	ISC
1989	March	5.59	−0.33	2.0	—	Kwashiman	GSD
1990	April	5.59	−0.34	3.0	3	Weija	GSD
1991	August	5.62	−0.33	3.9	—	Weija	GSD
1992	March	5.62	−0.33	2.1	—	Achimota	GSD
1993	June	5.59	0.32	2.5	—	Weija	GSD
1994	January	5.38	0.34	2.6	—	Nyanyanor	GSD
1995	October	5.5	−0.35	4.0	—	Kokrobite	GSD
1996	August	5.44	−0.48	2.5	—	Gomoa Fete	GSD
1997	March	5.6	−0.33	4.8	5.5	Weija	GSD
1998	December	5.52	−0.22	2.0	—	Nyanyanor	AMP
1999	May	5.79	−0.25	2.5	—	Abokobi	AMP
2000	November	5.83	−0.24	2.7	—	Aburi	AMP
2002	June	5.5	−0.3	3.0	—	Bortianor	AMP
2003	May	5.57	−0.32	2.9	—	Weija	AMP
2006	January	5.53	−0.21	3.7	—	Accra	GSD
2007	September	4.92	1.73	5.2	—	Takoradi	GSD
2018	December	5.56	−0.33	2.6	—	Weija	GSD
2019	January	5.6	−0.23	2.6	—	Accra	GSD
2020	June	5.59	−0.25	4.0	—	Accra	GSD
2022	June	5.57	−0.31	3.5	—	Gbawe	GSD
2023	December	5.55	−0.27	2.8	—	Accra	GSD

(Sources: ALY modified after Ambraseys and Adams [3]; AMB [3]; AMP [4]; GSD - Geological Survey Department [15]; ISC, International Seismological Centre [1]; and [17]. Abbreviations: N – the number of earthquakes with magnitudes greater than M for time period [18]; I_o – Epicentral Intensity [19]).

Table 1.
Ghana's earthquake catalogue from 1615 to 2023.

occurrence among others using the Gutenberg-Richter relation [18, 20]. The Gutenberg-Richter law states that there is a linear relationship between the logarithm of the frequency and the magnitude of the earthquake. The relationship is often plotted to the data that is accessible for any geographical area [18]. The Gutenberg-Richter relation can be represented as:

$$\log_{10}N = a - bM \text{ or } N = 10^{(a-bM)} \quad (1)$$

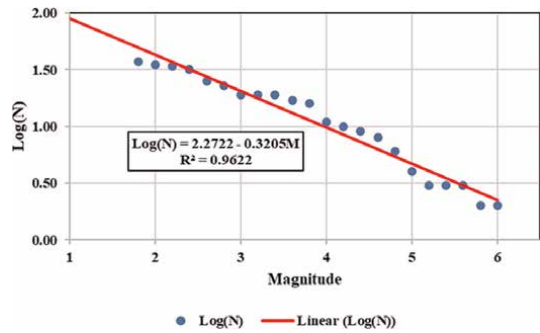


Figure 3.
Plot of $\log(N)$ versus magnitude.

where, N is a number of earthquakes having magnitude larger than M during a time period “ t ”, $\log N$ is a logarithm of the number of earthquakes with magnitude M , “ a ” is a constant that measures the total number of earthquakes at the given source or measure of seismic activity, and “ b ” is a slope of regression line or measure of the small versus large events. From **Figure 3**, parameters “ a ” and “ b ” in Eq. (1) can be found to be 2.2722 and -0.3205 respectively.

These parameters provide the basis for calculating some important values that help in estimating the likelihood of future earthquake occurrences. Some of these estimates are the annual frequency of exceeding the M event magnitude $N_1(M)$, the probability of occurrence of at least one earthquake of magnitude greater than M in the next t years $P(t)$ and the number of years in average that an earthquake occurs with magnitude greater than M (T_R) among others. These estimations as are given by the relations below after [20]:

$$N_1(M) = 10^{(a-bM-\log t)} \tag{2}$$

$$P(t) = 1 - e^{-N_1(M) * t} \tag{3}$$

$$T_R = \frac{1}{N_1(M)} \tag{4}$$

The first known magnitude of earthquakes recorded in Ghana was in 1636, thus 388 years duration of recorded earthquake activities in the country. Hence, the time period “ t ” considered was 388 years in calculating $N_1(M)$ (**Table 2**).

Magnitude	$N_1(M)$	P(t) (%)				T_R (Years)
		t = 2	t = 10	t = 50	t = 100	
4.0	0.025	4.91	22.27	71.63	91.95	39.69
4.5	0.017	3.42	15.99	58.15	82.49	57.40
5.0	0.012	2.38	11.35	45.25	70.02	83.01
5.5	0.008	1.65	7.99	34.06	56.52	120.06
6.0	0.006	1.15	5.60	25.02	43.78	173.63
6.5	0.004	0.79	3.90	18.05	32.85	251.12
7.0	0.003	0.55	2.72	12.86	24.07	363.19

Table 2.
Earthquake estimations for Ghana based on catalogued data.

The following deductions can be made from **Table 2**: considering a magnitude of 5 for instance, an annual frequency of earthquakes greater than 5 is expected to be 0.012; in 2 years, the probability of an earthquake with magnitude 5 occurring is 2.38%, whereas in 100 years, a similar magnitude earthquake has a 70.02% chance of occurring; the estimated return period of an earthquake with magnitude 5 to occur is 83.01 years.

4. Geophysical investigation

4.1 Shear wave velocity data collection and processing

The holisurface technique employs a holistic analysis of surface waves (Rayleigh and Love waves) expressing the fact that the method analyses the propagation of surface waves in a complete and holistic way. The uniqueness of this method over the traditional refractive analysis and Multichannel Analysis of Surface Waves (MASW) is the utilisation of the single three-component (3C) geophone in the acquisition of surface waves [21]. This acquires radial and vertical components of Rayleigh waves and the transversal component of Love waves. The technique follows the active geophysical principle, where an active source (sledgehammer) is used to trigger surface waves by employing a number of stackings. In this work, a total of 10 stacks were applied with a 20-tonne sledgehammer on a nylon strike plate for the survey over a total spread separation (offset) of 20 m.

Shear wave velocity (V_s) profiles are obtained after a series of processing stages. The HoliSurface™ software was used to conduct a joint inversion of two components (2C inversion). These components may be the vertical or radial components of the Rayleigh wave (ZVF or RVF) together with the transverse component of the Love wave. A group velocity spectrum is then generated from the datasets which displays the fundamental mode and other higher order modes. With the help of the fundamental and the higher modes, shear wave velocity profiles are then generated using the concept of frequency-depth relationship [22, 23]. The V_{s30} values are then calculated using the V_s within the first 30 m depth of the traverse. Essential geotechnical parameters that aid in estimating the ability of the ground to withstand seismic impacts are then computed [24].

In computing for the V_{s30} , Eq. (1) is used:

$$V_{s,30} = \frac{30 \text{ m}}{\sum_{i=1}^n \frac{d_i}{V_{s,i}}} \quad (5)$$

Where:

n = number of layers of the V_s profile up to 30 m.

d_i = thickness.

$V_{s,i}$ = shear wave velocity of each layer respectively.

Eqs. (6)–(9) were employed to compute the bulk density (ρ), shear modulus (G), Young's modulus (E) and Fundamental period (T) as stated by [25, 26].

$$\rho = \alpha V_s^\beta \quad (6)$$

$$G = \rho * V_s^2 \quad (7)$$

$$E = 2G(1 + \mu) \tag{8}$$

$$T = 4H/V_s \tag{9}$$

Where: α is 0.52; β is 0.2 [27]; H is 30 m.

4.2 Results and discussions

The site classification for this study was conducted using the Eurocode 8 Standard for seismic site classification. From the 22 sites that were surveyed, 19 of them fall within the C site class indicating subsurface deposits of medium-densified coarse-grained soils or medium-consistent fine-grained soils with substrate depths greater than 30 m and mechanical qualities that improve with depth. The shear wave velocity of this class ranges from 180 m/s and 360 m/s (**Table 3**). One (1) of the sites (Dansoman South) recorded the highest V_{s30} (371 m/s), making it to be classified as B. This signifies that the site is underlain by soft rocks and deposits of very dense coarse-grained soils or very consistent fine-grained soils, characterised by an increase in geo-mechanical properties with depth. This class of sites has shear wave velocities between 360 and 800 m/s. The Airport City and Tetegu East sites recorded relatively low V_{s30} values of 177 and 74 m/s respectively. The former was classified as D, indicating

SN.	Area	V_{s30} (m/s)	Bulk Density, ρ (g/cm ³)	Shear Strength, S_u (MPa)	Young's Modulus, E (MPa)	Fund. Period, T (s)	Eurocode 8 Class
1	Accra Central	332	1.66	183.02	461.61	0.36	C
2	Airport City	177	1.46	45.87	119.22	0.68	D
3	Alajo	273	1.60	119.00	298.65	0.44	C
4	Cantonments	326	1.65	175.83	446.76	0.37	C
5	Dzorwulu	294	1.62	140.08	362.70	0.41	C
6	Kaneshie	302	1.63	148.60	365.97	0.40	C
7	Korle-Bu	285	1.61	130.82	319.81	0.42	C
8	North Kaneshie	316	1.64	164.18	396.29	0.38	C
9	North Ridge	337	1.67	189.14	505.53	0.36	C
10	Roman Ridge	314	1.64	161.90	401.42	0.38	C
11	Weija North	250	1.57	98.06	229.29	0.48	C
12	Osu	307	1.63	154.07	408.42	0.39	C
13	McCarthy Hill	344	1.67	197.89	491.04	0.35	C
14	Kokrobite	337	1.67	189.14	466.40	0.36	C
15	New Bortianor	304	1.63	150.77	386.61	0.39	C
16	Bortianor	295	1.62	141.13	342.30	0.41	C
17	Dansoman South	371	1.70	233.68	585.01	0.32	B

SN.	Area	Vs ₃₀ (m/s)	Bulk Density, ρ (g/cm ³)	Shear Strength, S _u (MPa)	Young's Modulus, E (MPa)	Fund. Period, T (s)	Eurocode 8 Class
18	Tetegu East	74	1.23	6.73	16.92	1.62	E
19	Tetegu West	227	1.54	79.30	210.98	0.53	C
20	Dansoman North	307	1.63	154.07	379.93	0.39	C
21	Gbawe	321	1.65	169.95	423.53	0.37	C
22	Weija South	296	1.62	142.18	360.19	0.41	C

Table 3.
Geotechnical parameters and site classification from shear wave velocity.

subsurface deposits of poorly thickened coarse-grained soils or poorly consistent fine-grained soils, whereas the latter classified as E with unconsolidated or weak cohesion-less materials; thus, could take on the description of class D materials. These results were used to generate an interpolation map using the Inverse Distance Weighting (IDW) technique (**Figure 4**).

As presented in **Table 3**, the geotechnical parameters derived from the Vs indicate a direct correlation in the subsurface properties. The Tetegu East site which had the lowest shear wave velocity was observed to have recorded the least bulk density value of 1.23 g/cm³, shear modulus of 6.73 MPa and Young's modulus of 16.92 MPa. On the other hand, Dansoman South recorded the highest geotechnical parameters such as a bulk density of 1.70 g/cm³, shear modulus of 233.68 MPa and Young's modulus of 585.01 MPa; proving to be the most competent site.

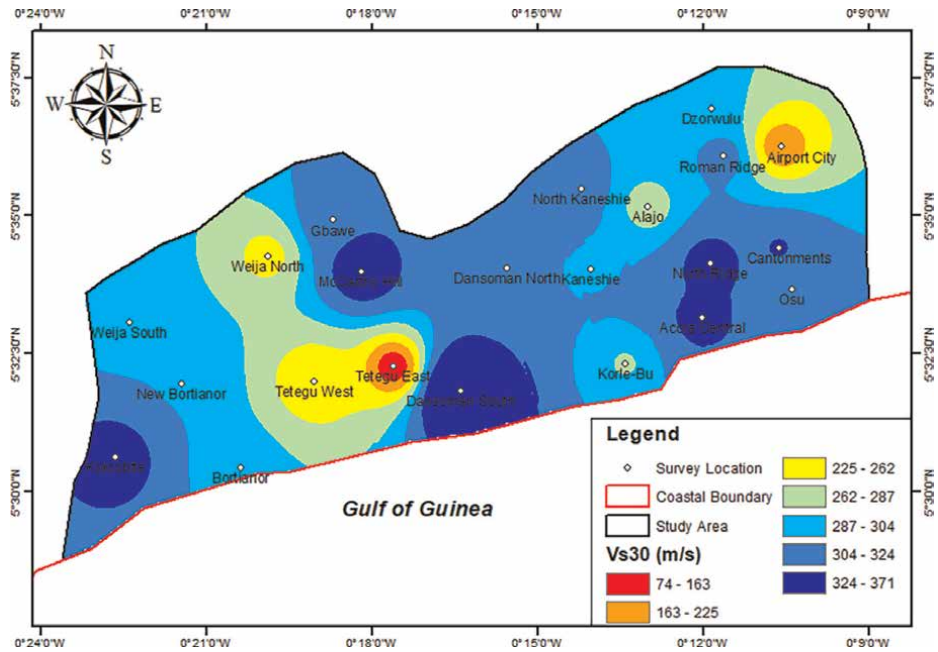


Figure 4.
Distribution of shear wave velocities in survey area.

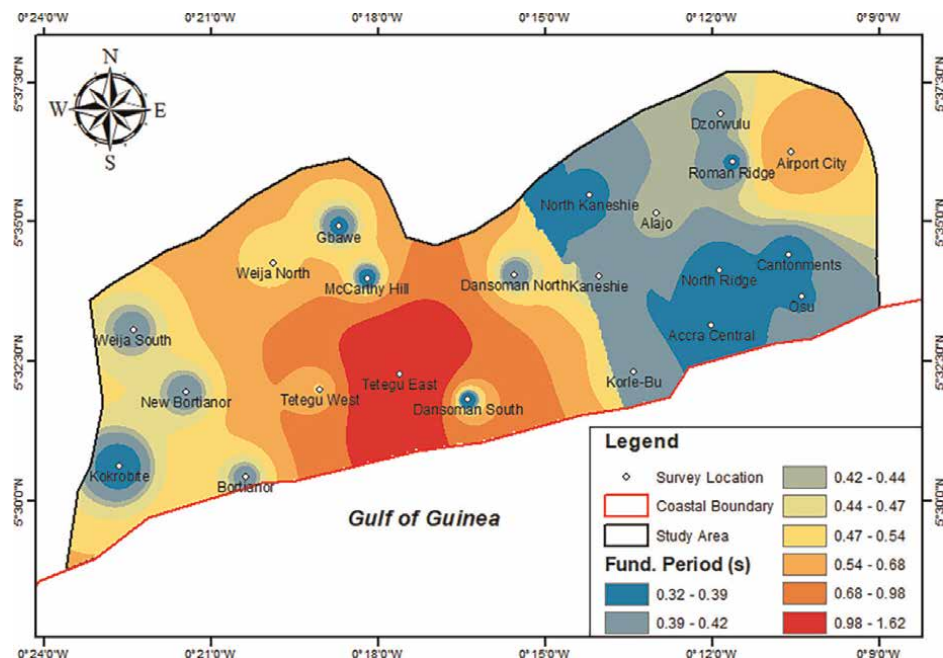


Figure 5.
 Distribution of fundamental periods of soil overburden in survey area.

Regarding the fundamental periods of the overburden materials in the respective survey locations, it was observed that the values ranged basically from 0.35 to 0.53 s, which corresponds to the C class of Eurocode 8. There were however outliers like 1.62 s (**Figure 5**) which corresponds to the E class of the Eurocode 8, 0.68 s belonging to class D and 0.32 s tallying with the B class. Based on the classification concentrically braced steel frame (CBF) storey buildings and their corresponding fundamental periods [28], storey buildings with 15 floors would have a fundamental period of 1.8 to 2.2 s, whereas that of 12 storeys would be 1.3 to 1.7 s, 6 storeys being 0.5 to 0.7 s and 3 storey to single storeys ranging from 0.2 to 0.33 s. it can thus be seen that the higher the storey building, the higher the fundamental period (T) and vice versa. On the other hand, the greater the thickness of an unconsolidated or overburden material, the higher the fundamental period. Also, the shallower the depth to bedrock or the more consolidated and thinner the overburden is, the lower the fundamental period.

5. Conclusions

With respect to the earthquake catalogue of the country, it can be said that there is the likelihood of a large magnitude earthquake occurrence owing to the continuous earth tremors being recorded in recent times. The intensity of an earthquake depends on a number of factors such as the ground conditions, which includes the faulting systems, the site's seismic response properties, the duration and magnitude of the earthquake, the frequency of the resulting seismic waves, the natural ground frequency and the peak frequency of the structures at the location of the earthquake. Based on the estimations made from the catalogue data using the Gutenberg-Richter

relations, it can be said that there is a looming earthquake threat in Ghana. It may take some decades to occur, but the focus should be on avoiding disaster whenever the phenomenon strikes.

From the geophysical and geotechnical parameters obtained, it could be said that majority of the sites within the earthquake-prone areas have relatively competent subsurface. Only Tetegu East and the Airport City showed relatively incompetent materials. With this, the nature of buildings should be carefully looked at to ensure there is no resonance effect in case an earthquake event occurs. Areas with weak overburden materials have low natural frequencies or high fundamental periods. If high rise buildings which also generally have low natural frequencies or high fundamental periods are situated in such sites, there will be a resonance effect in the event of a high magnitude earthquake. This may lead to the collapse of the buildings and other engineering structures in those areas, causing fatal disaster. Unfortunately, this is the situation in Airport city where a fundamental period of 0.68 s was obtained. As stated earlier, storey buildings with about 6 floors (which can be found in that area) would have a fundamental period of 0.5 to 0.7 s. During a significant seismic event, there would be resonance effect, since the building and the subsurface will be oscillating at the same frequency or period. Such an imminent disaster should be avoided by altering the building designs to avoid resonance.

Acknowledgements

Appreciation goes to the Ghana Geological Survey Authority (GGSA), Architectural and Engineering Services Limited (AESL) and HGL Consult Limited, all in Accra, Ghana for their support during the data collection and processing stages.

The authors also thank the University of Mines and Technology for funding the PhD programme from which this survey was conducted.

Conflict of interest

The authors declare no conflict of interest.

Author details


Albert Kafui Klu^{1*}, Edmund Nana Asare¹, Jamel Seidu¹ and Nicholas Opoku²

1 Geological Engineering Department, University of Mines and Technology, Tarkwa, Ghana

2 Seismology Division, Ghana Geological Survey Authority, Accra, Ghana

*Address all correspondence to: akklu@umat.edu.gh

IntechOpen

© 2023 The Author(s). Licensee IntechOpen. This chapter is distributed under the terms of the Creative Commons Attribution License (<http://creativecommons.org/licenses/by/3.0>), which permits unrestricted use, distribution, and reproduction in any medium, provided the original work is properly cited. 

References

- [1] Junner NR. The Accra earthquake of 22nd June, 1939. Gold Coast Geological Survey. 1941;**13**:3-41
- [2] Quaah AO. Microseismicity, Past Seismic Activity and Seismic Risk in Southern Ghana [Thesis]. London: University of London; 1980. p. 213
- [3] Ambraseys NN, Adams RD. Seismicity of West Africa. *Annales de Geophysique*. 1986;**4B**(6):679-702
- [4] Amponsah P, Leydecker G, Muff R. Earthquake catalogue of Ghana for the time period 1615-2003 with special reference to the tectono-structural evolution of south-East Ghana. *Journal of the African Earth Sciences*. 2012;**75**:1-13. DOI: 10.1016/j.jafrearsci.2012.07.002
- [5] Boore DM. Determining subsurface shear-wave velocities: A review. In: Third International Symposium on the Effects of Surface Geology on Seismic Motion. 2006. pp. 1-21. Available from: http://www.daveboore.com_www.daveboore.com/pubs_online/boore_103_revised_12july06.pdf
- [6] Moss RES. Quantifying measurement uncertainty of thirty-meter shear-wave velocity. *Bulletin of the Seismological Society of America*. 2008;**98**:1399-1411
- [7] Kamai R, Darvasi Y, Peleg Y. Measurement and interpretation uncertainty in site response of nine seismic network stations in Israel. *Seismological Research Letters*. 2018;**89**: 1796-1806
- [8] European Committee for Standardization (CEN). Eurocode 8: Design of Structures for Earthquake Resistance - Part 1: General Rules, Seismic Actions and Rules for Buildings. Brussels, Belgium: The European Union; 2004
- [9] Building Seismic Safety Council (BSSC). NEHRP (National Earthquake Hazards Reduction Program) recommended provisions for seismic regulations for new buildings and other structures. FEMA. 1997;**302**:303
- [10] Abrahamson N, Silva W. Summary of the Abrahamson & Silva NGA ground-motion relations. *Earthquake Spectra*. 2008;**24**:67-97
- [11] Kamai R, Abrahamson NA, Silva WJ. VS30 in the NGA GMPEs: Regional differences and suggested practice. *Earthquake Spectra*. 2016;**32**:2083-2108
- [12] Kesse GO. The Mineral and Rock Resources of Ghana. Rotterdam, Netherlands: A.A Balkema; 1985
- [13] Junner NR. Geology of the Gold Coast and western Togoland (with revised geological map). Gold Coast Geological Survey Bulletin. 1940;**11**:1-40
- [14] Kutu JM. Seismic and tectonic correspondence of major earthquake regions in Southern Ghana with mid-Atlantic transform-fracture zones. *International Journal of Geosciences*. 2013;**4**:1326-1332. DOI: 10.4236/ijg.2013.410128
- [15] Hirdes W, Toloczyki M, Davis DW, Agyei Duodu J, Loh GK, Boamah K, et al. Geological Map of Ghana 1:1000000. BGR: GSD; 2009
- [16] Amponsah PE. Seismic activity in Ghana: Past, present and future. *Annales de Geophysique*. 2004;**47**:539-543. DOI: 10.4401/ag-3319
- [17] Amponsah PE. Seismic activity in relation to fault systems in Southern Ghana. *Journal of the African Earth Sciences*. 2002;**35**:227-234

- [18] Gutenberg B, Richter CF. Seismicity of the Earth and Associated Phenomena. Princeton, USA: Princeton University Press; 1949
- [19] Bao X, Jin Z, Cui H, Chen X, Xie X. Soil liquefaction mitigation in geotechnical engineering: An overview of recently developed methods. *Soil Dynamics and Earthquake Engineering*. 2019;**120**:273-291. DOI: 10.1016/j.soildyn.2019.01.020
- [20] Noora S. Estimating the probability of earthquake occurrence and return period using generalized linear models. *Journal of Geoscience and Environment Protection*. 2019;**07**:11-24. DOI: 10.4236/gep.2019.79002
- [21] Dal Moro G. Surface Wave Analysis for Near Surface Applications. Amsterdam, Netherlands: Elsevier; 2015. DOI: 10.1016/C2013-0-18480-2
- [22] Dal Moro G, Moura RMM, Moustafa SSR. Multi-component joint analysis of surface waves. *Journal of Applied Geophysics*. 2015;**119**:128-138. DOI: 10.1016/j.jappgeo.2015.05.014
- [23] Dal Moro G, Keller L. Unambiguous determination of the vs profile via joint analysis of multicomponent active and passive seismic data. In: *Proceedings of 19th European Meeting of Environmental and Engineering Geophysics*. Bochum, Germany: European Association of Geoscientists & Engineers; 2013. pp. 9-11
- [24] Ewusi A, Miezah-Adams M, Klu AK, Ansah E, Seidu J. Application of Holisurface technique in MASW and HVSr surveys for site characterisation at Ewoyaa, Ghana. *Ghana Journal of Technology*. 2023;**7**:30-43
- [25] Park C. MASW for geotechnical site investigation. *The Leading Edge*. 2013; **32**:656-662. DOI: 10.1190/tle32060656.1
- [26] Takewaki I. Earthquake resilience evaluation of building structures with critical excitation methods. In: *Critical Excitation Methods in Earthquake Engineering*. 2nd ed. Butterworth-Heinemann, Elsevier; 2013. pp. 363-380. DOI: 10.1016/b978-0-08-099436-9.00015-8
- [27] Anbazhagan P, Uday A, Moustafa SSR, Al-Arifi NSN. Correlation of densities with shear wave velocities and SPT N values. *Journal of Geophysics and Engineering*. 2016;**13**:320-341. DOI: 10.1088/1742-2132/13/3/320
- [28] Christidis AA, Dimitroudi EG, Hatzigeorgiou GD, Beskos DE. Maximum seismic displacements evaluation of steel frames from their post-earthquake residual deformation. *Bulletin of Earthquake Engineering*. 2013;**11**:2233-2248. DOI: 10.1007/s10518-013-9490-z

Section 2

Site Effects

Physical Modeling of Liquefaction in Various Granular Materials

Vincenzo Fioravante and Daniela Giretti

Abstract

This paper compiles numerous experiences gained from physical models, to highlight the phenomena of triggering, propagation, and mitigation of liquefaction in granular soils. Results of tests at different scales, from the element volume (cyclic triaxial tests) to small-scale models in centrifuge, performed using several granular soils, will be presented to provide behavioral tools for predicting the phenomenon. Furthermore, the efficacy of vertical and horizontal drains as liquefaction mitigation techniques will be discussed.

Keywords: liquefaction, physical modeling, centrifuge, liquefaction assessment, mitigation

1. Introduction

Cyclic liquefaction is a sudden phenomenon of loss of shear strength and stiffness, which may occur when a granular and non-plastic soil, whose voids are saturated by an incompressible fluid, is vibrated at a frequency too high for the soil to comply with its tendency to contract discharging pore water.

The tendency to contract produced by cyclic and dynamic shear strain, as those induced by an earthquake, turns into accumulation of excess pore Δu . As Δu rises, hydraulic gradients establish within a deposit, triggering fluid flow from higher toward lower hydraulic load. If the tendency to dissipate excess pore pressure is overcome by the tendency to accumulate pore pressure, the contact pressure between grains may cyclically reset, zeroing shear strength and stiffness, and the soil starts to behave like a viscous fluid.

The effects on existing buildings or structures may range from settlement and tilting up to catastrophic failures.

This chapter deals with earthquake-induced liquefaction and its modeling, from the element volume scale to the small-scale physical models.

The first part of the chapter describes some experimental observations gained testing a natural soil that experienced liquefaction during the 2012 Emilia seismic sequence, in Italy. The most relevant liquefaction manifestations were observed during the May 20 shake in the Ferrara Province. The moment magnitude was $M_w = 6.1$, with an estimated peak ground acceleration $PGA \approx 0.26 g$. The affected sites, located about 15 km SE of the epicenter (estimated $PGA \approx 0.16 g$), exhibited various

phenomena, including craters, sand boils, surface cracks, and lateral spreading in free field areas. Additionally, there were reports of moderate building settlement and tilting at developed sites. The sandy stratum which underwent liquefaction resulted from the fluvial processes of the Apennine Reno river during the period spanning from 1450 to 1770. The sand within this layer is normally consolidated and loose. This sand was tested monotonically and cyclically to find a relationship between its state, and the cyclic resistance. In addition, it was noticed that sandy deposits of similar origin and age located in regions closer to the epicenter of the earthquake on May 20, 2012, did not experience liquefaction, suggesting the hypothesis of potential partial saturation of these soils. This supposition gains support from the recurring reports of gas emissions from the soil and the presence of gas within the groundwater, particularly within a few kilometers of the earthquake's epicenter. Therefore, cyclic triaxial tests were conducted on both saturated and unsaturated samples to determine the increase in liquefaction resistance resulting from partial saturation. P-wave velocity was assumed as a measurable variable to estimate the cyclic resistance ratio, CRR of partially saturated sand.

The area where extensive liquefaction occurred in 2012 was assumed as one of the case studies of the LIQUEFACT project (<http://www.liquefact.eu/>) and the ground conditions at those sites were taken as a reference for a large series of centrifuge tests, which are partly described in the second part of the chapter. The primary objective of the centrifuge tests was to investigate the seismic response of saturated sandy deposits when subjected to progressively increasing dynamic actions, ultimately leading to liquefaction. Concurrently, the campaign aimed to assess the efficacy of various mitigation strategies for liquefaction.

At the end of the chapter, a simplified method of liquefaction assessment is proposed, based on the analysis of more than 60 centrifuge cone penetration tests CPTs on sandy soils and on the results of cyclic laboratory tests.

2. Liquefaction, a case study in Italy

The onset of liquefaction depends on the cyclic shear loading generated by an earthquake and the cyclic resistance of the soil. The latter is influenced by various factors, including:

- Grain size and mineralogy (plasticity)
- State of the soil (void ratio and confinement stress)
- Degree of saturation
- Aging, bonding, structure
- Ground conditions (level ground, sloping ground, superficial loads)

Manifestations of liquefaction may range from sand boils, craters, and fissures in free field conditions to the floating of buried structures, building settlement and rotations, and lateral spreading of sloping areas. **Figure 1** shows, as an example, liquefaction evidences recorded at the site of San Carlo, in Italy, where liquefaction occurred during the 2012 Emilia seismic sequence [1]. Liquefied sand flooded out and submerged large areas of the village, surface ruptures, extensional fissures, sand boils,

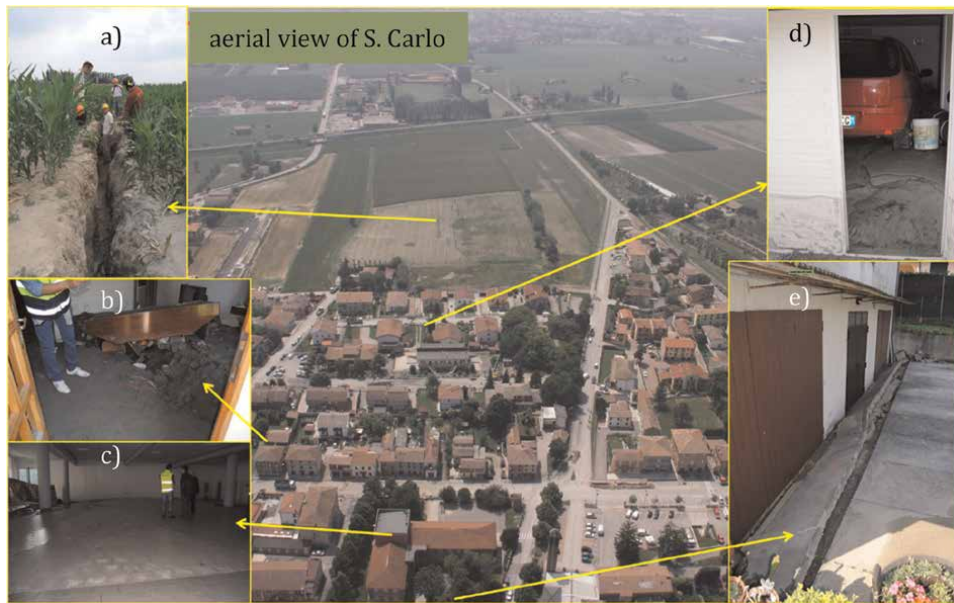


Figure 1. Evidence of liquefaction registered in Italy in 2012 at the site of S. Carlo: (a) external inhabited areas, extensional crack due to lateral spreading; (b) ground floor flooded by erupted sand; (c) basement floor lifted by sand under pressure; (d) car lifted up by the ejected sand; (e) building settlement.

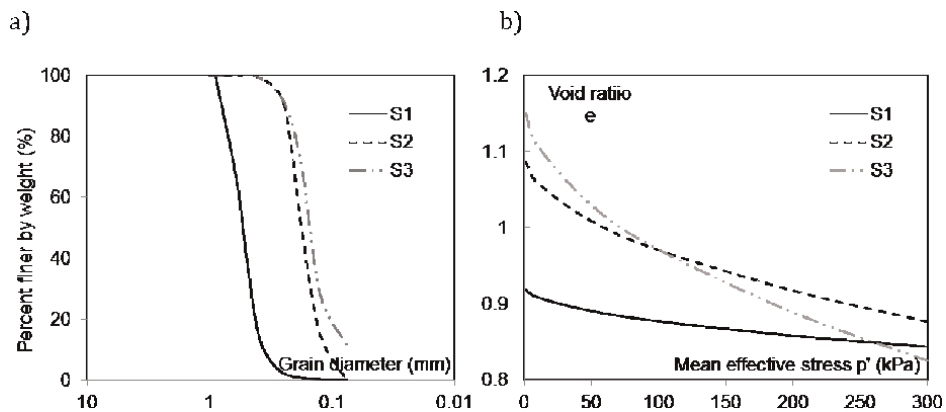


Figure 2. Testing sand's (a) grain size distribution and (b) critical state lines.

vents, sinkholes, and craters were observed. Technological networks and sub-services were damaged, while roads exhibited cracks. Tilting of foundations caused damage to the existing buildings.

The mechanism that takes place during liquefaction can be explained through cyclic undrained simple shear or triaxial tests carried out on saturated samples. **Figure 2** shows the grain size distribution of the sand liquefied at San Carlo (S3 in **Figure 2a**) and its critical state line CLS in the e - p' plane (**Figure 2b**). Data of two other sands, discussed in the following sections, are also shown in **Figure 2**.

Figure 3 shows undrained cyclic Tx tests on a sample of S3. The test was performed on a reconstituted sample isotropically normally consolidated at a mean effective stress

$p'_c = 100$ kPa. At the end of consolidation, the specimen was characterized by a void ratio $e = 0.79$ (state parameter $\psi = -0.073$ [2]) and was subjected to a stress deviator $\Delta q = \Delta \sigma_a = \pm 36$ kPa (i.e. to a cyclic stress ratio $CSR^{TX} = \Delta \sigma_a / 2p'_c = 0.18$).

Figure 3a and **b** display the variations in excess pore pressure (Δu) and axial strain (ϵ_a) plotted against the number of cycles (N). In **Figure 3c** and **d**, the deviatoric stress (q) is depicted in relation to both ϵ_a and the mean effective stress (p'). In **Figure 3d**, the critical state lines in compression and in extension (CSL) are also plotted, as deduced from monotonic tests.

Throughout the test, the specimen exhibits a characteristic behavior known as “cyclic mobility.” As loading progresses, positive Δu accumulates, while the mean effective stress p' approaches zero. From the first cycle onward, the specimen undergoes an alternating response with incremental dilation (p' increasing) and incremental contraction (p' decreasing). The passage from incremental contraction to incremental dilation is known as phase transformation and the line intersecting transition points, known as the phase transformation line (PTL), is plotted in the q - p' plane, as shown in **Figure 3d**.

The onset of liquefaction occurs when a significant accumulation of cyclic axial strain (ϵ_a) starts after approximately 7–8 cycles. At this stage, the pore pressure ratio $R_u = \Delta u / p'_c$ approaches 1, and the effective stresses approach zero. Then the stress path reverses direction, oscillating between the critical state line in extension and compression, and the specimen exerts strain hardening, mobilizing sufficient shear strength to withstand the applied deviatoric load. However, as depicted in **Figure 3b**, ϵ_a keeps on increasing as the cyclic loading goes on.

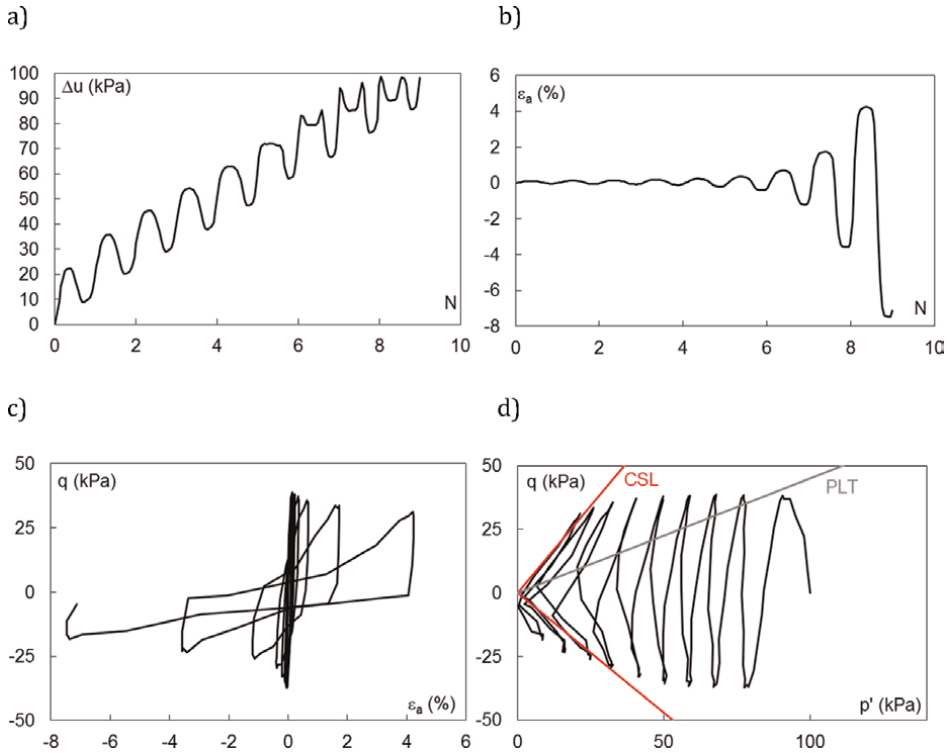


Figure 3.
 Example of a cyclic triaxial test on S3 (a) the excess pore pressure Δu as a function of the number of cycles N , (b) axial strain ϵ_a vs. N , (c) deviatoric stress q vs. ϵ_a , (d) q vs. p' .

A series of samples of S3 were reconstituted at three values of void ratio: high ($e_{avg} = 0.78$, which corresponds to $\psi_{avg} = -0.073$), medium ($e_{avg} = 0.73$, $\psi_{avg} = -0.134$) and low void ratio ($e_{avg} = 0.64$, $\psi_{avg} = -0.226$).

All the specimens exhibited negative ψ after consolidation, as illustrated in **Figure 4a**, which shows the initial conditions of the tested samples on the $\psi - p'$ plane. During the cyclic Tx tests, all the samples underwent cyclic mobility.

Failure, defined as the states at which double amplitude axial strain $\epsilon_a^{DA} = 5\%$, is depicted in **Figure 4b**. In this figure, the cyclic stress ratio applied in the triaxial condition (CSR^{TX}) is adjusted to the cyclic stress ratio for simple shear conditions (CSR^{SS}) in accordance with the methodology proposed in Refs. [3, 4].

$$CSR^{SS} = CSR^{TX}(1 + 2k_0)/3 \quad [-] \quad (1)$$

where $k_0 = \sigma'_r/\sigma'_a = 0.43$ = stress ratio at rest, from the equation of [5].

The pore pressure ratio R_u values at failure were generally larger than 0.9. The data in **Figure 4b** show that the lower the state parameter, the larger the cyclic resistance, as ψ is an indicator of the direction of volumetric strains, $\delta\epsilon_v$, (dilation or contraction) during shearing; the stress ratio required to induce liquefaction at a specific number of cycles is inversely proportional to ψ . This is because, at the same stress level, the denser the soil the lower the propensity to contract and develop Δu .

Samples corresponding to a particular average ψ_{avg} exhibit clear correlations between cyclic stress ratio and the number of cycles. The slope of these relationships in a semi-logarithmic plot is highly influenced by the value of ψ and the interpolating curves can be interpreted through the following function:

$$CSR^{SS} = \frac{a(1-\psi)^b}{N^{c(1-\psi)}} \quad [-] \quad (2)$$

where $a = 0.115$, $b = 3$, $c = 0.145$, empirical constants determined by fitting experimental data. For a given number of cycles N , Eq. (2) allows to estimate the cyclic resistance ratio, CRR.

Previous studies have highlighted that the cyclic resistance of soil undergoes a significant increase even with a minor decrease in the degree of saturation [6–9]. To investigate the impact of saturation on the cyclic resistance of S3, a series of cyclic tests were repeated using partially saturated samples. Achieving specific saturation levels required careful measurement of the amount of deaerated water introduced into

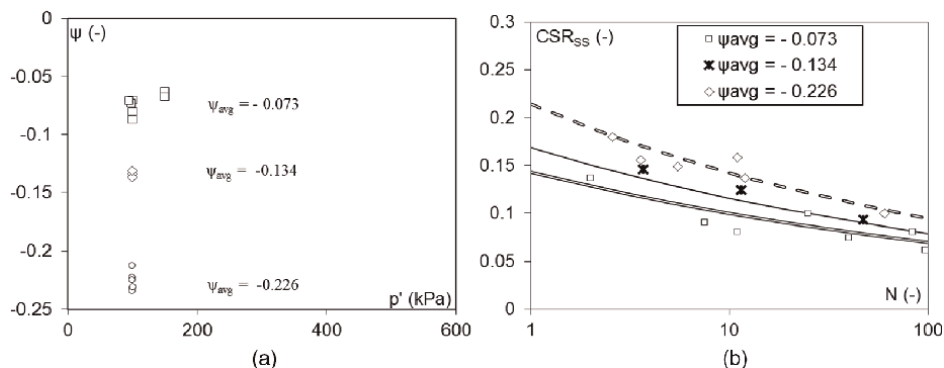


Figure 4.
 Cyclic triaxial tests on S3: (a) end of consolidation state parameter and (b) liquefaction resistance for variable state parameter.

the samples during flushing. Water circulation was halted once $S_r = 80\%$ or $S_r = 90\%$, was attained. Throughout this process, measurements of the Skempton parameter (B) and compression wave velocity (V_p) were conducted.

Figure 5a and **b** illustrate the relationship between V_p , the degree of saturation S_r , and B , respectively. V_p falls within the range of 750–800 m/s when $S_r = 80\%$ ($B = 0.1$) and within the range of 900–1200 m/s when $S_r = 90\%$ ($B = 0.3$ – 0.7). In fully saturated S3 samples ($S_r > 97\%$ and $B > 0.98$), V_p is approximately equal to 1800 m/s. For $V_p > 750$ m/s, the data in **Figure 5a** can be approximated using a logarithmic function:

$$S_r = 0.17 \ln(V_p) - 0.29 \quad [-] \quad (3)$$

After the partial saturation process, the specimens were isotropically compressed to 100 kPa, assuming negligible influence of partial saturation on the mean effective stress, i.e. $p'_c = 100$ kPa. The consolidated, partially saturated specimens had $e_{avg} = 0.7$ and $\psi_{avg} = -0.16$, classifying them as medium-dense samples.

It was observed that, under undrained cyclic conditions, the cyclic stress ratio required to induce double amplitude ε_a^{DA} increased as the degree of saturation decreased.

The tests revealed that, for the same state parameter and applied cyclic stress ratio, the development of axial strains and excess pore pressure was slower in unsaturated samples. The liquefaction condition was achieved for a larger number of cycles compared to saturated samples.

Unsaturated S3 at $S_r = 90\%$ and 80% has, on average, 1.2 and 2.2 times the resistance of fully saturated S3, as can be seen in **Figure 6**, where the CRR of unsaturated samples is normalized against the relating value at full saturation and plotted versus the degree of saturation, S_r in **Figure 6a** and versus the compression wave velocity V_p normalized to its full saturation value, $V_{p,sat}$ in **Figure 6b**.

The experimental data in **Figure 6a** can be fitted with an exponential function:

$$R = \frac{\text{CRR at partial saturation}}{\text{CRR at full saturation}} = 60e^{-4.1S_r} \quad [-] \quad (4)$$

which, combined with Eq. (3), becomes:

$$R = 197 V_p^{-0.7} \quad [-] \quad (5)$$

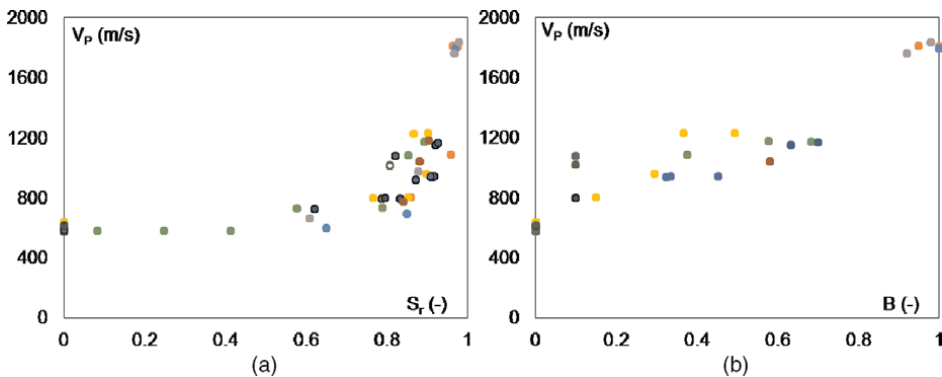


Figure 5.
(a) Compression wave velocity V_p vs. the degree of saturation S_r , (b) V_p vs. Skempton parameter B .

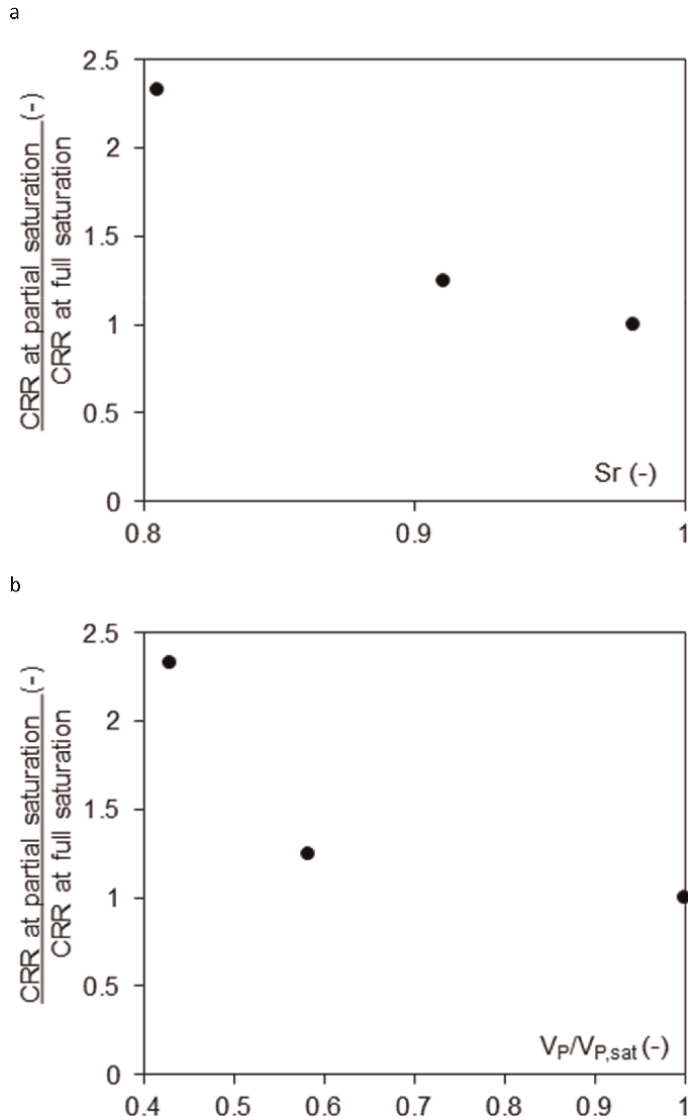


Figure 6. Cyclic resistance CRR of unsaturated samples normalized to the cyclic resistance of fully saturated samples plotted vs. (a) the degree of saturation S_r and (b) the normalised compression wave velocity $V_p/V_{p,sat}$.

while the data in **Figure 6b** can be interpreted through Eq. (6):

$$R = (V_p/V_{p,sat})^{-0.7} [-] \quad (6)$$

and the ratio R can be assumed to correct S3 liquefaction resistance accounting for the effect of partial saturation. Eq. (2) can then be re-written as:

$$CRR = \left(\frac{V_p}{V_{p,sat}} \right)^{-0.7} \frac{a(1-\psi)^b}{N^{c(1-\psi)}} [-] \quad (7)$$

3. The ISMGEO seismic centrifuge

The ISMGEO (Istituto Sperimentale Modelli Geotecnici, Italy) geotechnical centrifuge (**Figure 7**) is a beam centrifuge. Its symmetrical rotating arm has a diameter of 6 m and a nominal radius of 2.2 m to the model base. An external fairing rotates jointly with the arm for aerodynamic purposes. The centrifuge can reach an acceleration of 600 g bearing a payload of 400 kg [10].

On each side of the symmetric arm, there is a swinging platform that accommodates the model containers, for static tests on one side and dynamic tests on the other side. One end of the arm is instrumented with a single-degree-of-freedom shaking table (as depicted in **Figure 7b** and **8a**).

The swinging platform that bears the model for dynamic tests makes contact with the table in flight at 5 g and is released before further accelerating the centrifuge. The shaker is capable of replicating real input motions at the scale of the model [11].

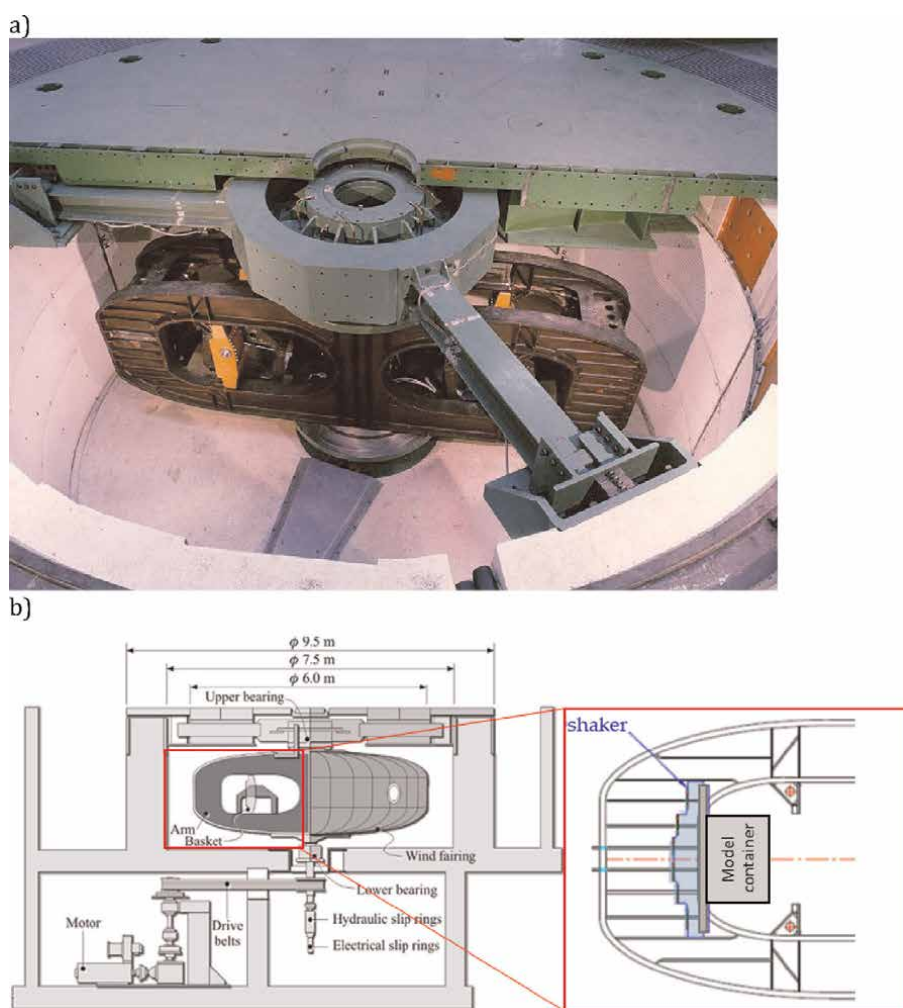


Figure 7. ISMGEO seismic centrifuge: (a) top view and (b) schemes of the centrifuge.

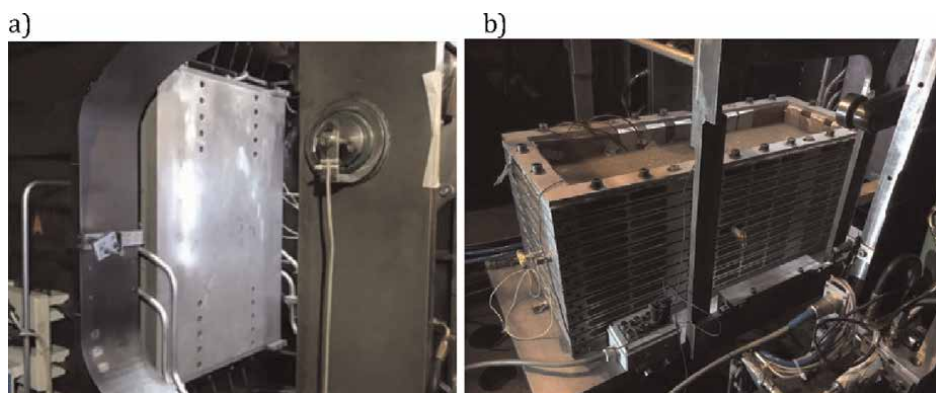


Figure 8.
 (a) shaking table installed on the rotating arm and (b) equivalent shear beam box.

An Equivalent Shear Beam (ESB) box [12, 13], **Figure 8b**, is used to simulate liquefaction. During the flight, the long side of the container is positioned vertically and aligned parallel to the centrifuge's rotation axis. This configuration prevents any distortion effects caused by rotation on the central section of the model, where the instruments are placed and minimizes complications associated with Coriolis acceleration, being the direction of shaking also aligned parallel to the centrifuge's rotation axis.

4. Centrifuge modeling of liquefaction

The LIQUEFACT project involved an extensive series of centrifuge tests conducted at ISMGEO. The objective of the tests was to investigate the seismic response of level ground-saturated sandy deposits, whether homogeneous or stratified, when subjected to progressively intensifying seismic excitations, ultimately leading to liquefaction. The experiments also aimed to assess the effectiveness of various liquefaction mitigation techniques. The tests provided a large database for numerical tools calibration [14, 15]. A more comprehensive description of the experimentation can be found in Refs. [16, 17].

In this section, an overview of the experimental details is provided, along with an analysis of selected results obtained from tests conducted to investigate the triggering mechanism and the efficacy of vertical and horizontal drains to be employed as mitigation techniques.

4.1 Modeling details

The tests reproduced level ground sandy deposits, around 14 m deep. The ground-water table was set at the soil surface. The geometrical scaling factor was $N = 50$ and the centrifugal acceleration of 50 g was imposed at the model's base.

The testing sands are Ticino Sand, herein referred to as S1; a natural, liquefiable sand named S3, and S2, which consists of S3 after the removal of particles finer than 0.075 mm. Grains size distribution and critical state line of the test sands in the e - p' plane are shown in **Figure 2**. The main physical and mechanical properties of the sands are given in **Table 1**.

		S1	S2	S3
γ_{\min}	(kN/m ³)	13.64	12.55	12.18
γ_{\max}	(kN/m ³)	16.67	15.75	15.77
G_s		2.68	2.69	2.69
D_{50}	(mm)	0.53	0.17	0.15
φ'_{cs}	(deg)	34	34.5	34.5
K^*	(m/s)	$2 \cdot 10^{-3}$	10^{-4}	$8.4 \cdot 10^{-5}$

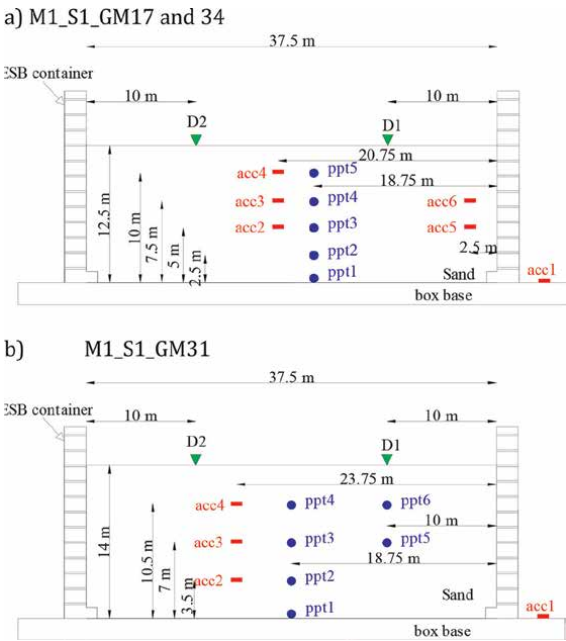
**End of consolidation values.*

Table 1.
Soil physical and mechanical properties.

Test ID	Soil	Density D_R^* (%)	Void ratio e^*	State parameter ψ^*
M1_S1_GM17	S1	47	0.761	−0.13
M1_S1_GM34	S1	50	0.748	−0.14
M1_S1_GM31	S1	47.5	0.757	−0.13
M1_S2_GM17	S2	65	0.82	−0.2
M1_S3_GM17	S3	56	0.89	−0.17
M1_S1_VD1 & VD2_GM31	S1	47	0.76	−0.13
M1_S1_HD1 & HD2_GM31	S1	54.5	0.74	−0.15

**Average values.*

Table 2.
Test program and model characteristics.



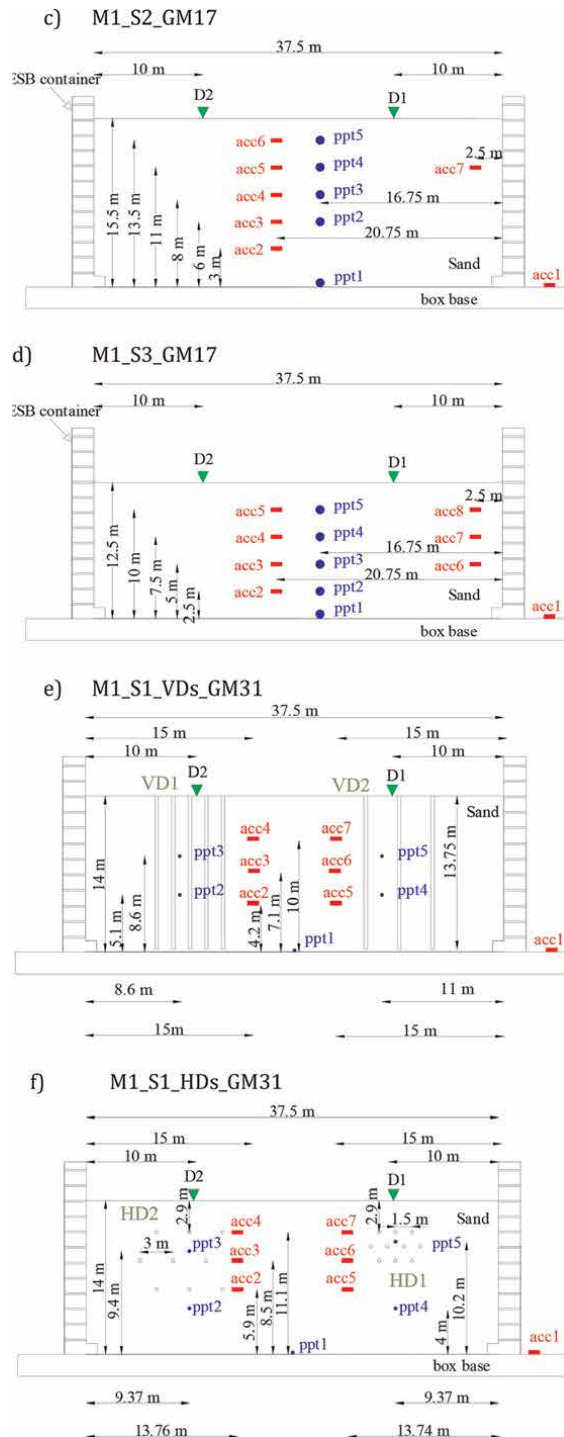


Figure 9. Model schemes: (a) homogeneous models (M1) made of S1 sand, tested applying GM17 and GM34 ground motions; (b) M1_S1 model, tested applying GM31; (c) M1 model of S2 sand, tested applying GM17; (d) M1 model made of S3 sand, tested applying GM17; (e) M1_S1 model equipped with vertical drains tested applying GM31; (f) M1_S1 model equipped with horizontal drains tested applying GM31.

The models were reconstructed at low density into the ESB container and saturated under a vacuum pressure of about -60 kPa using a viscous fluid, to avoid the discordance between the scaling ratios for time in dynamic phenomena and in diffusion phenomena [18].

Table 2 reports the average values of the void ratio and relative density of the models here discussed, referring to the pre-shaking condition. The average ψ value is also indicated. **Figure 9** depicts the model schemes of the discussed tests, with all measurements provided at the prototype scale.

The models were instrumented with miniaturized sensors (accelerometers, acc, pore pressure transducers, ppt, displacement transducers, D) placed along the mid-section.

Some models reconstituted using S1 sand were equipped with flexible silicon pipes, meant to simulate prefabricated vertical and horizontal drains. The pipe's external and internal diameters were 6 mm and 4 mm, respectively (300 mm and 200 mm at the prototype scale,) and their hydraulic conductivity to water was 1.7×10^{-2} m/s.

The mesh of vertical drains (VDs) was square, with a spacing (S) between drains set at 5 or 10 diameters (30 and 60 mm, equivalent to 1.5 and 3 m at the prototype scale) in models VD1 and VD2, respectively. The number of drains was 30 in VD1 and 12 in VD2 models, giving a treated area of about 45 m^2 and 54 m^2 at the prototype scale.

The mesh of horizontal drains was triangular, S was 5 or 10 diameters (30 and 60 mm, 1.5 and 3 m at the prototype scale) in models HD1 and HD2; the number of horizontal drains was 10 and 9, giving a treated area of about 9 m^2 and 31 m^2 in HD1 and HD2, respectively.

4.2 Ground motions

An overview of the principal properties of the input motions employed in the tests discussed here is provided in **Table 3**. **Figure 10** provides examples of the time histories generated by the shaking table, and **Figure 11** displays the Fourier Amplitude Spectra (FAS) corresponding to all the motions listed in **Table 3**. The accelerometer signals were converted into Fourier spectra using the FFT (Fast Fourier Transform) algorithm, including the tapering operation; spectra were smoothed using logarithmic smoothing with a triangular window.

Test ID	GMID	PGA (g)	d_{90} (s)	$I_{A,\max}$ (m/s)
M1_S1_GM17	GM17	0.215	15.09	0.348
M1_S1_GM34	GM34	0.222	24.23	0.451
M1_S1_GM31	GM31	0.198	18.63	0.601
M1_S2_GM17	GM17	0.226	13.53	0.32
M1_S3_GM17	GM17	0.211	11.61	0.27
M1_S1_VD1 & VD2_GM31	GM31	0.187	19.83	0.573
M1_S1_HD1 & HD2_GM31	GM31	0.185	19.1	0.467

GMID = ground motion ID; PGA = peak ground acceleration; d_{90} = duration calculated on the basis of Arias Intensity; $I_{A,\max}$ = maximum arias intensity.

Table 3.
Input motion characteristics.

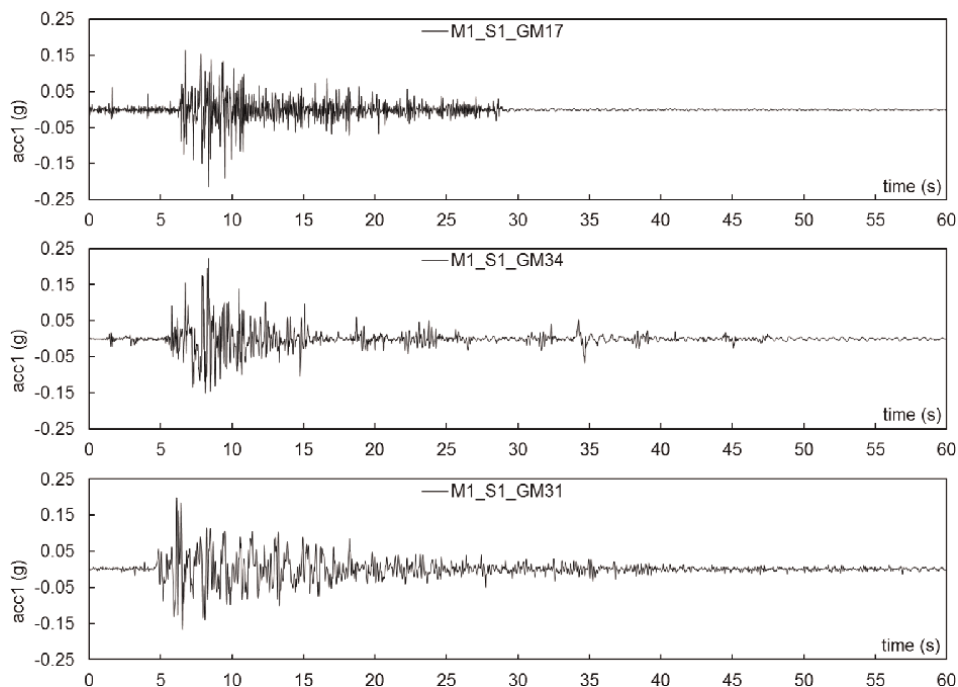


Figure 10.
 Examples of GMs times histories.

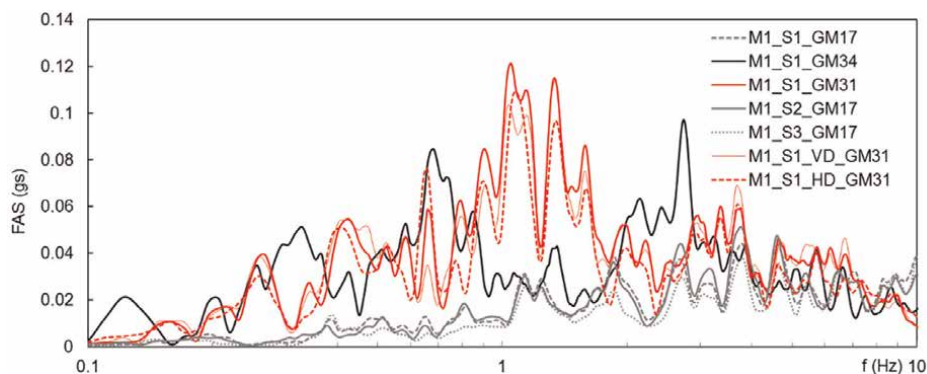


Figure 11.
 Fourier amplitude spectra of the input GMs.

4.3 Same sand, input motions of increasing intensity

In this section, the results are compared of tests M1_S1_GM17/34/31 (layout in **Figure 9a** and **b**). GM17, 34, and 31 had similar PGA but increasing $I_{A,max}$. The time history of the motions and their FAS are shown in **Figures 10** and **11**.

Figure 12 shows the isochrones of excess pore pressure of the three models for instants ranging from 0.3 to 5 times the duration (d_{90} in **Table 3**) of the input earthquake.

In interpreting the tests, the liquefaction criterion is assumed to be the point at which Δu approaches the pre-shock vertical effective stress σ'_{v0} (represented in the Figure by an inclined straight line).

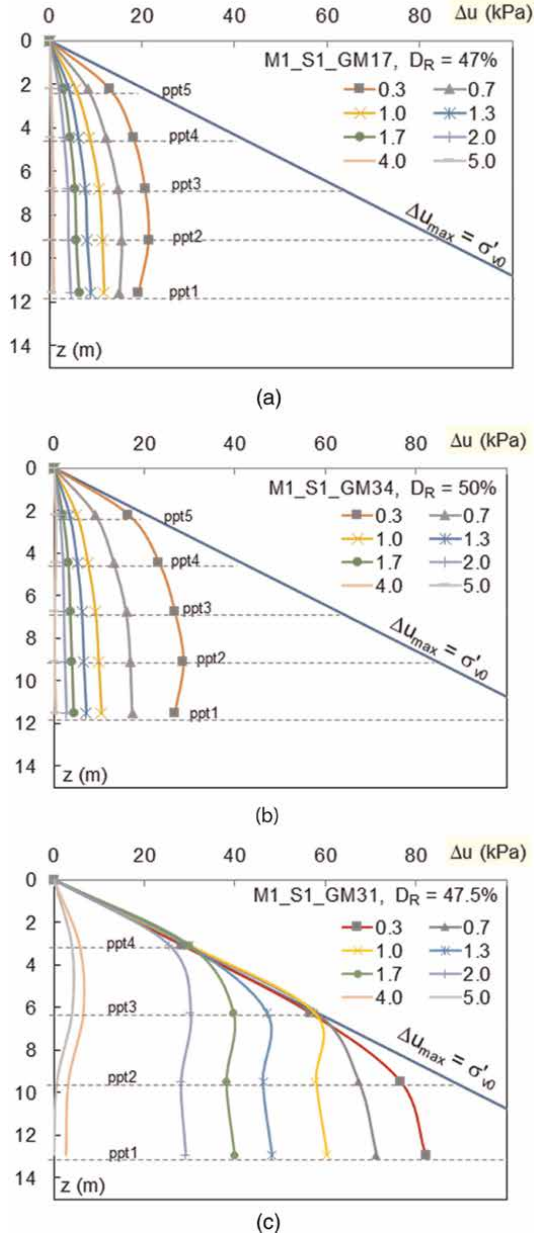


Figure 12. Excess pore pressure isochrones of models (a) M1_S1_GM17, (b) M1_S1_GM34, and (c) M1_S1_GM31 at time instants ranging from $0.3 d_{90}$ to $5 d_{90}$.

Based on this assumption, complete liquefaction was observed in only one model, M1_S1_GM31, at mid-depth (ppts 3) and near the ground surface (ppts 4), see **Figure 12c**. In this model, at all monitoring points, Δu initially increased to its maximum value within the first few seconds. Subsequently, at ppts 1 and 2, Δu began to decrease, nearly simultaneously and well before the conclusion of the ground motion. Conversely, at ppts 3 and 4, the excess pore pressure remained

at its maximum level throughout the entire dynamic loading and beyond: the excess pore pressure equalized the vertical effective stress up to d_{90} and up to $1.7d_{90}$, at the depth of ppt3 and ppt 4, respectively. In a few cycles of excitation, the model exhibited a clear separation into two distinct halves: the upper part became fluidized, while the bottom part remained in a solid state [19].

The fluid state persisted until the conclusion of the dynamic loading, after which ppt3 began registering a decrease in Δu , signifying that solidification had taken place at that particular depth. It took an additional period equal to 2 times d_{90} for the solidification front to reach ppt4. Following this, the entire soil column solidified, initiating a reconsolidation process to dissipate Δu .

The occurrence of decay from the model base upward during the earthquake suggests that the response of the sand to the seismic loading is a partially drained process. As the soil undergoes dynamic strain and starts to generate excess pore pressure, it simultaneously begins to dissipate this Δu [20, 21]. During the earthquake, Δu represents a balance between generation and dissipation.

In the lower half of the model, dissipation predominated over generation after a few loading cycles, leading to an upward fluid flow, that is, from higher Δu levels toward lower values at the surface. In the upper half (ppt3 and 4), the generation induced by the shaking and the inflow from greater depths outweighed dissipation. This led to a hydraulic gradient reaching a critical value, causing the soil to liquefy and remain in a fluidized state until the end of the seismic loading (d_{90} at the depth of ppt3) or even longer ($1.7d_{90}$ at the depth of ppt4).

The above is confirmed by the evolution of surface settlement, as depicted in **Figure 13**. At the conclusion of the recording, the total surface settlement S_t amounted to 265 mm. Notably, 30% of this settlement occurred within the initial 2.5 seconds, a period during which all the ppts recorded a rise in Δu ; 67% of the total settlement developed during the ground motion, resulting from the combination of drainage, sedimentation, and reconsolidation. Only 33% of the S_t could be attributed to post-seismic settlement, arising from solidification and reconsolidation.

Regarding models M1_S1_GM17 and M1_S1_GM34 (depicted in **Figure 12a** and **b**), the seismic motions applied had very similar PGA compared to GM31, but they had lower values of the maximum Arias Intensity ($I_{A,max}$), as detailed in **Table 3**. Specifically, $I_{A,max}$ was 0.348 for GM17, 0.451 for GM34, and 0.601 for GM31.

Both models exhibited a peak Δu at all depths within the first few seconds of loading but they did not liquefy; Δu began decreasing thereafter. The dominant

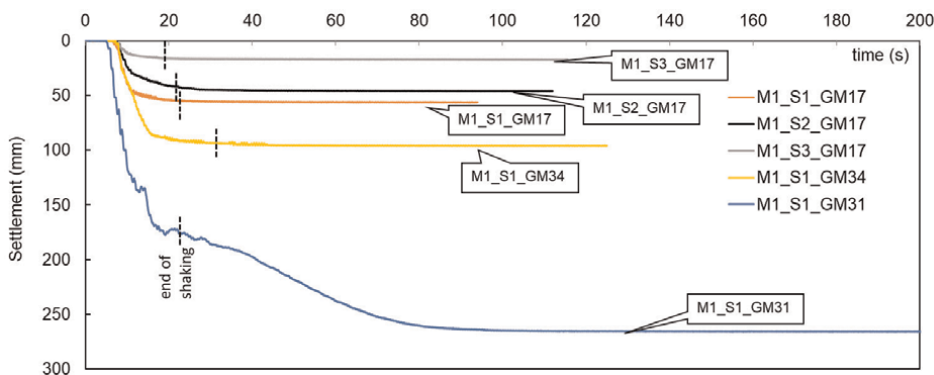


Figure 13.
Ground surface settlement.

mechanism was excess pore pressure generation only during the initial few seconds, after which dissipation and drainage became predominant.

Furthermore, the surface settlements in both models were predominantly associated with the seismic event and a great part of the final settlement in both models developed during the initial phase of excess pore pressure accumulation: 84% in model M1_S1_GM17 and 50% in model M1_S1_GM34. The settlement attributed to rapid drainage during the initial earthquake phase, characterized by the development of a high hydraulic gradient, was higher than the settlement resulting from post-earthquake reconsolidation.

4.4 Same input motion, different sands

In this section, an analysis is conducted on three tests performed on models reconstructed with various sands and subjected to the same input motions (model M1_S1_GM17, scheme in **Figure 9a**, results in **Figure 12a**; models M1_S2_GM17 and M1_S3_GM17, schemes in **Figure 9c** and **d**, results in **Figure 14a** and **b**). It should be noted that, although the same reconstitution procedure was followed, S2 and S3 exhibited greater compressibility (reflected in the slope of the critical state line, as shown in **Figure 2b**). During the saturation process and subsequent in-flight consolidation, these models settled more compared to S1.

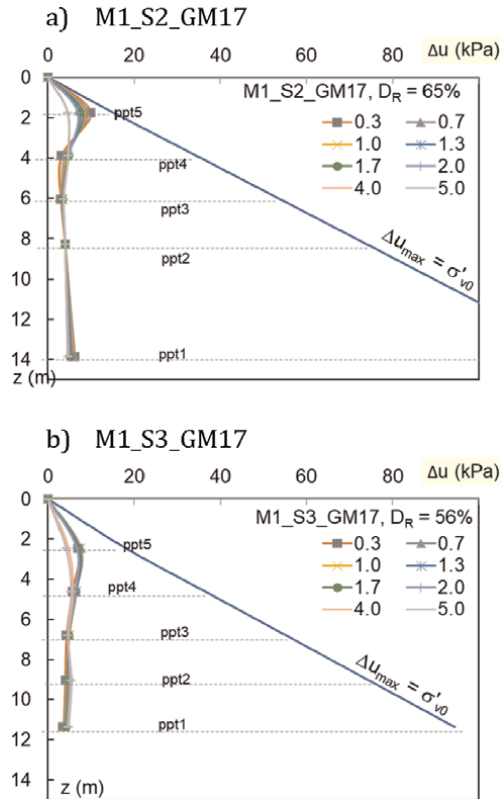


Figure 14. Excess pore pressure isochrones of models (a) M1_S2_GM17 and (b) M1_S3_GM17 at time intervals ranging from 0.3 d_{90} to 5 d_{90} .

As a result of these differences, M1_S2 and M1_S3 achieved a higher relative density than M1_S1 at the conclusion of the Ng consolidation phase. Specifically, the relative density of M1_S2 was 18% higher, and that of M1_S3 was 9% higher, as indicated in **Table 2**.

As model S1 described above, neither model S2 nor S3 experienced liquefaction ($\Delta u < \sigma'_{v0}$).

Model S2 (**Figure 14a**) developed very low pore pressure at every depth except at ppt5. At this depth, once the max Δu was attained, dissipation was triggered at a very low rate. The soil beneath ppt5, instead, continued to accumulate pore pressure slightly, even after the dynamic phase had concluded.

The lower values of Δu observed in S2 compared to S1 can be attributed to the lower initial ψ , as indicated in **Table 2**. This initial condition led to a reduced tendency for the soil to contract during dynamic loading and, consequently, resulted in minor soil surface settlement, as illustrated in **Figure 13**. In total, 90% of the ground surface settlement was associated with the seismic event, confirming the occurrence of partial drainage during seismic excitation.

In the case of the natural S3 sand model, which experienced a less intense earthquake, the values of excess pore pressure were similar to those observed in model 2 except near the ground surface (ppt5), where the Δu values were lower and dissipation onset during the earthquake but at a very slow rate, while the soil below continued to accumulate pore pressure slightly, even after the dynamic phase had concluded. As a result, the S3 deposit exhibited a lower overall ground settlement, as shown in **Figure 13**.

Figures 12a, 14a, and b reveal that S1 exhibited a considerably higher dissipation rate compared to both S2 and S3 sands. After the seismic shock had concluded, dissipation in S1 was at 50% at all depths. In contrast, S2 and S3 were still accumulating below the depth of ppt5, which was close to a permeable boundary represented by the surface.

When the data recording was interrupted, the lower half of models 2 and 3 had not yet initiated the dissipation of Δu . This observation aligns with the permeability values of the three sands at the test density, as presented in **Table 1**. Specifically, S1 exhibited a permeability that was an order of magnitude higher than that of S2 and S3. S3, despite having a fine content of 12%, being slightly looser during the test compared to S2 had similar permeability.

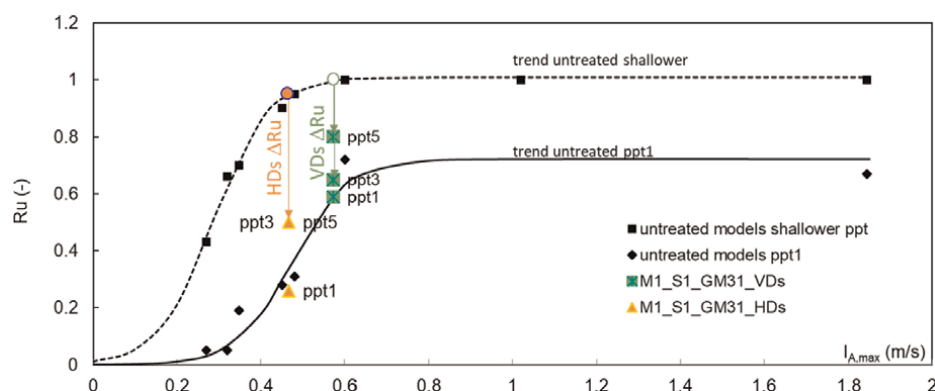


Figure 15.
Ru of shallower and deeper ppts vs. max arias intensity.

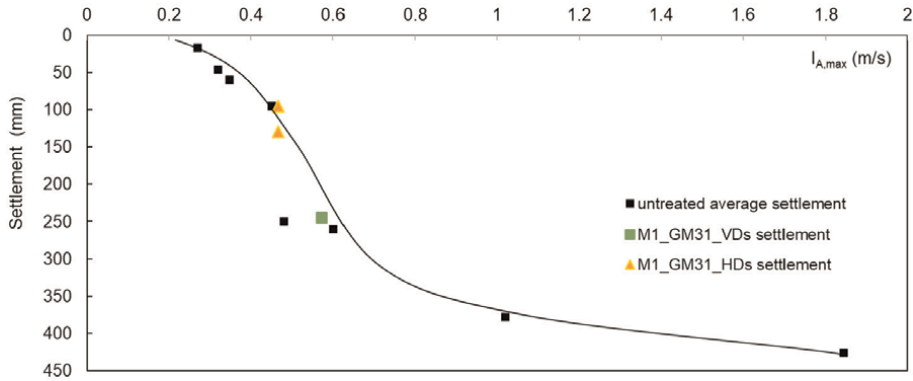


Figure 16.
Superficial settlement vs. max arias intensity.

From the Δu measures from tests in **Figures 12 and 14**, the pore pressure ratio $R_u = \Delta u / \sigma'_{v0}$ has been computed.

In **Figure 15** the max R_u registered at the base ppt (ppt1 in all models), and at the shallower ppts, are plotted as a function of the $I_{A,max}$ of the input earthquake (**Table 3**). The results of three additional tests (M1_S1 models equipped with a shallow foundation F) non-discussed herein are also reported (measures from the free field part of the models).

The distribution of R_u for both the deepest and the shallowest ppt seems unique and follows a sigmoid function, as indicated by the interpolation curves outlined in the Figure. For $I_{A,max}$ equal to 0.6, the shallower part of the model reaches the liquefaction condition, meanwhile, at the bottom of the container R_u does not exceed 0.6.

The end of recordings settlements are plotted in **Figure 16** vs the max Arias Intensity and describe an S-shape function.

4.5 Liquefaction mitigation using vertical and horizontal drains

Figure 17 shows the isochrones of excess pore pressure Δu measured in the models equipped with vertical and horizontal drains (test layout in **Figure 9e and f**, FAS of the applied input options in **Figure 11**).

As highlighted above, the shallower half of the untreated model M1_S1_GM31 underwent complete liquefaction, while liquefaction was prevented in the treated areas of both configurations of vertical drains.

As expected, the larger the spacing the lower the Δu reduction. The extent of VDs efficacy can be appreciated in terms of R_u in **Figure 15**, where ppts 1, 3 and 5 are shown and compared with the sigmoid functions obtained from untreated models.

The lower R_u observed at ppt3 and ppt5 is attributed to the influence of the drains. This conclusion is supported by the measurements at ppt1, which are consistent with the R_u function depicted in **Figure 15**: ppt1 was positioned at the model base, a significant distance (20 diameters) away from the treated area where the drains were installed.

In both VD1 and VD2 configurations, the maximum Δu was reached within a few seconds, followed by Δu decay. This decay process began well before the conclusion of the ground motion. Consequently, by the end of the seismic loading, more than 50% of the measured Δu had dispersed, in stark contrast to the untreated model.

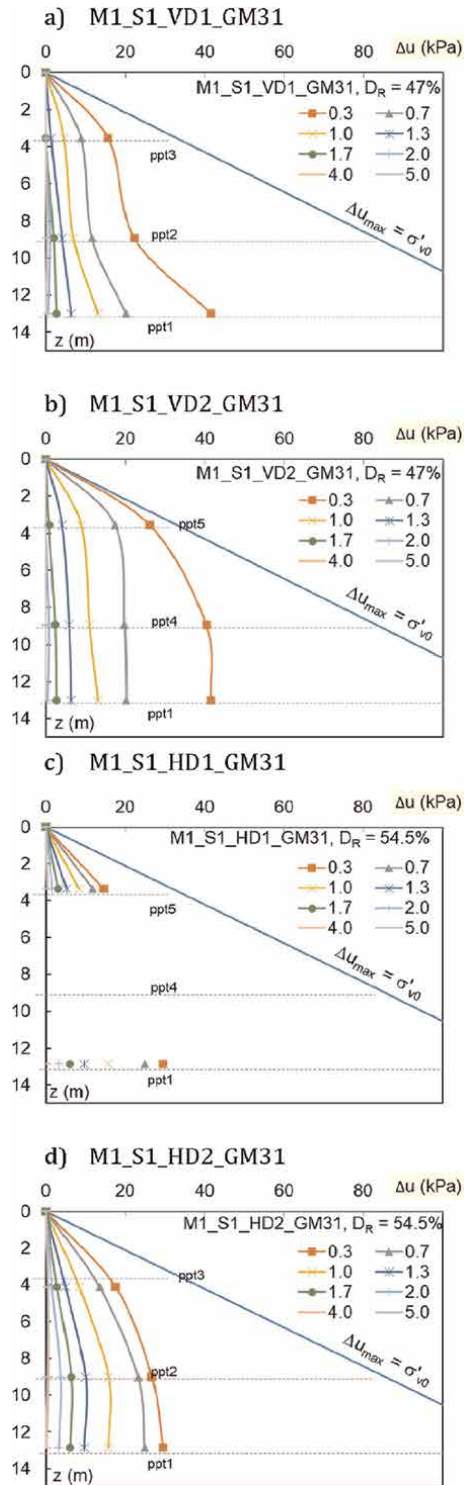


Figure 17.
Excess pore pressure isochrones of models (a) $M1_S1_VD1_GM31$, (b) $M1_S1_VD2_GM31$, (c) $M1_S1_HD1_GM31$, and (d) $M1_S1_HD2_GM31$ at time instants ranging from $0.3 d_{90}$ to $5 d_{90}$.

The superficial settlements were exclusively co-seismic. In terms of the balance between Δu generation and dissipation, vertical drains made the latter phenomenon prevalent after just a few cycles of loading. VDs reduced the rate of Δu accumulation, the maximum Δu , and accelerated the rate of Δu decay.

D2 (D1 not working) recorded a final settlement of 244 mm. The difference with the 265 mm measured in M1_S1_GM31, which is slightly less than -10% , is considered to be within the range of experimental variation and is consistent with the settlement expected for the applied intensity based on the Settlement-S-function depicted in **Figure 16**.

The primary effect of drains is indeed to prevent Δu accumulation. However, if no densification is induced by their installation they do not impact the sand's tendency to contract and generate excess pore pressure when subjected to seismic vibrations.

Thus, in free field conditions, the effectiveness of drains in limiting settlements is negligible, as drains primarily facilitate the dissipation of excess pore pressure (Δu) without preventing the soil from undergoing strain. However, in the presence of buildings, drains are also effective in mitigating settlements. By preventing soil liquefaction, they help prevent the sinking of buildings [22–24], provided that they are adequately distributed beneath the entire footprint of the structure [25].

As to the models treated with HDs, account has to be taken for the applied input motion weaker than in models with VDs and in the untreated model. As discussed above, tests on untreated models have shown that $I_{A,max}$ influences both the max R_u and the superficial settlements.

To assess the effect of horizontal drains (HDs) despite the weaker input motion, the R_u functions of **Figure 15** can be used as a reference. For $I_{A,max} = 0.467$, at the depth of ppt1 and ppts 3/5 R_u values of approximately 0.3 and larger than 0.9 were expectable. The measured values were 0.26 and 0.5.

$R_u = 0.26$ is comparable to the expected value and is considered within the range of experimental variation. $R_u = 0.5$ implies that HDs induced a reduction in R_u of about -45% , confirming their effectiveness.

Regarding surface settlements, the models with HDs developed settlements equal to 95 mm and 130 mm in HD1 and HD2, respectively. These values are consistent with what was expected for $I_{A,max} = 0.467$ based on untreated models (as shown in **Figure 16**). This confirms that HDs are effective in preventing the accumulation of excess pore pressure and liquefaction but do not significantly influence Δu generation and subsequent settlement due to reconsolidation.

As with vertical drains (VDs), in the presence of HDs, the maximum Δu was reached within a few seconds, and Δu decay began prior the end of the dynamic loading, albeit a little slower than in the models equipped with vertical drains.

5. Liquefaction assessment using a simplified procedure

Liquefaction resistance is typically determined through the interpretation of field test results using empirical correlations based on the results of standard penetration tests [26] or, more effectively and widely, cone penetration tests [27–31].

Both the cone penetration resistance q_c and the undrained cyclic resistance CRR of an uncemented and unaged soil depend on its nature, stress level, and density, that is,

on its state parameter ψ , which allows to anticipate the direction of volumetric strains, $\delta\epsilon_v$, (dilation or contraction) during shearing.

Therefore, ψ can be used to relate CRR to the tip resistance of CPTs.

In this section, the results of centrifuge CPT tests and cyclic undrained triaxial tests carried out on S1 sand are used to link CRR to the cone resistance.

5.1 Cyclic resistance of S1

Undrained cyclic Tx tests on S1 were performed on reconstituted samples, isotropically consolidated at $p'_c = 100$ kPa.

The consolidated void ratio of the specimens was: $e_{avg} = 0.742$, which corresponds to $\psi_{avg} = -0.132$, $e_{avg} = 0.676$, $\psi_{avg} = -0.201$ and $e_{avg} = 0.582$, $\psi_{avg} = -0.295$.

Figure 18 illustrates the applied cyclic stress ratio CSR as a function of the number of cycles at which the double amplitude axial strain ϵ_a^{DA} reached 5% (assumed as failure criterion). The R_u values at failure varied from 0.8 to 0.97. Only the samples TS4_14_01 and TS4_14_03 developed ϵ_a^{DA} less than 5%, so their failure condition was considered as the attainment of $R_u = 0.95$, at $N = 60$ and $N = 900$, respectively.

In **Figure 18**, CSR^{TX} is converted into CSR^{SS} via Eq. (1); for S1, $k_0 = 0.44$ and $CSR^{SS} = 0.63 \cdot CSR^{TX}$. **Figure 18** shows also the interpolation curves of the experimental data using Eq. (2), which, calibrated for S1, returns the following calibration coefficients: $a = 0.071$, $b = 7.8$, $c = 0.177$.

5.2 Calibration chamber centrifuge CPTs in S1

A series of 27 centrifuge CPTs were carried out on dry S1 models, reconstituted at low ($e \approx 0.63$), medium ($e \approx 0.73$), and high void ratio ($e \approx 0.82$). The tests were run at three levels of centrifugal acceleration: 30 g – 50 g – 80 g, corresponding to increasing values of effective stresses.

Calibration Chamber (CC) CPT tests carried out by [32, 33] show comparable penetration resistance for dry and saturated conditions.

A miniaturized electrical piezocone (diameter $d_c = 11.3$ mm, apex angle of 60° , sleeve friction 11.3 mm in diameter, and 37 mm long) was employed for the tests (**Figure 19**).

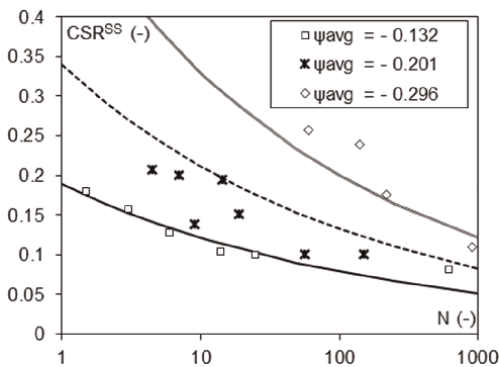


Figure 18.
Cyclic strength of S1.

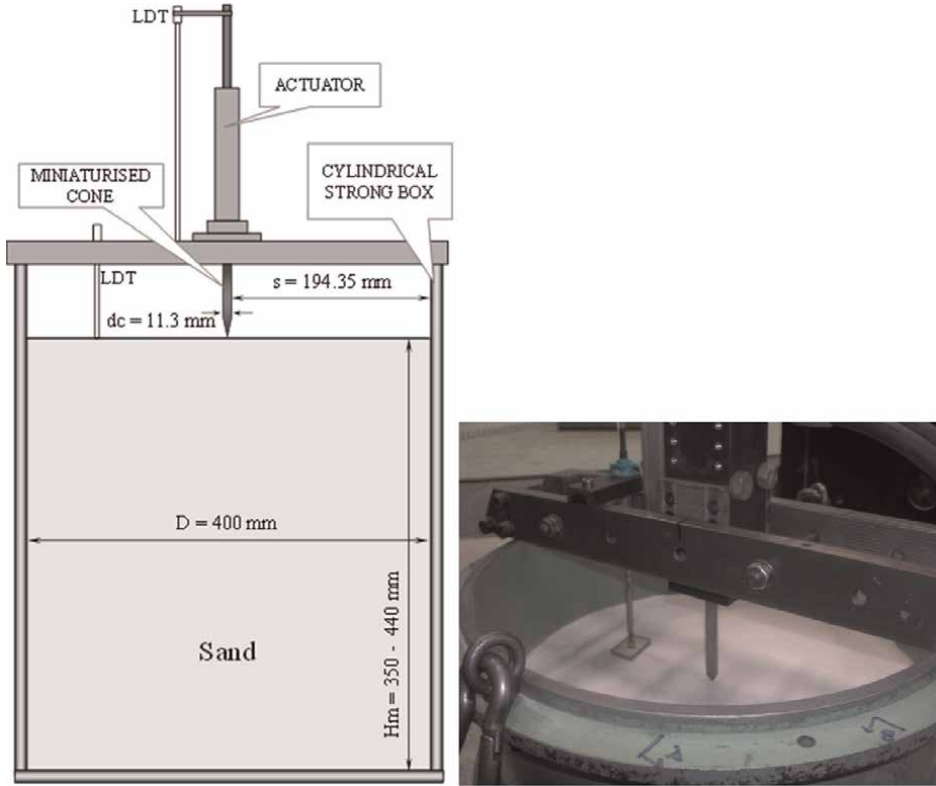


Figure 19.
Model scheme and model picture with a view of the ISMGEO miniaturized piezocone before penetration.

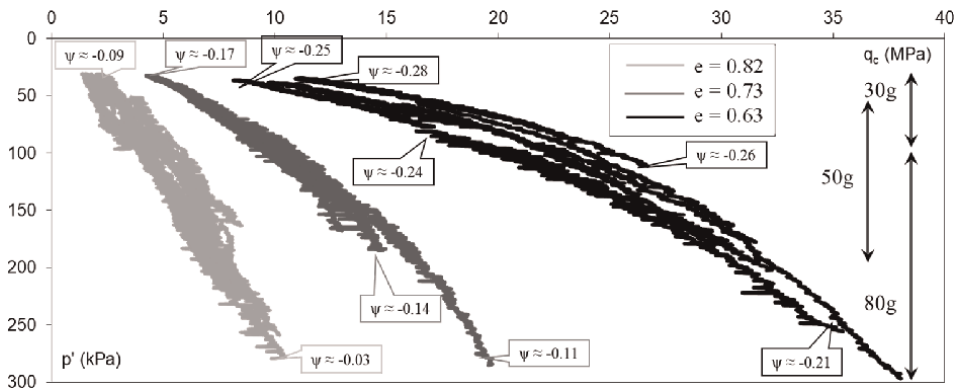


Figure 20.
CPTs in S1: tip resistance q_c as a function of mean effective stress p' (computed adopting $k_o = 0.44$).

Figure 20 shows the measured tip resistance q_c represented vs. the mean effective stress p' :

$$p' = \sigma'_v(1 + 2 k_o)/3 \text{ [kPa]} \quad (8)$$

σ'_v = vertical effective stress, computed accounting for the acceleration field distortion;

$k_0 = \sigma'_h / \sigma'_v$ = stress ratio at rest.

The values of ψ at rest at the beginning and stop of penetration are highlighted in **Figure 20**. The soil models are rather homogeneous and the tests are repeatable. A less-than-linear rise of q_c with p' , for a given void ratio, can be observed.

As shown by [34–37], during the penetration the void ratio can decrease (contraction) or, more likely, increase (dilation) due to shearing. Dilation causes a stress increment around the tip, with respect to the stress value at rest, proportional to the dilatancy. Dilatancy can be related to the state parameter ψ at rest, before penetration [37].

Consequently, the two major contributions of q_c can be considered:

- the overburden stresses at the depth of the tip, herein represented by the mean effective stress p' ;
- the increment of stresses around the tip caused by the penetration, due to dilatancy, representable by ψ .

In a homogeneous centrifuge model, ψ at rest increases with depth, so the dilative tendency of soil decreases.

So, what happens around the tip during the penetration is an increase in stress level which causes q_c to rise, and a contemporary decrease in the soil dilative tendency, so a rate of increase in q_c reduction.

To separate these two major effects, the following procedures were followed. The effect of stresses at rest at constant ψ has been defined as:

$$q_c / p_a = f \left(p' / p_a \right)^\beta \quad [-] \quad (9)$$

The exponential function represents the impact of the overburden stresses at the depth of the cone tip on q_c . The best fit of the experimental constant ψ cone resistance profiles gave $\beta = 0.8$, a slightly lower value than 1, as recommended by [38]. In this paper, the measured cone resistance was normalized using this β value as follows:

$$(q_c / p_a) \cdot (p_a / p')^{0.8} = q_c^* \quad [-] \quad (10)$$

and q_c^* is plotted as a function of p' in **Figure 21**.

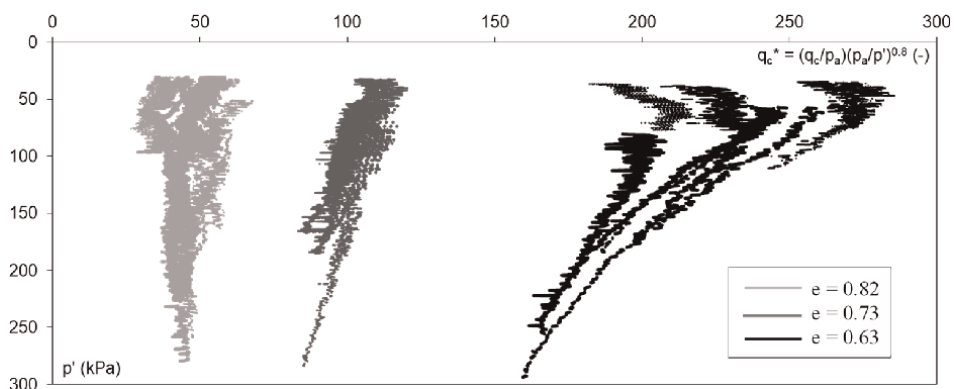


Figure 21.
 Normalized tip resistance q^* as a function of mean effective stress p' .

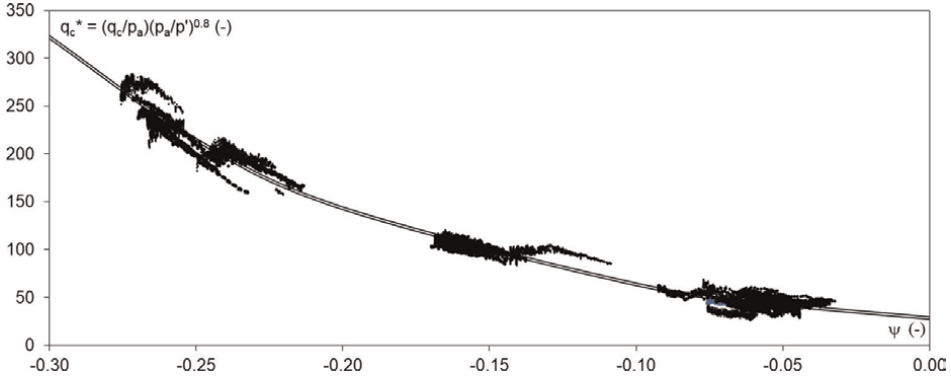


Figure 22.
Normalized q_c^* vs. the state parameter ψ .

Removing the influence of p' on q_c through the normalization, the effect of ψ on q_c can be appreciated in **Figure 21**: while crossing less dilative soil (rising of ψ with depth), the reduction of dilatancy around the tip causes a non-linearly q_c^* reduction. In a constant ψ soil profile, q_c^* would have been nearly constant with depth.

The effect of ψ on q_c^* is highlighted by plotting q_c^* vs. ψ , as shown in **Figure 22**. The trend in **Figure 22** can be interpreted with the following equation [38]:

$$q_c^* = k \cdot e^{-m\psi} [-] \quad (11)$$

where m and k are dimensionless fitting parameters, equal to:
 $m = 8.1$, $k = 28.3$ (12,720 data, $R^2 = 0.96$).

It's worth noting that k is the normalized q_c^* value when $\psi = 0$, while m indicates the influence of dilatancy on the cone resistance at a given of ψ .

The normalized cone resistance can be re-written as:

$$(q_c/p_a) \cdot (p'/p_a)^\beta = (p'/p_a)^\beta k \cdot e^{-m\psi} [-] \quad (12)$$

which represents the dependency of q_c on the overburden stresses acting at the depth of the cone and on the soil dilative tendency at that depth.

5.3 CRR from CPT trough ψ : a simplified method

Ψ can be assumed as an independent variable governing both the cyclic stress resistance and the normalized cone resistance of the tested soils, and the cyclic resistance ratio, CRR can be derived by combining Eqs. (2) and (12):

$$CRR = \frac{a \left[1 + \frac{1}{m} \ln \left(\frac{q_c^*}{k} \right) \right]^b}{N^c \left[1 + \frac{1}{m} \ln \left(\frac{q_c^*}{k} \right) \right]} [-] \quad (13)$$

where a , b , c , m , and k are the fitting parameters of Eqs. (2) and (12). These parameters have been calibrated for two sands other than S1: S3, described above (see [1]) and Toyoura sand (TOS [39]). These parameters are:

- Toyoura sand: $a = 0.037$, $b = 10.7$, $c = 0.247$, $m = 9.8$, $k = 23.9$

- S3: $a = 0.115$, $b = 3$, $c = 0.145$, $m = 7.42$, $k = 27.44$
- S1: $a = 0.071$, $b = 7.8$, $c = 0.177$, $m = 8.1$, $k = 28.3$

Values of m and k of Eq. (12) are also available for other two silica sands tested in centrifuge [40], Fontainebleau NE34 (FNE34S, 90% quartz, 8% feldspar, 2% mica) and Stava Sand (SS, 55–60% quartz, 20–25% feldspar, 16% fluorite, 7–8% calcite). The latter is a natural sand containing 30% of non-plastic silt, obtained from the mine tailings dam in Stava (Italy), which collapsed the 19th of July 1985 [41]. The fitting parameters are:

- FNE34S: $m = 9.4$, $k = 17$
- SS: $m = 5.3$, $k = 57$

The $q_c^*-\psi$ curves of all the tested sands are shown in **Figure 23**. A total of 64 CPTs are displayed. For each sand, a trendline is represented in **Figure 23**. An average relationship for all the sands is drawn in yellow. Its equation is:

$$q_c^* = 30.6 \cdot e^{-8\psi} [-] \tag{14}$$

Eq. (13) and the set of average fitting parameters given in **Table 4** can be used to derive CRR from q_c measured in situ. The parameter β of Eq. (10) is 0.8 in clean sand and can be assumed equal to 1 in the presence of silty sand.

Eq. (13) turns into Eq. (15) to account for the degree of saturation:

$$CRR = \left(\frac{V_P}{V_{P,sat}} \right)^{-0.7} \frac{a \left[1 + \frac{1}{m} \ln \left(\frac{q_c^*}{k} \right) \right]^b}{N^c \left[1 + \frac{1}{m} \ln \left(\frac{q_c^*}{k} \right) \right]} [-] \tag{15}$$

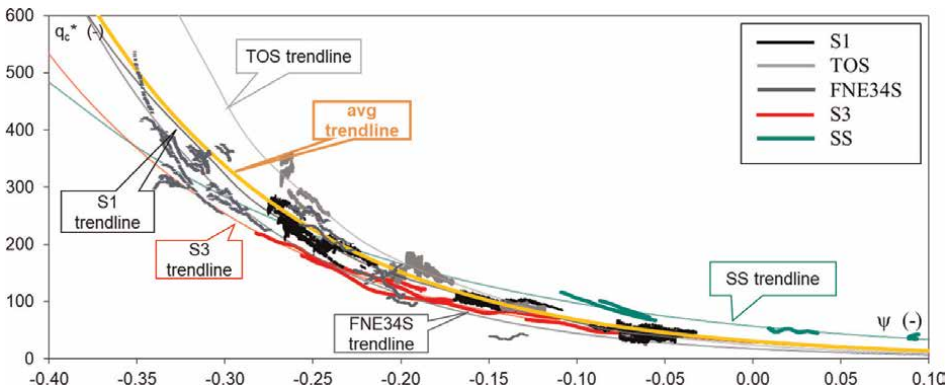


Figure 23.
Normalized q_c^* vs. ψ for five sands. The yellow curve is the average relationship.

A	b	c	m	k
0.074	7.17	0.19	−8	30.6

Table 4.
Average fitting parameters of Eq. (13).

6. Conclusions

This chapter deals with earthquake-induced liquefaction and its modeling, from the element volume scale to small-scale physical models.

The first part of the chapter describes a case study in Italy presenting some experimental observations gained through cyclic undrained simple shear and triaxial tests carried out on saturated samples of a natural soil that experienced liquefaction during the 2012 Emilia seismic sequence.

The cyclic resistance ratio CRR of a granular soil has been expressed as a function of the applied number of cycles N and on the state parameter ψ , through Eq. (2).

To evaluate the increase in liquefaction resistance due to the partial saturation reference can be made to the velocity of compression waves through Eq. (7).

The second part of the chapter describes the centrifuge modeling of liquefaction; some details of the Italian seismic apparatuses are given. Some results of a large campaign of physical model tests are presented. The tests have shown that in free field conditions, the distribution of $\max R_u$ vs. the \max Arias intensity follows a sigmoid function.

In the particular test layout discussed here, the function was found to be independent of the specific testing sand. This suggests that it can be adopted to predict R_u for earthquakes with varying maximum Arias Intensity. Also, the superficial free field settlements appear to follow a unique S-shaped settlement function.

Vertical and horizontal drains, applied as a liquefaction mitigation technique, do not affect Δu generation; instead, their action is to prevent the accumulation of excess pore pressure, thereby avoiding liquefaction. However, they do not mitigate the volumetric strains induced by dynamic loadings. As a result, the settlements observed in models equipped with both horizontal drains and vertical drains are comparable to those measured in untreated models for the same earthquake intensity. Therefore, in free field conditions, drains have limited effectiveness in reducing settlement.

The third part of the chapter describes the results of combined centrifuge and laboratory experiments conducted to derive the cyclic resistance of soil from the cone penetration resistance.

The cone penetration resistance may be linked to the state parameter *via* Eq. (12).

Eqs. (12) and (2), combined, turn into Eq. (13), which can be used to assess the liquefaction resistance of sandy soil from in situ CPTs, and which, with respect to the empirical correlations typically used in the geotechnical practice, has the advantage of a direct experimental calibration.

Acknowledgements

The LIQUEFACT project received funding from the European Union's Horizon 2020 Research and Innovation Programme under Grant Agreement No. 700748. This support is gratefully acknowledged by the authors.

All the experimental data available at <https://www.zenodo.org/record/1281598#.W-mWVOhKJIU>

The authors acknowledge the Istituto Sperimentale Modelli Geotecnici (ISMGEO) for carrying out the experimentation and making the results available for the elaborations and speculations described in this paper.

Author details


Vincenzo Fioravante^{1*} and Daniela Giretti²

1 University of Ferrara, Italy

2 University of Bergamo, Italy

*Address all correspondence to: vincenzo.fioravante@unife.it

IntechOpen

© 2024 The Author(s). Licensee IntechOpen. This chapter is distributed under the terms of the Creative Commons Attribution License (<http://creativecommons.org/licenses/by/3.0>), which permits unrestricted use, distribution, and reproduction in any medium, provided the original work is properly cited. 

References

- [1] Giretti D, Fioravante F. A correlation to evaluate cyclic resistance from CPT applied to a case history. *Bulletin of Earthquake Engineering*. 2017;**15**(5): 1965-1989
- [2] Been K, Jefferies MG. A state parameter for sands. *Géotechnique*. 1985;**35**(2):99-112
- [3] Ishihara K, Iwamoto S, Yasuda S, Takatsu H. Liquefaction of anisotropically consolidated sand. In: *Proceedings 9th International Conference on Soil Mechanics and Foundation Engineering*. Vol. 2. Tokyo, Japan: Japanese Society of Soil Mechanics and Foundation Engineering; 1977. pp. 261-264
- [4] Ishihara K, Yamazaki A, Haga K. Liquefaction of K₀ consolidated sand under cyclic rotation of principal stress direction with lateral constraint. *Soils and Foundations*. 1985;**5**(4):63-74
- [5] Jaky J. The coefficient of earth pressure at rest. *Journal of the Society of Hungarian Architects and Engineers*, Budapest. 1944:355-358
- [6] Ishihara K, Yamazaki A, Haga K. Liquefaction of K₀ consolidated sand under cyclic rotation of principal stress direction with lateral constraint. *Soils and Foundations*, Japanese Society of Soil Mechanics and Foundation Engineering. 1985;**5**(4):63-74
- [7] Eseller-Bayat E, Yegian MK, Alshawabkeh A, Gokyer S. Liquefaction response of partially saturated sands. I: Experimental results. *Journal of Geotechnical and Geoenvironmental Engineering*. 2013;**139**(6):863-871
- [8] Okamura M, Soga Y. Effects of pore fluid compressibility on liquefaction resistance of partially saturated sand. *Soils and Foundations*. 2006;**46**(5): 695-700
- [9] Tsukamoto Y, Ishihara K, Nakazawa H, Kamada K, Huang YN. Resistance of partly saturated sand to liquefaction with reference to longitudinal and shear wave velocities. *Soils and Foundations*. 2002;**42**(6):93-104
- [10] Baldi G, Belloni G, Maggioni W. The ISMES geotechnical centrifuge. In: Corté JF, editor. *Centrifuge 88*, Paris. Rotterdam: Balkema; 1988. pp. 45-48
- [11] Airolidi S, Fioravante V, Giretti D, Moglie J. Report on validation of retrofitting techniques from small scale models. In: *Deliverable D4.2 of Liquefaction project*, funded under the European Union's Horizon 2020 Research and innovation Programme, GA No. 700748. 2018
- [12] Zeng X, Schofield AN. Design and performance of an equivalent shear beam (ESB) model container for earthquake centrifuge modelling. *Geotechnique*. 1996;**46**:83-102
- [13] Brennan AJ, Madabhushi SPG, Houghton NE. Comparing laminar and equivalent shear beam (ESB) containers for dynamic centrifuge modelling. In: *Proc. 6th Int. Conf. On Physical Modelling in Geotechnics 06*. Vol. 1. Rotterdam, The Netherlands: Balkema; 2006. pp. 171-176
- [14] Özcebe AG, Giretti D, Bozzoni F, Fioravante V, Lai CG. Centrifuge and numerical modelling of earthquake-induced soil liquefaction under free-field conditions and by considering soil-structure interaction. *Bulletin of Earthquake Engineering*. 2021;**19**(1):47-75. DOI: 10.1007/s10518-020-00972-3

- [15] Fasano G, De Sarno D, Bilotta E, Flora A. Design of horizontal drains for the mitigation of liquefaction risk. *Soils and Foundations*. 2019;**59**:1537-1551
- [16] Fioravante V, Giretti D, Airoidi S, Moglie J. Effects of seismic input, fine crust and existing structure on liquefaction from centrifuge model tests. *Bulletin of Earthquake Engineering*. 2021;**19**:3807-3833. DOI: 10.1007/s10518-021-01139-4
- [17] Giretti D, Fioravante V. Centrifuge modelling of vertical and horizontal drains to mitigate earthquake-induced liquefaction. *Geosciences*. 2023;**13**(6): 174. DOI: 10.3390/geosciences13060174
- [18] Kutter BL. Recent advances in centrifuge modelling of seismic shaking. In: *Proceedings of the 3rd International Conference on Recent Advances in Geotechnical Earthquake Engineering and Soil Dynamics*; April 2–7, 1995. Vol. II. Missouri: St. Louis; 1995. pp. 927-941
- [19] Scott RF. Solidification and consolidation of a liquefied sand column. *Soils and Foundations*. 1986;**26**:23-31
- [20] Liu L, Dobry R. Seismic response of shallow foundation on liquefiable sand. *Journal of Geotechnical and Geoenvironmental Engineering—ASCE*. 1997;**123**(6):557-567
- [21] Adamidis O, Madabhushi SPG. Experimental investigation of drainage during earthquake-induced liquefaction. *Géotechnique*. 2018;**68**:655-665. DOI: 10.1680/jgeot.16.P.090
- [22] Rathje HRM, Ronnie Kamai RS, Boulanger R. Centrifuge modelling of prefabricated vertical drains for liquefaction remediation. *Journal of Geotechnical and Geoenvironmental Engineering*. 2012;**138**:261-271
- [23] Rasouli R, Towhata I, Akima T. Experimental evaluation of drainage pipes as a mitigation against liquefaction induced settlement of structures. *Journal of Geotechnical and Geoenvironmental Engineering*. 2016;**142**:04016041
- [24] Garcia-Torres S, Madabhushi GSP. Performance of vertical drains in liquefaction mitigation under structures. *Bulletin of Earthquake Engineering*. 2019;**17**:5849-5866
- [25] Rollins KM, Oakesm C, Meserev T. Liquefaction mitigation potential do prefabricated vertical drains from large-scale laminar shear box testing. In: *Geotechnical Engineering in the XXI Century: Lessons Learned and Future Challanes*. Washington, DC, USA: IOS Press; 2019
- [26] Seed HB, Idriss IM. *Ground Motions and Soil Liquefaction during Earthquakes*. Oakland, Calif: Earthquake Engineering Research Institute Monograph; 1982
- [27] Robertson PK, Campanella RG. Liquefaction potential of sands using the cone penetration test. *Journal of Geotechnical Engineering Division, ASCE*. 1985;**22**(GT3):298-307
- [28] Youd TL, Idriss IM, Andrus RD, Arango I, Castro G, Christian JT, et al. Liquefaction resistance of soils: Summary report from the 1996 NCEER and 1998 NCEER/NSF workshops on evaluation of liquefaction resistance of soils. *Journal of Geotechnical and Geoenvironmental Engineering, ASCE*. 2001;**127**(10):817-833
- [29] Moss RES, Seed RB, Kayen RE, Stewart JP, Der Kiureghian A, Cetin KO. CPT-based probabilistic and deterministic assessment of in situ seismic soil liquefaction potential. *Journal of Geotechnical and*

Geoenvironmental Engineering—ASCE. 2006;**132**(8):1032-1051

[30] Idriss IM, Boulanger RW. Soil Liquefaction During Earthquakes. Oakland: Earthquake Engineering Research Institute. Oakland, CA: MNO-12; 2008. 244 p

[31] Robertson P. Evaluation of flow liquefaction and liquefied strength using the cone penetration test. *Journal of Geotechnical and Geoenvironmental Engineering*. 2010;**136**(6):842-853

[32] Bellotti R, Crippa V, Pedroni S, Ghionna VN. Saturation of sand specimen for calibration chamber tests. In: *Proc. ISOPT-1 Orlando*. Vol. 2. Rotterdam: A.A. Balkema; 1988. pp. 661-672

[33] Schmertmann JH. An updated correlation between relative density DR and Fugro-type electric cone bearing, qc. Contract report DACW 39-76 M 6646 WES, Vicksburg, Miss. 1976

[34] Carter JP, Yeung SK. Analysis of cylindrical cavity expansion in a strain weakening material. *Computers and Geotechnics*. 1985;**1**:161-180

[35] Carter JP, Booker JR, Yeung SK. Cavity expansion in cohesive frictional soils. *Géotechnique*. 1986;**36**(3):349-358

[36] Salgado R, Mitchell J, Jamiolkowski M. Cavity expansion and penetration resistance in sand. *Journal of Geotechnical and Geoenvironmental Engineering*. 1997;**123**(4):344-354

[37] Jefferies M, Been K. *Soil Liquefaction. A Critical State Approach*. London: Taylor and Francis; 2006

[38] Been K, Crooks JHA, Becker DE, Jefferies MG. The cone penetration test in sands: Part I, state parameter

interpretation. *Géotechnique*. 1986; **36**(2):239-249

[39] Fioravante V, Giretti D. Unidirectional cyclic resistance of Ticino and Toyoura sands from centrifuge cone penetration tests. *Acta Geotechnica*. 2016;**11**:953. DOI: 10.1007/s11440-015-0419-3

[40] Fioravante V, Giretti D. State parameter of sands from centrifuge cone penetration test. In: Thorel, Bretschneider, Blanc, Escoffier, editors. *Proceedings of the 3rd European Conference on Physical Modelling in Geotechnics Eurofuge 2016*; 1-3 June 2016. France: IFSTTAR Nantes; 2016. pp. 67-72. ISBN 978-2-85782-716-0

[41] Chandler RJ, Tosatti G. The Stava tailings dams failure, Italy, July 1985. In: *Proceedings of the Institution of Civil Engineers: Geotechnical Engineering*. Vol. 113. London: Institution of Civil Engineers; 1995. pp. 67-79

Comparison of Site Response Analysis (SRA) According to Ground Modelling and Structure Consideration

Haeam Kim

Abstract

When an earthquake occurs, the seismic motion is amplified as it passes through the ground layers. In addition, even for the same earthquake, the magnitude of the ground response on the ground surface varies depending on the ground condition. Determining the response within the ground following an earthquake is called site response analysis (SRA), and a general standard procedure is to perform site response analysis using the 1D (one-dimensional) wave propagation theory. However, in the case of one-dimensional site response analysis, complex topography, ground surface changes, and effects on structures are not included. Therefore, evaluating the reasonable ground response that may occur in the actual field is necessary. This article analyses ground amplification phenomena according to modelling differences through 2D (two-dimensional) and 3D (three-dimensional) modelling that can consider complex topography in addition to 1D. In addition, the nonlinear characteristics of the soil and the interaction between the soil and the structure were considered, and time history analysis was performed to identify the realistic dynamic behaviour characteristics of the soil and structure.

Keywords: site response analysis, free-field analysis, time-history analysis, finite element method, dynamic geotechnical analysis, numerical method, soil-structure interaction (SSI)

1. Introduction

The amplitude and frequency characteristics of seismic waves propagated through bedrock change depending on the characteristics of the ground they pass through until they reach the surface. In the case of vibration characteristics, it is affected by various causes such as earthquake magnitude, distance to the epicentre, duration, and site support characteristics.

When examining past earthquake records, despite the same earthquake, different seismic accelerations occurred on the ground surface where the structure was located depending on the ground conditions, and the extent of the resulting damage was also

different. Therefore, the dynamic response of a structure during an earthquake is determined by the composition of the ground supporting the structure. Therefore, Site Response Analysis (SRA), which analyzes the amplification in the ground when an earthquake occurs, is the first step and an essential factor in evaluating the stability of a structure caused by the earthquake.

The SRA is an important factor that determines the dynamic characteristics of a structure, and various studies have been conducted on the reliability of the analysis. In the early stage of the study, due to the limitation of computer performance, the reliability study of equivalent linear analysis with simple input variables and short analysis time was the main focus. A representative study verifies the recorded motion of the rock outcrop and ground surface free field of the Northridge earthquake that occurred in Los Angeles, USA [1]. However, recent studies are focused on the lack of reliability of the results of equivalent linear analysis when the complex ground layer shape and surface cannot be considered, and the shear strain is significant. Therefore, various methods have been studied to solve these disadvantages, and various analysis methods and software have been developed for this purpose.

In this article, the Hardening soil in small strain material model, which is a non-linear model that can more accurately consider the deformation of the soil, was applied. And the ground was modelled in 1D, 2D, and 3D to compare the ground response results according to modelling changes. In addition, the structure was modelled in 2D and 3D models that can consider the structure, and the results of the site response were compared.

2. Site response analysis (SRA)

Site Response Analysis, also called free-field analysis, refers to a method and process for obtaining the response within the ground to a given seismic input in the unexcavated ground state before the structure is built when the location to be constructed is determined (**Figure 1**) [2].

Generally, 1D equivalent linear analysis, which is relatively simpler than other analysis methods, is widely used for SRA. This assumes that all soil layers are elastic halfspace horizontal bodies without separately modelling the soil layer, so it is

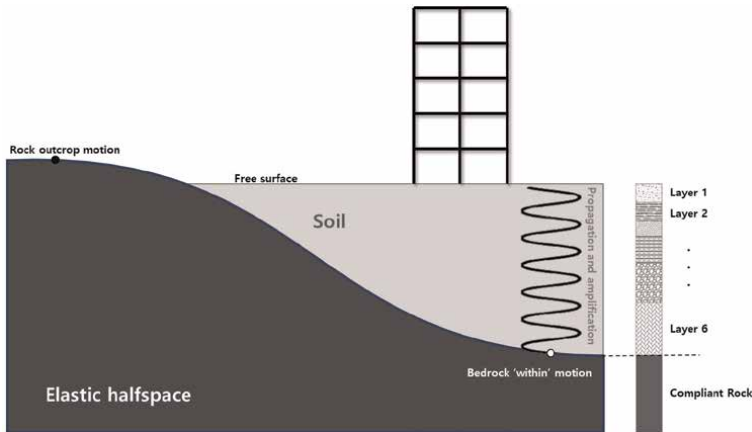


Figure 1.
Schematic representation of site response analysis.

assumed that the response of the ground is affected only by shear waves propagating vertically from the bedrock [3]. It can be expressed as the amplification function $A(\omega)$ when a shear wave is incident perpendicular to the fault elastic ground laid horizontally on the elastic rock halfspace.

$$A(\omega) = |H(\omega)| = \frac{|U(0, \omega)|}{|U(h_s, \omega)|} = \frac{1}{\left| \cos\left(\frac{\omega h_s}{V_s}\right) \right|} \geq 1 \quad (1)$$

Where $H(\omega)$ is the complex transfer function, $U(z, \omega)$ is the magnitude of horizontal displacement at depth, ω is angular frequency, h_s is the depth, and V_s is shear-wave velocity of the soil layer. For $\frac{\omega h_s}{V_s} = \frac{\pi}{2} + n\pi$, with $n = 0, 1, 2, 3 \dots$, the amplification function has a tendency to infinity, which means resonance. Here, when $n = 0$, ω is equal to the natural or fundamental frequency of the layer and is calculated as follows.

$$\omega_n = \frac{\pi V_s}{2h_s}, f_n = \frac{V_s}{4h_s} \quad (2)$$

The amplification function can be modified to account for the effect of energy dissipation in the soil. A straightforward approach is to assume that the material damping is viscous. Applying damping means that the displacement amplitude associated with the resonant frequency is no longer infinite, and Eq. (1) is modified by [2].

$$A^*(\omega) = |H^*(\omega)| = \frac{1}{\sqrt{\cos^2(k h_s) + (\xi k h_s)^2}} \quad (3)$$

where κ is the wave number and is the ξ damping ratio.

As mentioned above, in the case of 1D equivalent linear analysis, it is assumed that the ground is an elastic halfspace of horizontal material, so it cannot reasonably consider irregular strata or surface topography. In the case of a valley or basin ground shape with accumulated sediments, complex waves can be generated due to multiple refraction and reflection effects of seismic waves, leading to long-duration ground motions and high amplification [4]. Therefore, in this case, appropriate ground shapes should be considered through 2D and 3D model applications according to the site shape (Figure 2).

As such, 2D and 3D model evaluations must be performed to properly apply the irregular strata or topography of the actual site. However, going from one dimension

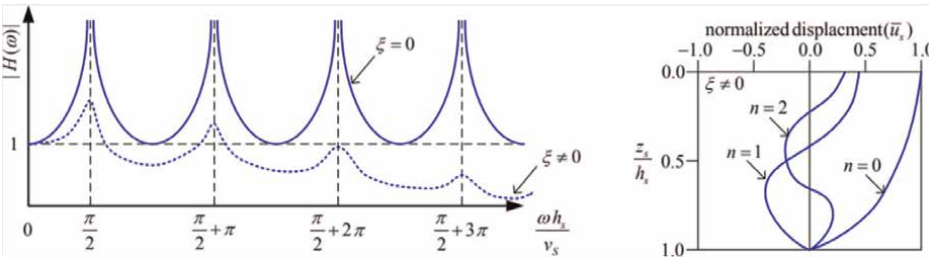


Figure 2.
 Complex transfer functions and mode shapes of fault soils on bedrock [5].

to the next involves several problems. First, it is impossible to construct a 2D shape that perfectly matches the dynamic motion of an actual 3D shape [6]. In addition, it is known that 2D models with the same dimensions and material properties generally overestimate the dynamic stiffness and radiation damping of soil due to geometric wave diffusion [2].

When a structure is built on soft ground, the seismic wave characteristics at the bottom of the foundation vary depending on the shape and characteristics of the structure. Therefore, the seismic behaviour of a structure built on soft ground also differs significantly from that built on bedrock [7].

3. Hardening soil (HS) model

Schanz et al. [8] designed the Hardening Soil (HS) model to reproduce basic soil macroscopic phenomena such as soil densification, stress-dependent stiffness, plastic yielding, etc. Unlike other models, such as the Cap model or the Modified Cam Clay (as well as the Mohr-Coulomb model), the magnitude of soil deformation can be more accurately modelled by incorporating three input stiffness parameters corresponding to the triaxial loading stiffness (E_{50}), the triaxial unloading-reloading stiffness (E_{ur}) and the oedometer loading factor (E_{oed}) (Figure 3) [9, 10].

4. Analysis conditions

For numerical analysis, PLAXIS software developed by Bentley Systems was used, and in the case of PLAXIS, various ground material models are loaded, enabling various deformation analyses of the ground. In addition, it is possible to simulate complex ground deformation, such as dynamic analysis by earthquake load.

This article studies the effect of ground amplification on modelling changes according to 1D, 2D, and 3D for the same ground condition during an earthquake. In addition, in 2D and 3D analysis, the effect of the structure on ground amplification is compared by applying the structure.

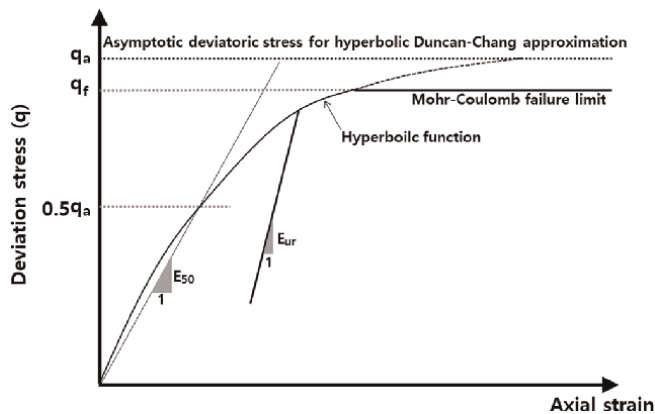


Figure 3.
Hyperbolic stress-strain relationship.

4.1 Element dimension

In dynamic analysis, an element's size is an important consideration. Unlike 1D modelling, which only considers height, 2D and 3D modelling must also consider width and depth. Discretizing the space is very important because the wave propagation in the continuum must be modelled in 2D or 3D. If the element size in the finite element analysis is too large, the results for high-frequency bands are inaccurate, and if the element size is too small, the results may appear unstable [11].

Therefore, to reduce this error, the maximum frequency transmitted by the analytical model can be estimated based on the largest element or zones within the slowest material, as shown in the following Eq. [6, 12].

$$\Delta l_{max} \leq \frac{\lambda_{min}}{10} \leq \frac{V_{s,min}}{10 f_{max}} \text{ or } f_{max} \leq \frac{V_{s,min}}{10 \Delta l_{max}} \quad (4)$$

where Δl_{max} is the maximum dimension of the element, λ the wavelength of the passing wave, V_s is the layer's shear-wave velocity and f_{max} is the maximum frequency of interest, which is typically around 10 to 15 Hz.

4.2 Boundary

Dynamic analysis using the finite element method, various ground boundary conditions can be applied. In particular, if the boundary conditions are not adequately established in the numerical analysis modelling process during dynamic analysis, correct results may not be derived because the input earthquake may be reflected from the modelling boundary conditions and may occur larger than the actual ground deformation due to the earthquake. Therefore, the boundary condition can be applied by dividing the bottom and side parts. The bottom part applied a compliant base (infinite boundary), and the side part was used with free-field conditions.

4.3 Input ground motions

Time-history analysis was applied for SRA, and determining the input seismic wave at this time is essential in securing the reliability of analysis and evaluation. Therefore, for seismic design, it is necessary to reflect the characteristics of the area where the structure is located and, at the same time, satisfy the design standards suitable for the level of the structure. However, in this analysis, since the effect on ground amplification is the main concern, Koyna and Nahanni earthquakes with different frequency characteristics were used to increase the reliability of the analysis (Figure 4).

The Koyna earthquake occurred in 1967 near Koynanagar town in Maharashtra, India. The magnitude 6.6 shock hit with a maximum Mercalli intensity of VIII. The Koyna earthquake is believed to be triggered by a fluid pressure change due to the reservoir's water percolation into the subsurface [13].

The Nahanni earthquake occurred in 1985 in the Nahanni region of the Northwest Territories, Canada. The magnitude 6.9 shock hit with a maximum Mercalli intensity of VI. The Nahanni earthquakes mainly occurred along fault planes, so fault activity is known as the leading cause of earthquakes [14].

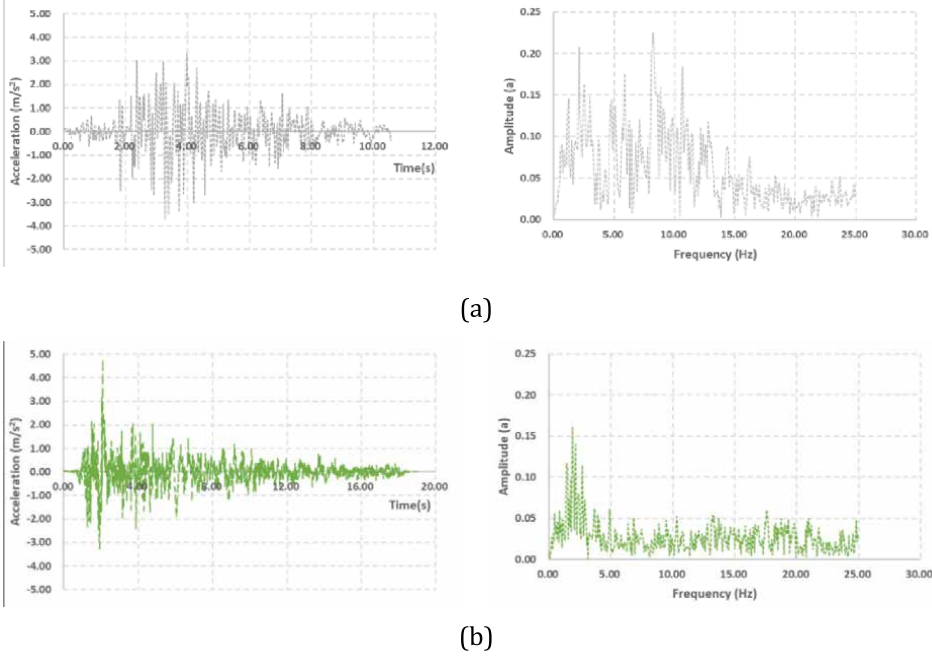


Figure 4.
Time history and fast Fourier transfer of (a) Koyna and (b) Nahanni earthquake record.

The Peak Ground Acceleration (PGA) of the Koyna earthquake recorded is 3.35 m/s^2 (0.34 g), and the characteristics of the frequency of the Koyna earthquake through the Fourier transform are confirmed to have frequency components in various intervals from 2.5 to 10 Hz. The PGA of the Nahanni earthquake recorded is 4.80 m/s^2 (0.49 g), and the frequency characteristics of 2.0 to 3.0 Hz are confirmed.

In the case of the Koyna earthquake, the PGA is lower than that of the Nahanni earthquake, but the frequency range is wide, and the shorter period characteristic is more significant than that of the Nahanni earthquake. In the case of the Nahanni earthquake, the PGA is significant, but the frequency is characterised by a long period. Through the characteristics of these different earthquakes, we tried to secure the reliability of the analysis by considering the effects of the other natural frequencies of the structure and the ground.

4.4 Damping

According to the Rayleigh damping formula, the damping matrix C is a linear sum of the mass matrix M and the stiffness matrix K as a function of the Rayleigh coefficients α and β .

$$[C] = \alpha[M] + \beta[K] \quad (5)$$

Here, α and β are proportional constants between mass and stiffness, and the relationship between the natural frequency and the damping ratio for the n th mode is as follows.

	ξ (%)	f_1 (or ω_1) (Hz)	f_2 (or ω_2) (Hz)	α	β
Structure	2.0	0.840	3.862	0.1734	0.0014
Soil	5.0	0.778	0.816	0.2502	0.0099

Table 1.
 Input value of Rayleigh damping.

$$\xi_n = \frac{1}{2} \left(\alpha \frac{1}{\omega_n} + \beta \omega_n \right) \quad (6)$$

If the damping ratios for the i th and j th modes, which are the two main modes, are ξ_i and ξ_j , α and β can obtain the following simultaneous equations.

$$\approx \begin{Bmatrix} \xi_i \\ \xi_j \end{Bmatrix} = \frac{1}{2} \begin{bmatrix} 1/\omega_i & \omega_i \\ 1/\omega_j & \omega_j \end{bmatrix} \begin{Bmatrix} \alpha \\ \beta \end{Bmatrix} \rightarrow \begin{Bmatrix} \alpha \\ \beta \end{Bmatrix} = \frac{2\omega_i\omega_j}{\omega_j^2 - \omega_i^2} \begin{bmatrix} \omega_j & -\omega_i \\ -1/\omega_j & 1/\omega_i \end{bmatrix} \begin{Bmatrix} \xi_i \\ \xi_j \end{Bmatrix} \quad (7)$$

Such damping is called Rayleigh damping, and the damping matrix at this time is called a Rayleigh damping matrix or a proportional damping matrix.

In applying Rayleigh damping, it is important to note that the two modes (i th and j th modes) must be properly calculated to guarantee a reasonable damping ratio for all vibration modes contributing to the response (**Table 1**).

	Set1 (limestone)	Set2 (sand)	Set3 (clay)	Set4 (sand)	Set5 (silt)	Set6 (fill)
E_{50}^{ref} (kN/m ²) Secant stiffness in standard drained triaxial test	190,000	75,000	15,000	8500	8500	10,000
E_{oed}^{ref} (kN/m ²) Tangent stiffness for primary oedometer loading	190,000	75,000	15,000	6150	6000	10,000
E_{ur}^{ref} (kN/m ²) Unloading/reloading stiffness	575,000	300,000	50,000	25,750	23,000	30,000
M (–) Power for stress-level dependency stiffness	0.3	0.55	0.7	0.7	0.9	0.5
c' (kN/m ²) Cohesion	200	1	25	6	30	10
ϕ' (°) Friction angle	35	38	20	28	32	25
ψ' (°) Dilatancy angle	0	6	0	6	10	0
ν_{ur} (–) Poisson's ratio for unloading/ reloading	0.2	0.2	0.15	0.29	0.3	0.2
K_0^{NC} (–) K_0 -value for normal consolidation	0.43	0.38	0.66	0.8	0.8	0.58

	Set1 (limestone)	Set2 (sand)	Set3 (clay)	Set4 (sand)	Set5 (silt)	Set6 (fill)
G_0^{ref} (kN/m ²) Reference value of the shear strain	1,000,000	281,250	90,000	59,883	53,076	50,000
$\gamma_{0.7}$ (-) Shear strain at which $G_s = 0.722G_0$	0.00005	0.0002	0.00025	0.0003	0.003	0.0002
γ (kN/m ³) Soil unit weight	23.0	19.0	19.0	18.5	18.5	20.0
E_s (kN/m ²) Soil Elastic modulus	1,040,000	277,000	151,400	150,900	139,100	89,480

Table 2.
Soil model parameters for hardening soil model with small strain [16].

4.5 Materials

In the case of soil material models, the most widely used model is the Mohr-Coulomb (MC) failure model. Numerical analysis is also widely used because the input parameters are more straightforward than other material models [15]. Therefore, the MC model is suitable for failure with large shear deformation during the collapse and is mainly used for stability analysis of dams, slopes, embankments, and shallow foundations [14]. However, in the case of the MC model, it is not easy to reasonably reflect other ground behaviour conditions during loading and unloading.

The Hardening Soil model was developed to more accurately reflect the ground behaviour by supplementing the disadvantages of the MC model. Among them, in the case of Hardening Soil in Small Strain, accurate simulation is possible in evaluating ground amplification caused by earthquakes (**Table 2**).

The structure was concrete, and a linear material model was used (**Table 3**).

In **Figure 5**, the shear-wave velocity according to each layer of the ground is to be evaluated, and the average shear-wave velocity of the entire ground can be confirmed. This soil profile belongs to site class ‘D’ as per the classification of ASCE/SEI 7-10 (**Figure 6**) [18].

The following is figure about the ground and structures applied to 2D and 3D numerical analysis. The 2D model is mainly used as a plane stress or plane strain model and has the advantage of less analysis time and fewer errors because it is simpler than 3D modelling. However, since the 2D model can be applied only when the evaluation target satisfies the model conditions, 3D model analysis is often required to evaluate the actual site’s response accurately.

	Foundation	Column	Wall
E (kN/m ²)/Elastic modulus	35.16×10^6 (35,160 MPa)		
γ (kN/m ³)/Unit weight	25.0		
ν (-)/Poisson’s ratio	0.2		
A (m ²)/Area	0.75	0.28	0.30

Table 3.
Structure material parameters.

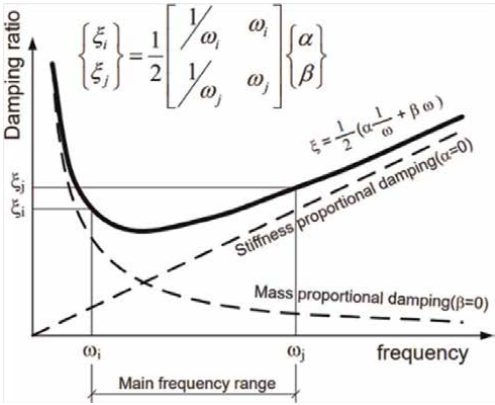


Figure 5.
Rayleigh damping [4].

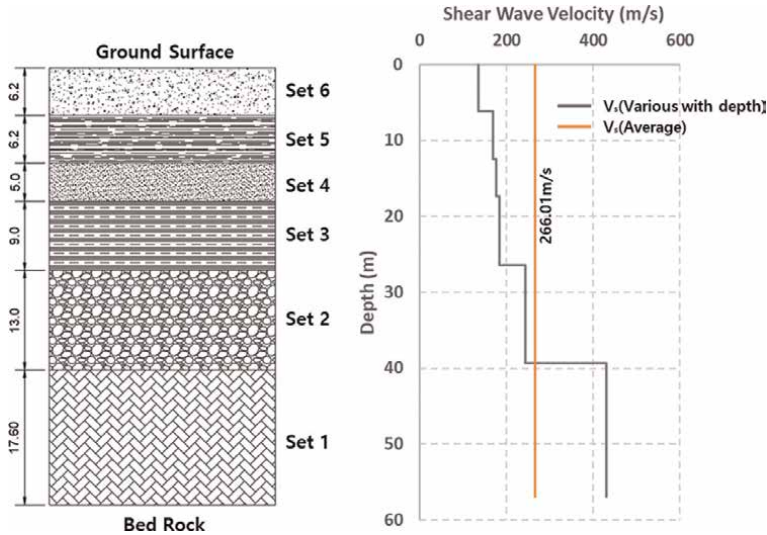


Figure 6.
Soil and shear-wave velocity profiles [17].

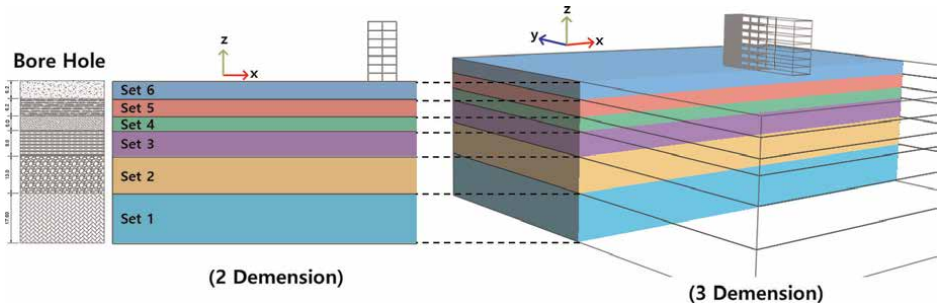


Figure 7.
Ground layer information in 2D and 3D analysis models.

To maintain the same conditions as possible with the 2D model during 3D modelling, the aspect ratio of the structure was set to 1:4. When applying an X-direction earthquake, it was modelled to behave in one direction like the 2D analysis (Figure 7).

4.6 Case study

In this article, the analysis is modelled in 1D, 2D and 3D to check the effect of ground amplification according to dimension. Therefore, modelling was conducted for each dimension to confirm this effect, and a sufficient distance was placed in the evaluation area to minimise the effect of boundary conditions (Figure 8).

In addition, an evaluation considering the structure was performed to find out the effect of the structure on the site response amplification (Figure 9).

5. Results

When an earthquake occurs, dynamic motion amplifies depending on the ground, and even for the same earthquake, the magnitude of the ground response on the surface varies depending on the consist of the ground. In this article, 2D and 3D modelling, including a basic 1D model, was performed for the same ground to simulate such ground conditions, and an analysis of ground dynamic motion amplification was conducted using PLAXIS software. In addition, modelling a structure in the centre of the ground, an analysis of the amplification change of the ground dynamic motion was also conducted when the structure was considered.

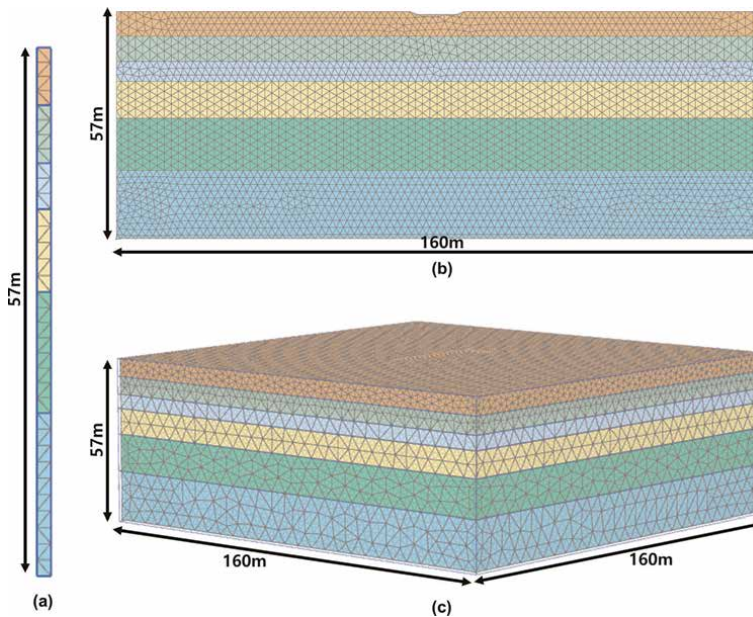


Figure 8.
Finite element analysis mesh without structure (a) 1D, (b) 2D, and (c) 3D [18].

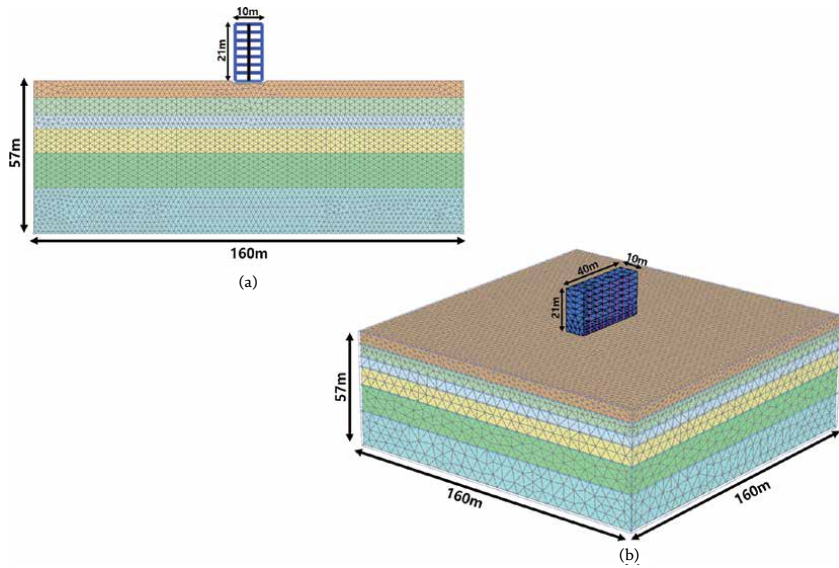


Figure 9.
Finite element analysis mesh with structure (a) 2D and (b) 3D.

5.1 Site response result according to modelling dimension

The following results from peak ground response acceleration in each stratum according to the difference between 1D, 2D, and 3D models. As a result of the analysis showed very similar peak acceleration results for both Koyna and Nahanni earthquakes in 1D and 2D models. However, in the case of the 3D model, a difference of up to 24% occurred in the case of the Koyna earthquake, and a difference in maximum acceleration

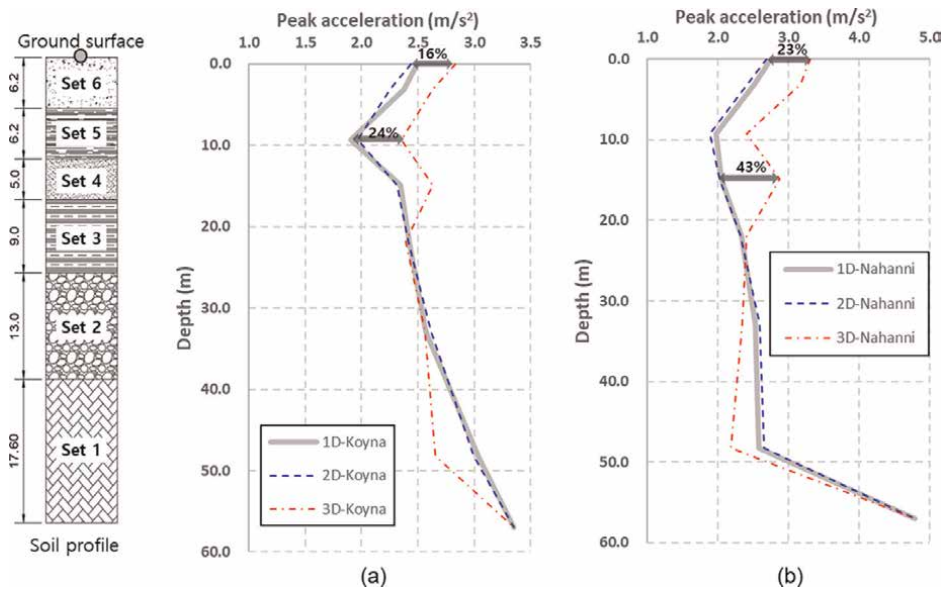


Figure 10.
Peak acceleration results of each dimension by the depth (a) Koyna and (b) Nahanni.

of 16% appeared on the surface. In addition, Nahanni earthquake results also showed a difference in peak acceleration of up to 43% and 23% on the surface (**Figure 10**).

As a result of 1D, 2D, and 3D analysis, the maximum acceleration occurred at the bottom level (–)57.0 m, which is Limestone (Set 1) for both Koyna and Nahanni seismic waves. In general, peak acceleration up to Sand (Set 4) tends to decrease, and then it tends to increase up to the ground surface.

In the soil profile applied to this analysis, the maximum acceleration occurs at the point where the earthquake is input, and no section amplified than the maximum acceleration of the input earthquake is generated within the soil.

For the ground surface, which is the location where the structure is installed and is the most important in ground response, the acceleration according to the time and response spectrum was also reviewed, and the change in peak acceleration according to the periods was also examined.

In the response spectrum results, the 3D model results showed a slightly different tendency from the rest of the analysis results. Overall, a higher response acceleration occurred in the 3D model results over the entire period.

As a result of the response spectrum, the maximum acceleration occurred when the period of the structure was 0.51 sec (1.96 Hz) in the Koyna earthquake, and the maximum difference in the magnitude of the acceleration occurred by 44%. In the Nahanni earthquake, when the period of the structure was 0.55 seconds (1.82 Hz), the magnitude of the acceleration showed a difference of up to 31% (**Figure 11**).

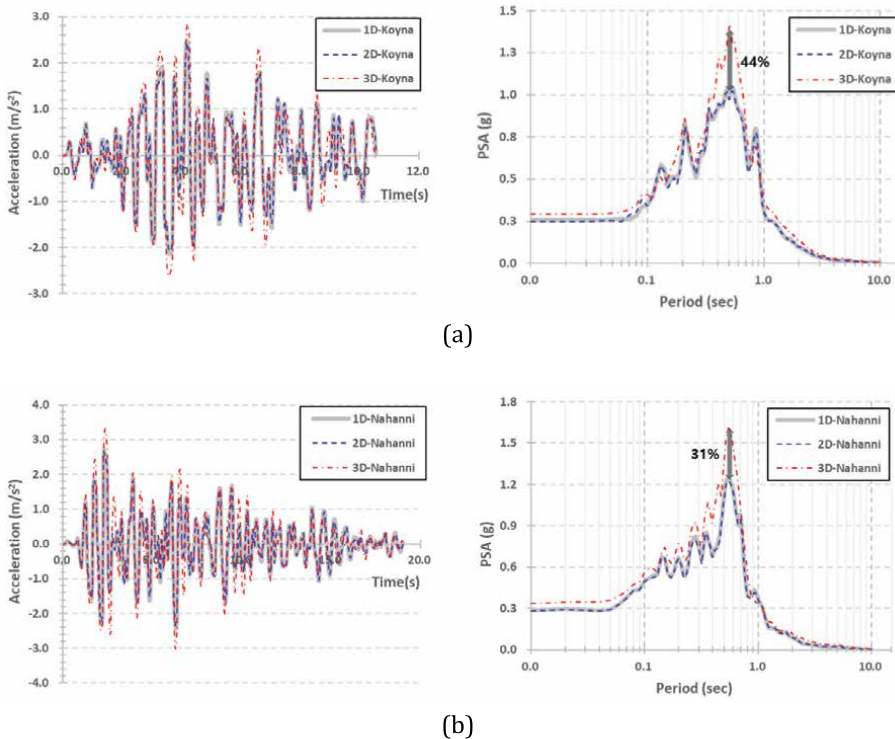


Figure 11.

Acceleration according to time and response spectrum results (a) Koyna and (b) Nahanni.

5.2 Site response change according to structure consideration

In the 2D model, ground amplification results according to the consideration of the structure resulted in a maximum amplification difference of 12% and 22%, respectively, in the case of maximum acceleration in the two earthquakes. In the case of the Koyna earthquake, the maximum acceleration at the surface was 2% depending on the presence or absence of structures, and the difference in amplification was not significant, but in the case of the Nahanni earthquake, a substantial difference of 22%

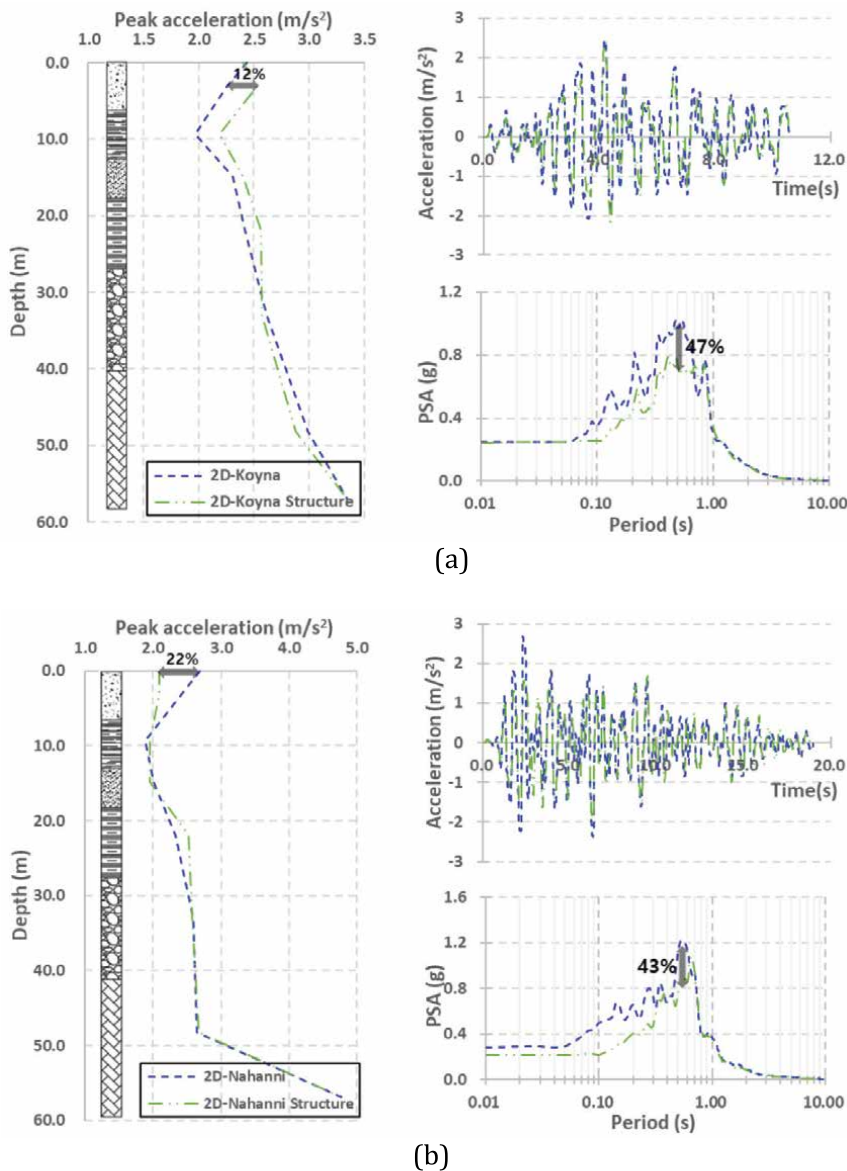


Figure 12.
Peak acceleration by depth, acceleration according to time and response spectrum results in the 2D model with or without structure (a) Koyna and (b) Nahanni.

occurred. In addition, the acceleration results tendency according to the surface's time was similar for both earthquakes.

However, in the case of response acceleration according to the period in the surface layer, the maximum response acceleration when applied to structures was reduced by 47% in the case of the Koyna earthquake and by 43% in the case of the Nahanni earthquake (**Figure 12**).

In the 3D model, the result of ground amplification according to the consideration of the structure showed that both earthquakes had the maximum acceleration difference in the ground surface and were amplified by 10 and 17%, respectively, when the structure was considered. In the 2D results, the maximum acceleration of the surface

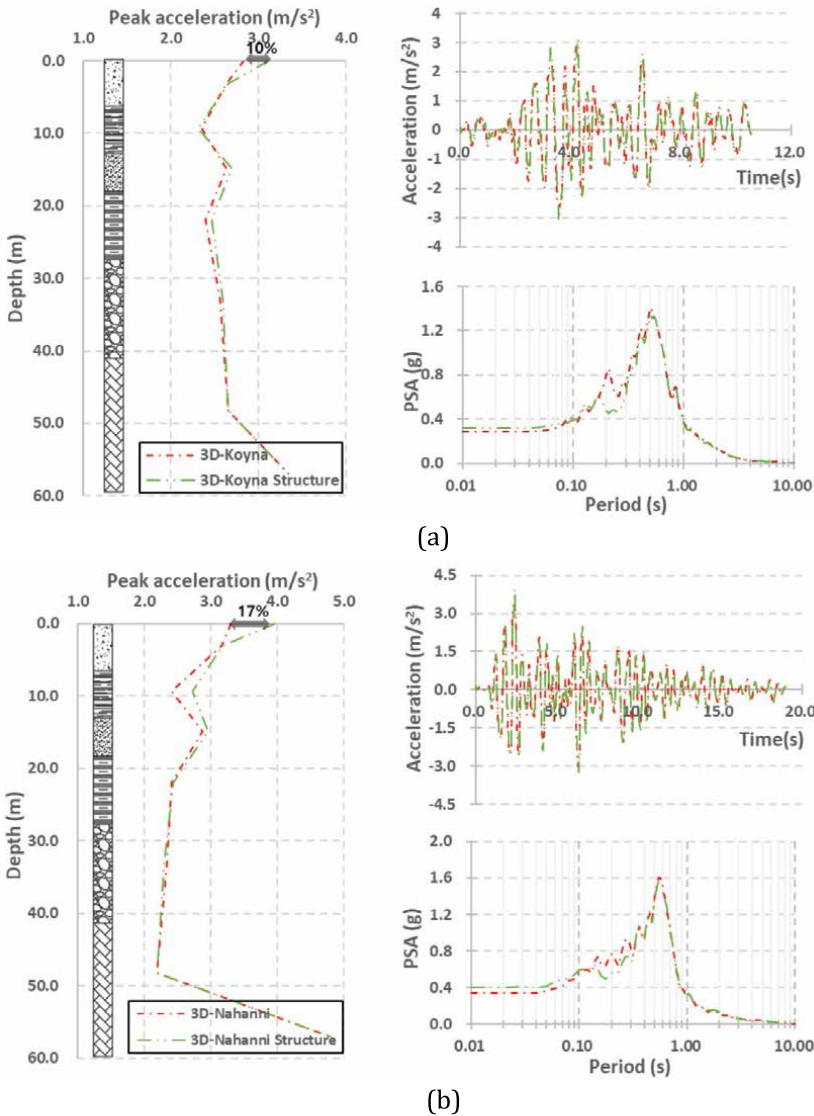


Figure 13. Peak acceleration by depth, acceleration according to time and response spectrum results in the 3D model with or without structure (a) Koyna and (b) Nahanni.

when the structure was considered was smaller than when the structure was not considered. The acceleration results over time showed similar trends for both earthquakes regardless of whether structures were considered. Despite the significant difference in the maximum response acceleration according to the period in the surface layer, the maximum response acceleration decreased by 5% in the Koyna earthquake and only 2% in the Nahanni earthquake when the structure was installed (**Figure 13**).

The following results from the shear stress-strain for each earthquake according to depth. Since the closer to the ground surface, the greater the effect of the structure, the shear stress-strain result also showed a more significant difference in the result with or without structure the closer to the ground surface.

In the case of the Koyna earthquake, a more considerable shear strain occurred than the result of the Nahanni earthquake. Depending on the depth, a difference in shear strain of up to about 10 times occurred, and a significant decrease in shear stiffness was confirmed in the Koyna results compared to Nahanni earthquake (**Figure 14**).

In the case of the Koyna earthquake, it is possible to check the strain hardening section due to the generation of max shear strain greater than that of the Nahanni earthquake. In addition, the difference in ground acceleration according to with or without the structure is considered to occur more in Nahanni than in the Koyna earthquake. However, shear strain showed a more significant difference in Koyna than in Nahanni.

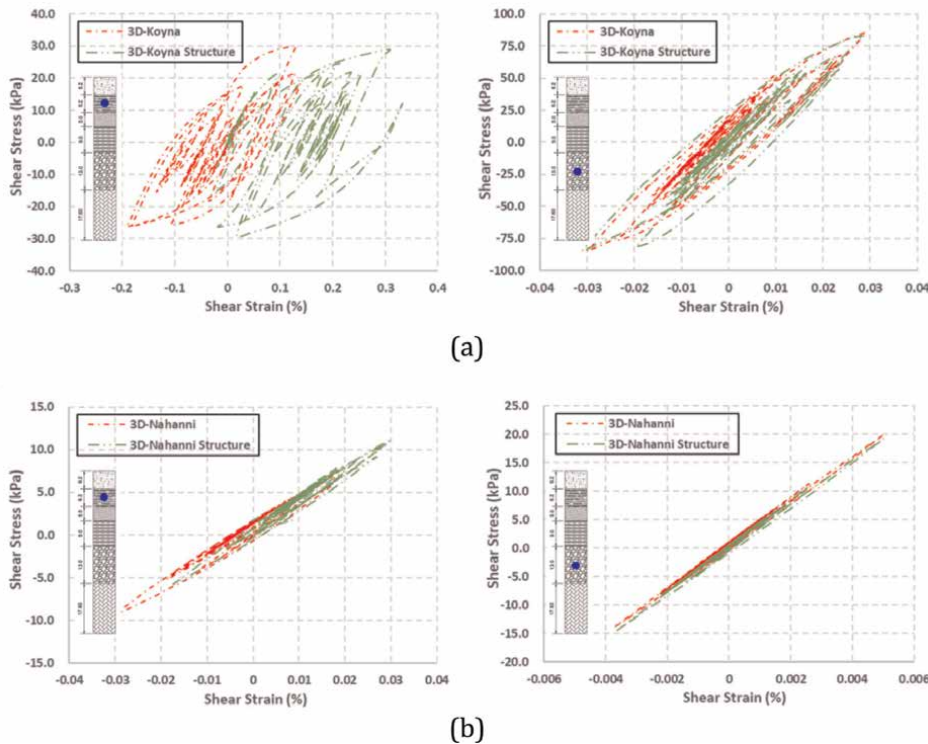


Figure 14.
Depending on the depth, the shear stress-strain hysteresis curve of results in the 3D model with or without structure (a) Koyna and (b) Nahanni.

That is, even in the same soil condition, the peak acceleration and shear strain occurring in the ground can vary greatly depending on the characteristics of the earthquake.

6. Conclusions

Ground amplification during an earthquake must be identified to determine the design response spectrum, liquefaction evaluation, and seismic load applied to the structure required for the seismic design of the structure. And since SRA is essential to predict this, it can be said that securing the reliability of the analysis is the most important thing.

Therefore, SRA was performed under several conditions in this article, and the following conclusions were obtained.

1. Regarding site response analysis considering only the ground, a significant difference occurred in the 3D analysis result from other results. In 1D and 2D models, vibration occurs only in the X direction, when is the direction in which the earthquake is applied, but in 3D analysis, vibration occurs in the Y direction even if the direction of the earthquake is in the X direction. In addition, SRA using a 3D model requires additional boundary conditions than other models, and since the Rayleigh damping value changes according to the range of the frequency during nonlinear analysis, it is judged that these differences gather and cause a large difference in the result value.
2. In the SRA considering the structure, if the vibration occurs due to the earthquake, inertial force is generated in the structure due to these vibrations. The forces transmitted to the structure in this way are dissipated through the foundation ground again in wave energy. In this analysis result, a significant difference in acceleration amplification was shown depending on whether or not a structure was considered in the response spectrum result of the 2D. In addition, it was found that the characteristics of the response spectrum showed an amplification effect in the low-frequency band compared to the case where the interaction between the ground and the structure was considered. In other words, when the structure was not considered, the ground amplified significantly.
3. Different results from the peak acceleration result were shown in the case of the shear strain occurring in the ground. In the case of the maximum ground acceleration, depending on whether or not the structure was considered, a larger difference occurred in the Nahanni than in the Koyna earthquake, but in the case of shear strain, on the contrary, a large difference was shown in the Koyna earthquake. Therefore, it is necessary to analyse the response amplification of the ground considering various earthquake records.


In conclusion, a larger acceleration amplification occurred when the 3D model was used than other results. Therefore, in the case of SRA using a 3D model, additional analysis of factors that can affect the response results, such as boundary conditions and Rayleigh damping, is required to analyse the differences from other analysis models.

Author details

Haeam Kim
University of Tasmania, Hobart, Tasmania, Australia

*Address all correspondence to: invirus@naver.com

IntechOpen

© 2023 The Author(s). Licensee IntechOpen. This chapter is distributed under the terms of the Creative Commons Attribution License (<http://creativecommons.org/licenses/by/3.0>), which permits unrestricted use, distribution, and reproduction in any medium, provided the original work is properly cited. 

References

- [1] Idriss IM. Assessment of Site Response Analysis Procedures. U.S Department of Commerce. NIST GCR 95-667; 2000
- [2] Wolf JP. Dynamic Soil-Structure Interaction. United States: Prentice Hall; 1985
- [3] Kramer SL. Geotechnical Earthquake Engineering. United States: Prentice Hall; 1996
- [4] Kuhlemeyer RL, Lysmer J. Finite element method accuracy for wave propagation problems. *Journal of the Soil Mechanics and Foundations Division*. 1973;**99**(SM5):421-427
- [5] Kim DK. Dynamics structures. South Korea: Goomibook; 2013
- [6] Volpini C, Douglas J, Nielsen AH. Guidance on conducting 2D linear viscoelastic site response analysis using a finite element code. *Journal of Earthquake Engineering*. 2019;**25**(4): 1-18. DOI: 10.1080/13632469.2019.1568931
- [7] Rizos DC, Stehmeyer EH. Simplified seismic analysis of soil-foundationstructure systems including soil-structure interaction effects. In: 13th World Conference on Earthquake Engineering. Canada. 2004
- [8] Schanz T, Vermeer P, Bonier P. Formulation and verification of the Hardening Soil model. In: *Beyond 2000 in Computational Geotechnics*. 1999
- [9] Obrzud RF, Truty A. The Hardening Soil Model: A Practical Guidebook. Switzerland: Zace Services; 2010
- [10] Obrzud RF. On the Use of the Hardening Soil Small Strain Model in Geotechnical Practice. Switzerland: Elmeppress International; 2010
- [11] Saenger EH, Gold N, Shapiro SA. Modeling the propagation of elastic waves using a modified finite-difference grid. *Wave Motion*. 2000;**31**(1):77-92
- [12] Flores Lopez FA, Ayes Zamudio JC, Vargas Moreno CO, Vázquez Vázquez A. Site response analysis (SRA): A practical comparison among different dimensional approaches. In: 15th Pan-American Conference on Soil Mechanics and Geotechnical Engineering. Mexico. 2015. DOI: 10.3233/978-1-61499-603-3-1041
- [13] Das D, Mallik J. Koyna earthquakes: A review of the mechanisms of reservoir-triggered seismicity and slip tendency analysis of subsurface faults. *Acta Geophysica*. 2020;**68**:1097-1112
- [14] Rock and Roll in the N.W.T. The 1985 Nahanni Earthquakes [Internet]. 2021. Available from: <https://www.earthquakescanada.nrcan.gc.ca/historic-historique/events/19851223-en.php> [Accessed: August 31, 2023]
- [15] Semet ÇELİK. Comparison of Mohr-coulomb and hardening soil models' numerical estimation of ground surface settlement caused by Tunneling. İğdir Üniversitesi Fen Bilimleri Enstitüsü Dergisi. / Igdir University Journal of the Institute of Science and Technology. 2017;**7**(4):95-102. DOI: 10.21597/jist.2017.202
- [16] Zhao C, Schmuddeh C, Barciaga T, Rochter L. Response of building to shallow tunnel excavation in different types of soil. *Computers and Geotechnics*. 2019;**2019**:4. DOI: 10.1016/j.compgeo.2019.103165
- [17] Nautiyal P, Raj D, Bharathi M, Dubey R. Ground response analysis:

Comparison of Site Response Analysis (SRA) According to Ground Modelling and Structure...
DOI: <http://dx.doi.org/10.5772/intechopen.1002922>

Comparison of 1D, 2D and 3D approach.
Singapore: Springer; May 2021. DOI:
10.1007/978-981-33-6564-3_51

[18] American Society of Civil
Engineers. Minimum Design Loads for
Buildings and Other Structures.
American Society of Civil Engineers
(ASCE); 2010

Generation of Site-Dependent Earthquake Ground Motion Parameters

Prem Nath Maskey

Abstract

The Kathmandu Valley, with many monumental and heritage structures, lies in a zone of high seismic risk. The neo-tectonic activities in the Himalayan region and the unconsolidated soil sediment are the major reasons for the high intensities of the ground motion in the valley. The conservation of the monument zones against the possible future earthquakes has been an issue of global concern. A probabilistic method to simulate the seismic ground motion parameters specific to sites lying in earthquake-prone region with a limited earthquake records is presented. Seismic hazard curves indicating the seismicity of a site is developed, risk consistent spectral shapes and corresponding power spectral density functions are obtained using empirical relationships, and ground acceleration time histories are simulated using Monte Carlo technique. One dimensional wave propagation analysis, with consideration of both linear and nonlinear behaviors of soils, is carried out to obtain the free field ground motion and the input response spectra for the structures. The method is illustrated by determination of site-specific seismic ground motion of three Bhaktapur city sites in the Kathmandu Valley. The significant influence of linear or nonlinear behavior of soil in the free field ground motion is observed in the monument zones.

Keywords: ground motion time histories, power spectral density functions, response spectrum, seismic hazard curve, wave propagation analysis

1. Introduction

Seismic response analysis of structures at a site is an essential step toward the earthquake risk mitigation. Apart from the determination of seismic hazard potential of the site, the ground motion parameters specific to the site are required for the analysis of the structures in the site. These values for a site depend on the earthquake source mechanism, geologic path from source-to-site, and soil sediment properties of the site. Most of the regions in developing countries are characterized by a long history of earthquakes but with the lack of adequate earthquake records.

The prevalent codes may give some features of design earthquake value for a site facilitating the general design process, but mere such codal values may not represent the realistic ground motion characteristics specific to the site. A realistic ground motion representation for a specific site may be considerably different from the values stipulated in the codes, which are basically developed for general purpose of design and applicable for a large region or zone. The development of ground motion parameters specific to a site in a probabilistic format could result into an improved method of design. A region with varying soil sediment characteristics may have to be microzoned with different possible ground motion at the free field.

The site-dependent earthquake ground motion for seismic input may be in the form of time histories, power spectral density, or response spectra. In the absence of enough earthquake records for a site, generation of such earthquake ground motions is the best alternative. The simulation of ground motion time histories for a specific region plays a vital role in generation of a realistic ground motion representation for a site.

Many researches have been carried out and results are available in the literature on generation of ground motion parameters based on the earthquake records. Tan [1] obtained response spectra from a set of simulated acceleration time histories generated based on evolutionary power spectrum, using 159 strong-motion records in Taiwan. A simulation technique for strong ground motion based on seismic hazard analysis for the Philippines was presented by Torregosa et al. [2]; using the database for historical earthquake occurrences from 1907 to 1998, ground motion time histories for major cities of Philippines were developed. Barranco-cicilia and Silva-ballesteros [3] developed a methodology to obtain ground motion time histories matching response spectra of seismic zones of Mexico City and compared with the real earthquake recorded in 1985. Ishii et al. [4] proposed a methodology for simulation of earthquake ground motion, for probabilistic risk assessment of structures, characterized by the parameters in terms of Peak ground acceleration, acceleration response spectra, and ground motion duration. Most of the researches carried out on generation of ground motion and reported in the literature are based on the historical earthquake records. The researches on ground motion applicable to regions with scanty or no earthquake records is not many.

In view of need to generate ground motion due to possible earthquakes in future specific to a region characterized by a long history of earthquake but with a limited record, a probabilistic method to simulate the ground motion is presented. In the method, probabilistic seismic hazard analysis is carried out to obtain the hazard curve, indicating the seismic hazard potential of a site. The hazard analysis is extended to determine the risk-consistent response spectra at the bedrock level using empirical relationship of spectral ordinate with earthquake magnitude and source-to-site distance. Risk-consistent acceleration time history is simulated from the power spectral density function based on the spectral shapes at the bedrock level. One-dimensional wave propagation analysis is carried out to estimate the soil sediment effect at the site for linear, as well as nonlinear conditions. Free field hazard curves and the ground motion parameters, especially the risk-consistent response spectra are obtained considering the soil amplification.

The proposed method is numerically illustrated by its application in generation of earthquake-induced ground motions for sites of Bhaktapur city, representing a typical area of Kathmandu Valley.

2. Probabilistic seismic hazard analysis

A probabilistic seismic hazard analysis is carried out to identify the seismic hazard potential of a site of interest. A seismic hazard curve, representing a relation between the seismic intensity parameter in terms of peak ground acceleration (PGA) and its annual probability of exceedance, can be used as basic information in estimation of seismic force on structures of the site of interest. The seismic hazard curve is obtained following the procedure outlined by Cornell [5] and Der Kiureghian and Ang [6]. The annual occurrence rate of the intensity parameter 'A' (PGA) exceeding a specified value 'a' for a particular site is obtained by

$$\nu(A \geq a) = \sum_k \nu_K \sum_j \sum_i P(A \geq a | m_i, r_j) P_K(m_i) P_K(r_j) \quad (1)$$

Where $P_K(m_i)$ and $P_K(r_j)$ represent the probability mass function of magnitude and distance from site to earthquake sources at the k^{th} zone, respectively. ν_K is the annual occurrence rate of earthquakes in the zone k . $P(A \geq a | m_i, r_j)$ is the conditional probability of 'A' exceeding 'a' given m_i and r_j .

The events of earthquake occurrence are assumed to be independent of each other in time and space, that is, Poisson's process, and accordingly, the annual probability of exceedance is obtained by the relation

$$P(A \geq a) = 1 - \exp \{-\nu(A \geq a)\} \quad (2)$$

Since the probability of occurrence of earthquakes of large magnitudes is very low, the distribution function for magnitude of earthquake is assumed to be a simple exponential distribution. The mean annual rate of exceedance of magnitude m is given by

$$\lambda_m = 10^{a-bm} = \exp(\alpha - \beta m) \quad (3)$$

Where 10^a is the mean yearly number of earthquakes greater than or equal to zero, and b describes the relative likelihood of large or small earthquakes. The probability density function (PDF) of the magnitude of earthquake is obtained by

$$P_M(m) = \beta e^{-\beta(m-m_0)} \quad (4)$$

In which, $\beta = 2.303b$ and m_0 is the lower threshold magnitude of earthquake, earthquakes smaller than which are eliminated, and m is the magnitude of earthquake.

3. Extended hazard analysis

The risk-consistent response spectrum at the site of interest is developed for given interval of seismic intensity parameter for the purpose of seismic input values for response analysis of structures. Peak ground acceleration (PGA) is adopted as the seismic intensity parameter to obtain the risk-consistent response spectra, as was considered in the development of seismic hazard curve.

The risk-consistent response spectrum at the bedrock is obtained by an empirical relationship, which relates the normalized ordinates of response spectrum with the

magnitude of earthquake and the source-to-site distance. The typical empirical attenuation equation of the spectral acceleration for the evaluation of spectral shape given by Takemura et al. [7] is:

$$\ln S_a(T) = a(T)M - b(T)\ln X + c(T) \quad (5)$$

in which, $S_a(T)$ is the spectral acceleration at bedrock in cm/s^2 , M is the magnitude of earthquake, X is the source-to-site distance in km, T is the time period in second, and $a(T)$, $b(T)$ and $c(T)$ are coefficients that are determined by regression analysis of earthquake motions and are given in the form of curves as shown in **Figure 1**. These values are valid for normalized response spectrum corrected to 2% damping.

The probabilistic estimation of the response spectra of ground motion is done by expanding the method to evaluate seismic hazard as described in Section 2. In the method, it is assumed that a normalized response spectrum normalized by its maximum acceleration $S_N(T)$ value is an empirically determined function of magnitude M and distance R (epicentral or hypocentral), and, as a second-order approximation that it is a log-normally distributed random variable. Accordingly,

$$S_N^* = \ln S_N(T) = \ln S_N(M, R, T) \quad (6)$$

in which, T represents the natural period.

The conditional probability mass function of magnitude and distance given that the intensity parameter A (PGA in the case) is between a_1 and a_2 due to an earthquake event in the k^{th} zone, denoted by $P_k(m_i, r_j / a_1 < A \leq a_2)$ is given by

$$\begin{aligned} P_k(m_i, r_j / a_1 < A \leq a_2) &= \frac{P(a_1 < A \leq a_2 / m_i, r_j) P_k(m_i) P_k(r_j)}{P_k(a_1 < A \leq a_2)} \\ &= \frac{P(a_1 < A \leq a_2 / m_i, r_j) P_k(m_i) P_k(r_j)}{\sum_j \sum_i P(A \geq a | m_i, r_j) P_k(m_i) P_k(r_j)} \end{aligned} \quad (7)$$

in which, $P_k(m_i)$ and $P_k(r_j)$ represent the probability mass functions of magnitude and distance from source-to-site distance at the k^{th} zone, respectively. The conditional mean value of the natural logarithm of response spectrum for the k^{th} zone is given by:

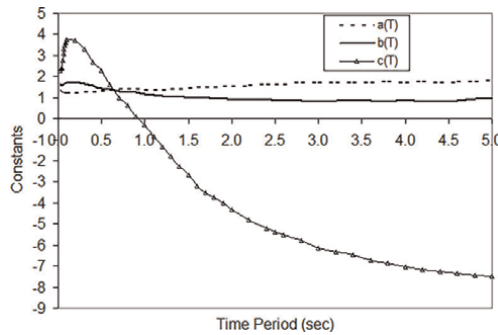


Figure 1.
Variation of constants with time period.

$$\begin{aligned}\bar{S}_{NK}^* &= E_k \{S_N^*(T) | a_1 < A \leq a_2\} \\ &= \sum_j \sum_i S_N^*(m_i, r_j, T) P_k(m_i, r_j | a_1 < A \leq a_2)\end{aligned}\quad (8)$$

The conditional mean value, considering all seismic zones, is given by:

$$\begin{aligned}\bar{S}_N(T) &= E \{S_N^*(T) | a_1 < A \leq a_2\} \\ &= \sum_j \sum_i S_N^*(m_i, r_j, T) P_k(m_i, r_j | a_1 < A \leq a_2)\end{aligned}\quad (9)$$

Where ν_k represents the annual occurrence rate of earthquake in the k -th zone.

4. Power spectral density function of ground motion

A power spectral density function (PSDF) is obtained from the response spectrum using an empirical relationship derived by various investigators. Der Kiureghian [6] has proposed the following relationship to obtain the PSDF, which is adapted in the present method.

$$S_b(\omega) = \frac{\omega^{(p+2)}}{\omega^p + \omega_f^p} \left[\frac{2\xi\omega}{\pi} + \frac{4}{\pi\tau} \right] \left[\frac{D(\omega, \xi)}{p_s(\omega)_0} \right]^2, \omega \geq 0 \quad (10)$$

in which, ω is frequency in radians per second, τ is the duration of earthquake shaking and is taken as 15 sec, $p_s(\omega)_0$ is the peak factor of white noise, and ω_f and p are two constants, which can be obtained by iteration procedure. In the present study, the values ω_f and p are taken as 0.705 and 3.0 as suggested by Der Kiureghian [6]. $D(\omega, \xi)$ is the ordinate of the risk-consistent response spectrum for displacement, and $S_b(\omega)$ is the PSDF of acceleration. The relationship given by Eq. 10 is ideally suited if the process is relatively broad-banded. If the process is narrow-banded, then suitable values of ω_f and p are to be obtained by iteration procedure and the method of spectral analysis no more remains attractive.

5. Simulation of ground motion time history

In general, the earthquake ground motions for a site are generated based on the seismic ground motion characteristics provided from real earthquake records. It has been well recognized that in the absence of adequate earthquake records and paucity of such records generation of earthquake-induced ground motion time histories compatible with an elastic response spectrum, such as stipulated in practical codes, will be an acceptable procedure.

Considering the strongest earthquake ground motion as a stationary zero-mean random process with Gaussian distribution, and being expressed by a spectral density function $S_b(\omega)$, sample ground acceleration time histories $\ddot{v}_g(t)$ are obtained by using the spectral representation method proposed by Shinozuka and Deodatis [8]. The strong ground motion, in this method, is considered of a series of harmonic components, having deterministic amplitudes and random phase angles:

$$\ddot{v}_g(t) = \sqrt{2} \sum_{n=1}^N A_n \cos(\omega_n t + \varphi_n) \quad (11)$$

where A_n is the amplitude of the harmonic component given by $A_n = \sqrt{2S_b(\omega_n)\Delta\omega}$; $\omega_n = n\Delta\omega$ is the frequency beyond which $S_b(\omega)$ can be considered zero, and φ_n are N independent random phase angles uniformly distributed between 0 and 2π . Thus, sample earthquake-like ground acceleration time histories, which are consistent with the risk considered, are simulated at the bedrock level.

6. Site response analysis

The hazard curve and the risk-consistent ground motion parameters obtained for bedrock level are modified considering the soil sediment amplification effect to obtain the free field parameters at a site. For the purpose, site response analysis is essentially carried out by a one-dimensional wave propagation analysis (**Figure 2**). The soil profile above the bedrock is generally multilayered having different soil properties in each layer. For a certain input excitation at the bedrock level, some of these layers can undergo nonlinear excursion. The one-dimensional wave propagation analysis is carried out by numerical integration of the equation of motion in the incremental form for a prescribed time history of acceleration at the bedrock level [9].

The PGA amplification due to the overlying soil is obtained considering two conditions, namely linear and nonlinear behavior of soil layers. The free field PGA is obtained by multiplying the PGA at the bedrock level by the PGA soil amplification factor. The conditional probability in Eq. (1) is then modified by considering the free field PGAs in place of bedrock PGAs to modify the bedrock seismic hazard curves into the free field hazard curves. The time history of the free field absolute ground acceleration is found by integrating the equation of motion for the soil layers subjected to the base acceleration for both linear and nonlinear conditions. The risk-consistent response spectrum of absolute acceleration at the free field is obtained from the free field time history of the absolute acceleration.

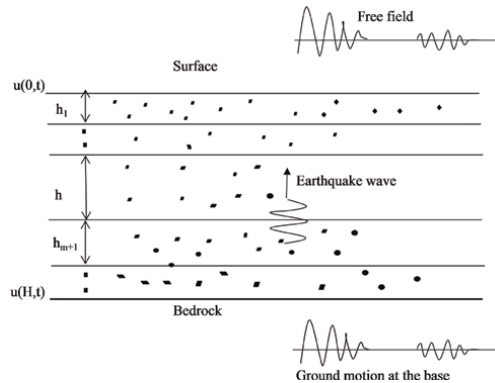


Figure 2.
One-dimensional wave propagation analysis.

7. Numerical illustration

The application of the proposed method is illustrated by determining the site-dependent earthquake ground motion parameters for sites of Bhaktapur City, a typical region of Kathmandu Valley. Seismic hazard curves and risk-consistent ground motion parameters are determined for sites of the Bhaktapur City, which is surrounded by eight identified active faults as the earthquake sources.

7.1 Ground motion parameters at the bedrock level

The seismic hazard curve and the risk-consistent ground motion parameters at the bedrock level are computed for the center of the city because these values do not significantly vary across the length and breadth of the city due to not large dimension of the city. The important parameters for the calculation of the seismic hazard curve are shown in **Table 1**.

The same table also presents the seismic characteristics of the eight earthquake sources. The average rate of threshold magnitude exceedance for each of the potential earthquake sources is given, based on Eq. (3), by the following:

$$\nu_i = \exp(\alpha_i - \beta_i m_o) \quad (12)$$

in which, $\alpha = 2.303a$ and $\beta = 2.303b$, and.

m_o = the lower threshold magnitude of earthquake, which is set to 4.5 in the study.

Since there is no attenuation law developed for the region due to scanty earthquake data, 24 various existing empirical attenuation relationships are used for calculation of the seismic intensity in terms of PGA at the bedrock level of Bhaktapur City. These 24 empirical attenuation laws, as described by Douglas [10] are by: 1. Taleb; 2. Donovan and Bornstein; 3. Donovan; 4. Esteva and Rosenblueth; 5. Davenport; 6. Merz and Cornell; 7. Cornell, Banon, and Shakal; 8. Battis; 9. Fukushima and Tanara; 10. Ambresseys and Bommer; 11. Tento, Franceschina and Marcellini; 12. McGuire; 13. Orphal and Lahoud; 14. Milne and Davenport; 15. Mickey; 16. Ohashi; 17. Joyner and Boore; 18. Sabetta and Pugliese; 19. Esteva and Villaverde; 20. Campbell; 21.

#	Active faults	Source-to-site distance (km)	Mean annual rate, ν_i	Value of coefficients		Probability density function of magnitude				
				A	β	M5	M6	M7	M8	M9
1	MCT- 3.3	34.51	5.012	14.279	2.073	0.7365	0.0927	0.0117	0.0015	0.0002
2	HFF-1.13	53.33	1.585	11.976	2.303	0.7304	0.0720	0.0073	0.0007	0.0001
3	LH-4.10	60.12	5.012	14.279	2.073	0.7394	0.0931	0.0117	0.0015	0.0002
4	MBT- 2.5	66.66	1.585	11.976	2.303	0.7293	0.0729	0.0073	0.0007	0.0001
5	MBT- 2.4	95.55	1.585	11.976	2.303	0.7304	0.0730	0.0073	0.0007	0.0001
6	MBT- 2.6	142.22	1.585	11.976	2.303	0.7384	0.0728	0.0073	0.0007	0.0001
7	MBT- 2.3	180.15	1.585	11.976	2.303	0.7288	0.0729	0.0073	0.0007	0.0001
8	MBT- 2.7	230.09	1.585	11.976	2.303	0.7288	0.0729	0.0073	0.0007	0.0001

Table 1.
Seismic parameters of the earthquake sources (faults).

Abrahamson and Litchiser; 22. Theodulidin and Papazachos; 23. Peng, Wu and Song (a); and 24. Peng, Wu and Song (b).

7.2 Hazard curve at the bedrock level

The seismic hazard curve for the center of Bhaktapur City at its bedrock level is constructed as described in Section 2, using the exponential function for PDF for earthquake magnitude, assuming earthquake occurrence as Poisson's Process and adopting 24 available attenuation laws as described above. The hazard curve at the bedrock level is presented in **Figure 3**.

7.3 Risk-consistent response spectrum (spectral shape) at the bedrock level

The normalized risk-consistent response spectrum (spectral shape) is obtained for this site using the empirical relationship between the magnitude of earthquake and the response spectrum ordinates given by Eq. (5). The values for coefficients $a(T)$, $b(T)$, and $c(T)$ in the equation are taken from Takemura et al. [7] and are shown in **Figure 1**. The normalized acceleration response spectra for the site are obtained for six various PGA intervals and median values of which are 0.03, 0.08, 0.13, 0.18, 0.23, and 0.28 g, respectively. Thus obtained risk-consistent spectral shapes for the center of Bhaktapur City at the bedrock level are shown in **Figure 4**. As is seen from the figure, the shape of the acceleration response spectrum is not very sensitive to the PGA intervals.

7.4 Power spectral density function at the bedrock level

The risk-consistent power spectral density functions are obtained at the bedrock level for all PGA intervals from their respective risk-consistent response spectrum, using Eq. (10). The power spectral density function at the bedrock obtained from the risk-consistent response spectrum for a PGA value of 0.13 g is shown in **Figure 5**.

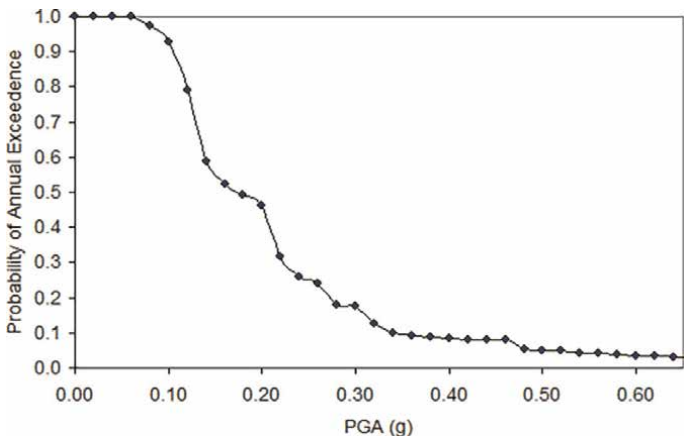


Figure 3.
Seismic hazard curve for the center of Bhaktapur City at the bedrock level.

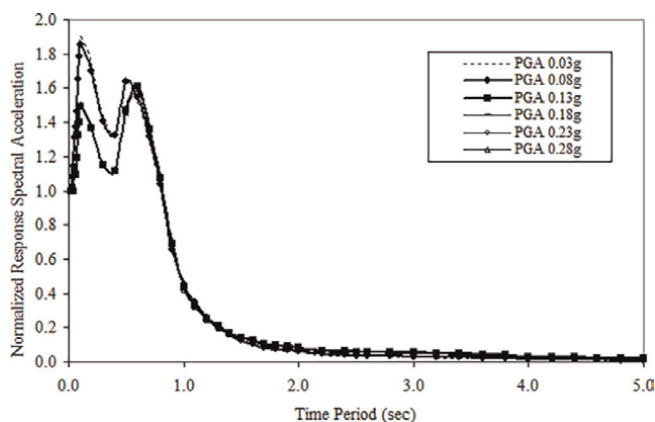


Figure 4.
 Risk-consistent response spectrum for the Center of Bhaktapur City at the bedrock level (for various PGA intervals).

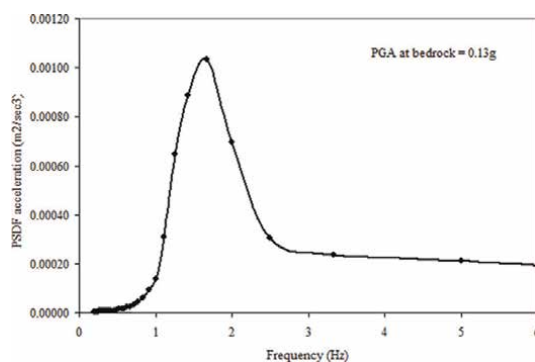


Figure 5.
 Risk-consistent power spectral density function for the Center of Bhaktapur City at the bedrock level.

7.5 Sample time history of ground acceleration at the bedrock level

Figure 6 presents a sample time history of ground acceleration generated from the PSDF for PGA level 0.13 g at the bedrock level. Note that PGA value, as read from the time history, is nearly equal to 0.13 g. The frequency contents of the time history obtained by Fourier decomposition are shown in **Figure 7**. It is observed from the figure that the frequency contents are quite large within the frequency band, where PSDF has high ordinates, as it would be expected.

7.6 Local soil sediment effects

The soil properties of Bhaktapur City vary from one place to another, and accordingly, the soil sediment effect on the ground motion parameters would not be the same. Three different sites of Bhaktapur city with their soil profiles are considered to assess the effect of local soil conditions on the hazard curve and the risk-consistent ground parameters obtained for the bedrock level. The majority of the soil layers are either clay or sandy clay. In order to obtain the hazard curve and the site-dependent

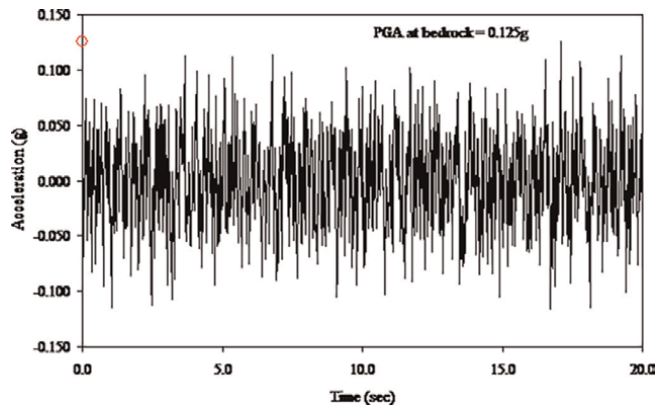


Figure 6.
Simulated time history of acceleration from the PSDF for the Center of Bhaktapur City at the bedrock level.

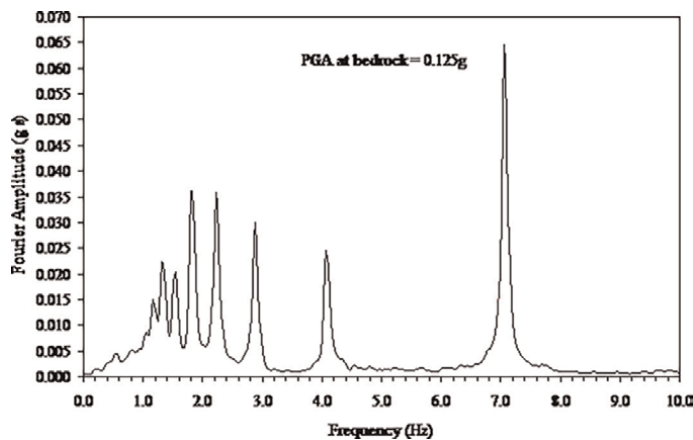


Figure 7.
Frequency contents of simulated time history of acceleration at the bedrock level of Bhaktapur City Center.

ground motion parameters at the top of each of the three sites, the risk-consistent time history of ground acceleration generated at the bedrock level is used as the input for carrying out site response analysis. One-dimensional wave propagation analysis is performed for both linear and nonlinear soil behaviors to obtain the time histories of the free field ground accelerations at the sites.

7.7 Free field ground motion parameters

The PGA amplification for the three sites when soil behavior is assumed to be linear, is shown in **Table 2**. Evidently, the PGA amplification substantially differs from one site to the other.

The free field seismic hazard curves constructed considering the PGA amplifications become different for the three sites. A typical hazard curve at the free field of the Site No.1 (Durbar Square, Khauma) is shown in **Figure 8**. The hazard curve at the bedrock level is also shown in the same figure. The figure indicates that the hazard curve for the free field provides significantly greater probabilities of exceedance of PGA values compared to the same for the bedrock.

Site No.	Location	PGA amplification
1	Durbar Square, Khauma	2.67
2	Taumadhi Square	2.10
3	Salan Ganesh Square	1.92

Table 2.
PGA amplification for three typical sites (linear).

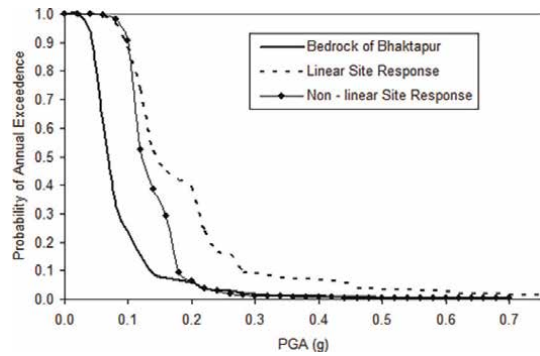


Figure 8.
Typical seismic hazard curve (free field and at the bedrock level). at site No. 1 Durbar Square, Khauma.

The PGA amplification for two sites for different levels of PGA values when nonlinear behavior of the soil is taken into consideration, is presented in **Table 3**. It may be seen from the table that the PGA amplification decreases with the increase in the input PGA value. It is because the nonlinear effect becomes more for higher level of excitation resulting in more dissipation of energy within the soil mass. For higher values of PGA (0.28 g), the free field PGA may be deamplified (amplification less than one). It is noteworthy that the PGA amplification is independent of the PGA level at the bedrock for linear behavior of the soil and is much greater than that for nonlinear soil behavior for higher values of bedrock PGA. Thus, consideration of actual soil behavior in the determination of the free field ground motion is extremely important, especially for higher levels of PGA at the bedrock level. The effect of the nonlinear soil behavior on the free field hazard curve is shown in **Figure 8** in which the hazard

PGA at Bedrock level	Sites	
	Site no. 1	Site No. 3
	Durbar Square, Khauma	Salan Ganesh Square
0.03 g	2.40	2.02
0.08 g	1.87	1.89
0.13 g	1.28	1.23
0.18 g	1.03	1.12
0.23 g	1.02	1.11
0.28 g	0.87	0.97

Table 3.
PGA amplification for two typical sites (nonlinear).

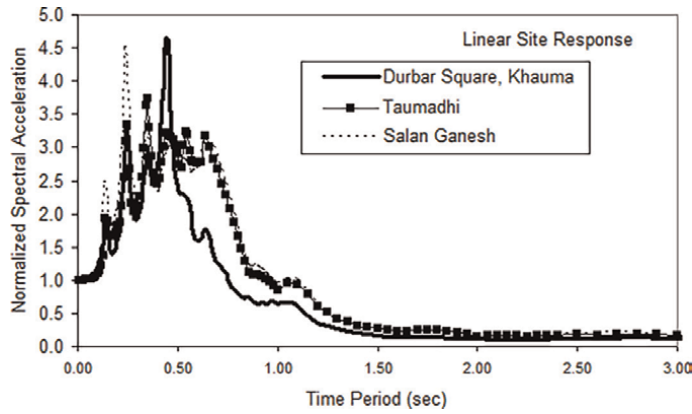


Figure 9.
Normalized risk-consistent response spectrum for free field absolute acceleration at three sites of Bhaktapur City (linear site response).

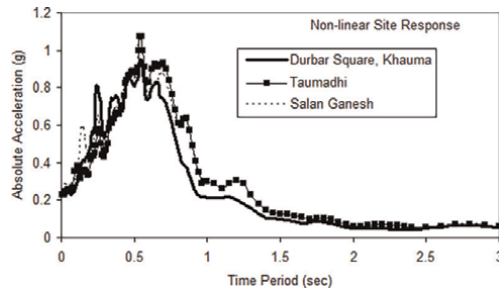


Figure 10.
Normalized risk-consistent response spectrum for free field absolute acceleration at three sites of Bhaktapur City for PGA at bedrock = 0.23 g (nonlinear site response).

curves for linear and nonlinear soil behavior are compared. It is seen that the probability of exceedance is more for linear soil behavior and difference between the two increases for higher values of PGA.

Figure 9 presents the free field spectral shapes for the three sites when linear behavior of the soil is considered. It exhibits that even though the input bedrock spectral shape remains the same, the shapes of the risk-consistent response spectra can be significantly different from one site to the other. Comparison of **Figures 4** and **9** shows that the peak of the risk-consistent spectrum at the free field may be significantly deviated from that at the bedrock level. This clearly shows that the input excitation to the structures may be significantly influenced by the soil conditions.

Figure 10 presents the risk-consistent spectral shapes for a PGA level 0.23 g for the same three sites when nonlinear behavior of soil is considered. It is again observed that the spectral shapes may significantly differ from one site to the other. Comparison of **Figures 9** and **10** shows that the spectral coordinates are drastically reduced near the peaks when nonlinear soil behavior is taken into consideration.

8. Conclusion

A probabilistic method is presented to generate seismic ground motions specific to sites, which are earthquake prone but do not have enough recorded data. The seismic

hazard curves are developed from the probabilistic seismic hazard analysis considering available attenuation laws. The hazard analysis is expanded using empirical relationship for the spectral ordinate with the earthquake magnitude to find the risk-consistent spectral shapes at the bedrock level. Sample ground acceleration time histories are simulated from the risk-consistent power spectral density function at the bedrock using Monte Carlo technique. The seismic risk is incorporated by using conditional probability of occurrence of PGA for a particular magnitude of earthquake, derived from the set of available attenuation laws. Site response analysis is carried out by one-dimensional wave propagation analysis to modify the hazard curves and the risk-consistent ground motion parameters considering the local soil amplification effect. Both linear and nonlinear soil behaviors are considered. The methodology is illustrated by generating the hazard curves and the risk-consistent ground motion parameters for three different sites of Bhaktapur City surrounded by eight earthquake sources. The results of the study lead to the following conclusions:

The annual probabilities of exceedance of a PGA level at the bedrock level and at the free field are different. The degree of difference depends upon the soil condition.

The probability of exceedance of a PGA level denoted by the hazard curve is reduced when the nonlinear behavior of soil is considered; the reduction is prominent for higher levels of PGA.

The PGA amplification is much less for the nonlinear soil condition, and may even become less than one.

The risk-consistent normalized acceleration response spectrum at the bedrock level of the Bhaktapur City is relatively broad-banded.

The spectral shapes at the free field are significantly modified due to the soil effect.

The spectral shapes become broader banded when nonlinear behavior of soil is taken into consideration in comparison to those corresponding to linear soil behavior.


Modification in spectral shapes due to nonlinearity depends upon the PGA level at the bedrock. For higher levels of PGA, the effect of nonlinearity is more, the spectral shape becomes more broad-banded, and more reduction of spectral ordinates takes place near the peak.

Author details

Prem Nath Maskey
Department of Civil Engineering, Pulchowk Campus, Institute of Engineering,
Lalitpur, Nepal

*Address all correspondence to: pnmaskey@hotmail.com

IntechOpen

© 2023 The Author(s). Licensee IntechOpen. This chapter is distributed under the terms of the Creative Commons Attribution License (<http://creativecommons.org/licenses/by/3.0>), which permits unrestricted use, distribution, and reproduction in any medium, provided the original work is properly cited. 

References

- [1] Tan RY. Alternate methods for construction of design response Spectrum. Proceedings of Natural Science Council ROC(A). 1998;22(6): 775-782
- [2] Torregosa RF, Sugito M, Nojima N. Strong motion simulation for the Philippines based on seismic hazard assessment. Journal of Natural Disaster Science. 2001;23(1):35-51
- [3] Barranco-Cicilia F, Silva-ballesteros J. Seismic ground motion signals from design spectrum for soft soil in Mexico City. In: Proceedings of the Twelfth World Conference on Earthquake Engineering. Auckland, New Zealand; 2000
- [4] Ishii K, Okumura T, Suzuki M. Earthquake ground motions consistent with probabilistic seismic hazard analysis. In: 5th International Conference on Structural Safety and Reliability. San Fransisco, CA; 1989
- [5] Cornell CA. Engineering seismic risk analysis. Bulletin of the Seismological Society of America. 1968;58(5): 1583-1606
- [6] Der Kiureghian A, Ang AHS. A fault rupture model for seismic risk analysis. Bulletin of the Seismological Society of America. 1977;67(4):1173-1194
- [7] Takemura M, Ishida H, Amano A, Mizutani M. A seismic PRA procedure in Japan and its application to a building performance safety estimation part 1. Seismic hazard analysis. In: 5th International Conference on Structural Safety and Reliability. San Fransisco, CA; 1989
- [8] Shinozuka M, Deodatis G. Simulation of stochastic processes by spectral representation. Applied Mechanics Reviews. 1991;44(4):191-204
- [9] Kramer SL. Geotechnical Earthquake Engineering. New Jersey: Prentice Hall; 1996. pp. 254-280
- [10] Douglas J. Engineering seismology and earthquake engineering a comprehensive worldwide summary of strong-motion attenuation relationships for peak ground acceleration and spectral ordinates (1969 to 2000). In: ESEE Report No. 01-1, 2001. London: Imperial College of Science, Technology and Medicine; 2001

Section 3

Infrastructure

Disasters and Housing Infrastructure: Evidence from the 2010 Chilean Earthquake

*Valeria Yanina Scapini Sánchez
and Cinthya Leonor Vergara Silva*

Abstract

In 2010, a severe earthquake occurred in Chile that brought high-impact destruction effects in the affected areas. It has studied the damage to homes, the determiners of the cost of reconstruction, and how households finance reconstruction using the Casen post-earthquake 2010 panel survey. A probit and an OLS model were used. The results show that houses closest to the epicentre were the most affected, where damage increased when roofs and walls were in worse condition or with more vulnerable materials. The reconstruction costs are related to the degree of destruction, the distance to the epicentre, the condition of the walls before the event and the house's value. Provinces with more bank branches are associated with a lower cost. Bank credit is more likely to be used to rebuild in urban areas, when the head of the household has more years of education and when the repair cost is higher. Own savings will be used when there is no insurance, the higher the income of the head of household and the lower repair costs. Finally, subsidies will be an option when there is no insurance, the repair cost is higher, and for lower income, age, and education.

Keywords: earthquake, housing damage, cost of reconstruction, funding sources, natural disaster

1. Introduction

Throughout human history, we have lived with great-scale natural phenomena that have generated all kinds of losses, altering both the dynamics of communities and the economic activities associated with the affected areas. The United Nations has carried out projects that have allowed the increase of attention toward the diverse threats with which man has to live, amongst the most highlighted is the International Natural Disaster Reduction Decade [1]. In the same manner, a series of development policies at an international level have focused on the protection of the vulnerable related to avoidable losses, leaving natural disasters as an exceptional fact that is not

part of the development theory [2]. However, social media and technology have taken a fundamental role in our lives, and this has increased the investigation in the natural science areas with the goal of improving the capacity to anticipate these disasters, face them, and mitigate their consequences.

Chile, located within the Pacific Ring of Fire, finds itself in constant exposure to earthquakes across its territory [3, 4]. These occurrences bring not only damage to homes and infrastructure but also high economic and social costs linked with reconstruction efforts [5–7]. This vulnerability was demonstrated when a seismic event on February 27th, 2010, struck. It registered a magnitude of 8.8, making it the sixth most powerful earthquake globally, and the second-largest earthquake ever recorded in Chilean history [8]. The earthquake’s epicenter was offshore, near the Maule Region, with a focal depth extending to approximately 35 kilometers beneath the Earth’s surface. This earthquake significantly affected six out of the country’s 15 regions, encompassing an expanse of 700 kilometers, where 80% of the population resides [9].



Figure 1.
Area affected by the earthquake in Chile, 2010. Source: [11]; United States geological survey (USGS) for epicentral location data.

The losses incurred by this event were estimated at 30 billion dollars, equivalent to 18% of the GDP [10]. **Figure 1** illustrates the extent of the affected zone by the earthquake and the regions involved.

In the aftermath, as Chile confronted the intricate interplay of physical destruction and social upheaval, the event stood as a lasting testament to the importance of fortifying preparedness, response, and mitigation efforts. It underscored the necessity of adopting a multidimensional approach that considers both the tangible losses of infrastructure and the intangible yet equally significant fabric of communities and societies. Amid an era marked by the proliferation of technology and the interconnectivity fostered by social media, the lessons drawn from this earthquake have spurred the exploration of innovative scientific avenues to enhance prediction, response strategies, and ultimately, the reduction of the toll exacted by natural disasters.

This earthquake is particularly interesting to be studied due to its magnitude, coverage, and quantity of homes affected. For this purpose, there is panel data with information at the home level that allows us to explore the destructive power of the disaster and its socioeconomic effects. This chapter explores the following questions: How does the distance of the earthquake's epicenter affect the probability of home damage, considering the state of the construction before the event? What are the primary factors influencing the cost of home reconstruction? Additionally, how do homeowners secure financing for their home repairs or reconstruction? Does the access to banking institutions affect the cost and capacity of the reconstruction? In Section 2, *The economic impact of natural disasters* a literature revision is conducted, in Section three *Methodology*, the used data and estimated models are described, in Section 4, *Results* the empirical results are presented in conjunction with the robust tests, and finally, in Section 5, *Conclusion* the main conclusion are presented.

2. The economic impact of natural disasters

A natural disaster is a catastrophic event caused by natural forces or processes that result in significant damage to the infrastructure of settlement, infrastructure damage, the loss of life, economic costs, and socio-environmental disruption in general. These events are out of human control and can have devastating consequences for the areas and affected populations [12]. Some examples of natural disasters include hurricanes, earthquakes, floods, forest fires, tsunamis, volcanic eruptions, and tornados. Although natural disasters mainly originate from natural factors, human activity might influence the gravity and impact. These are known as human factors or man-induced factors, which we can identify [13]:

1. Terrain and house development usage: Human settlements and infrastructure located in vulnerable areas can increase the risk and amplify the impact of natural disasters. For example, the construction in flood propensity planes or in unstable slopes can produce greater damages through floods or landslides.
2. Land degradation and deforestation: The logging for agriculture or housing development reduces the natural barriers against disasters. Trees play a crucial role in the prevention of land erosion, water flow regulation, and the mitigation of the impact of events, such as floods and landslides.

3. Climate change: Man-made climate change is altering the climate patterns and increasing the frequency and intensity of some natural disasters. The global temperature increase can contribute to the creation of hurricanes, heat waves, droughts, and severe storms.
4. Deficient housing infrastructure and planning: The inadequate housing planning, the inadequate zoning, and the weak infrastructure can exacerbate the impact of disasters. For example, inadequate drain systems can produce an increase in floods, and poorly constructed buildings are more susceptible to crumbling during earthquakes.
5. Overcrowding and population growth: The rapid population growth, particularly in areas prone to threats, can put more people at risk during a natural disaster. Overcrowding and inadequate preparation for emergencies can obstruct the efforts of evacuation and increase the number of victims.
6. Early alert and lack of preparation: Insufficient preparation for disaster, including the absence of early alert systems, can make the evacuation and opportune response more difficult. Education and awareness about natural dangers, as well as effective emergency planning, are crucial to mitigate the impact of disasters.

With it, natural disasters have been studied from different perspectives, including damage evaluation of infrastructure, risk mitigation, emergency preparation, preventive measures, logistic, social, work, sanitary, environmental, and economic effects amongst others [12].

Amongst the related studies of natural disasters, we find a line that estimates the social or economic costs that a seismic event generates in the zones, where it impacts. This line of study, the World Bank [14, 15] shows that the economic and social cost has increased in the last years due to growth in population. It also shows that the loss of life and the destruction of infrastructure in natural disasters delay every type of program that has as objective the overcoming of poverty given that it generates deviation of resources for recovery and reconstruction.

On the other hand, Sen [16] establishes that the associated costs of natural disasters are determined mainly by economic and social factors above the magnitude of the process. As an example, it points out the earthquakes occurred in Haiti and Chile in the year 2010, in which the first caused the death of 200.000 and 250.000 people and damages to the economic infrastructure of the country in more than 100% of the PIB of the country [17], while the second registered a greater intensity but caused less than 500 deaths and fewer damage to Haitians in relation to the size of its economy [18]. In this sense, it can be established that natural disasters cause great economic losses all over the world; however, the damage caused has a direct relation with the country's income [19]. Even though the economic losses are greater in developed countries, they are less in proportion to their PIB in comparison to developing countries [20].

The damages caused by natural disasters can be classified between direct damages and indirect damages [2]. The direct damages correspond to the damages of the fixed assets, capital, raw materials, extractable natural resources, mortality, and mobility as a direct consequence of the disaster. The indirect damages are related to the production of estates and services that will not be able to function after the disaster, additional costs that are incurred due to the necessity of producing or distributing

alternative assets, and the loss of resulting incomes due to lack of provision of assets and services or the destruction of the production. Additionally, the secondary effects correspond to those that have incidence in the global economic performance, and which measurement is performed through the macroeconomic variables such as the PIB, the commercial scale, the payment balance, the debt level, international reserves, and investment [21], where the sensitivity of a country in the face of the impact of natural disasters can increase according to its level of economic development. Kahn [22] concludes that in the richest countries less deaths are generated in the face of natural disasters of equal severity.

For its part, there is a series of studies oriented at quantifying the impact of a natural disaster, the financial risk associated, and the recovery time. Within this economic study, we find a strong emphasis on the analysis of the relationship between the economic situation of the government, the foreigner relations, and the level of maturity of the financial industry, especially in the insurance market and the risk transfer [23–27]. In relation to the recovery and the reconstruction at the microeconomic level, Noy [28] establishes that the financial flows play an important role in the recovery of disaster; therefore, the conditions of the financial market are another factor to consider to evaluate the consequences of natural disasters. It also points out that the bigger the domestic credit the costs of the disaster are reduced [17, 29–31].

Benson and Clay [14] study the economic impact of natural disasters considering government spending and the redistribution of resources to finance the initiative of the government. They identify that the disasters generate additional costs or partial financial resources reassignment that are destined for reconstruction, rehabilitation of public assets, and relay support for the victims. For the insurance and private capital support to be effective in the reduction of the impact of natural disasters, it is necessary to perform planning and assignments of funds that allow it to fulfill the consequences in an anticipated manner, as well as the mitigation and preparation of support. They conclude that the reassignment of funds after a disaster must be carried out through a formal process, designed after a careful strategic revision, and that it is necessary to increase the financial mechanisms that manage to correctly perform the risk transfers between different types of disasters and the impact mitigation.

In the same manner, Ghesquiere & Mahul [32] perform a financial analysis of both public and private with the objective of supporting the development of financial protection in the face of natural disasters related to different risk levels. It also identifies that for developing countries is of great importance to develop financial strategies given their greater vulnerability, as opposed to developed economies that possess a greater and prolonged usage of resources dedicated to reducing vulnerability, such as buildings with better structure or legislative systems that are more demanding in terms of usage of land and construction. It proposes that the recovery strategy must be tackled with public resources, as well as with private resources in relation to the frequency and severity of the risks so as to create a strategy of financial instruments according to the severity and frequency of each type of disaster. The proposal is summarized in **Table 1**.

The financial protection strategies address the symptoms and not the cause of catastrophes; therefore, a good strategy may help diminish the financial impact that a calamity can generate. However, it is important to point out that in a global strategy of catastrophe risk management financial protection is only one component. These sources of finance are separated into those delivered before and after the disaster. The tools that come after are sources that do not require planning such as the realignment of the budget, internal credit, external credit tax increase, and the help of donors. The

Frequency	Severity	Risk	Financial instrument
Low	Major	High-risk layer	Risk insurance for disasters
Mid	Mid	Mid risk layer	Contingency credit
High	Minor	Low-risk layer	Contingency budget and annual budget assignment

Source: Elaborated based on Ghesquiere & Mahul [32].

Table 1.
Financial strategy according to risk and severity.

financial tools of risk ex ante require anticipated planning and include disaster funds or reserves, budgetary contingency, and mechanisms of risk transference [32].

It is important to count on evaluation systems of natural disaster impacts, evaluate the fiscal sustainability, and vulnerability of the governments and have an optimal financial structure for the retention of risks and the transfer taking into account the contingency credits, reserves funds, insurance, and catastrophe bonuses [25].

Finally, there are studies that relate socioeconomic characteristics with the way natural disasters impact, and in these, it is indicated that when there is clear information about the risk zones, the homes located in the riskier zones are more expensive and are, therefore, in less demand, which should reduce the damage by natural disaster in the future [33].

3. Methodology

To perform the study different sources were used. First, the data panel house survey CASEN post-earthquake 2010 was used, of which the population sample reaches 75.986 people and 21.899 homes samples, which contain socioeconomic information at the home level. Second, the distance of the earthquake's epicenter distance in relation to the communal capital was used where the home was located, information that was constructed for the elaboration of the present study taking the distance in kilometers between the provincial capital and the epicenter. Finally, the number of banking branches that existed in each province in the year 2010 was used according to the information delivered by the superintendence of banking and financial institutions (SBIF).

In our analysis, we employed a controlled regression analysis approach to assess the relationships between predictor variables and the outcome variable. To ensure accurate and meaningful results, control variables were incorporated into the regression models. The inclusion of control variables is a common practice in statistical analysis to account for potential confounding effects and enhance the precision of our findings.

For the purpose of clarity and interpretation, we denoted the inclusion of control variables using the notation "YES" in the table, and this means that the regression models were constructed with the consideration of additional factors that could influence the outcome variable. In addition, we consider R-squared metrics that indicate how much of the variation of a dependent variable is explained by the independent variables in our recession model. In other cases, we used the term "Pseudo R-squared" to refer to the coefficient of determination (R-squared) when the explained variable is categorical and the coefficient of determination cannot be applied. This approach is

similar to R-squares, and they have a similar scale (from 0 to 1) and higher values indicate a better model.

Incorporating control variables aims to ensure that the analysis captures a comprehensive view of the relationships under investigation. This approach allowed us to mitigate potential bias and produce results that reflect the genuine influence of the predictor variables on the outcome variable.

The investigation questions are addressed from three thematic: home damage, repairation costs or home reconstruction, and financial sources.

3.1 Home damage

To study the relation between the earthquake epicenter distance and the home damage, a nonlinear probability model of binary selection probit is used (Eq. 1), where the explained variable corresponds to the damage of the home that can have values 1 or 0 (where 1 indicates that the homes were damaged and 0 that there was no damage as consequence of earthquake or tsunami). The explanatory variables considered are the distance from the home to the epicenter of the earthquake (Dis_i) and a categorical variable of control (X_i) that indicates the type of holding of the home, the material of the construction of the home, and its conservation status. Thus, model is as follows:

$$PR(Damage_i = 1) = F(\alpha + \beta Dis_i + \gamma X_i) \quad (1)$$

Where PR corresponds to the probability, F is the function of the accumulated normal standard of distribution, and the subindex i corresponds to the home. The parameters α , β , and γ were estimated by the maximum likelihood estimation. The results can be interpreted in probability terms so that the sign of parameter estimates indicates the direction in which the probability moves each time the explanatory variable increases. Subsequently, the interaction between Dis and X is included to evaluate if the earthquake has affected the homes in poor conditions in spite of the distance of these from the epicenter.

3.2 Repair cost

In relation to the main determiners of the costs of reconstruction or repairs of a home, we estimate an ordinary least squares (OLS) regression models (Eq. 2), where the dependent variable is the costs of repair or reconstruction of the home ($Cost$), and the explanatory variables considered are: the type of property of the home, the number of banks, the damage degree of the home, the rent value of the home, the distance of the epicenter, and the state of conservation of the walls, floors, and roofs, leaving the model to estimate as follows:

$$Cost_i = \alpha + \beta Prop_i + \vartheta Ban_i + \eta Damage_i + \rho Ren_i + \gamma Dis_i + \delta X_i + \varepsilon \quad (2)$$

Where $Cost_i$ represents the estimated cost of the homes repairs in millions of pesos, the variable Ban_i represents the number of banks that are in the province, and the degree of damage of the home $Damage_i$ is the variable that may take values 0,1,2, and 3 and represents a home without damage, with minor damages, major damages, or destruction due to the earthquake, respectively; the value of rent of the home Ren_i indicates how much rent is paid by the home or how much it would cost if it were to

be paid, Dis_i is the distance of the epicenter and X_i represents the state of conservation of the walls, floors, and roof. The parameters α , β , ϑ , η , ρ , γ , and δ were estimated by the ordinary least squares method that allows us to find the parameters that minimize the sum of the squared residuals in a linear regression model.

3.3 Financial sources

To understand how homes finance their reconstruction or repair a probit binary nonlinear selection of probability is used (Eq. 3), where the explained variable corresponds to the options of finance be it from banks, savings, or subsidies (Fin_i), and the considered explanatory variables are the home's income, age, education level, area, cost of reconstruction, insurance, number of banks, and distance of the epicenter of the home i .

$$PR(Fin_i) = F(\alpha + \beta Inc_i + \vartheta Age_i + \eta Edu_i + \rho Rur_i + \gamma Cost_i + \delta Insu_i + \mu Ban_i + \xi Dis_i) \quad (3)$$

Where the financial options can be from banks, savings, or subsidies and can take the values 1 or 0 (where 1 indicates that the home utilizes that option, and 0 that it does not). The considered explanatory variables are the home's income (Inc_i), the age (Age_i), education level (Edu_i), rural zone (Rur_i variable that indicates if the home belongs to a rural zone or not), $Cost_i$ represents the cost of the reconstruction or repair of the home, insurance ($Insu_i$ variable that indicates if the home has insurance or not), the number of banks (Ban_i), and distance from the epicenter (Dis_i). The parameters α , β , ϑ , η , ρ , γ , δ , μ and ξ were estimated by the maximum likelihood estimation, and the results can be interpreted in probability terms so that the sign of parameter estimates indicates the direction in which the probability moves each time the explanatory variable increases.

Finally, to verify the consistency of the statistical models, the statistical t was calculated, and the significance level of each variable was determined, as well as the coefficient of determination of each model.

4. Results

The preliminary results in relation to the number of affected homes, and the type of damage received show that 33.22% of the country's homes had some kind of damage after the earthquake and also after the tsunami. Specifically, 21.91% of homes showed minor damages, 8.06% major damages, and 3.24% were destroyed due to the earthquake or later due to the tsunami. These results are observed in **Table 2**.

In relation to the construction material of the homes under the study, the majority of homes were built from bricks (43.39%), followed by wood partition lined on both sides (36.42%), and in third place a small percentage of the constructed homes were adobe, wooden partition without linings and reinforced concrete (around 7% each one). In general, 20% of the homes showed some kind of damage prior to the seismic event, that is to say, they had poor conditions in some parts of the construction such as walls, roof, or floor. These results are observed in **Table 3**.

In relation to the destruction of the homes due to the earthquakes, we can point out that *de adobe* houses are the pens that show a higher rate of destruction (23.99% of

	All provinces		Affected provinces	
	Number of homes	Percentage	Number of homes	Percentage
Destroyed by earthquake	643	2.94	643	3.69
Destroyed by tsunami	66	0.30	66	0.38
Major damage	1.766	8.06	1.732	9.93
Minor damage	4.799	21.91	4.715	27.04
Not affected	14.625	66.78	10.280	58.96
Total	21.899	100	17,436	100

Source: Own elaboration.

Table 2.
Number of homes affected according to the type of damage.

Construction material	Destroyed homes	Destroyed homes
	% of the total homes	% of the construction material
Reinforced concrete	6.56	1.1
Brick	43.39	1.46
Wood partition lined (both sides)	36.42	1.52
Adobe	6.72	23.99
Wood partition unlined	6.82	2.74
Mud houses	0.36	17.33
Waste/recycled material	0.05	13.51
Others	0.02	0
Total	100	

Source: Own elaboration.

Table 3.
Number of homes destroyed according to the construction material.

adobe houses were destroyed), followed by mud houses (17.33% of them) and those built from waste material or recycled material (13.51% of them). We can conclude that the destruction of the homes has a direct relation with its construction material. This can be observed in **Table 3**.

4.1 Estimated models

In this section, the results of the estimated models are shown. It is important to note that the significance of the model attributes is evaluated according to the p-values with the standard scale where [34]:

1. $p < 0.01$ is considered highly statistically significant. It suggests that there is strong evidence to reject the null hypothesis, indicating a substantial effect or relationship in your analysis. This case is represented by three asterisks (***)

2. $p < 0.05$ indicates that there is statistically significant evidence to reject the null hypothesis, implying a meaningful effect or relationship. This case is represented by two asterisks (**).
3. $p < 0.1$ indicates that there is weak evidence against the null hypothesis, and the effect or relationship may be borderline significant. This case is represented by one asterisk (*).

The results of the first estimate shown in the methodology are presented in **Table 4**. These show that the type of property occupancy has a correlation with the home damage. In particular, owning a house or renting relates to a lesser probability of damage or destruction, with a significance of at least 5% while an irregular home occupancy is related with a higher probability of damage. The negative sign on the probability of housing damage (e.g., -0.0497 for “owned”) indicates that there is a 4.97% lower probability that an owned home will be damaged.

Second, we find a relationship between the distance from the epicenter and the damage level or destruction with a significance of 1% evidencing that the further the distance lesser the damage. Specifically, it means that as the distance to the earthquake epicenter increases by 200 kilometers, the probability of experiencing housing damage decreases by 10.11% (highly statistically significant). Similarly, the probability of experiencing housing major damage decreases by 3.27% and destruction by 1.01%. This means that homes farther away from the epicenter are substantially less likely to suffer damage, major damage, or destruction during an earthquake. However, this is an intuitive result, given that the earthquake’s epicenter intensity is greater and lessens as we move away from this spot.

Lastly, in relation to the poor quality of walls, the variable is highly significant to 1%, and the results show that it relates with a greater probability of damage or destruction, while the poor quality of floor or roof only correlates with damages and not destruction.

	Damage	Major damage	Destruction
Owned	-0.0497^{***}	-0.0289^{***}	-0.0099^{***}
Rented	-0.0279^*	-0.0162^*	-0.0048^*
Irregular	0.0492	0.0542*	0.0038
Distance	-0.1011^{***}	-0.0327^{***}	-0.0101^{***}
Poor wall condition	0.0801***	0.0676***	0.0189***
Poor floor condition	0.0276*	0.0117	-0.0019
Poor roof condition	0.1347***	0.0420***	0.0044
Fixed construction material effect	YES	YES	YES
Fixed region effect	YES	YES	YES
Observations	17,435	17,435	17,419
Pseudo R-squared	0.128	0.180	0.282

*** $p < 0.01$, ** $p < 0.05$, * $p < 0.1$. Results elaborated by authors based on post-earthquake survey.

Table 4.
Probability of home damage.

In the second estimate, we incorporate the variable between distance and the state of the conservation of the homes to evaluate if the earthquake has actually affected the homes in poor conditions, in spite of the distance from the epicenter. First, we evidence the correlation between the distance from the epicenter and the damage or destruction of the homes. Second, the type of occupancy of the property also shows a correlation with the damage of the home. In particular, an owned or rented home is related to a lesser probability of damage or destruction, while an irregular occupancy of a home is related to a higher probability of major damage. Third, it can be said that the poor conditions of the walls and the roof are related to a higher probability of damage and destruction, while the poor quality of the floor only correlates to damage. Lastly, the included interaction indicates that the homes in poor conditions have less probability of major damage if they are located farther from the epicenter.

Therefore, for all types of damage (damage, major damage, and destruction), variables that are highly statistically significant are: 1) Distance, where negative coefficients (-0.0993 , -0.0305 , -0.0097) indicate that increasing distance from the earthquake epicenter significantly reduces the probability of home damage, 2) Owned: Owning a house increase the probability of experiencing damage, major damage, and destruction decreases significantly were highly statistically significant (**), for all three types of damage, the negative coefficients (-0.0499 , -0.0292 , and -0.0100) suggest that probability of experiencing damage, major damage, and destruction decreases significantly, 3) Poor wall condition, where positive coefficients (0.0950 , 0.0838 , 0.0235) indicate that poor wall condition significantly increases the probability of all types of damage, and 4) Poor roof condition, where positive coefficients (0.1501 , 0.0568 , 0.0073) indicate that poor roof condition significantly increases the probability of all types of damage. For all types of damage, the variable “poor floor condition” is statistically significant and the variable “irregular” is marginally statistically significant for “destruction” ($p < 0.1$). It has a positive coefficient (0.0564) suggesting that irregular homes may have a slightly higher probability of experiencing destruction, but this result is less robust than the highly significant variables. In summary, distance, poor wall condition, and poor roof condition are highly statistically significant predictors of all types of damage, with distance having a negative effect, and poor wall/roof condition having a positive effect. Poor floor condition is statistically significant but at a lower level ($p < 0.05$) for all types of damage, with a positive effect. Irregular construction type is marginally significant ($p < 0.1$) for “destruction” only, with a positive effect. The interaction term “distance*poor quality” is not statistically significant for any type of damage. The results obtained are similar to the previous model and are presented in **Table 5**.

To respond to the second investigation question that has relation to the main determinants of the reconstruction cost, two estimates were conducted, and the results obtained are presented in **Table 6**. We can see that there is a correlation between the degree of damage and the cost of repair or reconstruction of the home, and an intuitive result given that the repair cost of a house with small damages should be less than the cost of the complete reconstruction. In addition, we observe a correlation between the rent and cost variables, in particular, the higher the rent value of the house, the greater the cost of its repair.

Therefore, in this analysis of “cost,” the number of banks consistently demonstrated a negative effect on cost, with coefficients ranging from -0.0003 to -0.0002 , suggesting that an increase in the number of banks is associated with lower costs of repair of the home. However, as the degree of damage increased across various model setups, “cost” also increased significantly, with coefficients ranging from 1.1627 to

	Damage	Major damage	Destruction
Owned	−0.0499***	−0.0292***	−0.0100***
Rented	−0.0280*	−0.0163*	−0.0048*
Irregular	0.0509	0.0564**	0.0042
Distance	−0.0993***	−0.0305***	−0.0097***
Poor wall condition	0.0950***	0.0838***	0.0235***
Poor floor condition	0.0416**	0.0238**	0.0001
Poor roof condition	0.1501***	0.0568***	0.0073*
Distance*poor quality	−0.0051	−0.0046**	−0.0010
Fixed construction material effect	YES	YES	YES
Fixed region effect	YES	YES	YES
Observations	17,435	17,435	17,419
Pseudo R-squared	0.128	0.180	0.282

*** $p < 0.01$, ** $p < 0.05$, * $p < 0.1$. Results elaborated by authors based on post-earthquake survey.

Table 5.
Probability of home damage.

	(1) Cost	(2) Cost	(1) Cost	(2) Cost
N° banks	−0.0003***	−0.0003**	−0.0002*	−0.0003**
Degree of damage	1.2466***		1.1627***	
Rent	0.0030***	0.0021***	0.0029***	0.0025***
Distance from the epicenter		−0.1126***		−0.0501
Quality of the wall		0.1852**		0.1847**
Quality of the floor		0.0392		0.0581
Quality of the roof		−0.0053		0.0345
Constant	1.8349***	2.5043***	1.7721***	2.0628***
Fixed construction material effect	NO	NO	YES	YES
Fixed region effect	NO	NO	YES	YES
Observations	3309	3275	3275	3275
R-squared adjusted	0.3280	0.1018	0.3450	0.1173

*** $p < 0.01$, ** $p < 0.05$, * $p < 0.1$. Results elaborated by authors based on post-earthquake survey.

Table 6.
Estimated coefficient of the cost of repair/reconstruction.

1.2466, indicating that more severe damage is consistently linked to higher costs. Higher rental costs were positively associated with “cost” in different model specifications, with coefficients ranging from 0.0021 to 0.0030, suggesting that areas with higher rental prices tend to have higher costs. Greater distance from the earthquake epicenter was found to significantly reduce “cost” in certain model configurations, with a coefficient of −0.1126, while the quality of walls was positively associated with

“cost” in various model setups, with coefficients ranging from 0.1847 to 0.1852 (which is to be expected given that the closer it is to the epicenter it generates more damage and vice versa.). Additionally, better roof quality was associated with higher “cost” in (4) model specifications, with a coefficient of 0.0345. However, the quality of the floor did not show a statistically significant effect on “cost” in certain model specifications but was positively related to “cost” in others, with coefficients ranging from 0.0392 to 0.0581. These findings provide valuable insights into the determinants of “cost” across different configurations of control variables.

This is congruent with our previous results that showed that in the epicenter the damage is greater, and therefore the cost of the repair should be greater. We also noticed that the walls in poor condition before the disaster are related to a more expensive repair. Just like in the previous model, a positive correlation is observed between the rent and cost variables, and we can observe that a greater number of banks is related to a lesser cost of repairs. Finally, the field material and region effects were included, and the results obtained are similar, only the variable of significance is lost that now captures the controls of the region.

When we consider the costs of repair or reconstruction obtained from technical agencies or construction specialists, the results obtained differ slightly and are shown in **Table 7**. We see a correlation between the degree of damage and the cost of repair of the homes; however, this correlation is slightly less in comparison with the previously obtained by the homeowner. In the same way, there is a positive correlation between the rent and cost variables, and we observe that a greater number of banks is related to a lower cost. The second estimate shows different results, given that it only evidences a relation between the distance from the epicenter and the cost of repair of the home, showing that at a greater distance, the cost diminishes. Finally, the fixed construction material effects and the fixed region effects are similar, there is only a loss of significance with the variables of distance that now are captured by the control of the region and the number of banks.

	(1) Cost	(2) Cost	(1) Cost	(2) Cost
Nº banks	−0.0006**	−0.0004	−0.0004	−0.0003
Degree of damage	1.1673***		1.1405***	
Rent	0.0018**	0.0008	0.0019***	0.0012
Distance of the epicenter		−0.1363***		−0.0625
Quality of the wall		0.1836		0.1434
Quality of the floor		0.0861		0.1435
Quality of the roof		−0.1543		−0.1313
Constant	2.7372***	3.5500***	2.6171***	3.0830***
Fixed construction material effect	NO	NO	YES	YES
Fixed region effect	NO	NO	YES	YES
Observations	755	755	755	755
R-squared adjusted	0.3628	0.1287	0.3650	0.1387

*** $p < 0.01$, ** $p < 0.05$, * $p < 0.1$. Results elaborated by authors based on post-earthquake survey.

Table 7.
Estimated coefficient of the cost of repair/reconstruction (technical agencies).

	Bank	Savings	Subsidies
Insurance	0.0221	−0.0505*	−0.0794***
Income	−0.0034	0.0571***	−0.0662***
Age	0.0005	0.0010*	−0.0018***
Education	0.0039***	0.0041*	−0.0115***
Rural Zone	−0.0556***	0.0080	0.0142
N° banks	−0.0001**	−0.0001**	0.0000
Cost	0.0229***	−0.0985***	0.0892***
Fixed construction material effect	YES	YES	YES
Fixed region effect	YES	YES	YES
Observations	3869	3869	3869
Pseudo R-squared	0.0463	0.0746	0.117

*** $p < 0.01$, ** $p < 0.05$, * $p < 0.1$. Results elaborated by authors based on post-earthquake survey.

Table 8.
Probability related to financial sources of reconstruction.

In relation to how homes finance their repair or reconstruction and considering three different financial sources, **Table 8** shows the results obtained in the estimates. They indicate that homes that have earthquake insurance have a lesser probability of financing their repair or reconstruction with their own savings or subsidies. In relation to the income level of homes, it can be observed that the higher incomes are related with a greater probability of home repair financed by savings, and it is correlated with less probability of obtaining subsidies. In the same way, we noticed that older homeowners have more probability of financing the repair with savings and less subsidies. The education level of the homeowners also affects the type of finance given to them, given that higher level of education is related to higher bank financing and savings and with less subsidies. The houses located in rural zones have less probability of obtaining banking finance, as well as in zones, where there is a bigger number of banks. Lastly, the variable, the estimated cost of repair is correlated with the three sources of finance: a greater cost is related to higher probability of banking finance and subsidies, and at the same time with less financing of saving.

5. Conclusions

Earthquakes generate damages and losses of infrastructure, and the reason that motivated the study of variables that affect the damage of a home, the main determiners of costs of the reconstruction, and how homes finance the reconstruction. The study is focused on the Chilean earthquake of 2010 and microdata was utilized from home surveys performed for three months after the disaster.

In relation to the destruction of homes, the results show that houses built from adobe are the ones that showed a higher rate of destruction, followed by mud-built houses, quincha, and pirca. In relation to the connection between the distance from the epicenter of the earthquake and the damage of a home, the results show that the houses located closer to the epicenter were, on average, more affected by the

earthquake. This effect is stronger in houses that had already deteriorated before the disaster, mainly in those that had walls in poor condition.

The second group of results shows that the costs of reconstructions associated with the earthquake are related to the degree of destruction of the house, the distance from the epicenter, the condition of the walls before the event, and the value of the house. The number of banking branches in the province is related to a lower cost of repair, being related to the results obtained by Atienza and Aroca [35], where a discussion is held on what relation there is between the spatial concentration and efficiency, which allows the diminishment of the commercial cost. Just like Noy [28] who observed that the internal credit reduces the cost of disaster in growth terms of the lost product, this work puts in evidence that the greatest competition of internal credit helps reduce the cost in terms of price.

These findings may have policy implications for disaster preparedness and recovery in Chile. Areas with a higher concentration of banks might have better access to financial resources or services that could aid in post-earthquake recovery efforts. Policymakers and disaster response agencies could consider leveraging this information to prioritize resource allocation and support in regions with less financial support. While the negative relationship between the number of banks and earthquake-related costs is noteworthy, further investigation may be needed to understand the underlying mechanisms. Exploring why regions with more banks tend to have lower costs could provide valuable insights for disaster planning, as well as explore why access to banking services, capital, and financial resources can significantly impact a community's ability to withstand and recover from natural disasters. By investigating the presence and role of banks or, in general, financial support in these areas, could be a contribution to the development of more effective disaster risk reduction and recovery policies.

Finally, it is characterized by how homes finance the reconstruction of their houses. Specifically, the study found that homes with higher incomes have more possibilities of financing the reconstruction with savings, while the homes of lower incomes are more prone to finance the reconstruction with subsidies from the government or other institutions. The families that live in rural zones have less possibilities of financing the reconstruction with banking entities. The bigger the cost of the reconstruction, the homes are less prone to finance with savings, and the probability of finance by banking loan or subsidies is increased. With all this, the human factors highlight the importance of comprehending and tackling the role of social and economic activities in relation to natural disasters. Once we recognize and tackle these factors, societies can take proactive measures to reduce the vulnerability and increase the resilience in the face of natural disasters.

In the course of this study, we have employed the epicentral distance as a key parameter in our analysis. However, in light of the extensive rupture areas observed in certain seismic events, it is prudent to consider alternative distance metrics to enhance the precision and scope of our analysis. Utilization of metrics, such as the Joyner & Boore distance, which accounts for the closest distance to the surface projection of the rupture, or even measuring the closest distance to the rupture itself, can be pivotal in capturing a more nuanced understanding of seismic events characterized by significant rupture areas. The potential benefits of adopting these alternative distance metrics are evident as they may provide improved insights and more accurate predictions. It is important to acknowledge that the current study has been conducted under the constraints of available data, and thus, our exploration has centered around the epicentral distance. Despite the acknowledged potential for improved results through the

use of alternative metrics, the present study remains anchored within the available data landscape.

As a suggestion for future research, we recommend the integration of these alternative distance metrics, such as the Joyner & Boore distance or the closest distance to the rupture, into the modeling framework. This extension could yield valuable insights, expanding the depth of analysis, and broadening the applicability of our findings. We believe that this line of research could lead to a more complete and accurate understanding of seismic events, especially those that generate large areas of rupture. We hope that future researchers can explore these metrics and assess their impact on seismic event analyses, which will ultimately improve our understanding of and ability to react to catastrophic events.

Author details

Valeria Yanina Scapini Sánchez^{1,2*} and Cinthya Leonor Vergara Silva³


1 Universidad Central de Chile, Santiago, Chile

2 Universidad de Valparaíso, Valparaíso, Chile

3 Departamento de Ingeniería Industrial Universidad de Chile, Santiago, Chile

*Address all correspondence to: valeria.scapini@ucentral.cl

IntechOpen

© 2023 The Author(s). Licensee IntechOpen. This chapter is distributed under the terms of the Creative Commons Attribution License (<http://creativecommons.org/licenses/by/3.0>), which permits unrestricted use, distribution, and reproduction in any medium, provided the original work is properly cited. 

References

- [1] Lavell A, Latina A. Viviendo en riesgo. In: Comunidades Vulnerables y Prevención de Desastres en América Latina. Compilador. Colombia: La Red, FLACSO, DEPRENAC; 1994
- [2] Pelling M, Özerdem A, Barakat S. The macro-economic impact of disasters. *Progress in Development Studies*. 2002; 2(4):283-305
- [3] Cisternas M, Atwater F, Torrejón F, Sawai Y, Machuca G, Lagos M, et al. Predecessors of the giant 1960 Chile earthquake. *Nature*. 2005;437:404-407
- [4] Lagos M. Tsunamis de origen cercano a las costas de Chile. *Revista de Geografía Norte Grande*. 2000;27:93-102
- [5] Hube MA, et al. Repaired Reinforced Concrete Wall Buildings in Chile after 2010 Maule Earthquake. In: 11th US National Conference on Earthquake Engineering. 2018
- [6] Jünemann R, De La Llera JC, Hube MA, et al. A statistical analysis of reinforced concrete wall buildings damaged during the 2010, Chile earthquake. *Engineering Structures*. 2015;82:168-185
- [7] Noji EK. The public health consequences of disasters. *Prehospital and disaster medicine*. 2000;15(4):21-31
- [8] USGS - 20 Largest Earthquakes in the World, online. Available from: <https://www.usgs.gov/programs/earthquake-hazards/science/20-largest-earthquakes-world-1900>
- [9] CEPAL. Terremoto en Chile Una primera mirada al 10 de marzo de 2010, Copyright © Naciones Unidas, marzo de 2010. <https://www.cepal.org/noticias/paginas/4/35494/2010-193-terremoto-ev1.pdf>
- [10] Comerio MC. Housing Recovery in Chile: A Qualitative Mid-Program Review. Berkeley, CA: Pacific Earthquake Engineering Research Center Headquarters at the University of California; 2013
- [11] The New York Time, 2010. Maps of the Chile Earthquake [online]. [image]. 2010. [Accessed 3 March 2019]. Available from: <https://archive.nytimes.com/www.nytimes.com/interactive/2010/02/27/world/americas/0227-chile-quake-map.html?hp>
- [12] David A. Natural disasters. 1st ed (July 3, 2017). New York, NY, USA: Routledge; 2017. ISBN-10: 1138424374
- [13] Verstappen HT. Natural and human factors in environmental disasters. *Geographia Polonica*. 2003; 76(2):1-40
- [14] Benson C, Clay E. Understanding the Economic and Financial Impacts of Natural Disasters. Washington, D. C.: The World Bank; 2004
- [15] Hallegatte S. The indirect cost of natural disasters and an economic definition of macroeconomic resilience. *World Bank Policy Research Working Paper*. 2015;7357:175-184
- [16] Sen A. ¿Por qué la equidad en salud? *Revista Panamericana de Salud Pública*. 2002;11(5-6):302-309
- [17] Cavallo E, Powell A, Becerra O. Estimating the direct economic damages of the earthquake in Haiti. *The Economic Journal*. 2010;120(546): F298-F312
- [18] Cavallo E, Noy I. The Aftermath of Natural Disasters: Beyond Destruction. En CESifo Forum. München: ifo Institut

für Wirtschaftsforschung an der Universität München; 2010. pp. 25-35

[19] Centre for Research on the Epidemiology of Disaster (CRED). The human cost of natural disasters: a global perspective. 2015. Available from: <https://climate-adapt.eea.europa.eu/en/metadata/publications/the-human-cost-of-natural-disasters-2015-a-global-perspective>

[20] Anderson MB. Which Costs More: Prevention or Recovery. Managing Natural Disasters and the Environment. Washington, DC: World Bank; 1991

[21] Banco Interamericano De Desarrollo. En México, Sede Subregional. In: Un tema del desarrollo: la reducción de la vulnerabilidad frente a los desastres. Distrito Federal (D. F.), México: CEPAL, BID; 2000

[22] Kahn ME. The death toll from natural disasters: The role of income, geography, and institutions. Review of Economics and Statistics. 2005;**87**(2):271-284

[23] Andersen T. Innovative Financial Instruments for Natural Disaster Risk Management. Washington, D. C.: Inter-American Development Bank; 2002

[24] Cardona O, et al. Fiscal impact of future earthquakes and country's economic resilience evaluation using the disaster deficit index. In: A: World Conference on Earthquake Engineering. Beijing: International Association for Earthquake Engineering Chinese Association of Earthquake Engineering; 2008. pp. 1-8. Available from: <https://www.preventionweb.net/event/14th-world-conference-earthquake-engineering>

[25] Cardona OD, et al. Probabilistic seismic risk assessment for comprehensive risk management: modeling for innovative risk transfer

and loss financing mechanisms. In: The 14th World Conference on Earthquake Engineering. 2008

[26] Keipi K, Tyson J. Planning and Financial Protection to Survive Disasters. Washington, D. C.: Inter-American Development Bank; 2002

[27] Marulanda Fraume MC et al. La gestión financiera del riesgo desde la perspectiva de los desastres: evaluación de la exposición fiscal del estado y alternativas de instrumentos financieros de retención y transferencia del riesgo. Barcelona, Spain: Centro Internacional de Métodos Numéricos en Ingeniería (CIMNE); 2008

[28] Noy I. The macroeconomic consequences of disasters. Journal of Development Economics. 2009;**88**(2): 221-231

[29] Hallegatte S. An adaptive regional input-output model and its application to the assessment of the economic cost of Katrina. Risk analysis: An. International Journal. 2008;**28**(3):779-799

[30] Horwich G. Economic lessons of the Kobe earthquake. Economic Development and Cultural Change. 2000;**48**(3):521-542

[31] Vigdor J. The economic aftermath of hurricane Katrina. Journal of Economic Perspectives. 2008;**22**(4):135-154

[32] Ghesquiere F, Mahul O. Financial Protection of the State against Natural Disasters: A Primer. Vol. no 5429. Cambridge, MA: World Bank Policy Research Working Paper; 2010

[33] Kellenberg D, Mobarak AM. The economics of natural disasters. Annual Review of Resource Economics. 2011; **3**(1):297-312

[34] Jerzy N, Pearson ES. On the use and interpretation of certain test criteria for purposes of statistical inference. Part II. *Biometrika*. 1928;**20A**(3/4):263-94. DOI: 10.2307/2332112

[35] Atienza M, Aroca P. Concentración y crecimiento en Chile: una relación negativa ignorada. *EURE* (Santiago). 2012;**38**(114):257-277

Section 4

Tsunamis

Non-seismic and Complex Source Tsunami: Unseen Hazard

Ali Akbar Firoozi and Ali Asghar Firoozi

Abstract

Tsunamis, commonly induced by undersea earthquakes, are formidable natural hazards capable of causing widespread devastation. This comprehensive chapter examines the complex dynamics of tsunamis, their generation mechanisms, and their broad-reaching impacts. The multifaceted nature of tsunami triggers, both seismic and non-seismic, is dissected, highlighting the role of undersea earthquakes, landslides, volcanic eruptions, and meteorological events in driving these devastating natural phenomena. The intricate interplay of seismic parameters such as magnitude, depth, and activity type is elaborated, underscored by an insightful case study on the 2011 Tohoku Earthquake and Tsunami. A pivotal part of the discussion lies in the exploration of non-seismic triggers of tsunamis, an area often overshadowed in tsunami studies. The impact of landslide-induced and volcanically triggered tsunamis is considered alongside the contentious topic of meteorologically influenced tsunami events. Delving further into the genesis of tsunamis, the chapter explores the influences of bathymetry and tectonic structures, particularly in the context of non-seismic tsunami generation. The chapter serves as a beacon for continuous research and predictive modeling in the field of tsunami studies, emphasizing the necessity for societal preparedness and strategic risk mitigation against these potent natural disasters.

Keywords: tsunamis, seismic triggers, non-seismic triggers, undersea earthquakes, landslides, volcanic eruptions, meteorological events, bathymetry, tectonic structures, tsunami modeling, risk mitigation

1. Introduction

Tsunamis, characterized as a series of ocean waves with long wavelengths and periods, have long been a source of fascination and fear. These remarkable natural phenomena, while beautiful in their raw power and scale, can also bring about catastrophic destruction and loss of life. Their impacts have been felt around the globe, in the Pacific Ocean's Ring of Fire, the Indian Ocean, the Atlantic Ocean, and even in enclosed bodies of water like the Mediterranean Sea. While tsunamis have traditionally been associated with seismic events such as undersea earthquakes, a growing body of research has shed light on a range of non-seismic triggers, including landslides, volcanic eruptions, and certain meteorological events [1–3]. These non-seismic and complex sources of tsunamis are the primary focus of this chapter.

The study of tsunamis spans several disciplines, including geology, oceanography, and disaster risk management. Understanding these phenomena requires a holistic perspective, encompassing not just the triggers of tsunamis but also their propagation, the coastal impact, and the aftermath of these events. Seismic events such as earthquakes are the most well-known triggers of tsunamis. When tectonic plates shift on the seafloor, they can displace large volumes of water, setting off a series of waves that travel across vast distances at high speeds [4, 5]. The 2004 Indian Ocean Tsunami, triggered by a massive undersea earthquake off the coast of Sumatra, is a notable example of a seismic tsunami. However, not all tsunamis originate from seismic events. Non-seismic sources, although less common, can also trigger tsunamis. For instance, landslides, whether they occur underwater or fall into water from the land, can displace water and generate a tsunami. Similarly, volcanic eruptions can trigger tsunamis in several ways, such as through the collapse of part of the volcanic edifice or the ejection of pyroclastic flows into the sea. Furthermore, certain meteorological phenomena, like atmospheric pressure changes associated with fast-moving weather systems, can generate meteotsunamis [6, 7].

The purpose of this chapter is to delve deeper into the less-studied realm of non-seismic and complex-source tsunamis. This exploration aims to contribute to a more comprehensive understanding of tsunamis, enhancing our collective ability to predict and mitigate the impact of these devastating events. The chapter is organized into several sections. Following the introduction, we will discuss the general characteristics of tsunamis and how they differ from regular ocean waves. The subsequent sections delve into seismic and non-seismic triggers of tsunamis, each accompanied by a relevant case study. The chapter concludes with a discussion of the current methods and technologies for early warning systems and the ongoing research in the field. The forthcoming discussions aim to provide readers with a robust understanding of the different triggers of tsunamis, the mechanics of wave propagation, and the impacts of these powerful events.

2. Understanding tsunamis: from origin to impact

Tsunamis are unique oceanic events with distinctive properties that differentiate them from regular waves. These differences are extensively outlined in **Table 1**. Refer to **Table 1** for a detailed comparison of tsunamis and regular ocean waves based on parameters such as wavelength, wave speed, wave height, and energy. Additionally, **Figure 1** provides a visual representation of the mechanisms behind tsunami generation, illustrating the profound impact of seismic activities beneath the ocean's surface.

In **Figure 1(a)**, titled “Faulting,” we see a cross-section of the ocean floor during tectonic activity. Here, a subducting plate moves beneath another, causing a displacement along a fault line. This shift results in an upward thrust of the seabed, which, in turn, propels the water above it, leading to the formation of a tsunami wave. The diagram shows a direct correlation between the seabed's upward movement and the elevation of the water surface, forming a wave that begins to travel across the ocean.

Figure 1(b), labeled “Submarine slump,” depicts an alternative tsunami-generating event. In this scenario, a mass of sediment on the ocean floor, destabilized perhaps by seismic shaking or other factors, slumps down a slope. This submarine landslide displaces the water column, generating a wave in a process analogous to that observed

	Tsunami	Regular Wave
Wavelength	200 to 500 kilometers	100 to 200 meters
Wave Speed	Dependent on water depth, typically 500 to 600 km/h in deep ocean	Dependent on wind speed, typically 5 to 90 km/h
Wave Height	In open ocean: usually less than 1 meter; near shore: can exceed 30 meters	In open ocean: 1 to 15 meters; near shore: can be higher due to wave shoaling
Energy	Very high, due to long wave periods and vast wavelengths. Energy does not dissipate quickly, allowing tsunamis to travel across entire ocean basins	Less than tsunamis, due to shorter wavelengths and wave periods. Energy dissipates more quickly, limiting the reach of waves

Table 1.
Characteristics of tsunamis vs. regular waves [8].

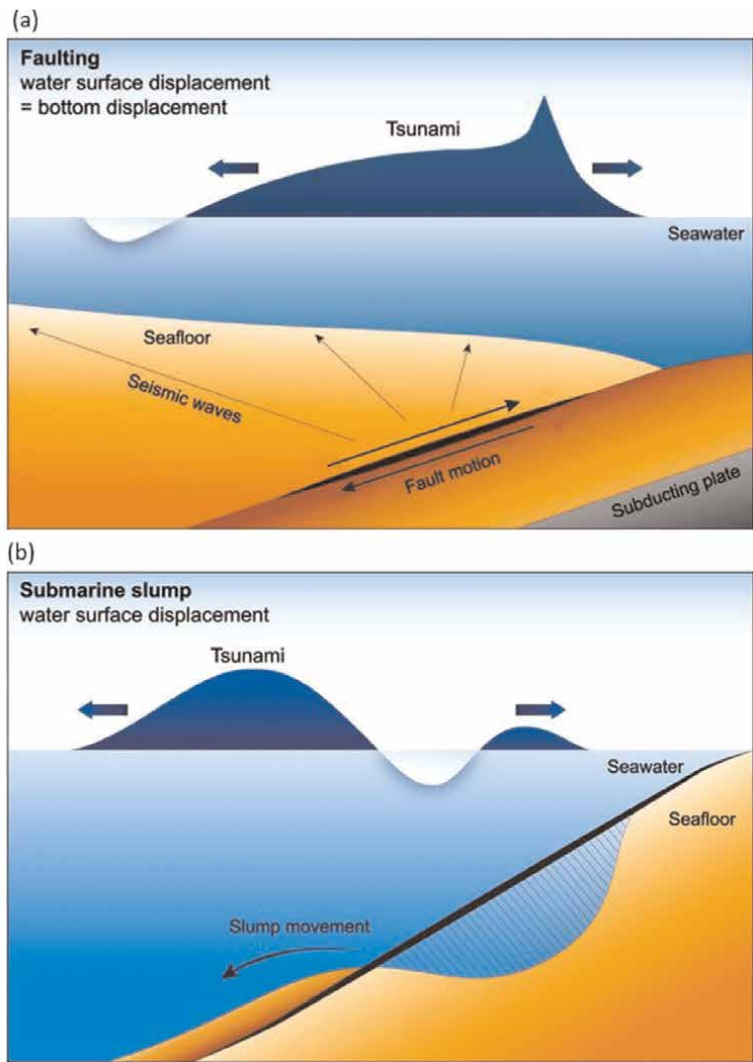


Figure 1.
The process of tsunami generation [9].

in **Figure 1(a)**. The resulting wave, or tsunami, then propagates away from the site of the slump, carrying the energy of the initial disturbance across the sea.

Through these illustrations, **Figure 1** effectively elucidates the initial seismic events that can lead to the powerful and often devastating phenomenon of tsunamis, highlighting the dynamics of fault motion and submarine landslides as primary catalysts.

2.1 General characteristics of tsunamis

Tsunamis are not typical sea waves. They are distinguished by their long wavelengths, often reaching hundreds of kilometers. This means that unlike surface waves, which involve a superficial layer of the sea, tsunamis engage the entire depth of the ocean, from the seabed to the surface. Consequently, the speed of a tsunami wave is dictated by the depth of the ocean. In the deep ocean, these waves can reach astonishing speeds of 500–600 kilometers per hour, comparable to a commercial jet's cruising speed [5, 10]. Despite their high speeds, tsunamis often go unnoticed in the open ocean. Their amplitude in deep water is usually less than one meter, and the wave crests can be hundreds of kilometers apart. Hence, ships at sea rarely detect a passing tsunami. However, as a tsunami approaches the shore and enters shallower water, its speed decreases while its amplitude grows. This transformation, known as wave shoaling, can result in destructive waves reaching heights of tens of meters when they hit the coastline. The energy a tsunami carries is immense, and it dissipates very slowly. The long wavelengths mean that tsunamis can travel across entire ocean basins with limited energy loss. This explains why a tsunami triggered off the coast of Chile can cause destruction in Japan, more than 10,000 kilometers away [11, 12].

Tsunamis are not single waves but a series of waves known as a wave train. The first wave is not always the largest, and subsequent waves may arrive minutes or even hours apart. This is why residents are often caught unaware by later, larger waves after a smaller initial wave. The devastation a tsunami can bring about is not limited to its colossal waves. Tsunamis can also cause strong ocean currents, rapid sea-level rise, and flooding, often referred to as tsunami run-up. Run-up refers to the maximum vertical height onshore above sea level reached by the tsunami. Tsunamis leave behind a distinctive sedimentary record that can provide critical insights into past events. These deposits can be used to reconstruct the frequency and magnitude of past tsunamis, thus informing risk assessments [2, 13, 14].

2.2 Distinction between tsunamis and regular ocean waves

At a casual glance, one might mistake a tsunami for an ordinary sea wave. However, tsunamis and typical ocean waves are fundamentally different in several ways, from their generation to their physical characteristics and behavior. Regular ocean waves, often referred to as wind waves, are primarily driven by the action of wind on the sea surface. These waves typically have wavelengths in the range of tens to hundreds of meters, and their period (time between successive waves) is usually between 5 and 20 seconds [15]. Wind waves involve only the uppermost layer of the ocean, and their energy rapidly dissipates with depth. In contrast, tsunamis are born from large-scale, violent disturbances in the ocean, often tectonic in origin. The wavelengths of tsunamis span hundreds of kilometers, and their period can range from several minutes to over an hour. Moreover, tsunamis engage the entire water column, meaning their energy extends all the way down to the sea floor. This gives

tsunamis their high speed in deep water and their capacity to travel vast distances with little energy loss. The behavior of tsunamis as they reach the shore is also different from regular waves. While wind waves break and dissipate their energy at the shoreline, tsunamis undergo wave shoaling, increasing their amplitude dramatically. A tsunami's energy can inundate the land, causing flooding and destruction far beyond the immediate coastline [5, 13]. Understanding these differences is crucial for effective tsunami hazard assessment and mitigation. It helps underscore why tsunamis cannot be treated like large regular waves and why they require unique approaches in terms of prediction, warning, and response.

3. Seismic triggers of tsunamis

Undersea earthquakes are the most common triggers of tsunamis. Their generation conditions, along with the influence of the earthquake's magnitude, depth, and type of seismic activity on the resulting tsunami, are complex and multifaceted. The 2011 Tohoku Earthquake and Tsunami serve as a case study illustrating these effects. **Table 2** lists major tsunami events triggered by undersea earthquakes, detailing the year, location, earthquake magnitude, depth, and the resulting tsunami's impact.

3.1 Undersea earthquakes; conditions leading to tsunami generation

Undersea earthquakes are the most common cause of tsunamis, and understanding their behavior is critical to our grasp of these devastating events. In the heart of tectonic plate interactions lies the driving force behind such earthquakes. These tectonic forces take shape in the form of plate boundaries, with convergent boundaries (also known as subduction zones) being of significant interest due to their tsunami-generating capacity. The conditions necessary for a tsunami to be generated by an undersea earthquake are nuanced. Firstly, earthquakes must occur beneath the ocean

Year	Location	Earthquake Magnitude	Depth	Tsunami Impact
2011	Pacific Ocean, off the east coast of Tohoku, Japan	9.0–9.1	29	Estimated 15,899 deaths, caused by nuclear accidents at Fukushima Daiichi Nuclear Power Plant
2004	Indian Ocean, off the west coast of northern Sumatra	9.1–9.3	30	Estimated 230,000–280,000 deaths across 14 countries, one of the deadliest natural disasters in history
1960	Pacific Ocean, near Valdivia, Chile	9.4–9.6	35	Estimated 1000–6000 deaths, caused damage in Hawaii, Japan, the Philippines, the east coast of New Zealand, southeast Australia, and the Aleutian Islands
1952	Pacific Ocean, off the east coast of Kamchatka Peninsula, Russia	9.0–9.3	30	No deaths were reported, caused damage in Hawaii and Japan
1755	Atlantic Ocean, near Lisbon, Portugal	8.5–9.0	30	Estimated 10,000–100,000 deaths, one of the deadliest earthquakes in history

Table 2.
Major tsunami events triggered by undersea earthquakes [16].

or sea floor. This ensures that there is sufficient water above the epicenter to be displaced by the earthquake's energy [17–19]. Secondly, the earthquake must be of a sufficient magnitude, generally considered to be a magnitude of 7.0 or higher on the Richter scale. Lower-magnitude earthquakes can still generate tsunamis but are less likely to result in significant wave heights upon reaching shorelines. Thirdly, the earthquake must result in significant vertical displacement of the sea floor. It is this displacement that transfers energy from the earth to the water, generating tsunami waves. Horizontal movements, which are typical of transform boundaries, do not cause significant displacement of water and thus are not typically associated with tsunamis [17, 20].

Subduction zones, where one tectonic plate is forced beneath another, are hotspots for these powerful, tsunami-generating undersea earthquakes. This is due to the intense pressure that builds up over time as the subducting plate is forced into the mantle. Eventually, this pressure is released in the form of an undersea earthquake. If the conditions mentioned above are met, a tsunami can be generated. One example of this is the 2004 Indian Ocean earthquake and tsunami, which was generated by a powerful undersea earthquake off the coast of northern Sumatra. The earthquake occurred in a subduction zone where the Indo-Australian Plate is being subducted beneath the Eurasian Plate. This event resulted in significant vertical displacement of the sea floor, generating a tsunami that killed hundreds of thousands of people around the Indian Ocean [21, 22].

3.2 Impact of magnitude, depth, and type of seismic activity

The impact of undersea earthquakes in generating tsunamis is dictated by several factors. The magnitude of the earthquake is a key factor – the greater the magnitude, the more energy is released and the greater the potential for a tsunami. Depth is also crucial, as shallow earthquakes are more likely to result in significant vertical displacement of the sea floor, which is necessary for tsunami generation. The type of seismic activity is also vital. As stated earlier, subduction zone earthquakes, which typically result in vertical displacement, are the most common cause of tsunamis. Other types of seismic activity, such as volcanic eruptions or landslides, can also generate tsunamis under the right conditions, but these are less frequent. There is a nuanced relationship between the magnitude, depth, and type of seismic activity. For instance, a high-magnitude earthquake at a very deep depth might not generate a tsunami due to the lack of displacement at the sea floor. Conversely, a lower-magnitude, shallow earthquake in a subduction zone could generate a large tsunami due to significant vertical displacement [22, 23].

3.3 Case study: 2011 Tohoku earthquake and tsunami

The Tohoku earthquake and tsunami on March 11, 2011, epitomizes the destructive power of tsunamis and highlights the role of undersea earthquakes in their generation. With a moment magnitude of 9.0–9.1, the Tohoku earthquake is the fourth largest earthquake on record and the largest ever recorded in Japan. The earthquake occurred off the northeast coast of Honshu, Japan's main island, in a subduction zone where the Pacific Plate is being forced beneath the North American Plate. The earthquake resulted in massive vertical displacement of the sea floor – up to 50 meters in some areas – generating a series of devastating tsunami waves [24, 25].

The tsunami waves reached up to 40.5 meters in height and traveled up to 10 kilometers inland in some areas. The tsunami resulted in over 15,000 deaths, and the subsequent Fukushima Daiichi nuclear disaster made it the costliest natural disaster in history. The Tohoku earthquake and tsunami demonstrated the critical need for improved tsunami forecasting and preparedness. Despite Japan's advanced tsunami warning system and strict building codes, the magnitude of the event far exceeded expectations, leading to widespread devastation. It underscored the fact that, while we have made significant advancements in our understanding of tsunamis and their seismic triggers, there is still much work to be done [26]. In conclusion, while under-sea earthquakes are the primary trigger of tsunamis, the conditions leading to their generation are multifaceted, involving the interplay of earthquake magnitude, depth, and type of seismic activity. Case studies such as the 2011 Tohoku Earthquake and Tsunami provide valuable insights into these processes, contributing to our understanding and potentially mitigating the devastation caused by these natural disasters.

3.4 Seismic triggers and their impact on tsunami generation

Understanding the seismic triggers of tsunamis begins with the realization that undersea earthquakes play a significant role due to their capability to displace substantial volumes of water abruptly. The relationship between an earthquake's characteristics and their impacts on ocean floor topography is a complex interplay significantly influencing tsunami genesis. The magnitude, depth, and location of an earthquake can directly affect the extent of seafloor deformation and, in turn, the size and energy of the resulting tsunami. Larger and shallower earthquakes typically cause more substantial displacement of the seafloor, potentially triggering more significant tsunamis. However, the tsunami's propagation and amplification depend on not only the characteristics of the earthquake but also the topographical and tectonic features of the ocean floor. These elements influence the tsunami waves as they traverse the ocean basin, causing them to refract, reflect, or amplify in certain conditions [27, 28].

While seismic tsunamis are common, their unpredictability and potential for causing widespread devastation necessitate continuous efforts in refining prediction methods and devising effective mitigation strategies. Another intriguing aspect of seismic activities associated with tsunamis is the sequence of earthquakes—namely, foreshocks, mainshocks, and aftershocks. Foreshocks precede the mainshock, the most significant earthquake in the sequence, while aftershocks follow it. The ability to distinguish foreshocks from mainshocks and aftershocks, however, is an area of ongoing research, indicating that seismic patterns may not always conform to this sequence and that generalizations should be made cautiously. The process of tsunami wave formation, triggered by undersea earthquakes, entails a series of stages. Starting from the initial seafloor displacement to the eventual propagation of waves across the ocean, each stage is a complex interplay of numerous factors. The energy released during the earthquake initiates seafloor displacement, thereby triggering the creation and propagation of tsunami waves [29, 30]. The understanding of seismic triggers and their role in tsunami generation, albeit complex, plays a pivotal role in enhancing our predictive capabilities and devising effective disaster management strategies. This condensed overview of seismic triggers provides an essential foundation for further exploring the other non-seismic triggers of tsunamis.

3.5 The role of seismic magnitude and depth in tsunami generation

The magnitude of an undersea earthquake plays a crucial role in determining the size of the resulting tsunami. Higher-magnitude earthquakes have the potential to displace larger volumes of water, creating more significant tsunami waves. However, the depth of the earthquake also plays a critical role. Shallow earthquakes can cause more substantial displacement of the seafloor and therefore generate more substantial tsunami waves than deep earthquakes with the same magnitude. The generation of tsunamis is inherently a multifaceted process influenced by a plethora of parameters. Among these, the seismic magnitude and depth of the initiating earthquake play crucial roles. Tsunamis can be instigated by undersea earthquakes of varying magnitudes and depths, affecting the amplitude, energy, and overall destructive potential of the resulting waves. Consequently, understanding the role of seismic magnitude and depth in tsunami genesis is of paramount importance, as it contributes to improved tsunami forecasting and preparedness measures. Influence of Seismic Magnitude Seismic magnitude fundamentally impacts the scale and power of the resulting tsunami. Typically, earthquakes with higher magnitudes displace larger volumes of water, leading to more substantial tsunami waves. For instance, the Great Chilean Earthquake in 1960, the most powerful earthquake ever recorded with a magnitude of 9.5, triggered a catastrophic tsunami that affected coastlines over a vast geographical area. Similarly, the 2011 Tohoku earthquake in Japan, with a magnitude of 9.0–9.1, generated a devastating tsunami that caused extensive damage and loss of life [31].

The Role of Depth The depth of the earthquake's hypocenter is another critical factor affecting tsunami genesis. Deep-focus earthquakes, despite possibly having high magnitudes, are less likely to generate destructive tsunamis due to the energy dissipating before reaching the ocean surface. On the contrary, shallow-focus earthquakes, particularly those occurring at depths less than 70 km, tend to produce more significant tsunamis, as the seismic energy is more directly transferred to the overlying water column. For example, the 2004 Indian Ocean Tsunami was triggered by a shallow undersea earthquake off the west coast of northern Sumatra, resulting in one of the deadliest natural disasters in recorded history. **The Interplay between Magnitude and Depth** Both the magnitude and depth of the earthquake must be considered concurrently to evaluate tsunami potential effectively. A high-magnitude, deep-focus earthquake may generate a less destructive tsunami compared to a lower-magnitude, shallow-focus earthquake due to differences in energy transfer to the ocean surface. As such, tsunami warning systems must account for both parameters to provide accurate and timely alerts [32, 33].

Implications for Tsunami Early Warning Systems Comprehending the role of seismic magnitude and depth in tsunami generation is integral to enhancing the effectiveness of tsunami early warning systems. These systems rely on rapid and accurate assessment of these earthquake parameters to estimate the potential tsunami threat and disseminate timely alerts to vulnerable coastal communities. Therefore, continued research and advancements in seismological studies and computational modeling are required to refine further our understanding of the complex interplay between seismic magnitude, depth, and tsunami generation. **Future Research Directions** Future research should focus on enhancing our understanding of the nuanced relationship between seismic magnitude, depth, and tsunami genesis. This may involve developing more sophisticated models that can accurately simulate the complex dynamics of undersea earthquakes and the resulting tsunami wave propagation. Additionally, further investigations into past tsunami events can provide valuable

insights and data that can be used to refine these models, ultimately leading to improved tsunami forecasting and mitigation strategies [34].

4. Non-seismic triggers of tsunamis

In addition to undersea earthquakes, tsunamis can also be triggered by other mechanisms, such as landslides, volcanic eruptions, and meteorological events. These non-seismic triggers each have unique conditions necessary for tsunami generation, which are summarized in **Table 3**. For a visual comparison of seismic and non-seismic tsunami triggers, refer to **Figure 2**.

4.1 Landslides

Landslides represent one of the significant non-seismic triggers of tsunamis, and understanding their potential to generate tsunamis is crucial for comprehensive tsunami risk assessments. A landslide occurs when a mass of rock, earth, or debris moves

Trigger Type	Conditions for Tsunami Generation	Examples
Landslide	Occur when a large amount of material slips into the water, displacing water and creating a wave.	The 1958 Lituya Bay landslide in Alaska generated a mega-tsunami with a recorded run-up of 525 meters.
Volcanic Eruption	Occur when there is a violent underwater explosion, or when a caldera collapses and displaces water.	The 1883 eruption of Krakatoa generated tsunamis that resulted in over 36,000 deaths.
Meteorological Events	Occur when atmospheric conditions cause sudden changes in sea levels. These tsunamis are also known as meteotsunamis.	In 2008, a meteotsunami hit Boothbay Harbor in Maine, resulting in significant damage to boats and waterfront property.

Table 3.
Non-seismic triggers of tsunamis [7, 35, 36].

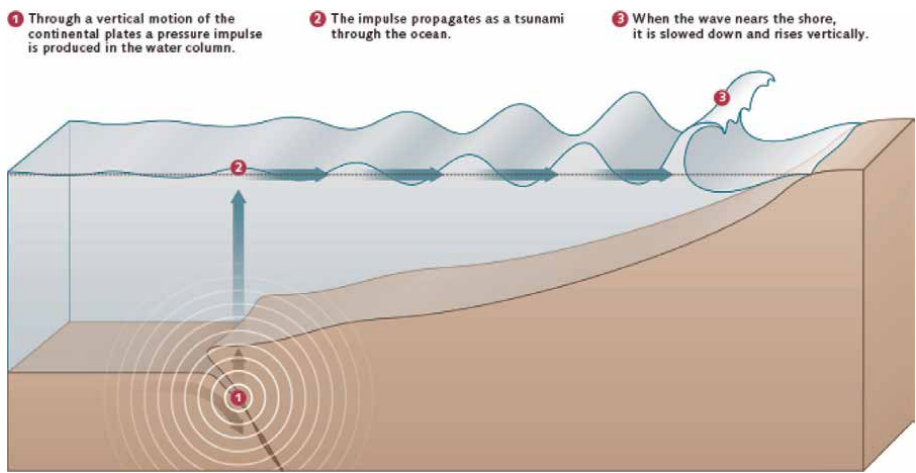


Figure 2.
Seismic tsunami wave propagation [37].

down a slope due to gravity. These movements can be slow or sudden, and when they happen underwater or impact the water from the land, they can displace large amounts of water and generate tsunamis. There are two main types of landslides that can cause tsunamis: subaerial and submarine. Subaerial landslides are those that occur on land and then slide into the water, displacing it and creating a tsunami. Submarine landslides occur directly underwater. Both types can cause significant displacement of water, leading to potentially devastating tsunamis [38].

The magnitude of a landslide and the potential tsunami largely depends on the volume and velocity of the displaced material. Larger and faster landslides displace more water, creating bigger waves. The topography of the seafloor also plays a role; slopes that are too steep or too shallow may not be conducive to tsunami generation, as the water displaced by the landslide might not propagate into a wave that travels far from the source. Moreover, landslides can either be triggered by seismic activity, such as an earthquake, or they can occur independently of any seismic event. It is also worth noting that while most landslides that cause tsunamis are natural, human activity like construction or mining can also contribute to landslide events and potentially induce a tsunami. Monitoring and modeling landslide events are essential in predicting their tsunami potential. The use of submarine mapping techniques, landslide-tsunami models, and sediment analysis can provide valuable insight into past events and improve our predictions for future landslide-induced tsunamis [6, 35, 39].

4.2 Volcanic eruptions as triggers for tsunamis

Volcanic eruptions are another prominent non-seismic source of tsunamis. Volcanic tsunamis can occur because of several different mechanisms, each dependent on the specific circumstances of the eruption. The most straightforward mechanism is through the pyroclastic flow or material from the eruption entering the sea, displacing water, and initiating a tsunami. Pyroclastic flows are rapid currents of hot gas and volcanic matter that flow down the side of a volcano during an eruption. When such a flow reaches the sea, it can displace large volumes of water, causing a tsunami. Another mechanism through which volcanic eruptions can cause tsunamis is the collapse of the volcanic edifice itself, either during or after the eruption. If a significant portion of the volcano collapses into the sea, it can displace enough water to create a tsunami. This is what occurred in the famous 1883 eruption of Krakatoa in Indonesia, which led to a devastating tsunami. Volcanic eruptions can also generate tsunamis through phreatomagmatic explosions – these occur when magma encounters water, creating steam, and causing an explosive reaction. If this reaction is significant enough, it can displace large volumes of water, leading to a tsunami [3, 40, 41]. It is worth noting that the characteristics of a volcanic tsunami – such as its initial wave height, wavelength, and speed – can be very different from those of a seismic tsunami. Therefore, different models and mitigation strategies may be required to effectively manage these types of events.

4.3 Meteorological events and tsunamis

Meteorological events such as storms and hurricanes do not typically generate tsunamis as they are generally understood. However, they can produce phenomena known as meteorological tsunamis or meteotsunamis, which are sea wave disturbances that are similar in their impact to seismic tsunamis, although they are generated by very different mechanisms. Meteotsunamis are most often caused by

fast-moving weather systems, such as squall lines, that generate pressure disturbances over the sea. These pressure changes can set up long-wavelength waves in the body of water. If the speed of the weather system is similar to the speed of the wave in the water, then resonance can occur, amplifying the wave and potentially leading to a meteotsunami. Meteotsunamis can cause significant damage and loss of life, particularly if they coincide with high tide or if they strike areas with a large population. Because the mechanisms of generation are so different, meteotsunamis require different prediction and mitigation strategies than seismic tsunamis. It is also noteworthy that some climate scientists are suggesting that climate change may increase the frequency and intensity of these meteorological events and hence meteotsunamis [7, 42]. Therefore, as our understanding of the potential impacts of climate change grows, it is becoming increasingly important to include the study of meteotsunamis in our assessments of tsunami hazards.

4.4 Case study: 1958 Lituya Bay landslide and tsunami

The 1958 Lituya Bay Landslide and Tsunami in Alaska provides a compelling example of the destructive potential of non-seismically generated tsunamis. This event remained the largest recorded mega-tsunami and was triggered by a landslide following an earthquake with a magnitude of 7.8 on the Richter scale. The earthquake itself did not generate a significant tsunami, but the secondary landslide did, dramatically illustrating the potential for non-seismic sources to generate tsunamis. The landslide caused 30 million cubic meters of rock to fall into the narrow inlet of Lituya Bay, displacing a massive amount of water. The subsequent wave was of unimaginable scale, reaching a height of 1720 feet (524 meters) and wiping out all vegetation and trees up to this elevation on the opposite shoreline [35]. While this event did not result in a high death toll (only two fatalities were reported), it nonetheless provides an excellent illustration of the incredible destructive potential of landslide-generated tsunamis. This case also emphasizes the importance of considering these types of non-seismic events in tsunami hazard assessments, particularly in areas prone to landslides. The Lituya Bay event remains a benchmark for tsunami studies, and its effects continue to be felt in the area. It stands as a powerful testament to the need for increased awareness and preparedness for all types of tsunami-generating mechanisms, whether seismic or non-seismic in origin.

4.5 Deepening the examination of non-seismic tsunami triggers

Non-seismic triggers of tsunamis are an increasingly recognized source of potential hazards. While they may not occur as frequently as seismic events, their impacts can be as devastating, if not more so, given the limited warning time and the unpredictability of such events. In the realm of landslide-generated tsunamis, there is a considerable amount of variation depending on the specific conditions and location of the landslide. For instance, the volume of displaced material, the velocity at which the landslide occurs, and the depth at which the landslide mass enters the water all play significant roles in determining the scale and impact of the tsunami [43]. Landslides can occur both above and below the water surface, and both types have the potential to generate tsunamis. Underwater landslides, however, may be particularly effective in generating tsunamis due to the proximity of the energy release to the water column and the potential for significant displacement of water.

Volcanic eruptions as tsunami triggers are multifaceted in nature. While the most straightforward cause is the collapse of the volcanic edifice or caldera into the sea, producing a landslide and, subsequently, a tsunami, other mechanisms are also at play. Pyroclastic flows and related phenomena can displace large volumes of water, as can the ejection of volcanic material into the sea. Even the seismic activity associated with the eruption can generate tsunamis, making this type of trigger particularly complex. Finally, meteorological events such as hurricanes and typhoons are another type of non-seismic trigger. These events can induce storm surges that have similar impacts as tsunamis, especially when combined with astronomical tides [44]. Furthermore, atmospheric pressure changes associated with severe weather events can generate meteotsunamis, a type of tsunami that is not caused by seismic activity or landslides but is nonetheless capable of causing significant damage. While there is a wealth of existing literature that discusses these non-seismic triggers, there is still much to be learned. As we increase our understanding of these processes, our ability to predict and mitigate the impacts of these types of tsunamis will undoubtedly improve.

4.6 Further expanding the scope of non-seismic tsunami triggers

Continuing from the above discussion, it is essential to mention that non-seismic triggers are not merely academic curiosities but have been the source of some of the most destructive tsunamis in recorded history. For example, the 1958 Lituya Bay tsunami, caused by a landslide in a fjord in Alaska, generated a wave that reached a record height of 524 meters when it surged up the opposite slope of the fjord. This event illustrates the potential for non-seismic tsunamis to exceed the scale of seismic tsunamis under specific local conditions. In the volcanic realm, the 1883 eruption of Krakatoa is an infamous example. The explosion and subsequent collapse of the volcano generated a tsunami that killed more than 36,000 people [45]. More recently, the 2018 Anak Krakatoa collapse in the same area also generated a significant tsunami, demonstrating that volcanic tsunamis are not only a historical concern but an ongoing hazard [46]. Regarding meteorological tsunamis, the 2011 Tohoku tsunami, though primarily seismic in origin, was accompanied by a meteotsunami that traveled across the Pacific, demonstrating the wide-ranging impacts of these events. Given these historical examples, it is clear that non-seismic triggers represent a significant and somewhat under-appreciated risk. Enhancing our understanding of these triggers and their effects will improve our predictive models and allow for better mitigation and preparedness efforts.

4.7 Tsunami generation through landslide and volcanic mechanisms

While seismic activities indeed constitute the majority of tsunami-triggering events, it is essential not to overlook non-seismic triggers like landslides and volcanic eruptions, which can also initiate these formidable natural phenomena. The potential of landslides to generate tsunamis arises when a considerable volume of material, like a portion of a mountain or hill, collapses into a water body. This abrupt displacement of water can set off waves that, depending on the volume and speed of the landslide, can escalate into devastating tsunamis. Landslide-triggered tsunamis have been responsible for some historically significant events. The Lituya Bay tsunami in Alaska in 1958 is a prime example, where a massive landslide triggered a mega-tsunami with wave run-up reported as high as 520 meters. Such examples provide a stark reminder of the enormous destructive potential of landslides as tsunami triggers [47]. Just like

landslides, volcanic eruptions are a potent non-seismic trigger for tsunamis. The mechanism of tsunami generation through volcanic eruptions can encompass multiple processes, such as pyroclastic flows entering water bodies, flank collapse, and caldera collapse. A striking instance of a tsunami generated by a volcanic eruption was observed during the infamous Krakatoa eruption in 1883. This catastrophic event generated a tsunami that led to widespread destruction and significant loss of life across the Indonesian archipelago. Though they may not be as frequent as their seismic counterparts, tsunamis induced by landslides and volcanic eruptions are far from negligible. Understanding these non-seismic sources and their associated complexities will undoubtedly enhance our predictive capabilities and preparedness, paving the way for effective tsunami hazard mitigation [48].

4.8 Meteorological events: a controversial non-seismic tsunami trigger

Meteorological tsunamis, also referred to as ‘meteotsunamis,’ are an intriguing category of non-seismic events known to trigger tsunamis. These are long ocean waves induced by swift changes in barometric pressure associated with fast-moving weather systems like squalls, frontal passages, and thunderstorms. Though not as formidable as seismic tsunamis, meteotsunamis can induce significant coastal inundation and damage, particularly in areas with a resonance-enhancing coastline configuration. They are primarily observed in enclosed or semi-enclosed basins like the Mediterranean Sea, the Adriatic Sea, and the Great Lakes, where the geographical configuration encourages the amplification of these waves. However, they have been observed along open coasts globally, including the East Coast of the United States and Japan. The generation of meteotsunamis is a complex interplay between the atmosphere, ocean, and coastline. Initial sea-level perturbations are caused by atmospheric pressure changes or wind stress. The wave thus generated travels across the ocean, undergoing modifications due to variations in water depth, seafloor topography, and current. Upon reaching the coast, it can be amplified or attenuated depending on the shape and orientation of the coastline and the water depth [49].

When a storm system travels over the ocean at a speed mirroring the speed of long ocean waves in that region, a phenomenon known as the “Proudman resonance,” it can induce a meteotsunami. The wave can then cross the ocean, undergoing modifications due to variations in water depth, seafloor topography, and current. Upon reaching the coast, it can experience amplification due to local resonances, causing potentially significant coastal flooding and damage. Numerical modeling and observational studies have proven instrumental in understanding meteotsunami genesis, propagation, and impact. Advancements in atmospheric and oceanic modeling now enable us to simulate meteotsunami events with considerable accuracy. These models typically employ equations of fluid dynamics to simulate the interaction between the atmosphere and ocean, and wave propagation [50].

Despite these advancements, there remain hurdles in accurately predicting meteotsunamis, particularly in real-time. The rapid temporal and spatial changes in barometric pressure and wind speed associated with storm systems, which are challenging to predict, are primarily responsible. Furthermore, the resonance conditions that can substantially amplify these waves at the coast are complex and site-specific, necessitating high-resolution bathymetric and topographic data. In conclusion, continuous research and technological advancements are progressively enhancing our understanding of meteotsunamis, their impact on coastlines, and our ability to predict them. This understanding is crucial for devising appropriate mitigation strategies and

early warning systems to minimize these events' impact. With meteotsunamis emerging as a recognized hazard, increased research is required to comprehend their occurrence patterns, the conditions leading to significant events, and their potential impact under future climate change scenarios [51].

4.9 Case study: 1958 Lituya Bay landslide and tsunami

The 1958 Lituya Bay tsunami, triggered by a landslide in Alaska, serves as a noteworthy case study for understanding the mechanisms and impacts of non-seismically induced tsunamis. Occurring on July 9, 1958, in Lituya Bay, located on the Fairweather Fault in the Alaska Panhandle, the event remains one of the most significant landslide-induced tsunamis in recorded history. The event was triggered by an earthquake with a magnitude of 7.8 on the Richter scale. This earthquake induced a massive landslide on the steep slopes of the Gilbert Inlet at the head of the bay. An estimated 30 million cubic meters of rock fell from a height of several hundred meters into the bay, displacing an equivalent volume of water and triggering a massive wave. The wave surged up the opposite slope, reaching an unprecedented run-up height of 524 meters (approximately 1722 feet) and removing all vegetation and soil down to bedrock. This run-up height remains the highest ever recorded for a tsunami and offers a stark reminder of the potential for substantial wave amplification in narrow, steep-sided inlets. Observations of the aftermath and analysis of the event provided valuable insights into the generation and propagation of landslide-induced tsunamis. It highlighted the role of the initial impulse – both the magnitude and direction – given by the landslide to the water body in determining the wave characteristics. The steepness of the slope, the velocity of the landslide, and the volume of the displaced material were key factors influencing the magnitude and direction of the tsunami [35].

The incident emphasized the potential for significant local amplification of the tsunami height, particularly in enclosed or semi-enclosed water bodies with specific topographic features. In the case of Lituya Bay, the narrow, steep-sided inlet served to focus the wave energy, leading to the extraordinary run-up height observed. The event also highlighted the importance of local geological and geomorphological conditions in tsunami generation and propagation. The presence of the Fairweather Fault, one of the fastest-moving transform faults globally, likely contributed to the instability of the slopes around the bay and the triggering of the massive landslide [35]. Despite being a rare event, the Lituya Bay landslide and tsunami underscore the importance of considering non-seismic tsunami triggers in hazard assessment and mitigation strategies. It demonstrates that non-seismic events can induce tsunamis, with local effects far surpassing those of seismic tsunamis.

Since the 1958 event, continued research has improved our understanding of landslide-induced tsunamis. Advances in numerical modeling techniques now allow for more accurate simulations of such events, contributing to enhanced tsunami hazard assessments. While significant progress has been made, challenges remain. Predicting the occurrence of landslides, particularly submarine landslides, is difficult due to the multitude of contributing factors and their inherent unpredictability. More research is required to better understand these triggers and enhance our predictive capabilities, ultimately reducing the risk posed by these devastating events [52]. In conclusion, the 1958 Lituya Bay event serves as a potent reminder of the hazards posed by non-seismic tsunamis. It emphasizes the need for continued research and investment in monitoring and early warning systems to mitigate these events' impacts.

5. Modeling tsunami generation from non-seismic sources

Tsunami modeling is a critical tool for understanding the dynamics of tsunami generation and propagation, particularly from non-seismic sources. The non-seismic triggers, such as landslides, volcanic eruptions, and meteorological phenomena require different computational models and methodologies as compared to seismic tsunamis. Non-seismic tsunamis have specific characteristics that pose unique challenges for modeling. For instance, landslides and volcanic eruptions often involve a complex interplay of solid and fluid dynamics, making their modeling a multi-physics problem. Meteorological tsunamis, on the other hand, require detailed knowledge of atmospheric processes and their interaction with the ocean [52].

One of the pioneering efforts in the modeling of non-seismic tsunamis was the work of Harbitz [53], who developed a two-phase flow model to simulate submarine landslide-induced tsunamis. This model considers the momentum exchange between the solid landslide material and the water, allowing for a more realistic representation of the tsunami generation process [53]. Such multiphase flow models have since been extended and refined by many researchers, incorporating features like complex landslide kinematics, granular flow physics, and varying bathymetry. Today, these models form the basis for our understanding and prediction of landslide-induced tsunamis. The modeling of volcanic tsunamis is a similarly complex task. It involves understanding and simulating processes such as the collapse of volcanic edifices, the interaction of hot pyroclastic flows with water, and the explosive entry of magma into a water body. Recent advancements in computational fluid dynamics (CFD) have made it possible to simulate such complex processes with reasonable accuracy. Researchers have used CFD to study various volcanic processes and their potential to generate tsunamis, contributing significantly to our understanding of these phenomena [54].

Despite these challenges, considerable progress has been made in the modeling of non-seismic tsunamis over the past few decades. Numerical models have become increasingly sophisticated, incorporating more realistic physics and higher levels of detail. These models have provided invaluable insights into the generation and propagation mechanisms of non-seismic tsunamis, contributing to improved hazard assessments and mitigation strategies. However, there is still much work to be done. The inherent unpredictability and complexity of non-seismic tsunami triggers require the continual refinement of models and methodologies. Ongoing research and investment in computational resources are needed to advance our understanding of these events and to mitigate their risks effectively. In summary, modeling tsunami generation from non-seismic sources is a complex but essential task. Continued research in this area is critical for improving our understanding of these phenomena, enhancing tsunami hazard assessments, and developing effective mitigation strategies.

6. Role of bathymetry in non-seismic tsunami generation

Bathymetry, the underwater topography of ocean floors, plays an intricate role in the generation and propagation of non-seismic tsunamis. This role is amplified considering the complex interactions involved in the non-seismic triggers of tsunamis, such as landslides, volcanic eruptions, or meteorological phenomena. Bathymetry directly affects the initiation and development of landslides, both submarine and coastal, which are crucial triggers of non-seismic tsunamis. The stability of slopes underwater and their likelihood of failure, leading to a landslide, depend heavily on

their geometry, which is determined by bathymetry. Steeper slopes are more likely to fail, while underwater canyons can guide the path of a sliding mass of sediments, directing the energy of the resulting tsunami in specific directions. The propagation of a tsunami wave, once generated, is significantly affected by bathymetric features. The wave's speed, direction, and amplitude can be altered by the underwater topography as the wave travels across the ocean floor. Shoaling effects, where the wave height increases as the water depth decreases, can significantly amplify a tsunami's destructive power in coastal regions. Volcanic eruptions occurring underwater or on islands can also generate tsunamis, and bathymetry plays a significant role here as well. Submarine volcanic eruptions can directly displace water, triggering a tsunami. The bathymetry around the volcano determines how this initial wave evolves and propagates [48, 55].

An interesting aspect of bathymetry's role in non-seismic tsunamis comes from the study of meteorological tsunamis, which are generated by atmospheric disturbances. Bathymetry can modulate these tsunamis, with the resonance between the wave frequency and the natural frequencies of semi-enclosed basins, such as the Mediterranean and Adriatic Seas, increasing the wave's amplitude. Bathymetry's influence on non-seismic tsunamis cannot be overstated, making accurate bathymetric data essential for assessing the potential impact of these events. Advanced technologies like multibeam sonar have allowed for detailed mapping of the ocean floor, providing the necessary data for more accurate modeling and prediction of non-seismic tsunamis [8, 56].

Despite the progress made, challenges remain in understanding and predicting the interactions between bathymetry and non-seismic tsunamis. For instance, the complexities of landslide dynamics, the influence of various bathymetric features on wave propagation, and the resonance effects in semi-enclosed basins all require further study. In summary, bathymetry plays an essential role in the generation and propagation of non-seismic tsunamis. Ongoing research and data collection are crucial to deepen our understanding of these interactions and improve our ability to predict and mitigate the impacts of these potentially devastating events.

7. Role of tectonic structures in non-seismic tsunami generation

Tectonic structures, whether undersea or terrestrial, play an integral role in the generation and propagation of non-seismic tsunamis. Non-seismic tsunamis occur due to triggers that do not involve tectonic earthquakes but are often closely tied to tectonic features. Understanding these features and how they interact with the generation and propagation of tsunamis is crucial for predicting the impact and formulating mitigation strategies. Undersea landslides, an important cause of non-seismic tsunamis, can be associated with tectonic structures. Submarine landslides occur where sediment deposited on a sloping sea floor becomes unstable and moves downslope. This instability can be caused by a variety of factors, but a key one is the geometry of the sea floor, which is largely determined by tectonic processes [57]. Fault lines and the presence of weak, fractured, or deformed sedimentary layers due to tectonic activity can act as zones of weakness that make a slope susceptible to failure.

Similarly, volcanic eruptions and associated processes can cause non-seismic tsunamis, and these volcanoes are typically located near tectonic plate boundaries. The violent release of magma and gases can cause deformation of the sea floor, leading to displacement of water and the generation of a tsunami. In some cases, a flank or side

of the volcano might collapse, triggering a massive landslide and subsequent tsunami, as happened in the case of the 1883 Krakatoa eruption. A significant source of non-seismic tsunamis is meteor impacts, which, while not directly influenced by tectonic structures, interact with the bathymetry and undersea topography that are tectonically formed. The impact crater and its size and shape, determined by the impactor's size, speed, and angle of impact, also influence the initial tsunami generation [58].

The propagation and impact of non-seismic tsunamis, once generated, can also be influenced by tectonic structures. Submarine ridges and trenches can focus or defocus tsunami energy, leading to larger or smaller wave amplitudes at certain locations. Tsunamis also experience refraction due to changes in water depth, which is primarily controlled by tectonic processes. In summary, tectonic structures play a significant role in the generation and propagation of non-seismic tsunamis, and understanding these roles is crucial for assessing the potential impact and risk associated with these events.

8. Modeling non-seismic tsunami generation

Modeling tsunami generation, especially those resulting from non-seismic triggers such as landslides, volcanic eruptions, and meteorological phenomena, is a challenging task due to the intricate dynamics and unique features associated with these events. Recent advancements in computational techniques and the growing availability of high-resolution bathymetric and topographic data have started to enable more accurate and detailed modeling of these tsunamis.

Modeling non-seismic tsunamis involves many complex processes, including the initial trigger (like a landslide or a volcanic eruption), the propagation of the tsunami waves across the ocean, and their interaction with the coastline. These processes occur over different temporal and spatial scales, demanding highly flexible and efficient computational models. For example, simulating a landslide-triggered tsunami may require modeling the landslide motion, the wave generation, and wave propagation, each of which occurs on a different time scale and may require different model parameters. When modeling landslide-triggered tsunamis, one has to consider the dynamics of the landslide itself, which include its initial position, volume, shape, and motion. This is often done using geotechnical models, which are then coupled with hydrodynamic models to simulate wave generation and propagation. Several numerical methods have been employed for these purposes, including finite element, finite difference, and boundary integral equation methods, each with its unique strengths and limitations. One of the challenges in modeling landslide-triggered tsunamis is accurately representing the underwater topography and the landslide geometry. Advances in seafloor mapping technologies and satellite imagery have provided more detailed bathymetric and topographic data, enabling more precise landslide and tsunami modeling. Generation of tsunamis triggered by volcanic activities requires a different approach. It demands a comprehensive understanding of the various processes involved in volcanic eruptions, such as the explosion, the collapse of the volcanic edifice, the ejection of pyroclastic material, and the resultant displacement of water. Each of these processes can contribute to the generation of a tsunami and should be accurately represented in the model [59, 60].

Another challenge in modeling volcanic tsunamis is the unpredictability of volcanic behavior. The timing, size, and type of eruption can vary greatly, making it difficult to develop a generic model. Nevertheless, progress has been made in modeling specific types of volcanic events, such as flank collapses and pyroclastic flows,

which are known to generate tsunamis. Tsunamis induced by meteorological phenomena, often referred to as meteotsunamis, present their unique modeling challenges. These tsunamis are generated by atmospheric disturbances, such as pressure jumps, squalls, or frontal passages, which create wave trains in the ocean. The wave trains can amplify under certain conditions, such as resonance with the natural frequencies of the basin or coastline [8, 54, 61].

Modeling meteotsunamis require coupling atmospheric and oceanic models, which is a complex task. The atmospheric model should be able to represent the spatial and temporal variations in atmospheric pressure, while the oceanic model should be able to simulate the wave response to these pressure variations. One of the key challenges in this process is capturing the resonance effects, which can greatly amplify the wave heights. While significant progress has been made in modeling non-seismic tsunamis, there is still room for improvement. The current models can often provide valuable insights into the potential tsunami hazards associated with different events and guide the development of mitigation strategies. However, they are typically based on simplified assumptions, such as linear wave theory or idealized bathymetry, which may not accurately represent the complex reality. Future advancements in tsunami modeling will likely come from several directions. On the one hand, further developments in computational techniques and technologies, such as high-performance computing and machine learning, could allow more accurate and efficient simulations. On the other hand, more detailed and comprehensive data collection, through advanced seafloor mapping, satellite imagery, and oceanographic observations, could provide the necessary inputs for these models. In addition, there is a growing interest in developing probabilistic tsunami hazard assessments, which incorporate the uncertainties in the source parameters and provide estimates of the likelihood of different tsunami scenarios. This approach, already used in seismic hazard assessment, could offer a more comprehensive understanding of the tsunami risks and inform the planning and design of coastal infrastructure [62–65].

Table 4 provides a comparison of different tsunami modeling techniques, outlining their underlying assumptions, computational requirements, and typical use cases. The table juxtaposes linear wave theory-based models, which are primarily used for initial simulations and long-distance propagation studies, with more complex Nonlinear models that provide greater accuracy for near-field simulations and inundation studies. It also introduces the coupled atmospheric-oceanic models, which consider both atmospheric and oceanic dynamics to study phenomena like meteotsunamis. The computational requirements increase with the complexity and sophistication of the model, underscoring the trade-off between model accuracy and computational efficiency. The choice of a suitable modeling approach depends on the specific research question and the resources at hand. The Linear Wave Theory is governed by the wave equation, which measures the wave elevation, i.e., the vertical displacement of the water surface, as a function of gravity and the spatial part of the wave. This equation is especially useful for predicting the behavior of smaller, less complex waves but may not adequately capture the behavior of larger or more complex tsunamis. The governing equation for linear wave theory can be expressed as:

$$\partial^2 \eta / \partial t^2 = g \nabla^2 \eta \quad (1)$$

where η is the wave elevation (the vertical displacement of the water surface), g is the acceleration due to gravity, t is time, and ∇^2 is the Laplace operator representing the spatial part of the wave (it gives us the divergence of the gradient of η).

For more complex modeling, particularly in shallow water environments where most tsunami impact occurs, the Nonlinear Shallow Water Equations, or Saint–Venant equations, are often employed. These equations are derived from the Navier–Stokes equations and represent a system of hyperbolic partial differential equations. The Saint–Venant equations model the total water depth and velocities in two directions, considering gravity, bathymetry, and spatial coordinates. Although these equations simplify real-world conditions, they provide a solid foundation for tsunami simulation models, helping predict wave propagation and run-up with greater accuracy. As with all models, the accuracy of predictions based on these equations depends on the quality of the input data and how well the assumptions of the model match real-world conditions. The Saint-Venant equations are a set of hyperbolic partial differential equations derived from the Navier-Stokes equations. They are used to model the shallow water approximations and are particularly useful for tsunami wave propagation and run-up simulations. The Saint-Venant equations can be written as:

$$\partial h / \partial t + \partial(hu) / \partial x + \partial(hv) / \partial y = 0. \tag{2}$$

$$\partial(hu) / \partial t + \partial(hu^2 + \frac{1}{2}gh^2) / \partial x + \partial(huv) / \partial y = gh \partial b / \partial x \tag{3}$$

$$\partial(hv) / \partial t + \partial(huv) / \partial x + \partial(hv^2 + \frac{1}{2}gh^2) / \partial y = gh \partial b / \partial y \tag{4}$$

where h is the total water depth, u and v are the velocities in the x and y directions, respectively, g is the acceleration due to gravity, t is time, b is the bathymetry (depth of water at rest), and x and y are the spatial coordinates.

In the ever-evolving field of tsunami research, various modeling techniques have been developed to understand and predict the behavior of these massive wave events. **Table 4** presents a comparative analysis of the most prominent tsunami modeling

Modeling Technique	Underlying Assumptions	Computational Requirements	Typical Use Cases	References
Linear wave theory-based models (Shallow Water Equations)	Neglects nonlinear wave interactions, assumes small wave amplitudes and wave speeds are determined solely by water depth	Lower computational cost, less computationally intensive	Ideal for initial simulations, studying long-distance tsunami propagation	[66]
Nonlinear models (Boussinesq Equations)	Considers nonlinear wave interactions, allows larger wave amplitudes and wave speeds are determined by both water depth and wave amplitude	Higher computational cost, more computationally intensive	More accurate for near-field simulations, studying wave run-up and inundation	[67]
Coupled atmospheric-oceanic models (WRF-HyCOM)	Represents atmospheric pressure variations and oceanic wave response, integrates both atmospheric and oceanic dynamics	Complex, requires both atmospheric and oceanic data	Needed for meteotsunami modeling, studying the impact of atmospheric disturbances on the ocean	[68]

Table 4.
Comparison of tsunami modeling techniques.

techniques. The table contrasts these techniques based on factors like computational efficiency, accuracy, application range, and underlying principles. By understanding the strengths and limitations of each method, researchers and policymakers can make informed decisions in both academic and real-world tsunami mitigation efforts. As tsunamis continue to pose significant threats to coastal communities worldwide, such comprehensive comparisons are crucial for the advancement of preventative strategies and response mechanisms.

9. Characteristics of tsunamis: wavelength, speed, energy, and destructive power

Tsunamis, often incorrectly referred to as tidal waves, are a series of waves with long wavelengths and periods that are typically caused by large-volume displacements of water due to undersea earthquakes, landslides, volcanic eruptions, or meteor impacts. Understanding the key characteristics of tsunamis – namely their wavelength, speed, energy, and destructive power – is crucial for predicting their behavior and mitigating their impact. This knowledge is particularly relevant for communities living in coastal areas, where the effects of tsunamis are most devastating [69].

9.1 Explanation and importance of these characteristics

- *Wavelength:* The wavelength of a tsunami refers to the distance between successive wave crests. Tsunamis have exceptionally long wavelengths, often exceeding hundreds of kilometers, which distinguish them from typical wind-generated waves with lengths of just tens of meters [70]. The long wavelength means tsunamis are classified as shallow-water waves, regardless of the depth at which they travel. This property impacts the way tsunamis behave as they approach shorelines, with implications for the resultant flooding and destruction.
- *Speed:* Tsunami speed depends on the depth of the water in which it's traveling. In the open ocean, tsunamis can reach incredible speeds of over 700 km/h, roughly the speed of a jet airplane. This high speed allows tsunamis to cover vast distances across ocean basins in a relatively short time [71].
- *Energy:* Tsunamis carry enormous energy, sourced from the initial geophysical event that triggered them. This energy is initially spread across the wave front as it propagates through the ocean. As a tsunami nears the shore and the water depth decreases, wave speed drops, and wave height increases as the energy is compressed into a smaller volume of water. This compression often leads to the devastating impact of tsunamis when they hit land [72, 73].
- *Destructive Power:* The destructive power of a tsunami is determined by a combination of its size, speed, and the local topography of the land it impacts. The long wavelength and high energy lead to extensive inundation of coastlines. Moreover, tsunamis do not arrive as a single destructive wave but as a series, with successive waves causing additional damage [72, 73].

9.2 How these properties change as tsunamis approach shorelines

As tsunamis travel from the deep ocean toward the shore, their characteristics transform dramatically, largely due to decreasing water depth. Understanding these transformations can help predict the likely impact of a tsunami on coastal regions. As the depth of water decreases, the speed of the tsunami reduces due to drag along the seafloor. This slowing down of the tsunami wave causes the energy of the wave to be compressed into a smaller volume, causing an increase in the wave's height – a process known as wave shoaling. The wave can grow to be many meters high, far exceeding typical ocean waves [69, 74]. The long wavelength of tsunamis also results in wave run-up on the shore, which is the vertical height above sea level that a wave reaches up a slope or structure. The run-up can exceed the height of the tsunami in deep water by many times, resulting in further inundation and potential damage. The interaction of a tsunami wave with the coastal topography can also create local effects that influence its impact. For example, bays, inlets, and the shape of the seafloor can focus or defocus the tsunami energy, significantly influencing the height and power of the tsunami at the point of impact [70, 71]. In summary, understanding the characteristics of tsunamis and how they change as tsunamis approach shorelines is crucial for the development of accurate tsunami warning systems and the implementation of effective mitigation strategies. It allows for a more precise prediction of the areas at risk, the potential extent of inundation, and the likely destructive power of an incoming tsunami.

10. Coastal impact and inland penetration

Tsunamis pose a significant threat to coastal communities around the world. Once these waves reach the shoreline, they can cause widespread devastation, loss of life, and extensive economic damage. Understanding how tsunamis interact with coastal features and penetrate inland is key to effective disaster management planning and risk mitigation. This includes understanding the run-up process, the extent of inland penetration and inundation, and learning from past events such as the 2004 Indian Ocean Tsunami.

- *The Run-up Process: What Happens When a Tsunami Reaches the Shore?* The run-up process begins when a tsunami wave reaches shallow water near the coast. At this point, the wave slows down and starts to grow in height due to the wave shoaling effect. This height increase can be amplified by local topographic features, such as the shape of the seafloor, coastal embayment's, and offshore reefs. As the wave reaches the shoreline, it continues to rise above the normal sea level, a phenomenon known as run-up. The vertical height of the wave above the mean sea level at its maximum inundation point is referred to as the run-up height. This is typically the most destructive part of a tsunami, as the water rushes onto land, causing extensive damage to infrastructure and loss of life [70, 75]. The run-up process is influenced by a range of factors, including the characteristics of the tsunami (e.g., wave height, period, and wavelength), the bathymetry (shape of the seafloor), and the local coastal topography. Given the complexity of these interactions, numerical models are often used to predict the run-up height and extent of inundation in specific coastal settings [76].

- *Inland Penetration and Inundation Extent:* The extent of inland penetration and inundation of a tsunami wave is largely determined by the local topography, the tsunami's energy and momentum, and the coastal land use and vegetative cover. Flat, low-lying areas are particularly vulnerable to extensive inland penetration and inundation. Coastal vegetation, such as mangroves, can provide some level of natural defense by absorbing energy and reducing the speed of the incoming water, although their effectiveness depends on the tsunami's size and the vegetation's density [77]. The process of inundation extends beyond the initial impact of the tsunami wave. As the wave retreats toward the sea, it carries with it debris and sediment, causing further damage and reshaping the coastal landscape. Additionally, tsunamis often consist of multiple waves, each with the potential for run-up and inundation. Therefore, the damage from a tsunami event can continue for several hours after the first wave impact. Predicting the extent of inland penetration and inundation is crucial for coastal risk management. Numerical models are commonly used for these predictions, incorporating data on tsunami characteristics, bathymetry, and coastal topography. However, these models require validation and calibration based on field observations from past tsunami events [75, 76].
- *Case Study: 2004 Indian Ocean Tsunami:* The 2004 Indian Ocean Tsunami, triggered by one of the most powerful earthquakes in recorded history off the west coast of northern Sumatra, offers a stark illustration of the devastating impact of tsunamis on coastal communities. The earthquake, with a magnitude of 9.1–9.3, generated a tsunami that radiated across the entire Indian Ocean, causing widespread damage and loss of life in 14 countries. In terms of the run-up process and inland penetration, the impacts varied greatly across the affected regions, reflecting differences in local topography, coastal features, and the magnitude of the tsunami waves. The highest recorded run-up height was over 50 meters on the west coast of Sumatra, near the earthquake epicenter. On the coasts of Thailand, Sri Lanka, India, and the Maldives, run-up heights of 2 to 15 meters were commonly reported [78]. The extent of inundation was also highly variable, reaching up to 5 kilometers inland in Sumatra's flat coastal plains. In other areas, the inundation was less extensive but still caused significant damage due to the high population density and extensive infrastructure along the coasts [79]. The 2004 Indian Ocean Tsunami underscored the need for comprehensive tsunami risk management, including early warning systems, public education, and land-use planning in coastal areas. It also highlighted the importance of understanding the complex processes of tsunami run-up, coastal impact, and inland penetration for predicting the potential impacts of future events and developing effective mitigation strategies.

11. Mitigation measures and warning systems

Tsunamis, due to their destructive nature and potential for significant loss of life and property, necessitate robust mitigation measures and early warning systems. Effective warning systems for tsunamis involve a combination of seismic activity monitoring, deep-ocean assessments, and coastal sea-level monitoring. **Figure 3** encapsulates the intricate system designed for tsunami monitoring, early warning, and hazard assessment, detailing the sequence from seismic detection to community response.

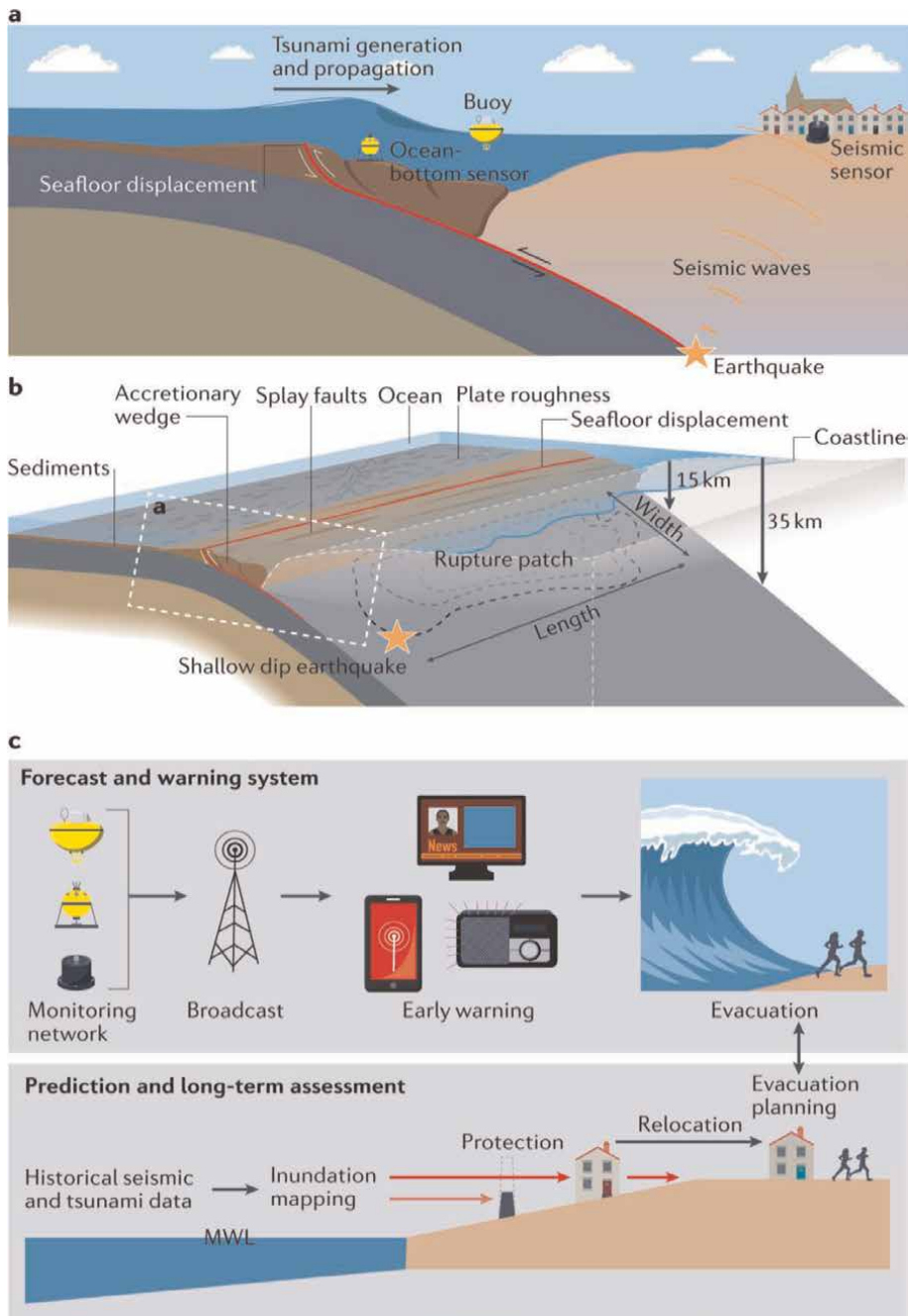


Figure 3.
Tsunami monitoring, early warning, and hazard assessment [80].

Panel a of **Figure 3** depicts the initial phase where an earthquake occurs, causing a shift in the seafloor and potentially generating a tsunami. This seismic activity is detected by ocean-bottom sensors, which relay information to seismic sensors on land. The data collected is critical for determining the magnitude of the earthquake and the likelihood of a tsunami.

In Panel b, the focus shifts to the underwater topography and fault dynamics that contribute to tsunami generation. The diagram illustrates an earthquake occurring along a shallow dip fault, with parameters such as the rupture patch length and width, and the sediment layers that might influence the nature of the seismic event. The accretionary wedge, splay faults, and plate roughness are labeled, showcasing the complexity of the ocean floor where tsunamis originate.

Panel c is divided into two key components of tsunami risk management: the forecast and warning system, and the prediction and long-term assessment. In the forecast and warning section, a flowchart illustrates the progression from a monitoring network, which could include instruments like DART buoys, to the broadcast of warnings through various communication channels, culminating in the evacuation of people to safer areas. The lower part of Panel c highlights the importance of historical data for predicting future events, inundation mapping for understanding potential impact areas, and the development of protection and relocation strategies to minimize risk.

Together, these visuals in **Figure 3** present a comprehensive overview of the sophisticated approach to managing the threat of tsunamis, from undersea detection to strategic community planning. This multi-tiered strategy is vital for safeguarding coastal regions from the often catastrophic consequences of these formidable natural events.

11.1 Traditional and modern tsunami warning systems

Historically, people living in tsunami-prone regions have relied on natural signs, such as the sudden recession of the sea, ground shaking, or specific animal behaviors, to warn of an incoming tsunami. However, these traditional warning signs provide little advance warning and may not be recognized by all community members, especially visitors or those who are asleep or indoors. Modern tsunami warning systems, in contrast, leverage scientific and technological advancements to rapidly detect seismic events, determine their tsunami generation potential, and disseminate warnings to potentially affected communities. These systems typically involve a network of seismometers to detect undersea earthquakes, tide gauges and deep-sea pressure sensors to measure changes in sea level and wave characteristics, and computer models to forecast tsunami propagation and inundation. Upon detection of a potentially tsunamigenic earthquake, the warning system analyzes the seismic data to estimate the earthquake's location, depth, and magnitude. If the event is deemed to have high tsunami generation potential, a tsunami warning is issued, typically through a range of channels to ensure broad dissemination. This may include sirens, broadcast media, text messages, and social media alerts [81, 82].

11.2 Coastal defenses and their effectiveness

A range of coastal defenses can be employed to mitigate the impacts of tsunamis, from natural systems such as mangroves and coral reefs to engineered structures such as seawalls and breakwaters. The effectiveness of these defenses varies widely and depends on the size of the tsunami, the specific characteristics of the coastal area, and the design and maintenance of the defense structures. Engineered defenses, such as seawalls and breakwaters, are designed to absorb the energy of incoming waves and prevent or reduce inundation. While these structures can be effective against smaller tsunamis, they may be overwhelmed by larger events, as was the case in the 2011

Tohoku Earthquake and Tsunami in Japan. Moreover, these structures can be expensive to build and maintain, and they can have negative impacts on coastal ecosystems and beach accessibility. Natural defenses, such as mangroves, coral reefs, and sand dunes, can also protect against tsunamis by absorbing wave energy and reducing the speed and height of incoming waves. These natural systems offer the added benefits of enhancing coastal biodiversity, sequestering carbon, and providing recreational opportunities. However, their effectiveness is limited by their extent and density, and they may not provide sufficient protection against large tsunamis [21, 83].

11.3 Community preparedness and education

In addition to warning systems and physical defenses, community preparedness and education are critical components of tsunami risk mitigation. This includes developing evacuation plans, conducting regular drills, educating community members about tsunami risks and response strategies, and building resilient infrastructure. Evacuation plans should include clearly marked evacuation routes and assembly points, and they should be designed to ensure that all community members can reach a safe location within the available warning time. Regular drills can help to familiarize community members with these plans and identify potential issues before a real event occurs. Education programs can raise awareness of tsunami risks, provide information on natural warning signs and appropriate response actions, and promote a culture of preparedness. These programs can target various audiences, including students, residents, and visitors, and they can utilize a range of formats, from school curriculums and community workshops to informational signs and online resources [84, 85].

11.4 Case study: tsunami warning and mitigation in Japan

Japan, as a country located in a highly seismic region, has developed one of the most advanced tsunami warning and mitigation systems in the world. This includes a dense network of seismometers and sea-level monitoring stations, sophisticated tsunami forecasting models, extensive coastal defenses, and comprehensive community preparedness programs. In the wake of the 2011 Tohoku Earthquake and Tsunami, Japan has made significant improvements to its tsunami warning system, including installing additional deep-sea pressure sensors and developing improved tsunami prediction models. Despite these advances, the 2011 event underscored the limitations of engineered defenses and the importance of timely and accurate warnings. The event also highlighted the need for continued improvements in community preparedness, particularly in terms of evacuation planning and public education [86, 87].

12. Emerging research and future directions

The past two decades have seen significant advancements in our understanding of tsunamis and their triggers. This progress has been driven by several major tsunami events, which have provided new data and insights, as well as technological advances in fields such as seismology, oceanography, and numerical modeling. In this section, we review some of the key developments and outline potential directions for future research.

- *Recent Developments in Understanding Tsunami Generation:* Several recent developments have improved our understanding of the processes involved in tsunami generation. These advancements have been facilitated by an increase in the quality and quantity of data available for analysis, as well as advancements in numerical modeling techniques. A significant development is the recognition that non-seismic sources, such as landslides and volcanic eruptions, can also generate tsunamis. This understanding has been advanced by events such as the 1958 Lituya Bay landslide in Alaska and the 2018 Anak Krakatau eruption in Indonesia, which generated significant tsunamis. Researchers are now investigating the specific conditions under which these non-seismic events can trigger tsunamis, and how the characteristics of these tsunamis may differ from those triggered by seismic events [88, 89]. Another area of advancement is in our understanding of how the characteristics of seismic events, such as their magnitude, depth, and type, affect tsunami generation. For instance, researchers have found that larger magnitude earthquakes are more likely to generate tsunamis and that the depth and type of the earthquake can also play a crucial role. In addition, there have been significant advances in the modeling of tsunami generation and propagation. These models incorporate complex bathymetric and topographic features, as well as realistic representations of the seafloor displacement caused by seismic events. Such models can help researchers better understand and predict the behavior of tsunamis and are an important tool for tsunami hazard assessment [21, 90].
- *Directions for Future Research:* There are several areas that warrant further exploration in future research. One of these is a deeper understanding of non-seismic tsunami sources. While significant progress has been made, there is still much to learn about the conditions under which landslides, volcanic eruptions, and meteorological events can generate tsunamis and how these tsunamis may differ from those caused by seismic events. Another area of potential research is in the development of more accurate and comprehensive models of tsunami generation and propagation. Recent advancements in computational power and artificial intelligence offer promising opportunities for the development of high-resolution, multi-dimensional models that can accurately simulate complex tsunami behaviors [91, 92]. In addition, future research could focus on the impact of tsunamis on coastal and inland areas. This could involve investigations into the process of tsunami run-up and inundation and the development of methods for assessing the vulnerability of coastal communities and infrastructure to tsunami hazards. Finally, there is a need for research that translates scientific understanding of tsunamis into effective mitigation strategies. This could involve the development of effective tsunami warning systems, the design of tsunami-resistant infrastructure, and the implementation of community education programs to enhance public awareness and preparedness for tsunamis [93, 94].
- *Improved Understanding of Non-Seismic Tsunami Sources:* While seismic events remain the most significant source of tsunamis, recent events have underscored the importance of non-seismic triggers, such as landslides and volcanic eruptions. There remains much to learn about these triggers, particularly in terms of their frequency, geographic distribution, and tsunami-generating potential. Future research in this area could provide valuable insights for hazard assessment and mitigation efforts [90].

- *Advancements in Tsunami Modeling*: There is an ongoing need for advancements in tsunami modeling. This includes the development of more accurate and comprehensive models of tsunami generation, propagation, and inundation, as well as the integration of these models into real-time warning systems. Recent advances in high-performance computing and artificial intelligence offer promising opportunities in this regard [92].
- *Enhanced Coastal Defenses and Evacuation Planning*: Effective tsunami mitigation requires a multifaceted approach that combines physical defenses, such as seawalls and tsunami evacuation buildings, with well-planned evacuation strategies. Research in this area could focus on the design and evaluation of these measures as well as the development of innovative solutions, such as floating tsunami shelters [85].
- *Strengthening Community Preparedness and Response*: Given the potentially devastating impacts of tsunamis, it is critical to enhance community preparedness and response. This could involve research on risk perception and behavior, the development of effective education and awareness programs, and the evaluation of communication strategies for tsunami warnings [94].

13. Conclusion

In this comprehensive exploration of tsunami generation and impact, we have delved deeply into both seismic and non-seismic sources, underpinning the significant threats they pose to global coastal communities. Tsunamis, distinguished from regular ocean waves by their extraordinary energy and far-reaching impacts, are complex natural phenomena that demand our undivided attention and rigorous scientific investigation.

- Seismic activities, particularly undersea earthquakes, have been recognized as predominant triggers of tsunamis. Throughout this chapter, we have explored how the magnitude, depth, and type of seismic activity influence tsunami generation. The 2011 Tohoku Earthquake and Tsunami served as a key case study, highlighting the destructive potential of seismic tsunamis and the profound effects they can have on ocean floor topography. We have also delved into the dynamics of foreshocks, mainshocks, and aftershocks and their respective roles in tsunami genesis.
- In the realm of non-seismic triggers, we have examined the potent potential of landslides, volcanic eruptions, and meteorological events in generating tsunamis. Each of these triggers presents unique challenges and necessitates further research for a comprehensive understanding. The case study of the 1958 Lituya Bay Landslide and Tsunami underlines the profound potential for destruction these triggers can possess.
- We have navigated the complex terrain of modeling tsunami generation from these diverse sources. Despite the inherent challenges, advances in technology and methodology are continually enhancing our ability to predict and respond to these devastating events. This chapter has also underscored the crucial roles of bathymetry and tectonic structures in tsunami generation, emphasizing the necessity of considering these factors in our predictions and preparations.

- When it comes to non-seismic triggers, our discussion has underscored their significance in the broader context of tsunami generation. The devastating impact of the 1958 Lituya Bay Landslide and Tsunami, examined as a key case study, highlights the importance of extending our focus beyond earthquakes to include other triggers such as landslides, volcanic eruptions, and even meteorological events. However, these non-seismic sources pose unique challenges due to their varied nature, thereby necessitating specialized investigation and predictive modeling techniques.
- The endeavor to model tsunami generation from non-seismic sources is undoubtedly complex but vital for improving our understanding and predictive capabilities. Advances in technology and computational methods have propelled progress in this domain, but the path toward accurate and reliable prediction is paved with continuous exploration and learning.
- Moreover, the intricate roles of bathymetry and tectonic structures in tsunami generation cannot be overlooked. The bathymetric features of an area can dramatically influence how a tsunami forms and propagates, while tectonic structures may serve as hotspots for both seismic and non-seismic tsunami triggers. This understanding has significant implications for risk assessment, disaster preparedness, and mitigation strategies in coastal regions worldwide.
- In the face of these complexities, this chapter has reinforced the need for interdisciplinary collaboration. From geophysicists and oceanographers to engineers and disaster management experts, the collective efforts of many disciplines are required to piece together the jigsaw puzzle that is tsunami genesis. Our quest for understanding is far from over, but each new piece of knowledge takes us one step closer to the goal: the protection of life and property against the devastating impacts of tsunamis.
- It is crucial to acknowledge that non-seismic triggers also hold the potential to generate tsunamis, sometimes with catastrophic effects. Landslides, volcanic eruptions, and meteorological events can induce tsunamis, contributing significantly to our understanding of these natural disasters' diverse origins. The 1958 Lituya Bay Landslide and Tsunami serve as a testament to the substantial impacts of these non-seismic triggers, further reinforcing the need for comprehensive investigations and advanced modeling techniques that consider these distinct sources.
- Modeling tsunami generation, particularly from non-seismic sources, remains a complex yet essential endeavor, pivotal for enhancing our predictive capabilities and devising effective disaster management strategies. As technology advances and computational methods become more refined, the progress made in this realm can significantly improve the accuracy and reliability of our models.
- The comprehensive roles of bathymetry and tectonic structures in tsunami generation warrant profound attention. These aspects can significantly influence the formation, propagation, and subsequent impact of tsunamis, with important implications for disaster risk assessment, preparedness, and mitigation efforts in vulnerable regions worldwide.

- In closing, this chapter highlights the importance of continuous vigilance and research in our quest to understand tsunamis. Although significant strides have been made in our comprehension of these natural disasters, there is still much to uncover. By persistently enhancing our research techniques, refining our models, and advancing our disaster management strategies, we can progressively mitigate the powerful impacts of tsunamis. It is hoped that the insights shared in this chapter will inspire ongoing research and contribute to a deeper understanding of tsunamis, ultimately promoting the safety and well-being of vulnerable coastal communities worldwide.
- In conclusion, this chapter underscores the vastness of the field of tsunami studies and highlights the essentiality of continuing research efforts. It emphasizes the necessity of not only understanding the geophysical mechanisms of tsunamis but also the critical need for preparing societies to better cope with the impacts of these often-devastating natural events. The hope is that the knowledge gleaned from this chapter, combined with future research efforts, will lead to more accurate tsunami prediction methods, more effective mitigation strategies, and ultimately safer coastal communities.

Acknowledgements


The author would like to express gratitude to all the researchers and scientists who have contributed their valuable work to our collective understanding of tsunamis. Their diligent efforts form the foundation upon which future research can be built.

Author details

Ali Akbar Firoozi* and Ali Asghar Firoozi
Faculty of Engineering and Technology, Department of Civil Engineering, University of Botswana, Gaborone, Botswana

*Address all correspondence to: a.firoozi@gmail.com

IntechOpen

© 2024 The Author(s). Licensee IntechOpen. This chapter is distributed under the terms of the Creative Commons Attribution License (<http://creativecommons.org/licenses/by/3.0>), which permits unrestricted use, distribution, and reproduction in any medium, provided the original work is properly cited. 

References

- [1] Goff J, Witter R, Terry J, Spiske M. Palaeotsunamis in the Sino-Pacific region. *Earth-Science Reviews*. 2020;**210**:103352. DOI: 10.1016/j.earscirev.2020.103352
- [2] Harig S, Immerz A, Weniza GJ, Weber B, Babeyko A, et al. The tsunami scenario database of the Indonesia tsunami early warning system (InaTEWS): Evolution of the coverage and the involved modeling approaches. *Pure and Applied Geophysics*. 2020;**177**: 1379-1401. DOI: 10.1007/s00024-019-02305-1
- [3] Zorn EU, Orynbaikyzy A, Plank S, Babeyko A, Darmawan H, Robbany IF, et al. Identification and ranking of subaerial volcanic tsunami hazard sources in Southeast Asia. *Natural Hazards and Earth System Sciences*. 2022;**22**(9):3083-3104. DOI: 10.5194/nhess-22-3083-2022
- [4] Bolin H, Yueping Y, Renjiang L, Peng Z, Zhen Q, Yang L, et al. Three-dimensional experimental investigation on hazard reduction of landslide-generated impulse waves in the Baihetan reservoir, China. *Landslides*. 16 May 2023:1-12. DOI: 10.1007/s10346-023-02068-w [Received: 29 September, 2022], [Accepted: 12 April, 2023]
- [5] Satake K, Atwater BF. Long-term perspectives on giant earthquakes and tsunamis at subduction zones. *Annual Review of Earth and Planetary Sciences*. 2007;**35**:349-374. DOI: 10.1146/annurev.earth.35.031306.140302
- [6] Karstens J, Berndt C, Urlaub M, Watt SF, Micaleff A, Ray M, et al. From gradual spreading to catastrophic collapse–reconstruction of the 1888 Ritter Island volcanic sector collapse from high-resolution 3D seismic data. *Earth and Planetary Science Letters*. 2019;**517**:1-13. DOI: 10.1016/j.epsl.2019.04.009
- [7] Vilibić I, Denamiel C, Zemunik P, Monserrat S. The Mediterranean and Black Sea meteotsunamis: An overview. *Natural Hazards*. 2021;**106**:1223-1267. DOI: 10.1007/s11069-020-04306-z
- [8] Monserrat S, Vilibić I, Rabinovich AB. Meteotsunamis: Atmospherically induced destructive ocean waves in the tsunami frequency band. *Natural Hazards and Earth System Sciences*. 2006;**6**(6):1035-1051. DOI: 10.5194/nhess-6-1035-2006
- [9] Satake K, Tanioka Y. The July 1998 Papua New Guinea earthquake: Mechanism and quantification of unusual tsunami generation. *Pure and Applied Geophysics*. 2003;**160**:2087-2118. DOI: 10.1007/s00024-003-2421-1
- [10] Kanoğlu U, Titov V, Bernard E, Synolakis C. Tsunamis: Bridging science, engineering and society. *Philosophical Transactions of the Royal Society A: Mathematical, Physical and Engineering Sciences*. 2015;**373**(2053):20140369. DOI: 10.1098/rsta.2014.0369
- [11] Chacón-Barrantes S, Rivera-Cerdas F, Murillo-Gutiérrez A. Impact of the tsunami caused by the Hunga Tonga–Hunga Ha’apai eruption in Costa Rica on 15 January 2022. *Bulletin of Volcanology*. 2023;**85**(6):36. DOI: 10.1007/s00445-023-01648-x
- [12] Liu PLF, Cho YS, Briggs MJ, Kanoglu U, Synolakis CE. Runup of solitary waves on a circular island. *Journal of Fluid Mechanics*. 1995;**302**:259-285. DOI: 10.1017/S0022112095004095

- [13] Aránguiz R, Martínez C, Rojas O, Hoffmann C, López P. The generation of new tsunami risk areas due to an intentionally biased reconstruction process: Case study of Ilico after the 2010 Chile tsunami. *International Journal of Disaster Risk Reduction*. 2020;**50**:101727. DOI: 10.1016/j.ijdrr.2020.101727
- [14] Chagué-Goff C, Schneider JL, Goff JR, Dominey-Howes D, Strotz L. Expanding the proxy toolkit to help identify past events—Lessons from the 2004 Indian Ocean tsunami and the 2009 South Pacific tsunami. *Earth-Science Reviews*. 2011;**107**(1–2):107–122. DOI: 10.1016/j.earscirev.2011.03.007
- [15] Young IR. *Wind Generated Ocean Waves*. Amsterdam, Netherlands: Elsevier; 1999
- [16] Suppasri A, Imamura F, Koshimura S. Tsunamigenic ratio of the Pacific Ocean earthquakes and a proposal for a tsunami index. *Natural Hazards and Earth System Sciences*. 2012;**12**(1):175–185. DOI: 10.5194/nhess-12-175-2012
- [17] Saito T, Kubota T, Chikasada NY, Tanaka Y, Sandanbata O. Meteorological tsunami generation due to sea-surface pressure change: Three-dimensional theory and synthetics of ocean-bottom pressure change. *Journal of Geophysical Research: Oceans*. 2021;**126**(5): e2020JC017011. DOI: 10.1029/2020JC017011
- [18] Yao H, Beghein C, Van Der Hilst RD. Surface wave array tomography in SE Tibet from ambient seismic noise and two-station analysis-II. Crustal and upper-mantle structure. *Geophysical Journal International*. 2008;**173**(1):205–219. DOI: 10.1111/j.1365-246X.2007.03696.x
- [19] Zhu G, Yang H, Lin J, Zhou Z, Xu M, Sun J, et al. Along-strike variation in slab geometry at the southern Mariana subduction zone revealed by seismicity through ocean bottom seismic experiments. *Geophysical Journal International*. 2019;**218**(3):2122–2135. DOI: 10.1093/gji/ggz272
- [20] Lee JW, Irish JL, Weiss R. Rapid prediction of alongshore run-up distribution from near-field tsunamis. *Natural Hazards*. 2020;**104**(2):1157–1180. DOI: 10.1007/s11069-020-04209-z
- [21] Fujii Y, Satake K, Watada S, Ho TC. Re-examination of slip distribution of the 2004 Sumatra–Andaman earthquake (mw 9.2) by the inversion of tsunami data using green’s functions corrected for compressible seawater over the elastic earth. *Pure and Applied Geophysics*. 2021;**178**(12):4777–4796. DOI: 10.1007/s00024-021-02909-6
- [22] Heidarzadeh M, Rabinovich A, Kusumoto S, Rajendran CP. Field surveys and numerical modeling of the 26 December 2004 Indian Ocean tsunami in the area of Mumbai, west coast of India. *Geophysical Journal International*. Sep 2020;**222**(3):1952–1964. DOI: 10.1093/gji/ggaa277
- [23] Løvholt FJMR, Griffin J, Salgado-Gálvez MA. Tsunami hazard and risk assessment on the global scale. In: *Complexity in Tsunamis, Volcanoes, and their Hazards*. Berlin, Heidelberg: Springer; 2022. pp. 213–246. DOI: 10.1007/978-1-0716-1705-2_642
- [24] Hua Y, Zhao D, Toyokuni G, Xu Y. Tomography of the source zone of the great 2011 Tohoku earthquake. *Nature Communications*. 2020;**11**(1):1163. DOI: 10.1038/s41467-020-14745-8
- [25] Sugawara D. Numerical modeling of tsunami: Advances and future challenges after the 2011 Tohoku earthquake and tsunami. *Earth-Science Reviews*. 2021;

214:103498. DOI: 10.1016/j.earscirev.2020.103498

[26] Shinozaki T. Geochemical approaches in tsunami research: Current knowledge and challenges. *Geoscience Letters*. 2021;**8**(1):6. DOI: 10.1186/s40562-021-00177-9

[27] Gallen SF, Clark MK, Godt JW, Roback K, Niemi NA. Application and evaluation of a rapid response earthquake-triggered landslide model to the 25 April 2015 mw 7.8 Gorkha earthquake, Nepal. *Tectonophysics*. 2017;**714**:173-187. DOI: 10.1016/j.tecto.2016.10.031

[28] Okal EA, Synolakis CE. Source discriminants for near-field tsunamis. *Geophysical Journal International*. 2004; **158**(3):899-912. DOI: 10.1111/j.1365-246X.2004.02347.x

[29] Obara K. Characteristics and interactions between non-volcanic tremor and related slow earthquakes in the Nankai subduction zone, Southwest Japan. *Journal of Geodynamics*. 2011;**52**(3-4): 229-248. DOI: 10.1016/j.jog.2011.04.002

[30] Schwarz B. An Introduction to Seismic Diffraction. In: *Advances in Geophysics*. Amsterdam, Netherlands: Elsevier; 2019. pp. 1-64. DOI: 10.1016/bs.agph.2019.05.001

[31] Satake K, Fujii Y, Harada T, Namegaya Y. Time and space distribution of coseismic slip of the 2011 Tohoku earthquake as inferred from tsunami waveform data. *Bulletin of the Seismological Society of America*. 2013; **103**(2B):1473-1492. DOI: 10.1785/0120120122

[32] Cui Y, Zheng C, Jiang L, Huang J, Sun F, Zou Z, et al. Variations of multiple gaseous emissions associated with the great Sumatra earthquakes in

2004 and 2005. *Chemical Geology*. 2023; **618**:121311. DOI: 10.1016/j.chemgeo.2023.121311

[33] Titov VV, Moore CW, Greenslade DJM, Pattiaratchi C, Badal R, Synolakis CE, et al. A new tool for inundation modeling: Community modeling Interface for tsunamis (ComMIT). *Pure and Applied Geophysics*. 2011;**168**: 2121-2131. DOI: 10.1007/s00024-011-0292-4

[34] Álvarez O, Pechuan Canet S, Gimenez M, Folguera A. Megathrust slip behavior for great earthquakes along the Sumatra-Andaman subduction zone mapped from satellite GOCE gravity field derivatives. *Frontiers in Earth Science*. 2021;**8**:581396. DOI: 10.3389/feart.2020.581396

[35] Fritz HM, Mohammed F, Yoo J. Lituya Bay landslide impact generated mega-tsunami 50 th anniversary. In: *Tsunami Science Four Years after the 2004 Indian Ocean Tsunami: Part II: Observation and Data Analysis*. Basel: Birkhäuser; 2009. pp. 153-175. DOI: 10.1007/978-3-0346-0064-4_9

[36] Mutaqin, BW, Lavigne F, Hadmoko DS, Ngilawani MN. Volcanic eruption-induced tsunami in Indonesia: A review. In: *IOP Conference Series: Earth and Environmental Science*. International Conference on Environmental Resources Management in Global Region. Vol. 256. no. 1. UK: IOP Publishing; 2019. p. 012023. DOI 10.1088/1755-1315/256/1/012023

[37] Pelinovsky E. *Hydrodynamics of Tsunami Waves*. Vienna: Springer; 2006. pp. 1-48. DOI: 10.1007/978-3-211-69356-8_1

[38] Gales JA, McKay RM, De Santis L, Rebesco M, Laberg JS, Shevenell AE, et al. Climate-controlled submarine

landslides on the Antarctic continental margin. *Nature Communications*. 2023; **14**(1):2714. DOI: 10.1038/s41467-023-38240-y

[39] Huhn K, Arroyo M, Cattaneo A, Clare MA, Gràcia E, Harbitz CB, et al. Modern submarine landslide complexes. In: Ogata K, Festa A, Pini GA, editors. *Submarine Landslides*. 2019. DOI: 10.1002/9781119500513.ch12

[40] Carey R, Soule SA, Manga M, White JD, McPhie J, Wysoczanski R, et al. The largest deep-ocean silicic volcanic eruption of the past century. *Science Advances*. 2018;**4**(1):e1701121. DOI: 10.1126/sciadv.1701121

[41] Terry JP, Goff J, Winspear N, Bongolan VP, Fisher S. Tonga volcanic eruption and tsunami, January 2022: Globally the most significant opportunity to observe an explosive and tsunamigenic submarine eruption since AD 1883 Krakatau. *Geoscience Letters*. 2022;**9**(1):24. DOI: 10.1186/s40562-022-00232-z

[42] Tojčić I, Denamiel C, Vilibić I. Performance of the Adriatic early warning system during the multi-meteotsunami event of 11–19 may 2020: An assessment using energy banners. *Natural Hazards and Earth System Sciences*. 2021;**21**(8):2427–2446. DOI: 10.5194/nhess-21-2427-2021

[43] Ward SN. Landslide tsunami. *Journal of Geophysical Research: Solid Earth*. 2001;**106**(B6):11201–11215. DOI: 10.1029/2000JB900450

[44] Needham HF, Keim BD, Sathiaraj D. A review of tropical cyclone-generated storm surges: Global data sources, observations, and impacts. *Reviews of Geophysics*. 2015;**53**(2):545–591. DOI: 10.1002/2014RG000477

[45] Simkin T, Fiske RS. *Krakatau 1883 - the volcanic eruption and its effects*. Washington, D.C.: Smithsonian Institution Press; 1983. DOI: 10.1080/00431672.1983.9930158

[46] Grilli ST, Tappin DR, Carey S, Watt SF, Ward SN, Grilli AR, et al. Modelling of the tsunami from the December 22, 2018 lateral collapse of Anak Krakatau volcano in the Sunda Straits, Indonesia. *Scientific Reports*. 2019;**9**(1):11946. DOI: 10.1038/s41598-019-48327-6

[47] Rui Y, Yin M. An analytical solution for the run-out of submarine debris flows. *Marine Geodesy*. 2019;**42**(3):246–262. DOI: 10.1080/01490419.2019.1583146

[48] Esposti Ongaro T, de Michieli Vitturi M, Cerminara M, Fornaciai A, Nannipieri L, Favalli M, et al. Modeling tsunamis generated by submarine landslides at Stromboli Volcano (Aeolian Islands, Italy): A numerical benchmark study. *Frontiers in Earth Science*. 2021;**9**:628652. DOI: 10.3389/feart.2021.628652

[49] Rabinovich AB. Twenty-seven years of progress in the science of meteorological tsunamis following the 1992 Daytona Beach event. *Pure and Applied Geophysics*. 2020;**177**(3):1193–1230. DOI: 10.1007/s00024-019-02349-3

[50] Romero R, Vich M, Ramis C. A pragmatic approach for the numerical prediction of meteotsunamis in Ciutadella harbour (Balearic Islands). *Ocean Modelling*. 2019;**142**:101441. DOI: 10.1016/j.ocemod.2019.101441

[51] Churchill DD, Houston SH, Bond NA. The Daytona Beach wave of 3–4 July 1992: A shallow-water gravity wave forced by a propagating squall line. *Bulletin of the American Meteorological Society*. 1995;**76**(1):21–32. DOI: 10.1175/

1520-0477(1995)076<0021:TDBWOJ>2.0.CO;2

[52] Tappin DR, Watts P, Grilli ST. The Papua New Guinea tsunami of 17 July 1998: Anatomy of a catastrophic event. *Natural Hazards and Earth System Sciences*. 2008;**8**(2):243-266. DOI: 10.5194/nhess-8-243-2008

[53] Harbitz CB. Model simulations of tsunamis generated by the Storegga slides. *Marine Geology*. 1992;**105**(1-4):1-21. DOI: 10.1016/0025-3227(92)90178-K

[54] Paris R, Switzer AD, Belousova M, Belousov A, Ontowirjo B, Whelley PL, et al. Volcanic tsunami: A review of source mechanisms, past events and hazards in Southeast Asia (Indonesia, Philippines, Papua New Guinea). *Natural Hazards*. 2014;**70**:447-470. DOI: 10.1007/s11069-013-0822-8

[55] Chapman CR, Morrison D. Impacts on the earth by asteroids and comets: Assessing the hazard. *Nature*. 1994;**367** (6458):33-40. DOI: 10.1038/367033a0

[56] Smith WH, Sandwell DT. Global Sea floor topography from satellite altimetry and ship depth soundings. *Science*. 1997; **277**(5334):1956-1962. DOI: 10.1126/science.277.5334.1956

[57] Papadopoulos GA, Triantafyllou I, Vassilopoulou A. The mid-6th century AD enigmatic mega earthquake and tsunami in Central Greece: A seismotectonic, archeological, and historical reexamination. *The Holocene*. 2023;**33**(3):267-280. DOI: 10.1177/09596836221138330

[58] Abadie S, Paris A, Ata R, Le Roy S, Arnaud G, Poupardin A, et al. La Palma landslide tsunami: Calibrated wave source and assessment of impact on French territories. *Natural Hazards and*

Earth System Sciences. 2020;**20**(11): 3019-3038. DOI: 10.5194/nhess-20-3019-2020

[59] Geist EL, Parsons T. Probabilistic analysis of tsunami hazards. *Natural Hazards*. 2006;**37**:277-314. DOI: 10.1007/s11069-005-4646-z

[60] Harbitz CB, Løvholt F, Pedersen G, Masson DG. Mechanisms of tsunami generation by submarine landslides: A short review. *Norwegian Journal of Geology/Norsk Geologisk Forening*. 2006;**86**(3):255-264

[61] Giachetti T, Paris R, Kelfoun K, Ontowirjo B. Tsunami hazard related to a flank collapse of Anak Krakatau Volcano, Sunda Strait, Indonesia. *Geological Society, London, Special Publications*. 2012;**361**(1):79-90. DOI: 10.1144/SP361.7

[62] Šepić J, Vilibić I, Rabinovich AB, Monserrat S. Widespread tsunami-like waves of 23-27 June in the Mediterranean and black seas generated by high-altitude atmospheric forcing. *Scientific Reports*. 2015;**5**(1):11682. DOI: 10.1038/srep11682

[63] Rabinovich AB, Fritz HM, Tanioka Y, Geist EL. Introduction to “Global tsunami science: Past and future, Volume II”. *Pure and Applied Geophysics*. 2017;**174**:2883-2889. DOI: 10.1007/s00024-017-1638-3

[64] Synolakis CE, Bernard EN. Tsunami science before and beyond Boxing Day 2004. *Philosophical Transactions of the Royal Society A: Mathematical, Physical and Engineering Sciences*. 2006;**364** (1845):2231-2265. DOI: 10.1098/rsta.2006.1824

[65] Parsons T, Geist EL, Ryan HF, Lee HJ, Haeussler PJ, Lynett P, et al. Source

- and progression of a submarine landslide and tsunami: The 1964 Great Alaska earthquake at Valdez. *Journal of Geophysical Research: Solid Earth*. 2014; **119**(11):8502-8516. DOI: 10.1002/2014JB011514
- [66] Kowalik Z, Murty TS. *Numerical Modeling of Ocean Dynamics*. Vol. 5. Singapore: World Scientific; 1993
- [67] Hu YX, Yu ZY, Zhou JW. Numerical simulation of landslide-generated waves during the 11 October 2018 Baige landslide at the Jinsha River. *Landslides*. 2020; **17**(10):2317-2328. DOI: 10.1007/s10346-020-01382-x
- [68] Narayanaswami NK, Ramasamy V. Tropical cyclone intensity modulated by the oceanic eddies in the bay of Bengal. *Oceanologia*. 2022; **64**(3):445-456. DOI: 10.1016/j.oceano.2022.02.005
- [69] Madsen PA, Fuhrman DR. Run-up of tsunamis and long waves in terms of surf-similarity. *Coastal Engineering*. 2008; **55**(3):209-223. DOI: 10.1016/j.coastaleng.2007.09.007
- [70] Escalante C, Dumbser M, Castro MJ. An efficient hyperbolic relaxation system for dispersive non-hydrostatic water waves and its solution with high order discontinuous Galerkin schemes. *Geophysical Monograph Series, advancing earth and space science. Journal of Computational Physics*. 2019; **394**:385-416. DOI: 10.1016/j.jcp.2019.05.035
- [71] Deng H, An C, Cai C, Ren H. Theoretical solution and applications of ocean bottom pressure induced by seismic waves at high frequencies. *Geophysical Research Letters*. 2022; **49**(9):e2021GL096952. DOI: 10.1029/2021GL096952
- [72] Xu Z, Wang Z, Shi J, Li H. The 30 October 2020 Samos Island, Greece earthquake: Focal mechanism of the Mainshock and tsunami simulation. In: *The 32nd International Ocean and Polar Engineering Conference*. Shanghai, China: OnePetro; Jun 2022a
- [73] Xu WJ, Zhou Q, Dong XY. SPH-DEM coupling method based on GPU and its application to the landslide tsunami. Part II: Reproduction of the Vajont landslide tsunami. *Acta Geotechnica*. 2022; **17**(6):2121-2137. DOI: 10.1007/s11440-021-01387-3
- [74] Schambach L et al. Response to: Comment on “new simulations and understanding of the 1908 Messina tsunami for a dual seismic and deep submarine mass failure source” by L. Schambach, ST Grilli, DR Tappin, MD Gangemi, G. Barbaro [marine geology 421 (2020) 106093]. *Marine Geology*. 2021; **442**:106636. DOI: 10.1016/j.margeo.2021.106636
- [75] Rödder S, Schaumann F. “It’s something that I do every day.” exploring interdisciplinarity and stakeholder engagement in tsunami science. *Frontiers in Earth Science*. 2022; **10**:949803. DOI: 10.3389/feart.2022.949803
- [76] Liu C, Yu Z, Zhao S. A coupled SPH-DEM-FEM model for fluid-particle-structure interaction and a case study of Wenjia gully debris flow impact estimation. *Landslides*. 2021; **18**:2403-2425. DOI: 10.1007/s10346-021-01640-6
- [77] Post AL, Przeslawski R, Nanson R, Siwabessy J, Smith D, Kirkendale LA, et al. Modern dynamics, morphology and habitats of slope-confined canyons on the northwest Australian margin. *Marine Geology*. 2022; **443**:106694. DOI: 10.1016/j.margeo.2021.106694

- [78] Niu X. Resonance of long waves around a circular island and its relation to edge waves. *European Journal of Mechanics-B/Fluids*. 2021;**86**:15-24. DOI: 10.1016/j.euromechflu.2020.11.007
- [79] Ye L, Lay T, Kanamori H. The 25 march 2020 MW 7.5 Paramushir, northern Kuril Islands earthquake and major ($MW \geq 7.0$) near-trench intraplate compressional faulting. *Earth and Planetary Science Letters*. 2021;**556**: 116728. DOI: 10.1016/j.epsl.2020.116728
- [80] Mori N, Satake K, Cox D, Goda K, Catalan PA, Ho TC, et al. Giant tsunami monitoring, early warning and hazard assessment. *Nature Reviews Earth and Environment*. 2022;**3**(9):557-572. DOI: 10.1038/s43017-022-00327-3
- [81] Amaratunga D, Haigh R, Ashar F, Senevirathne M. A preparedness index (PI) to assess the capacities for tsunami warning and evacuation planning: A case Study from Padang City, Indonesia. In: *Multi-Hazard Early Warning and Disaster Risks*. Cham, Switzerland: Springer International Publishing; 2021. pp. 499-513. DOI: 10.1007/978-3-030-73003-1_34
- [82] Lindell MK, Bostrom A, Goltz JD, Prater CS. Evaluating hazard awareness brochures: Assessing the textual, graphical, and numerical features of tsunami evacuation products. *International Journal of Disaster Risk Reduction*. 2021;**61**:102361. DOI: 10.1016/j.ijdr.2021.102361
- [83] Williamson A, Allen RM. Improving efficacy of tsunami warnings along the west coast of the United States. *Pure and Applied Geophysics*. 2023;**180**:1661-1678. DOI: 10.1007/s00024-023-03277-z
- [84] Lindell MK, Jung MC, Prater CS, House DH. Improving Cascadia subduction zone residents' tsunami preparedness: Quasi-experimental evaluation of an evacuation brochure. *Natural Hazards*. 2022;**114**(1):849-881. DOI: 10.1007/s11069-022-05415-7
- [85] Ochiai N, Nakayama J, Izato YI, Miyake A. Lessons learned from the 2011 great East Japan earthquake: A case study of tsunami risk assessment in a Japanese chemical corporation. *Process Safety Progress*. 2022;**41**(2):283-292. DOI: 10.1002/prs.12315
- [86] Pal I, Ghosh S, Dash I, Mukhopadhyay A. Review of tsunami early warning system and coastal resilience with a focus on Indian Ocean. *International Journal of Disaster Resilience in the Built Environment*. 2022;**13**:1-18. DOI: 10.1108/IJDRBE-12-2020-0124
- [87] Zeng H, Wei S, Rosakis A. A travel-time path calibration strategy for Back-projection of large earthquakes and its application and validation through the segmented super-shear rupture imaging of the 2002 mw 7.9 Denali earthquake. *Journal of Geophysical Research: Solid Earth*. 2022;**127**(6):e2022JB024359. DOI: 10.1029/2022JB024359
- [88] Fornaciai A, Favalli M, Nannipieri L. Numerical simulation of the tsunamis generated by the Sciara del Fuoco landslides (Stromboli Island, Italy). *Scientific Reports*. 2019;**9**(1):18542. DOI: 10.1038/s41598-019-54949-7
- [89] Takabatake T, Han DC, Valdez JJ, Inagaki N, Mäll M, Esteban M, et al. Three-dimensional physical modeling of tsunamis generated by partially submerged landslides. *Journal of Geophysical Research: Oceans*. 2022;**127**(1):e2021JC017826. DOI: 10.1029/2021JC017826
- [90] Androsov A, Harig S, Rakowsky N. Simulating Landslide Generated

Tsunamis in Palu Bay, Sulawesi,
Indonesia. *Geosciences*. 2023;**13**(3):72.
DOI: 10.3390/geosciences13030072

[91] Arnaud GE, Krien Y, Abadie S, Zahibo N, Dudon B. How would the potential collapse of the cumbre Vieja Volcano in La Palma Canary Islands impact the Guadeloupe Islands? Insights into the consequences of climate change. *Geosciences*. 2021;**11**(2):56. DOI: 10.3390/geosciences11020056

[92] Ayca A, Lynett PJ. Modeling the motion of large vessels due to tsunami-induced currents. *Ocean Engineering*. 2021;**236**:109487. DOI: 10.1016/j.oceaneng.2021.109487

[93] Nakamura M, Hattori T, Kariya M. Comparison of structural changes in the agriculture and fisheries industries before and after the great East Japan earthquake: A case study of Iwate Prefecture's coastal area. *Fisheries Science*. 2022;**88**(2):345-361. DOI: 10.1007/s12562-021-01579-6

[94] Omira R, Baptista MA, Quartau R, Ramalho RS, Kim J, Ramalho I, et al. How hazardous are tsunamis triggered by small-scale mass-wasting events on volcanic islands? New insights from Madeira–NE Atlantic. *Earth and Planetary Science Letters*. 2022;**578**: 117333. DOI: 10.1016/j.epsl.2021.117333

Section 5

Instrumentation

Perspective Chapter: Application of Gyroscopes in Geophysics

*Yanjun Chen, Lanxin Zhu, Fangshuo Shi, Yan He
and Zhengbin Li*

Abstract

More researchers have gradually realized that gyroscopes are powerful rotational measurement sensors, and the use of high-performance gyroscopes in geophysics began in the last decade and continues to deepen. This chapter will present the applications of gyroscopes in geophysics. In rotational seismology, large gyroscopes are used in the observation and analysis of natural earthquakes; miniaturized and portable fiber-optic gyroscopes are used in practical applications, including high-speed-railway seismology, natural earthquake observation, and subsurface structure imaging. In the study of the Earth's rotation, the angular velocity of the Earth's rotation is observed with large optical gyroscopes. In gravimetry, high-performance fiber-optic gyroscopes are used to measure the rotational motion generated by the gravitational field and, hence, the gravity gradient.

Keywords: gyroscope, geophysics, rotational seismology, high-speed-railway seismology, Earth's rotation, universal time measurement, gravimetry, gravity gradient

1. Introduction

Gyroscopes are sensors that measure rotational motion and can be used to measure the rotational parameters of an object, such as angle, angular velocity, and angular acceleration. In the field of geophysics, there are many phenomena related to rotational motion, such as the Earth's rotation, the rotational component of seismic waves, etc.; thus, gyroscopes can play a vital role in geophysics.

In fact, the first well-known application of gyroscopes was in the field of geophysics. In 1852, J. Foucault used the directional stability of a high-speed rotating rigid body to design the first gyroscope for verifying the Earth's rotation [1]. The phenomenon caused by the Earth's rotation can only be seen for about 10 minutes due to the friction of the mechanical rotor. This is also known as the basis for electro-mechanical gyroscopes based on classical mechanics.

With the development of Einstein's theory of relativity, G. Sagnac proposed the Sagnac effect in 1913 [2], that is, the phase difference between two light waves traveling opposite each other along the closed optical path is proportional to the angular velocity of the normal direction of the closed optical path. This has become

the sensing principle of the current optoelectronic gyroscopes. In 1925, A. A. Michelson and H. G. Gale used a large ring interferometer with a circumference of about 2 km to increase sensitivity and were able to measure the Earth's rotation [3]. After the advent of the He-Ne gas laser, Macek and Davis validated the ring laser gyroscope in 1963 [4]. Fiber-optic gyroscope (FOG) is developed on the basis of the fiber-optic communication device. In 1966, K. C. Kao proposed that the high loss of optical fiber material is caused by its impurities, and the loss can be reduced to 20 dB/km by reducing the impurities in the material [5]. This became the beginning of the practical use of optical fibers. In 1967, G. Pincher and G. Hepner first proposed the idea of making FOG by enhancing the Sagnac effect with multi-turn fiber-optic coils [6]. In 1976, Victor Vali and Richard W. Shorthill successfully demonstrated the first FOG in the laboratory, marking the birth of the FOG [7].

Due to the fact that rotational phenomena in geophysics are usually small, the requirements for the performance of gyroscopes are very high. With the development of optical devices such as optical cavities, lasers, and optical fibers, optical gyroscopes based on the Sagnac effect have gradually become the first choice for high-performance applications. Furthermore, as the performance of gyroscopes has improved, new branches of geophysics have been born in the last two decades, such as rotational seismology and high-speed-railway seismology. The following sections show applications of high-performance gyroscopes in seismology, Earth's rotation, and gravimetry.

2. Applications in seismology

2.1 Rotational component of seismic wave

In seismology, the classical linear elastic theory is commonly used to describe the distortion of a medium. With the assumption of infinitesimal deformations, a function of the space $\mathbf{u} = \mathbf{u}(\mathbf{x})$ is used to denote the translational displacement of the points \mathbf{x} . For a point $\mathbf{x} + \delta\mathbf{x}$ in its vicinity, the displacement $\mathbf{u}(\mathbf{x} + \delta\mathbf{x})$ can be written as [8]:

$$\mathbf{u}(\mathbf{x} + \delta\mathbf{x}) = \mathbf{u}(\mathbf{x}) + \boldsymbol{\varepsilon}\delta\mathbf{x} + \boldsymbol{\omega} \times \delta\mathbf{x}, \quad (1)$$

where $\boldsymbol{\varepsilon}$ denotes the strain tensor, and $\boldsymbol{\omega}$ represents the rotation vector. Under the assumption of small and linear deformations, the rotation vector $\boldsymbol{\omega}$ is neglected. On the one hand, this is due to the small amplitude of the rotation relative to the translational motion. On the other hand, this is also because the rotational phenomena in seismic waves are not obvious, and the performance of the measurement sensors is not sufficient.

But the fact is that the rotational properties of seismic waves do exist and cannot be neglected. The earliest recorded rotation of buildings and tombstones caused by an earthquake was the shifting of two obelisk-shaped pillars during an earthquake in Calabria in 1783 [9]. This record attracted the attention of many researchers, and seismologists set out to find and design the sensors for observing the rotational component of seismic waves.

The introduction of gyroscopes into the field of view of seismologists and the measurement of the rotational component of seismic waves dates back to 1968. W. E. Farrell developed a gyroscope with two counter-rotating pendulums. During the Borrego earthquake of April 9, 1968 (M 6.5), static dislocations of less than 1 cm and

rotations of less than 5×10^{-4} rad were observed at La Jolla, California, 115 km from the source [10].

With the development of optical devices, optical gyroscopes have replaced electro-mechanical gyroscopes in geophysical applications due to their high sensitivity. Built on October 5, 2001, the Ring Laser Gyroscope G is located at the Wettzell Geodetic Observatory in Bavaria, Germany. It observed the Tokachi-Oki earthquake (M 8.1) which occurred in Hokkaido, Japan on September 25, 2003. In this work, the translational and rotational components of the earthquake are compared. This is the first reported observational record of rotational motion about a vertical axis induced by a large distant earthquake consistent with the shape of translational motion [11]. An FOG placed at the National Time Service Center in Xi'an, China, obtained the rotational motion record of an earthquake (M 4.9) that occurred in Yingcheng, Hubei Province, China, at 18:36:34 on December 26, 2019 (UTC + 8) [12]. The distance from the FOG to the epicenter of the earthquake is about 580 km.

2.2 Rotational seismology

Rotational seismology, a branch of seismology that studies the rotational ground motion induced by earthquakes, has seen significant advances over the years. It has emerged as an essential component of earthquake studies, providing valuable insights into the complex dynamics of seismic events [13].

The development of rotational seismology dates back to the mid-twentieth century, when scientists began to recognize the importance of rotational ground motion. Early observations were primarily made through the use of simple pendulum-type rotational sensors [14]. As seismology has expanded, it has become clear that the rotational component of seismic waves carries valuable information that cannot be adequately captured by traditional translational seismometers alone. Advances in technology and instrumentation in recent decades have led to the establishment of dedicated rotational seismology networks, facilitating the systematic study of these complex rotational signals.

To promote the research of rotational seismology, an international working group on rotational seismology (IWGoRS) was organized to promote investigations of rotational motions and their implications and to share experience, data, software, and results in an open web-based environment. Researchers can join IWGoRS at <http://www.rotational-seismology.org>, subscribe to mailing lists, and contribute to the content (publications, data, links, etc.). Nowadays, rotational seismology has gained considerable momentum in earthquake research. Seismologists have come to appreciate the significance of rotational ground motions in understanding the rupture process, seismic focal mechanisms, and seismic wave propagation [15, 16]. The rotational components of ground motion have been observed and analyzed in various seismic events worldwide, enhancing our understanding of seismic source processes and their associated complexities.

2.3 Gyroscopes as rotational seismometers

The successful implementation of rotational seismology relies on high-performance rotational seismometers. Rotational seismometers are critical in capturing and analyzing the rotational components of ground motion during seismic events. The core of a rotational seismometer lies in its angular velocity sensor

(i.e., gyroscope), which comes in various types, such as mechanical gyroscopes [17], MEMS (Micro-Electro-Mechanical System) gyroscopes [18], electrochemical gyroscopes [19], laser gyroscopes [20], and FOGs [21–23]. Based on actual observation cases, researchers at Ludwig-Maximilians University specified the following *a priori* requirements of seismic rotational sensors [24]:

1. The sensor needs to be effectively insensitive to linear motion, or at any rate, distinct measurement of linear and rotational motions must be possible.
2. For installing networks of temporary stations, the instrument needs to be small and stable with respect to ambient conditions, including changes in temperature.
3. The electrical power supply should be easily managed with batteries, at least in combination with solar panels or fuel cells.
4. A useful instrument for weak motion seismology needs to be able to measure amplitudes in the order of 10^{-7} rad/s at periods from 10 to 100 s.

Mechanical and MEMS gyroscopes use the principle of angular momentum conservation to measure rotational motion. They are simple and reliable; however, they have relatively low sensitivity and are susceptible to the influence of vibrations and shocks, leading to potential measurement errors. Electrochemical gyroscopes measure the change in capacitance of charged particles to measure the angular velocity. They are cost-effective but suffer from low sensitivity and limited frequency response as well as dynamic range. Both laser gyroscopes and FOGs are high-precision rotational sensors that employ the Sagnac effect to measure angular rotation. However, the larger size and complexity of laser gyroscopes limit their portability, and they are also more expensive compared to other gyroscopes. The FOG-based rotational seismometer is an all-solid-state device without any moving parts, enabling the design of compact, lightweight, and energy-efficient rotational seismometers. This makes FOG-based rotational seismometers highly suited for easy deployment and integration into existing seismic networks. Besides, FOG exhibits a wide dynamic range, allowing it to probe a wide range of rotational motions, from large-scale seismic events to microseismic events. This capability ensures that FOG-based rotational seismometers can capture and analyze a wide spectrum of rotational ground motions, providing comprehensive data for seismic research. In the following content, we choose two representative FOG-based rotational seismometers to introduce, the BlueSeis-3A and the Three-component Dual-Polarization Fiber-Optic Rotational Seismometer (DP-Rot3C) (**Figure 1**).

2.3.1 BlueSeis-3A

BlueSeis-3A is the first commercially available FOG-based rotational seismometer. This rotational seismometer has gained widespread recognition for its high sensitivity and stable performance in measuring ground rotational motions. It utilizes three closed-loop FOGs, each with a 5 km long fiber-optic coil, assembled in mutually orthogonal orientations, forming a three-component rotational seismometer.

Specifically, the self-noise of the rotational seismometer determines the minimum detectable angular rate and is typically represented by the power spectral density (PSD) or the square root of the power spectral density (root PSD) obtained from static



(a)



(b)

Figure 1.
The pictures of (a) BlueSeis-3A and (b) DP-Rot3C.

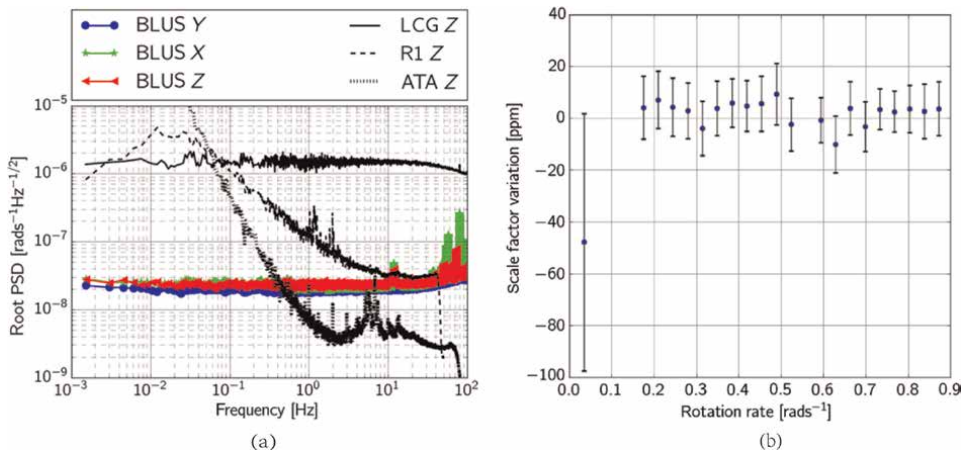


Figure 2.
(a) The self-noise and (b) scale factor nonlinearity of BlueSeis-3A [22].

tests. Currently, BlueSeis-3A exhibits a root PSD of $20 \text{ nrad/s}/\sqrt{\text{Hz}}$ within the frequency range of 0.001–100 Hz [22], as shown in **Figure 2(a)**.

The nonlinearity of the scale factor is an indicator of the nonlinear error between the input and output angular velocities of the rotational seismometer. Typically, the entire measurement range is tested, and the maximum error is compared to the measured range to calculate the ratio. Displayed in **Figure 2(b)**, in the angular rate range from 0.035 to 0.873 rad/s, the nonlinearity level of the scale factor is maintained within 50 ppm (parts per million) [22], meeting the performance requirements in seismology.

2.3.2 DP-Rot3C

DP-Rot3C, proposed and implemented by Peking University, is another high-precision FOG-based rotational seismometer. DP-Rot3C consists of three orthogonal

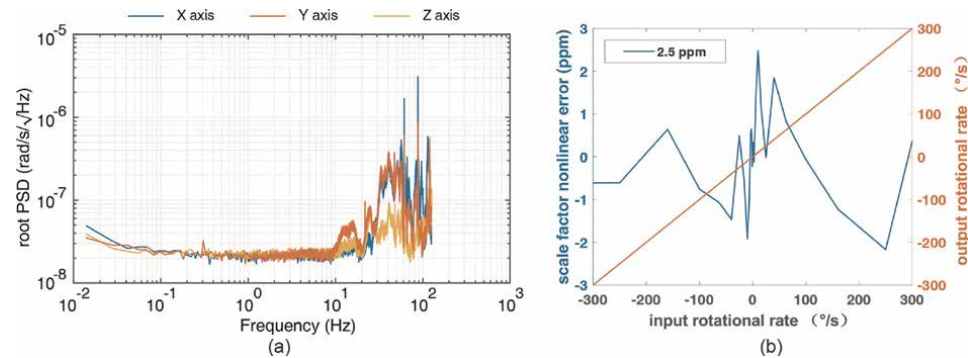


Figure 3.
(a) Self-noise and (b) scale factor nonlinearity of DP-Rot₃C.

open-loop FOGs, each with a fiber-optic coil of length 6 km. Notably, each FOG component in DP-Rot3C adopts a dual-polarization configuration [25], enabling the multiplexing of two orthogonal polarization states originating from the same light source, thus allowing enhanced simultaneous measurement of rotational ground motions.

Essentially, each component consists of two sets of highly consistent gyroscopes that act as mutual reference signals. Through the implementation of cooperative processing of two polarization states, the relative intensity noise (RIN), which is the most significant factor affecting the self-noise of FOG, is substantially suppressed. As shown in **Figure 3(a)**, the root PSD of three components of DP-Rot3C reaches $20\text{nrad/s}/\sqrt{\text{Hz}}$ from 0.01 to 125 Hz. The fluctuations observed in the high-frequency segments of the root PSD are mainly attributed to environmental vibrations.

DP-Rot3C utilizes an open-loop configuration, where the nonlinearity of the scale factor has been a limiting factor in achieving high-precision measurements and applications in seismic wave observations. The primary source of nonlinearity errors stems from the nonlinear characteristics of components in optoelectronic detection systems, including photodetectors, amplifiers, analog-to-digital converters, and piezoelectric phase modulators. To address this issue, a simple and effective compensation

Name	Self-noise ($\text{nrad/s}/\sqrt{\text{Hz}}$)	Bandwidth (Hz)	Scale factor nonlinearity (ppm)	Size ($\text{mm} \times \text{mm} \times \text{mm}$)
BlueSeis-3A	20	0.001–100	<50	318diameter \times 335
DP-Rot3C	20	0.01–125	<10	200 \times 200 \times 200
RotSensor3C [23]	120	0.005–125	<10	190 \times 190 \times 165
DP-Rot1C [27]	9	0.01–125	<3	330diameter \times 100
FOSREM-BB [28]	32	0.1 ^a –328.12	No data	360 \times 360 \times 160
FOSREM-SS [28]	49	0.01 ^a –328.12	No data	470 \times 360 \times 230
R-2 [29]	60	0.03–50	No data	120 \times 120 \times 102

^aEstimated from Allan variance curve.

Table 1.
Key performance indicators of current portable rotational seismometers.

algorithm named the k-value compensation algorithm has been proposed [26]. This algorithm models the nonlinear response error of the detection system and effectively compensates for the output angular velocity in real time within the demodulation system. Experimental results demonstrate that even after expanding the measurement range from $\pm 30^\circ/s$ to $\pm 300^\circ/s$, the k-value compensation algorithm successfully achieves a scale factor nonlinearity of only 2.5 ppm. This makes DP-Rot3C the open-loop FOG with an ultra-small scale factor nonlinearity. This enhancement ensures an accurate and linear response over a wide range of ground motion amplitudes, contributing to improved accuracy in seismic event characterization.

Table 1 gives the key performance indicators of current portable rotational seismometers.

2.4 Applications cases

Gyroscopes have emerged as crucial tools in rotational seismology, providing significant advances in various fields. In this section, three typical examples are presented, including high-speed-railway seismology, natural earthquake observation, and subsurface structure imaging.

2.4.1 High-speed-railway seismology

High-speed railway, as a critical transportation infrastructure, is characterized by its stable, punctual, and high-speed operation. In seismology, high-speed railways also generate vibration signals at different frequencies during their operation. While previous studies of high-speed railway vibrations have focused on their interference with seismic station monitoring and damage to buildings near the railway, train vibrations have rarely been considered as a source for studies of underground structure detection. Zhang et al. have proved that this signal can be regarded as a passive source

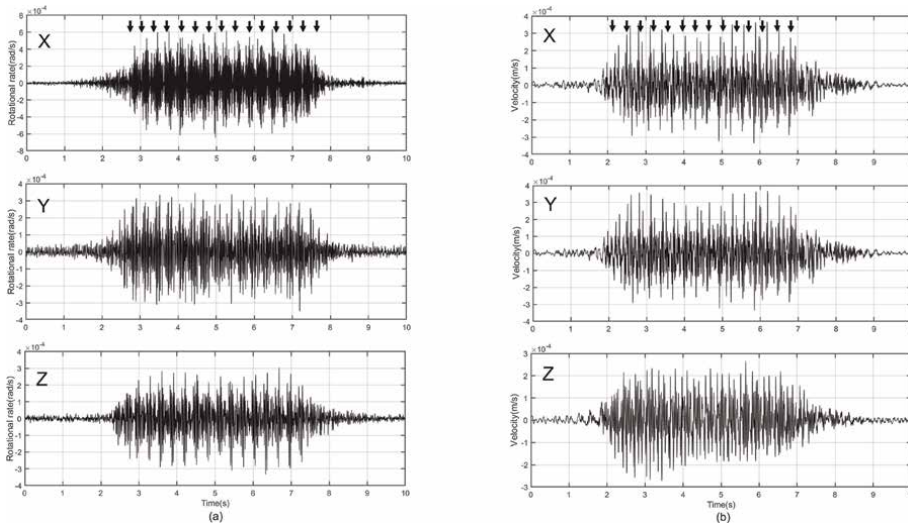


Figure 4.
Three-component waveforms recorded by a (a) rotational seismometer and (b) translational seismometer as the high-speed train passes by.

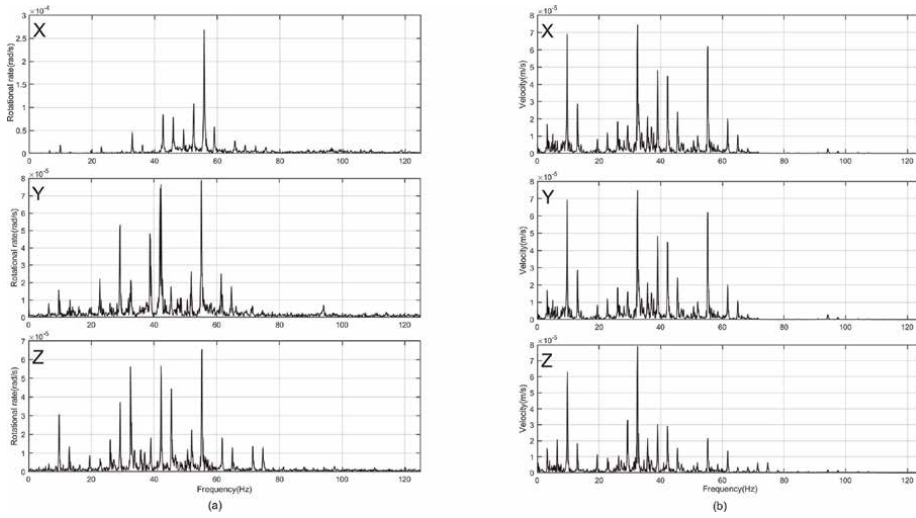


Figure 5. Amplitude spectra of the waveforms recorded by a (a) rotational seismometer and (b) translational seismometer as the high-speed train passes by.

signal that is generated regularly, which can provide new methods for geological exploration, structure detection, resource prospecting, etc. [30]. FOG-based rotational seismometers play a crucial role in accurately measuring the rotational ground motion induced by a high-speed train along a railway.

Signals from high-speed trains have been observed using FOG-based seismometers in the vicinity of high-speed railways and viaducts near Dingxing, Hebei Province, China. Vibrational signals excited by different trains were analyzed in both time and frequency domains. Additionally, a comparison was made with the signals recorded simultaneously and at the same location using a separate set of three-component translational seismometer [31].

As shown in **Figure 4**, in the time domain, both the rotational and translational signals of the ground vibration induced by the moving high-speed train show periodic phenomena caused by the grouping of 16 carriages. The period of 16 consecutive stable periodic waveforms is 0.31 s. It is deduced that the actual travel speed of the train recorded is 281 km/h. In **Figure 5**, the amplitude spectra of the signal received by the rotational seismometer and translational seismometer have 16 obvious discrete spectral lines, and the amplitude spectra energy is basically concentrated between 20 and 60 Hz, and the spacing between the discrete spectral lines is mostly 3.3 Hz. This is most likely related to the wave nature of the high-speed railway signals, which is worthy of further study.

2.4.2 Natural earthquake observation

Observations and characterization of natural earthquake events are fundamental to understanding seismic mechanisms and earthquake hazards. In addition to the examples presented in Section 2.1, a high-precision FOG-based seismic seismometer located in Wuhan successfully detected the earthquake signal of a M 6.4 earthquake in Yangbi, Yunnan province, China, which occurred at a distance of 1510 km from the observation station [32]. Using the relationship between the translational and

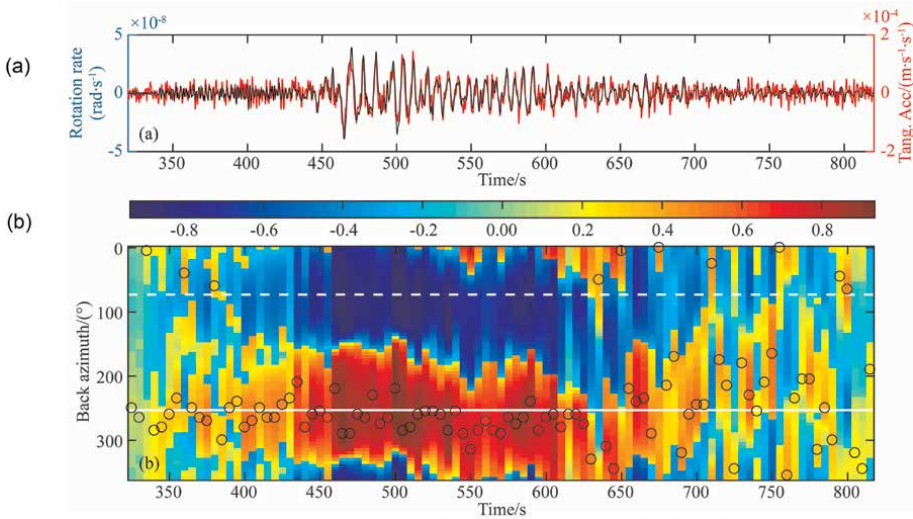


Figure 6.
(a) Vertical rotation rate and converted rotation rate from theoretical transverse accelerations. (b) back-azimuths (BAzs) estimation [32].

rotational components of the seismic wave fields, the Love wave phase velocity and incident angle beneath the station are estimated (**Figure 6**). The estimated phase velocity values are comparable to those obtained through model analysis and array processing, revealing distinct dispersion characteristics. The back-azimuth estimation suggests that the Love wave deviates slightly from the great circle path but significantly from the tail wave portion. These findings demonstrate the potential of single-point, multicomponent seismic rotation and translational wave field records in related seismological research.

2.4.3 Subsurface structure imaging

As seismic waves pass through subsurface structures, their wave fields undergo changes such as refraction, reflection, scattering, and other phenomena, which provide information about the underground structure. According to the characteristics of the seismic wave propagation, the observed seismic wave velocity, amplitude attenuation, and other information can be used to infer the underground structure, so as to complete the underground structure imaging. With the application of gyroscopes in rotational seismology, the rotational component of the seismic wave field is supplemented, and more complete information about the seismic wave field can be obtained for the study of subsurface structures.

Keil et al. conducted a single station test near the geothermal well SWMHK and BRUD station in Munich [33]. In this test, a BlueSeis-3A rotational seismometer and a Nanometrics Trillium Compact translational seismometer were used. They calculated the dispersion curves of the Love wave and Rayleigh wave, combined with the horizontal and vertical component spectral ratio (HVSr or H/V) technology of the translational component. These dispersion curves and H/V ratio are used in joint inversion, and the inversion is constrained to a three-layer model to obtain the most reliable P-wave and S-wave velocity profiles, as shown in **Figure 7**. As an application, the

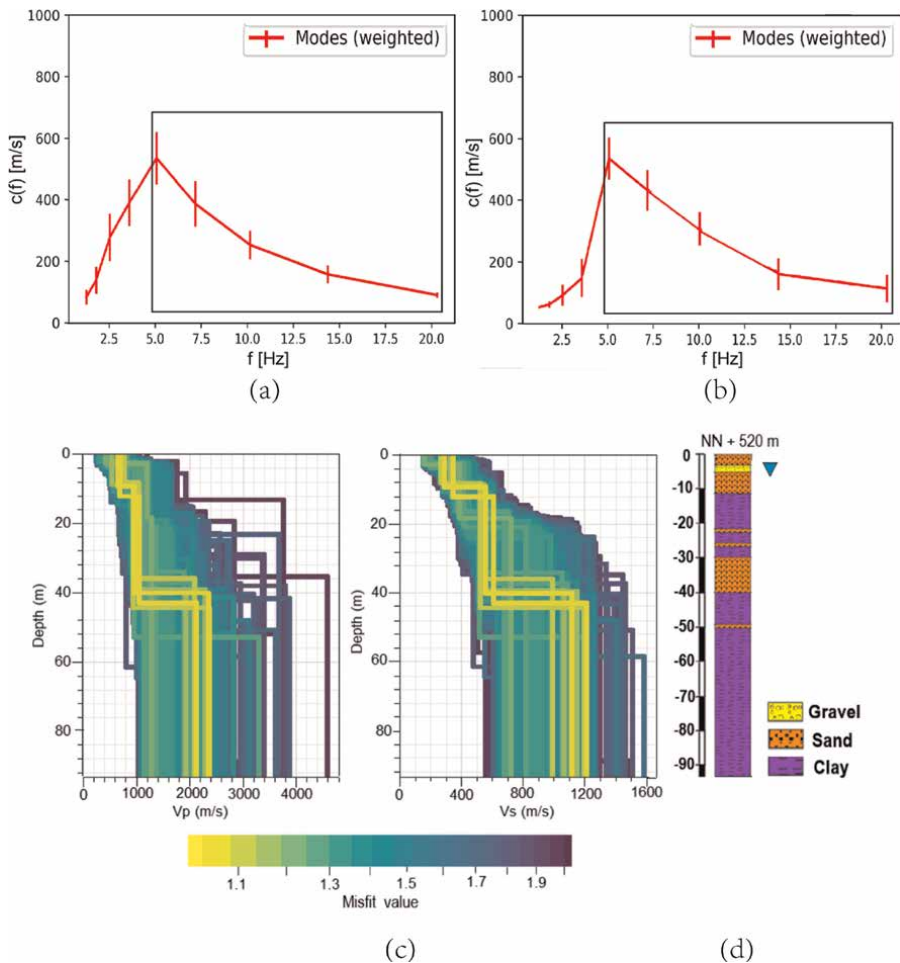


Figure 7. Estimation of (a) Love and (b) Rayleigh wave dispersion curves with BlueSeis-3A and a translational seismometer, and the resulting (c) three-layer P- and S-wave velocity profiles and (d) lithologic profile [33].

resulting 1D velocity profile will be used in future studies to estimate the local shaking characteristics in Munich.

3. Applications in the Earth's rotation

As a rotational motion sensor, the earliest application of gyroscopes was to measure the Earth's rotation. However, due to the overall stability of the Earth's rotation, variations in rotation are small. Therefore, quantitative studies of the Earth's rotation rely on high-precision gyroscopes. With the development of laser technology and optical devices, high-precision real-time measurements of the Earth's rotation using large optical gyroscopes have become the first choice.

Optical gyroscopes can directly measure the Sagnac effect caused by the Earth's rotation. Its configuration is a Sagnac interferometer, consisting of two symmetric optical paths. Inside, a path of light emitted by the light source travels in one

direction, passing through the loop and returning to the starting point. The other path of light is also emitted from the source but travels in the opposite direction, also passing through the loop and returning to the starting point. When light passes through an optical loop, it creates a phase difference caused by rotation due to the projection of the Earth's angular velocity in the plane where the loop is located. The interference phase difference ϕ_s between the two paths is

$$\phi_s = \frac{8\pi}{\lambda c} \mathbf{S} \cdot \boldsymbol{\omega}, \quad (2)$$

where λ is the central wavelength of the light, c denotes the speed of light in vacuum, \mathbf{S} represents the area vector of the closed optical loop, and $\boldsymbol{\omega}$ is the rotation velocity vector of the Earth.

At present, the technology for measuring universal time is mainly based on Very Long Baseline Interferometry (VLBI). Measurements of the Earth's rotation using this method are indirect and require observations of reference objects such as satellites beyond the Earth, the Moon, stars, or extragalactic radio sources. In contrast to VLBI, measurements using optical gyroscopes have high real-time performance and do not require the observation of a reference target source outside the Earth.

Since the end of the last century, the team led by G. E. Stedman began to build a ring laser gyroscope in New Zealand to study the Earth's tides and lunar nutations [34]. After that, the team successively built a series of large-scale laser ring gyroscopes with higher precision. A laser gyroscope named "G" for continuous Earth rotation monitoring was built by K. U. Schreiber and located at the Geodetic Observatory Wettzell, Germany [35]. As shown in **Figure 8**, the ring laser body forms a square with a side length of 4 m. The average noise level at subdaily frequencies is less than 1 part in 10^9 after an integration time of about 10^4 s [36]. This puts the detection limit for subdaily signals to 2 nrad for polar motion and 0.15 ms for length of day. In 2016, a large-scale laser gyroscope called "ROMY" (Rotational Motions in Seismology) was built and funded by the European Research Council. **Figure 9** illustrates the sensor layout in the construction. The gyroscope has four triangular square rings. It has the

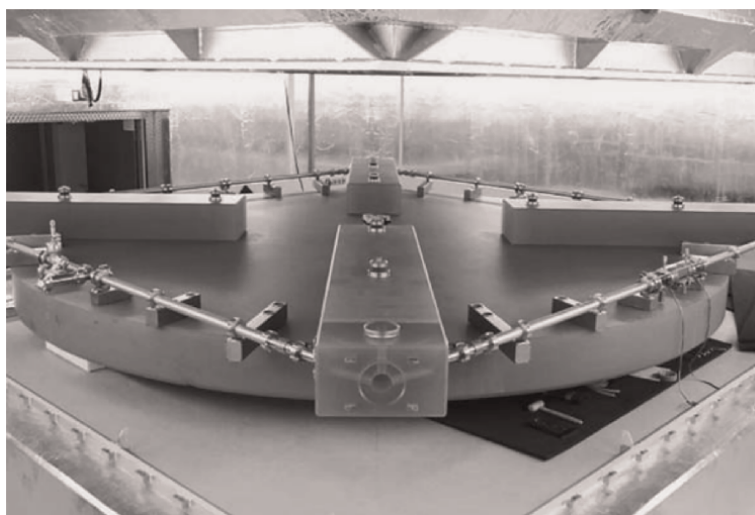


Figure 8.
 The construction of the G ring laser [35].

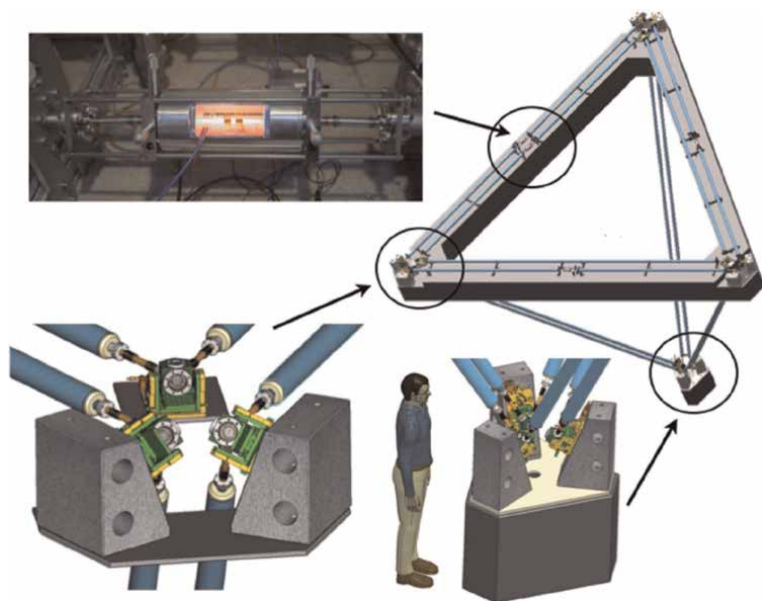


Figure 9.
The construction of ROMY [37].

advantage of being able to measure the angular velocity of the Earth's rotation in different directions simultaneously. Thus, the change of the Earth's angular velocity vector is obtained, and reconstruction of the full Earth rotation vector can be achieved with sub-arcsecond resolution over more than 6 weeks [37].

With the continuous development and maturity of fiber-optic technology, FOGs, using optical fibers instead of ring resonators, can also approach the accuracy of laser gyroscopes. With advances in fiber winding technology, researchers are able to wind larger and longer fiber-optic coils. A reference level FOG was reported in 2016 by



Figure 10.
Photograph of the large fiber-optic gyroscope and the test environment.

Honeywell. The sensing area of the fiber-optic coil is about 1000 m^2 , and the corresponding sensitivity is $4.6 \times 10^{-9}\text{ rad/s}/\sqrt{\text{Hz}}$. During a one-month test, the bias instability reached $3 \times 10^{-5}^\circ/\text{h}$ [38]. The research group at Peking University has developed a FOG for the monitoring of the Earth's rotation. As shown in **Figure 10**, a large FOG with a fiber length of 20 km and a diameter of 0.5 m has been implemented for precision measurement of universal time. It has a sensitivity of $3 \times 10^{-9}\text{ rad/s}/\sqrt{\text{Hz}}$ and a bias instability of $5 \times 10^{-6}^\circ/\text{h}$ [12, 39]. This FOG has also captured a series of seismic events during continuous operation, demonstrating its long-term capability and reliability.

4. Applications in gravimetry

The gravity field of the Earth is an important physical field in geophysical research, which is mainly determined by the density distribution of the Earth. Due to the inhomogeneous distribution of matter density on the Earth, the Earth's gravity field is inhomogeneous. The strength and direction of the gravity field will vary at different locations on the Earth. It is precisely because of this fact that through the use of gravity measuring instruments, changes in the Earth's gravity field can be measured, and thus, information can be obtained about the crustal movement, groundwater resources, and so on. The study of the Earth's gravity field is also widely used in satellite navigation, geological exploration, mapping, and other fields. In gravimetry, the parameters of the gravity field that are often measured include gravity acceleration and gravity gradient. The former is the first spatial derivative of gravity potential, while the latter is the second spatial derivative of gravity potential.

Existing gravity measurement instruments usually employ atomic interferometry [40–42] or superconducting technology [43] to achieve higher sensitivity. Among them, instruments with atomic interferometry use cold atoms as test masses to sense the gravity field. However, in the use of atomic interferometry, vacuum tubes are required to achieve a vacuum environment, and seismic isolation platforms are required to reduce the impact of ground vibrations. Besides, there are obstacles to miniaturization. Instrument with superconducting technology uses mechanical test mass as a component of sensitive gravity field, and uses a superconducting quantum interference device (SQUID) to sense changes in superconducting current caused by the displacement of test mass. SQUID converts the external motion into a displacement change, which is converted into a current response by means of inductance modulation, and finally converts it into a voltage signal by an amplifier. However, the implementation of superconducting technology relies on the construction of a stable low-temperature environment, which also requires the large environmental control equipment of magnetic shields, vacuum tubes, and cryogenic systems.

Optical fibers are generally made of quartz, which means that external electromagnetic interference (EMI) will not affect the fiber as it affects electrical wires. This allows the optical fiber to operate normally, even in a strong EMI environment. In addition, the Sagnac effect is not sensitive to the translational motion in the detection plane but only to the rotational motion of the plane [21]. This makes a FOG, which is based on the Sagnac effect and uses optical fibers as a medium, a rotational motion sensor with strong environmental adaptability. If FOG can be used in gravimetry, a new solution to the problem of environmental adaptability in existing gravity measurement instruments will be yielded.

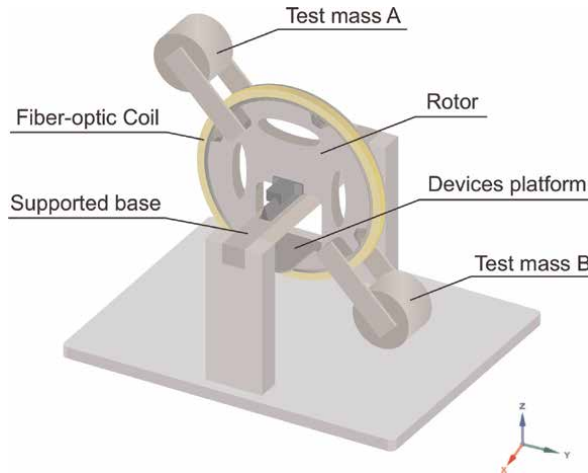


Figure 11.
Schematic diagram of the gravity gradient sensitive structure based on the fiber-optic gyroscope.

As the first attempt to apply gyroscopes to gravimetry, the research group in Peking University designed a structure based on two test masses. It used FOG to detect rotational motion due to gravity gradients [44]. As shown in **Figure 11**, the spatial distribution of the gravity field is inhomogeneous due to the existence of gravity gradient, which generates torque on the rotor by changing the gravity of the test masses at two different positions in space. This torque generates the rotational motion of the rotor and is detected by the FOG. The gravity gradient can be obtained by the relationship between the angular acceleration of rotation and the gravity gradient [44].

As shown in **Figure 12**, without the installation of a seismic isolation platform, magnetic shield, vacuum chamber, and other environmental control equipment, the self-noise level of the proposed system is estimated to be $1 \times 10^{-2} E/\sqrt{\text{Hz}}$ [$1 E \equiv 10^{-9} \text{ s}^{-2}$, where E (Eötvös) is a unit of gravity gradient]. Moreover, the self-noise of this system decreases at smaller frequencies, suggesting that long-term observations will have lower self-noise. Considering that the experimental results were observed in the nonideal experimental environment of room temperature, nonvibrational isolation, and nonmagnetic isolation, the proposed scheme has an

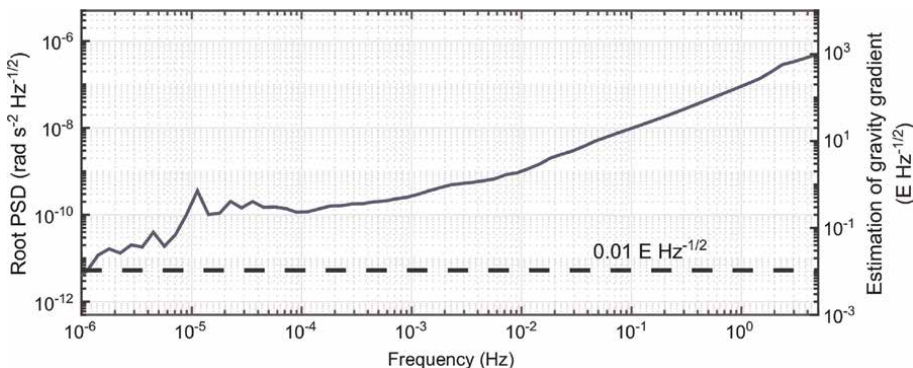


Figure 12.
Noise root power spectral density of static observations of FOG-based gravity gradient measurement system.

optimistic prospect of performance improvement. For seismic isolation, the method of differential-mode measurement can be used, using two rotors with FOG to suppress vibration in the environment [45]. At the same time, the self-noise in FOGs can be further suppressed by means of differential-mode measurements. For the temperature and magnetic field variation in the surrounding environment, on the one hand, high-order modulation can be used to reduce the temperature sensitivity of the FOG [46]; on the other hand, dual-polarization configuration can be used to improve the adaptability of the FOG to temperature and magnetic field [47, 48].

5. Conclusions


Gyroscopes have had an indissoluble relationship with geophysics since they were manufactured. With the development of gyroscopes, high-precision gyroscopes, especially optical ones, have become powerful tools for geophysical applications. In summary, the role of gyroscopes can be divided into two categories: direct and indirect measurements. In terms of direct measurements, such as the acquisition of the rotational component of seismic waves, observations of Earth's rotation, etc., it relies on the high-precision and high sensitivity properties of gyroscopes. In indirect measurements, such as the measurement of the rotational motion of a sensing probe for gravity field, the high sensitivity with strong environmental adaptability of gyroscopes is required. In the future, in terms of direct measurements, continued progress in reducing noise and improving the performance of gyroscopes will enable more precise measurements of geophysical parameters; in indirect measurements, new sensing principles based on gyroscope should continue to be explored, bringing the advantages of gyroscope, especially the strong environmental adaptability, into play in geophysical applications.

Author details

Yanjuan Chen*, Lanxin Zhu, Fangshuo Shi, Yan He and Zhengbin Li
State Key Laboratory of Advanced Optical Communication Systems and Networks,
School of Electronics, Peking University, Beijing, China

*Address all correspondence to: chenyanjuan@pku.edu.cn

IntechOpen

© 2023 The Author(s). Licensee IntechOpen. This chapter is distributed under the terms of the Creative Commons Attribution License (<http://creativecommons.org/licenses/by/3.0>), which permits unrestricted use, distribution, and reproduction in any medium, provided the original work is properly cited. 

References

- [1] Foucault L. Sur les phénomènes d'orientation des corps tournants entrainés par un axe fixe à la surface de la terre-Nouveaux signes sensibles du mouvement diurne. *Comptes rendus de l'Académie des Sciences*. 1852;**35**:424
- [2] Post EJ. Sagnac effect. *Reviews of Modern Physics*. 1967;**39**(2):475. DOI: 10.1103/RevModPhys.39.475
- [3] Michelson AA, Gale HG. The effect of the Earth's rotation on the velocity of light. *Journal of Astrophysics*. 1925;**61**:140. DOI: 10.1086/142879
- [4] Macek WM, Davis D Jr. Rotation rate sensing with traveling-wave ring lasers. *Applied Physics Letters*. 1963;**2**(3):67-68. DOI: 10.1063/1.1753778
- [5] Kao KC, Hockham GA. Dielectric-fibre surface waveguides for optical frequencies. In: *Proceedings of the Institution of Electrical Engineers*. Vol. 113. London, UK: IET; 1966. pp. 1151-1158. DOI: 10.1049/ptee.1966.0189
- [6] Pircher G, Hepner G. Perfectionnements aux dispositifs du type gyromètre à laser. French Patent. 1967:1563720
- [7] Vali V, Shorthill R. Fiber ring interferometer. *Applied Optics*. 1976; **15**(5):1099-1100. DOI: 10.1364/AO.15.001099
- [8] Aki K, Richards PG. *Quantitative Seismology*. Mill Valley, CA, USA: University Science Books; 2002
- [9] Oldham RD. Report of the Great Earthquake of 12th June, 1897. Office of the Geological Survey; 1899
- [10] Farrell W. A gyroscopic seismometer: Measurements during the Borrego earthquake. *Bulletin of the Seismological Society of America*. 1969; **59**(3):1239-1245. DOI: 10.1785/BSSA0590031239
- [11] Igel H, Schreiber U, Flaws A, Schuberth B, Velikoseltsev A, Cochard A. Rotational motions induced by the M8. 1 Tokachi-oki earthquake, September 25, 2003. *Geophysical Research Letters*. 2005;**32**(8):2365-2374. DOI: 10.1029/2004GL022336
- [12] Chen Y, Cao Y, Wang W, He Y, Zhou T, Li Z. A low self-noise fiber optic gyroscope based on dual-polarization configuration for geophysical rotation sensing. In: *Asia Communications and Photonics Conference*. Washington D.C., USA: Optica Publishing Group; 2021. pp. T4A-T49A. DOI: 10.1364/ACPC.2021.T4A.9
- [13] Jaroszewicz LR, Kurzych A, Krajewski Z, Marć P, Kowalski JK, Bobra P, et al. Review of the usefulness of various rotational seismometers with laboratory results of fibre-optic ones tested for engineering applications. *Sensors*. 2016;**16**(12):2161. DOI: 10.3390/s16122161
- [14] Kozák JT. Tutorial on earthquake rotational effects: Historical examples. *Bulletin of the Seismological Society of America*. 2009;**99**(2B):998-1010. DOI: 10.1785/0120080308
- [15] Yuan S, Gesselle K, Gabriel AA, May DA, Wassermann J, Igel H. Seismic source tracking with six degree-of-freedom ground motion observations. *Journal of Geophysical Research: Solid Earth*. 2021;**126**(3):e2020JB021112. DOI: 10.1029/2020JB021112
- [16] Lee WH, Igel H, Trifunac MD. Recent advances in rotational

seismology. *Seismological Research Letters*. 2009;**80**(3):479-490.
 DOI: 10.1785/gssrl.80.3.479

[17] Solarz L, Krajewski Z, Jaroszewicz LR. Analysis of seismic rotations detected by two antiparallel seismometers: Spline function approximation of rotation and displacement velocities. *Acta Geophysica Polonica*. 2004;**52**(2):197-218

[18] D'Alessandro A, Scudero S, Vitale G. A review of the capacitive MEMS for seismology. *Sensors*. 2019;**19**(14):3093.
 DOI: 10.3390/s19143093

[19] Evans JR, Kozák JT, Jedlička P. Developments in new fluid rotational seismometers: Instrument performance and future directions. *Bulletin of the Seismological Society of America*. 2016; **106**(6):2865-2876. DOI: 10.1785/0120150265

[20] Igel H, Schreiber KU, Gebauer A, Bernauer F, Egdorf S, Simonelli A, et al. ROMY: A multicomponent ring laser for geodesy and geophysics. *Geophysical Journal International*. 2021;**225**(1): 684-698. DOI: 10.1093/gji/ggaa614

[21] de Toldi E, Lefèvre H, Guattari F, Bigueur A, Steib A, Ponceau D, et al. First steps for a giant FOG: Searching for the limits. In: 2017 DGON Inertial Sensors and Systems (ISS). New York, USA: IEEE; 2017. pp. 1-14. DOI: 10.1109/InertialSensors.2017.8171491

[22] Bernauer F, Wassermann J, Guattari F, Frenois A, Bigueur A, Gaillot A, et al. BlueSeis3A: Full characterization of a 3C broadband rotational seismometer. *Seismological Research Letters*. 2018;**89**(2A):620-629.
 DOI: 10.1785/0220170143

[23] Cao Y, Chen Y, Zhou T, Yang C, Zhu L, Zhang D, et al. The development

of a new IFOG-based 3C rotational seismometer. *Sensors*. 2021;**21**(11):3899.
 DOI: 10.3390/s21113899

[24] Bernauer F, Wassermann J, Igel H. Rotational sensors—A comparison of different sensor types. *Journal of Seismology*. 2012;**16**:595-602.
 DOI: 10.1007/s10950-012-9286-7

[25] He D, Cao Y, Zhou T, Peng C, Li Z. Sensitivity enhancement through RIN suppression in dual-polarization fiber optic gyroscopes for rotational seismology. *Optics Express*. 2020; **28**(23):34717-34729. DOI: 10.1364/OE.409377

[26] Zhu L, Cao Y, Huang H, Chen Y, Wang W, Ma X, et al. Compensation of scale factor nonlinear error introduced by harmonic distortion for open-loop fiber optic gyroscopes. *Optics Letters*. 2023;**48**(6):1351-1354. DOI: 10.1364/OL.483911

[27] Zhou T, Zhu L, Cao Y, Chen Y, Huang H, Li Z. Realization and performance tests of a dual-polarization fiber optic gyroscope. In: Eighth Symposium on Novel Photoelectronic Detection Technology and Applications. Vol. 12169. Bellingham, WA, USA: SPIE; 2022. pp. 1995-1998. DOI: 10.1117/12.2625105

[28] Kurzych A, Jaroszewicz LR, Krajewski Z, Sakowicz B, Kowalski JK, Marć P. Fibre-optic Sagnac interferometer in a FOG minimum configuration as instrumental challenge for rotational seismology. *Journal of Lightwave Technology*. 2018;**36**(4): 879-884. DOI: 10.1117/12.2625105

[29] Agafonov V, Neeshpapa A, Shabalina A. Electrochemical seismometers of linear and angular motion. In: *Encyclopedia of Earthquake*

Engineering. Berlin, Germany: Springer-Verlag; 2015. pp. 1-19. DOI: 10.1007/978-3-642-36197-5_403-1

[30] Zhang H, Wang B, Ning J, Li Y. Interferometry imaging using high-speed-train induced seismic waves. *Chinese Journal of Geophysics*. 2019; **62**(6):2321-2327. DOI: 10.6038/cjg2019M0676

[31] Cao Y, Teng Y, Li Z, Zhang D, Zeng W. Signal characteristics of rotation seismograph records in ground vibration induced by high-speed train running. In: *Proceedings of CGU, 2020*. Chongqing: Institute of Geophysics, China Earthquake Administration; 2020. pp. 2177-2180

[32] Cao Y, Zeng X, Li Z. Rotational and translational motions induced by the Ms6.4 Yunan Yangbi earthquake recorded by co-located FOGs and seismometer. *Chinese Journal of Geophysics*. 2022;**65**(2):663-672. DOI: 10.6038/cjg2022P0551

[33] Keil S, Wassermann J, Igel H. Single-station seismic microzonation using 6C measurements. *Journal of Seismology*. 2021;**25**:103-114. DOI: 10.1007/s10950-020-09944-1

[34] Stedman G, Hurst R, Schreiber K. On the potential of large ring lasers. *Optics Communications*. 2007;**279**(1): 124-129. DOI: 10.1016/j.optcom.2007.07.011

[35] Schreiber KU, Klügel T, Velikoseltsev A, Schlüter W, Stedman G, Wells JPR. The large ring laser G for continuous Earth rotation monitoring. *Pure and Applied Geophysics*. 2009;**166**: 1485-1498. DOI: 10.1007/s00024-004-0490-4

[36] Di Virgilio A, Terreni G, Basti A, Beverini N, Carelli G, Ciampini D, et al.

Overcoming 1 part in 10^9 of Earth angular rotation rate measurement with the G Wettzell data. *The European Physical Journal C*. 2022;**82**(9):824. DOI: 10.1140/epjc/s10052-022-10798-9

[37] Gebauer A, Tercjak M, Schreiber KU, Igel H, Kodet J, Hugentobler U, et al. Reconstruction of the instantaneous Earth rotation vector with sub-arcsecond resolution using a large scale ring laser array. *Physical Review Letters*. 2020;**125**(3):033605. DOI: 10.1103/PhysRevLett.125.033605

[38] Sanders GA, Sanders SJ, Strandjord LK, Qiu T, Wu J, Smiciklas M, et al. Fiber optic gyro development at Honeywell. In: *Fiber Optic Sensors and Applications XIII*. Vol. 9852. Bellingham, WA, USA: SPIE; 2016. pp. 37-50. DOI: 10.1117/12.2228893

[39] Chen Y, Cao Y, Zhu L, Wang W, He Y, Huang H, et al. A bias-instability-enhanced dual-polarization fiber-optic gyroscope for precision measurement. In: *CLEO: Fundamental Science*. Washington D.C., USA: Optica Publishing Group; 2023. pp. JTu2A-JTu30A. DOI: 10.1364/CLEO_AT.2023.JTu2A.30

[40] Sorrentino F, Bodart Q, Cacciapuoti L, Lien YH, Prevedelli M, Rosi G, et al. Sensitivity limits of a Raman atom interferometer as a gravity gradiometer. *Physical Review A*. 2014; **89**(2):023607. DOI: 10.1103/PhysRevA.89.023607

[41] Wu X, Pagel Z, Malek BS, Nguyen TH, Zi F, Scheirer DS, et al. Gravity surveys using a mobile atom interferometer. *Science Advances*. 2019; **5**(9):eaax0800. DOI: 10.1126/sciadv.aax0800

[42] Mao DK, Deng XB, Luo HQ, Xu YY, Zhou MK, Duan XC, et al.

A dual-magneto-optical-trap atom gravity gradiometer for determining the Newtonian gravitational constant. Review of Scientific Instruments. 2021; **92**(5):053202. DOI: 10.1063/5.0040701

[43] Moody M. A superconducting gravity gradiometer for measurements from a moving vehicle. Review of Scientific Instruments. 2011;**82**(9): 094501. DOI: 10.1063/1.3632114

[44] Chen Y, Wang W, He Y, Cao Y, Zhu L, Huang H, et al. Fiber-optic Sagnac interferometry for gravity gradient measurements. IEEE Transactions on Instrumentation and Measurement. 2023;**72**:1-11. DOI: 10.1109/TIM.2022.3229732

[45] Chen Y, Zhu L, Cao Y, Wang W, Huang H, He Y, et al. Suppression of self-noise and environmental disturbances by fusion in fiber-optic gyroscopes for precision measurement. IEEE Sensors Journal. 2023;**23**(13): 14084-14094. DOI: 10.1109/JSEN.2023.3272042

[46] Chen Y, Cao Y, Zhu L, He Y, Wang W, Huang H, et al. Suppression of effects of temperature variation by high-order frequency modulation in large fiber-optic gyroscopes. Applied Physics Letters. 2023;**122**(14):141102. DOI: 10.1063/5.0135848

[47] Luo R, Li Y, Deng S, He D, Peng C, Li Z. Compensation of thermal strain induced polarization nonreciprocity in dual-polarization fiber optic gyroscope. Optics Express. 2017;**25**(22):26747-26759. DOI: 10.1364/OE.25.026747

[48] Liu P, Li X, Guang X, Xu Z, Ling W, Yang H. Drift suppression in a dual-polarization fiber optic gyroscope caused by the Faraday effect. Optics Communications. 2017;**394**:122-128. DOI: 10.1016/j.optcom.2017.03.030



Edited by Walter Salazar

Earthquake Ground Motion is a compilation of ten chapters covering tectonics, seismicity, site effects, tsunamis, infrastructure, and instrumentation. It presents state-of-the-art techniques for retrieving rupture models, seismogenic structures, and validation of focal mechanisms. It also presents macroseismic archiving tools for historical and instrumental earthquakes and the fundamentals of seismic tomography. The book describes the site response analysis in 2D and 3D, considering topographic and soil structure interactions, its incorporation in a seismic hazard analysis, and the impact of earthquakes on the cost of reconstruction. The final sections are devoted to the genesis of earthquakes tsunamis, non-seismic tsunamis, and the new role of gyroscopes in rotational seismology.

Published in London, UK

© 2024 IntechOpen
© Leoco / iStock

IntechOpen

